Semiconductors, Vol. 37, No. 7, 2003, pp. 741–743. Translated from Fizika i Tekhnika Poluprovodnikov, Vol. 37, No. 7, 2003, pp. 769–771.

CONFERENCE. REVIEW

III International Conference on Amorphous and Microcrystalline Semiconductors (July 2–4, 2002)

E. I. Terukov (the Chairperson of Organizing Committee of the Conference)

Ioffe Physicotechnical Institute, Russian Academy of Sciences, Politekhnicheskaya ul. 26, St. Petersburg, 194021 Russia
e-mail: eug.terukov@pop.ioffe.rssi.ru

The III International Conference on Amorphous and Microcrystalline Semiconductors was held in St. Petersburg on July 2–4, 2002. This conference was organized by the Russian Academy of Sciences represented by the Ioffe Physicotechnical Institute; the chairperson of the organizing committee of the conference was E.I. Terukov, the cochairperson was K.D. Tséndin, and the secretary of the organizing committee was I.N. Trapeznikova.

There were 181 papers presented at the conference. The participants included scientists from France, Bulgaria, Canada, Latvia, and a number of scientists from the Commonwealth of Independent States (Russia, Ukraine, Belarus, Kazakhstan, Moldova, and Azerbaijan).

The traditional "Kolomiets lecture," concerned now with the embedding of metallic nanoclusters in amorphous carbon, was delivered by Doctor of Physical and Mathematical Sciences V.I. Ivanov-Omskiĭ (who is now in charge of the laboratory headed previously by B.T. Kolomiets at the Ioffe Physicotechnical Institute). During the plenary session, the lectures were delivered by leading scientists in the field of unordered semiconductors; these scientists included S.P. Vikhrov (Ryazan State Academy of Radio Engineering), Yu.S. Tver'yanovich (St. Petersburg State University), K.D. Tséndin (Ioffe Physicotechnical Institute, Russian Academy of Sciences, St. Petersburg), É.N. Voronkov (Moscow Power Engineering Institute), D.A. Kurdyukov (Ioffe Physicotechnical Institute, Russian Academy of Sciences, St. Petersburg), T.A. Yurre (St. Petersburg Technological University), and Jean-Paul Kleider (L.G.E.P-SUPERLEC, CNRS, France). The aforementioned lectures included reviews of the recent progress in the physics of chalcogenide vitreous semiconductors, amorphous materials, and photoconductive polymers.

The scope of the conference encompassed the following topics:

(1) Amorphous hydrogenated silicon and its solid solutions;

(2) Amorphous and diamond-like carbon;

(3) Microcrystalline and nanocrystalline semiconductors;

(4) Photoconductive polymers;

(5) Chalcogenide vitreous semiconductors; and

(6) Technical applications.

In the papers devoted to amorphous silicon, much attention was given to various technologies for fabricating amorphous films and to the interrelation between methods for fabricating films and properties of impurity and defect states, which affect such physical properties as electrical conductivity, luminescence, and optical absorption. The attention of participants was attracted to the papers delivered by V.A. Yukhimchuk (Institute of Semiconductor Physics, National Academy of Sciences of Ukraine, Kiev), A.A. Sherchenkov (State Institute of Electronic Engineering, Zelenograd), S.P. Vikhrov (Ryazan State Academy of Radio Emgineering), A.N. Nazarov (Institute of Semiconductor Physics, National Academy of Sciences of Ukraine, Kiev), A.V. Medvedev (Ioffe Physicotechnical Institute, Russian Academy of Sciences, St. Petersburg), and M.M. Mezdrogina (Ioffe Physicotechnical Institute, Russian Academy of Sciences, St. Petersburg). The papers delivered by A.N. Nazarov dealing with the study of defect formation in films of hydrogenated amorphous silicon doped with erbium were of particular interest. The use of thermally activated, current, and capacitance spectroscopies made it possible to determine the positions of deep levels introduced into the band gap of amorphous silicon owing to doping with erbium. The corresponding studies are particularly topical in connection with the potential use of this material in electroluminescent and laser structures designed for the emission wavelength of 1.54 μm. We should mention the studies concerned with developing physical models for charge transport in a system consisting of a metal and an unordered semiconductor (a team of scientists from the Ryazan State Academy of Radio Engineering under the supervision of Professor S.P. Vikhrov) and with mechanisms of charge transport in heterostructures composed of amorphous semiconductor and crystalline silicon (A.A. Sherchenkov and coworkers); these studies are of interest for practical applications.

Much attention of the conference's participants was attracted to the technology of fabrication and to properties of nanostructured and microcrystalline silicon samples obtained by different methods. Interest in these materials is caused, on the one hand, by their high stability under illumination and, on the other hand, by the emergence of new size-related effects.

1063-7826/03/3707-0741$24.00

In the papers concerned with amorphous and diamond-like carbon, various methods for obtaining films of these materials were considered. Particular interest was attracted to the methods for doping the corresponding films and to studies of the special morphological features of these films using scanning electron microscopy, electron spin resonance, and small-angle X-ray scattering. The approach reported in the papers by Yu.F. Biryulin (Ioffe Physicotechnical Institute, Russian Academy of Sciences, St. Petersburg) and related to the possibility of forming diamond films obtained using chemical-vapor deposition and nanodiamond precursors was highly interesting. In this session, much attention was payed to thin films of other wide-gap semiconductors, in particular, of GaN and AlN (V.V. Krivolapchuk from the Ioffe Physicotechniocal Institute, Russian Academy of Sciences, St. Petersburg; and V.P. Afanas'ev, Electrotechnical University, St. Petersburg) and to films of hydrogenated boron carbide (A.S. Anan'ev, Ioffe Physicotechnical Institute, Russian Academy of Sciences, St. Petersburg).

A session devoted to organic semiconductors was included in the conference program for the first time. This session focused on polymeric semiconductors, which can find application both in solar power conversion and in microelectronics. The review paper concerned with organic materials for photovoltaics was delivered by T.A. Yurre (St. Petersburg Technological University) and the one concerned with light-sensitive polymeric semiconductors was presented by E.L. Aleksandrova (Research Institute of Optical Materials Technology "Vavilov State Optical Institute," All-Russia Scientific Center, St. Petersburg). Interesting and original papers concerned with electroluminescnce of inhomogeneous thin-film organic structures and with photosensitive and electroluminscent polymer–semiconductor composites were delivered by A.V. Kukhto (Institute of Molecular and Atomic Physics, Minsk) and M.A. Kurbanov (Institute of Physics, Academy of Sciences of Azerbaijan, Baku), respectively.

The fourth topic in the conference scope was widely represented by papers concerned with nanocrystalline, microcrystalline, and porous silicon, as well as with iron disilicide. An interesting paper concerned with the effect of impurity vibrations on the luminescence of erbium ions in an opal–erbium composite and delivered by V.G. Golubev (Ioffe Physicotechnical Institute, Russian Academy of Sciences, St. Petersburg) is worth mentioning. An unusual approach, reported in the paper delivered by M.E. Kompan (Ioffe Physicotechnical Institute, Russian Academy of Sciences, St. Petersburg), was concerned with the Coulomb mechanism for the self-formation of structure in porous silicon. The papers concerned with the formation of $FeSi_2$ precipitates as a result of solid-state crystallization of amorphous Si doped with Fe (E.I. Terukov and coworkers, Ioffe Physicotechnical Institute, Russian Academy of Sciences, St. Petersburg) deserve attention. A series of studies concerned with the formation of diamond clusters during preparation of nanoporous carbon in silicon carbide (A.A. Danishevskiĭ and coworkers, Ioffe Physicotechnical Institute, Russian Academy of Sciences, St. Petersburg) deserves attention. The papers delivered by A.G. Kazanskiĭ (Moscow State University, I.A. Kurova (Moscow State University), K. Koughia (University of Saskatchewan, Canada), V.V. Sobolev (Izhevsk State University), and É.A. Lebedev (Ioffe Physicotechnical Institute, Russian Academy of Sciences, St. Petersburg) were aimed at gaining insight into the structural, optical, and transport properties of microcrystalline, nanosstructered, and porous materials.

In the field of chalcogenide (and other) vitreous semiconductors, major attention was attracted to papers devoted to the structure and properties of chalcogenide vitreous semiconductors doped with rare-earth elements; these papers were presented by M.S. Iovu (Institute of Applied Physics, Academy of Sciences of Moldova, Chisinau), S.A. Kozyukhin (Institute of General and Inorganic Chemistry, Russian Academy of Sciences, Moscow), B.G. Tagiev (Institute of Physics, Academy of Sciences of Azarbaijan, Baku), and A.S. Tver'yanovich (St. Petersburg State University). The aforementioned semiconductors are promising materials for active and passive components designed for operation in the infrared region of the spectrum. The use of these materials in planar devices is of particular interest; in this context, much attention is given to the problem of obtaining homogeneous thin films which are formed of the materials under consideration and have a specified composition. Attention was attracted to the papers concerned with electrical conductivity of As_2S_3 glasses doped lightly with Au (A.A. Babaev, Institute of Physics, Dagestan Scientific Center, Russian Academy of Sciences, Makhachkala), simulation of streamer breakdown in thin films of chalcogenide vitreous semiconductors (A.P. Faĭrushin, Moscow Power Engineering Institute), and electron-stimulated variations in optical properties of amorphous Ge–As(Sb)–S films (V. Pamukchieva, Bulgarian Institute of Physics, Sofia). A series of studies performed by a team headed by V.V. Sobolev (Izhevsk State University) and concerned with calculations of the spectra of fundamental optical functions of selenides, sulfides, and chalcogenides of various elements is worth mentioning.

Many papers dealing with technical applications were presented at the conference. The paper presented by M.Sh. Abdulvagabov (Dagestan State University, Makhachkala) was devoted to the development of electroluminescent structures that emitted in the blue region of the spectrum and were based on amorphous *a*-C:H films. Special features of light-emitting devices based on monolayers of a luminophor microcrystal were reported in the paper presented by A.I. Andreev (Academy of Civil Defense, Ministry of Emergency Situations, Novogorsk, Moscow oblast). V.P. Afanas'ev and coworkers (Electrotechnical University, St. Petersburg) presented a paper devoted to the development of photodetector structures that were based on aluminum nitride

and were photosensitive in the ultraviolet region of the spectrum. Particular attention should be paid to the papers concerned with the development of electroluminescent microminiature displays based on porous silicon (S.K. Lazaruk and coworkers, Belarussian State University of Information Science, Minsk) and with electroluminescent *p–i–n* structures that are based on amorphous silicon doped with erbium and emit at a wavelength of 1.54 μm under a forward bias (E.I. Terukov *et al.*). There has been progress in the field of holographic recording of information (a team headed by Ya. Teteris at the Physical Institute of Latvian University, Riga).

It was noted at the closing round-table discussion that the conference was timely and topical and that the presented papers were of high scientific quality. A great number of studies were carried out at a high scientific level, which corresponds with the current state of world science and is evidenced by participation of scientists from Russia and the Commonwealth of Independent States in international conferences with the same scope as this conference. The treatment of many problems was innovative, and the corresponding results are very important. For example, I can mention the development and study of photonic crystals based on opal–GaP(N) nanocomposite, the use of chemical vapor deposition and nanodiamond precursors to synthesize diamond films on various substrates, the production of amorphous boron carbide films for passivation of the walls in tokamak reactors, the development of new photoconductive materials based on polymers, the use of porous silicon in the development of microdisplays, and visualization of surface defects in semiconductors using nematic liquid crystals.

The degree of provision of the field under consideration with scientific personnel corresponds to contemporary state of Russian science; in particular, this circumstance manifests itself in the fact that a great number of the studies reported at the conference were supported by international agencies (INTAS, NATO, CRDF). According to the data mentioned in the abstracts of the papers presented at the conference, 23 participants of the conference are supported in their studies by the Russian Foundation for Basic Research; 31, by the Ministry of Education; and 13, by the Ministry of Industry and Science.

Scientific level of all presented papers was quite high. Proceedings of the conference were published The Program Committee recommended to publish the most interesting papers from the conference in this issue of “Fizika i tekhnika poluprovodnikov” (“Semiconductors”).

The conference was made possible owing to the support of the Russian Foundation for Basic Research (project no. 02-02-26084) and the Ioffe Physicotechnical Institute, Russian Academy of Sciences.

Translated by A. Spitsyn

Semiconductors, Vol. 37, No. 7, 2003, pp. 744–747. Translated from Fizika i Tekhnika Poluprovodnikov, Vol. 37, No. 7, 2003, pp. 772–775.

CONFERENCE. ELECTRONIC AND OPTICAL PROPERTIES OF SEMICONDUCTORS

Electron Diffraction Investigation of Structural Diversity of Amorphous Films of Polymorphic $TlInS_2$

D. I. Ismailov[1], M. V. Alieva, E. Sh. Alekperov, and F. I. Aliev

Institute of Physics, Academy of Sciences of Azerbaijan, pr. Dzhavida 33, Baku, 370143 Azerbaijan
e-mail: physic@physics.ab.az

Submitted December 23, 2002; accepted for publication December 27, 2002

Abstract—The conditions of film formation in the Tl–In–S system are investigated by electron diffraction. It is shown that the system of alloys with a gradually varying composition involves all compounds of this system. It is found that forming amorphous films composed of $TlInS_2$ are polymorphic. Three various amorphous films, which crystallize at different values of $S = 4\pi\sin\theta/\lambda$ in tetragonal, monoclinic, and orthorhombic crystal systems, are observed at the condensation plane. *© 2003 MAIK "Nauka/Interperiodica".*

1. INTRODUCTION

Among ternary semiconductor compounds, whose semiconductor properties can be controlled in a wide range the $A^{III}B^{III}C_2^{VI}$ compounds of elements of Groups III and VI of the periodic table attract the greatest attention.

Numerous publications are devoted to the structural analysis of $A^{III}B^{III}C_2^{VI}$ compounds, and the X-ray diffraction investigations of various compounds of this system are reported [1–12]. Despite this fact, films of $A^{III}B^{III}C_2^{VI}$ compounds have not yet been investigated in detail. Preliminary data on these films are still very limited. We have investigated $TlInSe_2$, $TlInTe_2$, and $TlGaSe_2$ thin films [13–15] in a wide range from room temperature to –50°C and at substrate temperatures approximately 50–70°C below the melting points of compounds.

We found the conditions for obtaining the above films in the amorphous state with corresponding values of $S = 4\pi\sin\theta/\lambda$ and determined their kinetic parameters of crystallization. We also explored the possibility of the existence of long-period superstructural phases in these films.

The purpose of this study is to obtain thin films of alloys in the TlInS system with a gradual variation of the component content (in the case of simultaneous and sequential evaporation) in the alloys obtained and to determine the conditions for the formation of thin films of the $TlInS_2$ ternary compound.

2. EXPERIMENTAL

Films of the TlS–InS system were evaporated in vacuum at a residual pressure no higher than 10^{-5} Pa. Three sources made of W conical coils were positioned over the condensation plane. The end coils, from which Tl and In were evaporated, were 15 cm apart. These sources were placed 7 cm above freshly cleaved single-crystals of rock salt, which served as the substrate for the condensation of individual elements. A third S source was positioned 8 cm above the substrate plane exactly between the Tl and In sources. Such an arrangement of the evaporators relative to the substrates, which were degassed in vacuum at 250°C for 2 h, made it possible to obtain films with the highest homogeneity. Initially, separate Tl, In, and S layers were obtained, and the distribution law of the prepared elements over the substrate was found. Then, we determined the atomic concentration over the wedges, and chose the evaporation mode such that the simultaneous or sequential evaporation of Tl, In, and S yielded uniform atomic concentrations corresponding to the compounds of the Tl–In–S system in the evaporation plane. The system of alloys thus obtained approximately contains 0 to 100% Tl, 100 to 0% In, and 100% S in the center to 0% at the edges of the plane. Such a system with gradually varying composition involves all compounds of this system.

Upon obtaining the films of the Tl–In–S system, the films were placed into carbon capsules [16–18] to prevent oxidation of Tl and reevaporation of S and In during subsequent heat treatment. The phase composition of the films formed under simultaneous and sequential deposition of Tl, In, and S was studied by the transmission method using ÉG and an ÉMR-102 electron diffractometers. The total thickness of the films was ~500 Å including carbon films, whose thickness was no larger than 100 Å. According to the published data, the following phases are formed in the Tl–In–S system: Tl_2S, Tl_4S_3, TlS, TlS_2, Tl_8S_{17}, Tl_2S_5, In_2S, InS, In_6S_7, In_4S_5, In_3S_4, and In_2S_3. There are no crystallographic data on In_2S and InS in the literature. The structural characteristics of compounds of the Tl–In–S system for bulk samples and the values of $S = 4\pi\sin\theta/\lambda$, which correspond to diffuse lines in the electron diffraction

Characteristics of amorphous and crystalline phases of the Tl–In–S system

Phase	Crystal system	Space group	*a*, Å	*b*, Å	*c*, Å	$S = 4\pi\sin\theta/\lambda$				Reference
Tl_2S	Hexagonal	R_3	12.20		18.17	1.420	2.200	3.410		[16, 19]
Tl_4S_3	Monoclinic	$P2_1/a$	7.87	7.76	13.03	2.200	3.760			[16, 20]
TlS	Tetragonal	$I4/mcm$	7.79		6.80	1.780	2.150	3.430	5.41	[16, 21]
TlS_2	Tetragonal	$P4_2/nmc$	23.20		54.80					[16, 22]
Tl_2S_5 (red)	Orthorhombic	$P2_12_12_1$	6.66	6.52	16.75	1.440	2.200	4.300		[16, 23]
Tl_2S_5 (black)	Orthorhombic	$Pbcn$	23.45	8.88	10.57					[16, 21]
Tl_8S_{17}	Cubic		10.60							[16]
In_2S										[24]
InS										[24]
In_6S_7	Monoclinic	$P2_1/m$	9.09	3.89	17.71	1.930	3.110	4.700		[25]
In_3S_4	Hexagonal		9.86		20.50					[26]
In_2S_3	Tetragonal	$I4/amd$	7.61		32.24	2.110	3.380	5.360		[27]
In_4S_5	Hexagonal		7.59		20.30	2.450	3.810	4.200		[26]
$TlInS_2$	Tetragonal	$I4/mcm$	7.74		30.03	2.361	3.925	6.274		[1]
$TlInS_2$	Tetragonal	$I4/mcm$	8.00		6.72					[28]
$TlInS_2$	Tetragonal	$I4/mcm$	7.68		29.76					[28]
$TlInS_2$	Hexagonal	$P6/mcm$	7.67		14.98					[29]
$TlInS_2$	Monoclinic	$P2_1/m$	7.76	7.76	30.01					[29]
$TlInS_2$	Monoclinic	$P2_1/m$	7.77	7.74	24.0	2.032	2.606	3.843		[29]
$TlInS_2$	Monoclinic	$Cs^4C_{2h}^6$	10.95	10.95	15.14					[5]
$TlInS_2$	Orthorhombic	D_{6h}^2	6.56	3.81	14.94	1.502	2.473	3.886		[5]

patterns obtained in this study from amorphous films of a specific phase, are given in the table.

3. RESULTS AND DISCUSSION

The electron diffraction investigation was carried out initially for the films formed with the simultaneous deposition of Tl, In, and S vapors on the substrate kept at room temperature. The substrate regions were outlined for which, according to the calculated concentrations of starting components, the formation of series of compounds of the Tl–S and In–S systems should most likely be expected. Investigations showed that these regions contain four and three amorphous phases, respectively.

The values of $S = 4\pi\sin\theta/\lambda$ corresponding to diffuse halos observed in electron diffraction patterns obtained from various compounds of the Tl–In–S system are listed in the table. The heat treatment of the films in an electron diffractometer column at 150–250°C caused their crystallization. All of the films that crystallized, namely, Tl_2S, T_4S_3, TlS, Tl_2S_5, In_6S_7, In_2S_3, and In_3S_5, excluding Tl_4S_3, are polycrystalline. The Tl_4S_3 films are textured. The structure axis *c* is directed normally to the substrate surface.

It turned out that, in the temperature range investigated, in contrast with other compounds of the $A^{III}B^{III}C_2^{VI}$ system ($TlInSe_2$, $TlGaSe_2$, $TlInTe_2$, $TlGaTe_2$, and $TlGaS_2$), the $TlInS_2$ compound possesses certain unique features. The first of these specific features is the polymorphism of amorphous $TlInS_2$ films formed upon simultaneous evaporation. Specifically, three different amorphous films which are closely spaced are observed in the condensation plane. These films possess different values of $S = 4\pi\sin\theta/\lambda$ and are tetragonal [28], monoclinic [5], or orthorhombic [5]. Depending on the method of obtaining the films, for example, in the case of sequential evaporation, amorphous phases can only be either tetragonal or monoclinic irrespective of the order of component deposition.

In this case, amorphous films of the orthorhombic phase are not formed. A second specific feature of this ternary compound is the observed dimorphism of the $TlInS_2$ monoclinic phase.

The third specific feature consists in the fact that the higher the evaporation rate and, correspondingly, the interdiffusion rate, the farther apart are the interfaces between amorphous phases of the $TlInS_2$ films. Finally, it is known that only the In_2S_3 amorphous phase exists

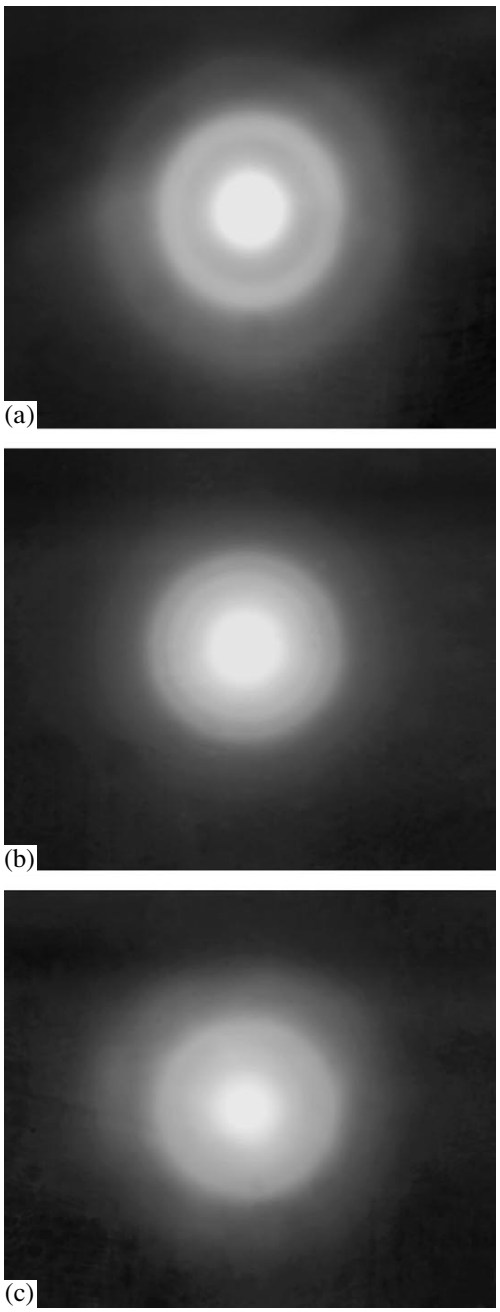

Electron diffraction patterns of (a) tetragonal, (b) monoclinic, and (c) orthorhombic films.

in the films of the In–S system [30] in contrast with the Tl–S system [16], where amorphous films are formed in a wide composition range. The presence of the third component in the Tl–In–S system causes the formation of the In_6S_7 and In_3S_5 amorphous phases along with the In_2S_3 phase.

Reliable data concerning the influence of Tl on the formation of amorphous In–S films is not available. However, we assume that this phenomenon is the consequence of the influence of Tl atoms that differ greatly in ion radius from In and S ions, which prevents the formation of a crystal lattice with strong bonds. Therefore, similarly to the Tl–S system, amorphous films in this system are formed in a rather wide composition range.

The amorphous films which were obtained on substrates spaced 55 mm apart from the Tl evaporator center towards the S evaporator and positioned in the middle of the condensation plane were heat treated. This allowed us to reveal the monoclinic polycrystalline $TlInS_2$ compound [29] with lattice constants a = 7.77, b = 7.74, and c = 24.04 Å, and the space group $P2_1/m$. The further recrystallization heat treatment of this film at 400°C leads to the phase transition and to the formation of the known monoclinic cell with parameters a = 7.76, b = 7.76, and c = 30.01 Å [29]; the space group remains unchanged.

Upon the heat treatment (at 220°C) of amorphous films which were obtained on the substrate positioned directly under the S source the $TlInS_2$ films are tetragonal [1]. The crystallization of the amorphous films which were placed at ~240°C on the substrates spaced 5–7 mm from the center of the condensation plane towards the In evaporator allowed us to ascertain an orthorhombic $TlInS_2$ phase [5]. The electron diffraction patterns from the amorphous $TlInS_2$ phases are shown in the figure.

The issue concerning the formation of polymorphic amorphous $TlInS_2$ films is more complicated. However, it is known that the formation of amorphous structures is more probable for systems whose ratio of atomic radii is larger than 1.10 [31].

For the TlS–InS system under consideration, this ratio is 1.8 for the Tl–S pair and 1.7 for the In–S pair (Tl ~ 1.71 Å, In ~ 1.66 Å, and S ~ 0.95 Å). Therefore, here, the formation of amorphous systems is most probable, which explains the production of neutral complexes of the type of amorphous films for various polymorphs of the $TlInS_2$ compound.

Thus, the same $TlInS_2$ compound forms amorphous films which differ in structure and are stable at room temperature. The fact that there are no considerable voids over the cell volume that have 64 atoms fixed in them in tetragonal, monoclinic, and orthorhombic polymorphs of $TlInS_2$ is also favorable for this phenomenon. For such internally stressed and, as a rule, easily deformed lattices with partial disclinations, lattice dislocations, and other strain sources localized in them, the free energy is sharply increased. Therefore, the probability of emergence of energy dips during formation of crystal structures is high for such lattices. Because of this circumstance, the formation of polymorphic amorphous structures of the same $TlInS_2$ compound is inevitable in the films.

4. CONCLUSION

Irrespective of the evaporation mode, during the sequential deposition of Tl, In, and S, as well as during

simultaneous evaporation of components, different compounds (eight differing in the composition and ten differing in the structure) are identified: Tl_2S, Tl_4S_3, TlS, Tl_2S_5, In_6S_7, In_2S_3, In_3S_5, $TlInS_2$ (tetragonal), $TlInS_2$ (monoclinic), and $TlInS_2$ (orthorhombic). It is found that it is possible to obtain various thin films of the amorphous phases of polymorphic $TlInS_2$, which are assigned to one or another structural modification of $TlInS_2$.

REFERENCES

1. H. Hahn and B. Weltman, Naturwissenschaften **2**, 42 (1967).
2. T. I. Issacs, Z. Kristallogr. B **141**, 104 (1971).
3. T. I. Isaacs, J. Appl. Crystallogr. **6**, 413 (1973).
4. R. Muller, D. Von, G. Eulenberger, and H. Hahn, Z. Anorg. Allg. Chem. **398**, 207 (1973).
5. D. Muller, F. E. Poltman, and H. Hahn, Z. Naturforsch. **296** (1/2) (1974).
6. K. J. Range, E. Engert, W. Muller, and K. Weisse, Z. Naturforsch. **296** (3,4), 181 (1974).
7. M. Gottlieb, T. I. Isaacs, J. D. Feichtner, and G. W. Roland, J. Appl. Phys. **45**, 5145 (1974).
8. R. S. Kobre, M. M. Jouln-Pousal, and M. Guittard, Bull. Soc. Chim. Fr. **9**, 1884 (1974).
9. T. I. Isaacs and R. H. Hopkins, J. Cryst. Growth **29**, 121 (1975).
10. T. I. Isaacs and J. D. Feichtner, J. Solid State Chem. **14**, 260 (1975).
11. K. J. Range and G. Mahlberg, Z. Naturforsch. **32**, 1354 (1977).
12. D. Muller and H. Hahn, Z. Anorg. Allg. Chem. **438**, 258 (1978).
13. D. I. Ismailov, F. I. Aliev, R. M. Sultanov, and R. B. Shafizade, Izv. Akad. Nauk SSSR, Neorg. Mater. **27**, 474 (1991).
14. D. I. Ismailov, R. M. Sultanov, F. I. Aliyev, and R. B. Shafizade, Thin Solid Films **205** (1–5), 1 (1991).
15. D. I. Ismailov, É. Sh. Alekperov, M. F. Alieva, *et al.*, Poverkhnost **12**, 113 (1999).
16. F. I. Aliev, D. I. Ismailov, I. V. Ivanova, and R. B. Shafizade, Izv. Akad. Nauk SSSR, Neorg. Mater. **23**, 574 (1986).
17. F. I. Aliev, D. I. Ismailov, R. M. Sultanov, and R. B. Shafizade, Izv. Akad. Nauk SSSR, Neorg. Mater. **23**, 1643 (1987).
18. D. I. Ismailov, F. I. Aliev, R. M. Sultanov, and R. B. Shafizade, Izv. Akad. Nauk SSSR, Neorg. Mater. **27**, 474 (1991).
19. M. Hansen and K. Anderko, *Constitution of Binary Alloys*, 2nd ed. (McGraw-Hill, New York, 1958; Metallurgizdat, Moscow, 1962), Vol. 2.
20. B. Leclerc and M. B. Baielly, Acta Crystallogr. B **29**, 2334 (1973).
21. H. Hahn and W. Klingler, Z. Anorg. Chem. B **260**, 110 (1949).
22. M. Soulard and M. Tournoux, Bull. Soc. Chim. Fr. **3**, 791 (1971).
23. V. I. Vasil'ev, A. V. Nikol'skaya, and Ya. I. Gerasimov, Izv. Akad. Nauk SSSR, Neorg. Mater. **9**, 553 (1973).
24. Z. S. Medvedeva, *Chalcogenides of III-B Subgroup of the Periodical System* (Nauka, Moscow, 1968).
25. W. J. Dujjin and J. H. Hogg, Acta Crystallogr. **20**, 66 (1966).
26. M. I. Zargarova and R. Z. Gamidov, Izv. Akad. Nauk SSSR, Neorg. Mater. **3**, 1085 (1967).
27. G. King, Acta Crystallogr. **15**, 512 (1962).
28. G. D. Cuseinov, E. Mooser, E. M. Kerimova, *et al.*, Phys. Status Solidi **34**, 33 (1969).
29. T. I. Isaacs, Z. Kristallogr. B **141**, 104 (1971).
30. É. G. Éfendiev, F. I. Aliev, and R. B. Shafizade, Izv Akad. Nauk SSSR, Neorg. Mater. **8**, 728 (1987).
31. D. I. Ismailov, Candidate's Dissertation (Baku, 1968).

Translated by N. Korovin

Semiconductors, Vol. 37, No. 7, 2003, pp. 748–750. Translated from Fizika i Tekhnika Poluprovodnikov, Vol. 37, No. 7, 2003, pp. 776–778.

CONFERENCE. ELECTRONIC AND OPTICAL PROPERTIES OF SEMICONDUCTORS

The Influence of a High and Low Content of Au Impurity on the Photoluminescence of Stoichiometric and Nonstoichiometric Arsenic Sulfide

A. A. Babaev*, I. K. Kamilov*, Z. V. Vagabova*, S. M. Sultanov*, A. M. Askhabov*, E. I. Terukov, and I. N. Trapeznikova****

**Institute of Physics, Dagestan Scientific Center, Russian Academy of Sciences, ul. 26 Bakinskikh komissarov 94, Makhachkala, 367003 Russia*

e-mail: kamilov@datacom.ru

***Ioffe Physicotechnical Institute, Russian Academy of Sciences, Politekhnicheskaya ul. 26, St. Petersburg, 194021 Russia*

Submitted December 23, 2002; accepted for publication December 27, 2002

Abstract—The photoluminescence and photoluminescence excitation spectra of stoichiometric and nonstoichiometric glasses with Au impurity were investigated for the first time at $T = 77$ K. It is found that the photoluminescence spectrum of nonstoichiometric glasses with low content of impurity is split into two bands, one of which is impurity-induced. *© 2003 MAIK "Nauka/Interperiodica".*

In order to solve many problems in the physics and engineering of semiconductors, the controlled introduction of impurities into crystalline semiconductors, which form deep levels in the band gap of a semiconductor, is widely used. Specifically, the operation of the overwhelming majority of semiconductor devices and units is based on the use of doped crystals with specified properties. This circumstance also stimulated the investigation of impurity behavior in chalcogenide vitreous semiconductors (chalcogenide glasses). However, even the first investigations [1, 2] demonstrated that most of the impurities introduced into glass from a melt during synthesis weakly (if at all) affect the physical properties of chalcogenide glasses (CGs). The impurities are optically and electrically inactive; i.e., they form no localized states in the band gap. Such an anomaly in the behavior of impurities introduced into CGs was long considered as their distinctive feature. However, there are facts that are indicative of impurity influence on the physical properties of CGs. It was demonstrated that some impurities, for example, Cu and Ag, substantially change the conductivity and other characteristics of CGs containing As and Ge [3–6]. However, the amount of impurity introduced was very large. Therefore, it was difficult to conclude whether the conductivity varies due to the emergence of donor states or within an increase in the conductivity was caused by a decrease in the band gap E_g of a newly formed compound. The number of studies devoted to the investigation of impurity behavior in CGs has been increasing. Despite this fact, the fundamental questions concerning the search for impurities that would make it possible to effectively control the physical properties of CGs remain unresolved, and the anomalous behavior of most impurities in glasses has not been explained to date. This is due primarily to the fact that there are few direct methods for studying the state of an impurity (the structure of the impurity center, its nature, charge states, and local symmetry in the glass matrix) in CGs. The applicability of these methods is restricted. However, photoluminescence (PL) in CGs and corresponding crystalline analogs were found [7]. PL analysis is a rapid and efficient method for investigating band energy spectra. Thus, this finding made it possible to perform a series of investigations aimed at revealing the influence of various impurities on PL properties. These investigations showed that doping CGs with various impurities, as a rule, does not lead to the formation of new emission bands within a wide range of energies and temperatures. The centers that are responsible for the radiative recombination with $E \approx E_g/2$ in CGs are intrinsic defects with a negative correlation energy. A new band peaked at 0.81 eV was found in the PL spectra of $(GeS_3)_{100-x}Bi_x$ glasses, whereas no new emission bands were found in the PL spectra of $(As_2S_3)_{100-x}Bi_x$ glasses [8]. The new band observed in the PL spectra of $(GeS_3)_{100-x}Bi_x$ glasses was also detected in the spectra of powder samples of the same composition [9]. Studies [8, 9] were aimed at revealing the specific features of the influence of Bi impurity on the PL properties of glasses with a tetrahedral and chain–layer structure. It should be noted that the corresponding analogs of CGs are GeS_2 and As_2S_3 crystals, whereas the GeS_3 glass is nonstoichiometric.

The aim of this study is to investigate the influence of Au impurity on the properties of stoichiometric and nonstoichiometric CGs and to reveal their specific features.

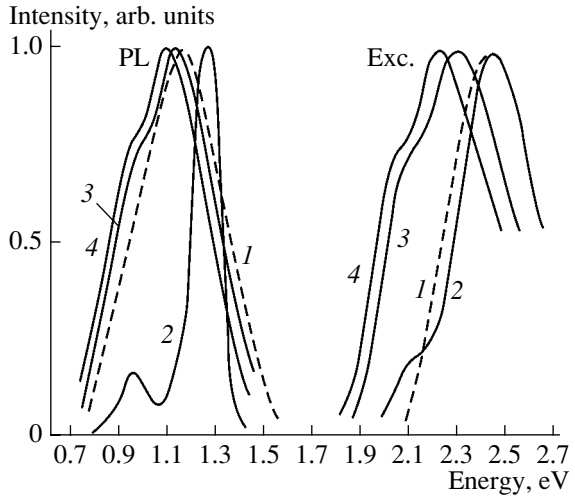

Fig. 1. Photoluminescence (PL) spectra and PL-excitation (Exc.) spectra of $(As_2S_5)_{100-x}Au_x$ glasses at $T = 77$ K. x: (*1*) 0, (*2*) 0.01, (*3*) 0.02, and (*4*) 0.04.

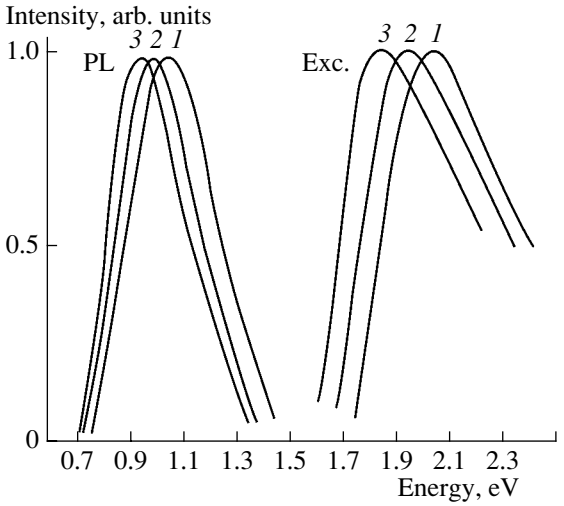

Fig. 2. Photoluminescence (PL) spectra and PL-excitation (Exc.) spectra of $(As_2S_3)_{100-x}Au_x$ glasses at $T = 77$ K. x: (*1*) 0, (*2*) 0.01, and (*3*) 0.04.

As the objects of investigation, the $(As_2S_3)_{100-x}Au_x$ stoichiometric system and the $(As_2S_5)_{100-x}Au_x$ nonstoichiometric system were chosen, where $0.1 > x \geq 0$.

Undoped and Au-doped Bi-containing glasses were synthesized by direct alloying of corresponding amounts of elemental As and S with Au of 99.99999% purity in evacuated quartz cells using vibrational stirring of the melt. To prevent explosion of cells, synthesis was carried out in two stages. In the first stage, cells were heated in a tube furnace to 800–850 K at a rate of 0.1–0.2 K/s with subsequent holding at this temperature for 15–20 h. In the second stage, the furnace temperature was increased to the melting point of the element with the highest melting temperature at a rate of 0.05–0.1 K/s and kept constant for 20–25 h. The melt was then quenched in salt water with ice. All glasses synthesized were annealed at 500–530 K for 25–30 h to relieve stresses. The atomic Au content in alloys $x = 0$, 0.01, 0.02, and 0.04.

The absence of lines in the Debye–Scherrer powder patterns, diffuse X-ray scattering, and absence of microinclusions and inhomogeneities on polished surfaces and cleavages of the samples visually inspected by a Neofot microscope served as criteria of the vitreous state of the materials.

Steady-state luminescence was excited by a DKSL xenon lamp with a power of 1000 W. The PL and PL-excitation spectra were investigated at $T = 77$ K. To exclude possible distortion of emission spectra due to self-absorption, the emission was detected from the illuminated side of the sample. Silicon and germanium photodiodes were used as photodetectors. The PL-excitation spectra were recorded in the vicinity of the peak of the PL spectrum, whereas the PL spectra were recorded using excitation by quanta with energies corresponding to the peak of the PL-excitation spectrum. Since the "fatigue effect" of PL was observed in the glasses under investigation, the spectra were measured after the establishment of the quasi-steady state of emission, i.e., when the fatigue effect could be disregarded during spectra recording.

The PL spectrum of undoped glasses is represented by a single broad band peaked at $E_{pl} \approx E_g/2$, which can be attributed to intrinsic defects with a negative correlation energy. A single peak is observed in the exponential portion of the self-absorption edge of the PL spectrum of glass which corresponds to the value of the absorption coefficient $\alpha \approx 10^2$ cm^{-1}. The PL and PL excitation spectra of undoped and doped glasses are shown in Figs. 1 and 2. An increase in the impurity content in stoichiometric glass with $x > 0$ leads simultaneously to the shift of the peak of the main emission band at $E = E_g/2$ to lower energies and to a decrease in intensity. The introduction of small amounts of impurity into the nonstoichiometric glass leads to the emergence of a new emission band. For nonstoichiometric glasses, splitting of the PL spectrum results in the appearance of peaks at $E_{pl1} = 1.26$ eV and $E_{pl2} = 0.95$ eV with the half-maximum $\delta \approx 0.1$ eV observed at $x = 0.01$. The peaks of the emission bands E_{pl1} and E_{pl2} in the PL-excitation spectra correspond to $E_{ex1} = 2.4$ eV and $E_{ex2} = 2.1$ eV, respectively. Note that (i) the peaks of the main emission band in the PL and PL-excitation spectra shift to lower energies with increasing impurity content ($x > 0$), (ii) the peaks in the PL and PL-excitation spectra at E_{pl1} and E_{pl2} undergo no substantial changes, and (iii) a single broad band of emission and excitation of luminescence is observed for glasses with $x > 0.04$.

The experimental results obtained show that the impurities in CGs can induce new states in the mobility gap of nonstoichiometric glasses. It is likely that some fraction of Au atoms introduced into nonstoichiometric

glass occupy sites in the glass network and can be considered as an impurity, and the remaining Au atoms saturate dangling bonds, thus forming a new compound. This causes splitting of the PL spectrum of the initial sample with the formation of a new emission level, which is induced by the Au impurity.

REFERENCES

1. B. T. Kolomiets and T. F. Nazarova, *Solid State Physics* (Nauka, Moscow, 1959), Vol. 2, p. 21.
2. B. T. Kolomiets, in *Proceedings of 6th International Conference on Amorphous and Liquid Semiconductors* (Leningrad, 1975), p. 23.
3. V. L. Vaninov and S. K. Novoselov, Fiz. Khim. Stekla **2**, 546 (1976).
4. T. Ishikawa, M. Ritao, H. Akao, and S. Yamada, Phys. Status Solidi A **57**, 373 (1980).
5. T. S. Rykova and Z. U. Borisova, Fiz. Khim. Stekla **5**, 563 (1979).
6. D. I. Bletskan, V. S. Gerasimenko, and I. M. Mitrovskiĭ, Ukr. Fiz. Zh. **29**, 1074 (1984).
7. B. T. Kolomiets, T. N. Mamontova, and A. A. Babaev, J. Non-Cryst. Solids **8**, 1004 (1972).
8. A. A. Babaev and S. P. Vikhrov, in *Scientific Works*, Ser.: *Plazma in Semiconductors* (Inst. Fiz., Dagest. Fil. Akad. Nauk SSSR, Makhachkala, 1984), No. 3, p. 135.
9. A. A. Babaev, in *Abstracts of International Conference on Amorphous Semiconductors-84* (Gabrovo, 1984), Vol. 2, p. 144.

Translated by N. Korovin

Semiconductors, Vol. 37, No. 7, 2003, pp. 751–756. Translated from Fizika i Tekhnika Poluprovodnikov, Vol. 37, No. 7, 2003, pp. 779–783.

CONFERENCE. ELECTRONIC AND OPTICAL PROPERTIES OF SEMICONDUCTORS

Spectra of Fundamental Optical Functions of BeSe

V. Val. Sobolev* and V. V. Sobolev

Udmurt State University, ul. Studencheskaya 7, Izhevsk, 426034 Russia

**e-mail: sobolev@uni.udm.ru*

Submitted December 23, 2002; accepted for publication December 27, 2002

Abstract—Spectra of sets of fundamental optical functions of BeSe were derived for the range of 0–25 eV. Calculations were performed using an experimental $\varepsilon_2(E)$ spectrum and integral Kramers–Kronig relations. Using combined Agrand diagrams, the spectra of permittivity and characteristic energy losses of electrons were decomposed into elementary transverse and longitudinal components. The main parameters of these components were determined. The results obtained were compared with theoretical spectra of optical functions calculated using the OPW and APW methods and with the energy bands obtained in an *ab initio* GW approximation.

1. INTRODUCTION

Among II–VI compounds, beryllium chalcogenides are notable for their wide band gap, high cubic phase stability, and covalent bonding [1]. Recently, increasing interest has been drawn to BeSe owing to the facts that the BeSe and GaAs lattices are isoperiodic and intrinsic emission from BeSe falls in the blue–green region of the spectrum.

The optical properties of BeSe have not been adequately investigated. The photoluminescence spectra of BeCdSe [2] and BeZnSe [3] solid solutions were used to estimate the energies of direct (E_{gd}) and indirect (E_{gi}) transitions: $E_{gd} \approx 5.5$ eV and $E_{gi} \approx 3.7$ eV. Ellipsometry was used to determine the spectra of the imaginary part of the permittivity $\varepsilon_2(E)$ of the BeSe layer grown on GaAs substrate in the range $E = 2.5$–25 eV [4, 5]. The energy bands [6–8] and the spectra of ε_2 [6] and $E^2\varepsilon_2$ [7] were calculated theoretically.

It is generally believed that the most complete data on a semiconductor's electronic structure can be obtained from the spectra of a set of a large number of fundamental optical functions [9]. These include the imaginary (ε_2) and real (ε_1) parts of the permittivity; the reflection (R) and absorption (μ) coefficients; the refractive (n) and absorption (k) indices; the real ($\mathrm{Re}\varepsilon^{-1}$, $\mathrm{Re}(1+\varepsilon)^{-1}$) and imaginary ($-\mathrm{Im}\varepsilon^{-1}$, $-\mathrm{Im}(1+\varepsilon)^{-1}$) parts of the characteristic bulk and surface energy losses of electrons; the integral function of the bound density of states, which is equal (to within a constant factor) to $E^2\varepsilon_2$ if the probability of transitions is fixed; the effective number of valence electrons $n_{ef}(E)$ involved in transitions with a final energy E; and so on. All of these functions are interrelated; however, each of them has significance in its own right. The physical meaning and interplay of these functions can be derived directly from the Maxwell equations.

The aim of this study is to obtain the spectra of the complete set of fundamental optical functions for beryllium selenide crystal, to determine the complete set of interband transitions and their parameters, and to perform theoretical analysis of the data obtained.

2. METHODS FOR CALCULATIONS

Typically, a set of optical functions is calculated using special software packages, the Kramers–Kronig integral relations, and analytical formulas interrelating the above functions on the basis of known experimental spectra $\varepsilon_2(E)$ or $R(E)$ in a wide energy range.

The problem of determining the parameters of a fine structure in the spectra of transverse optical transitions (the energy E_i of the peak; the half-width H_i and amplitude I_i of the ith band; the area S_i under the curve outlining the band; and the oscillator strength f_i is typically solved by one of two methods: (i) by representing the integrated curve of the $\varepsilon_2(E)$ spectrum by a set of N Lorentzian oscillators with a large number of adjustable parameters $3N$ (this number can be as large as 30 for $N = 10$) and (ii) using Argand diagrams also in the classical model of Lorentzian oscillators (albeit without adjustable parameters due to simultaneous analysis of the $\varepsilon_2(E)$ and $\varepsilon_1(E)$ spectra). The parameters of longitudinal components of transitions are calculated similarly on the basis of $-\mathrm{Im}\varepsilon^{-1}$ and $\mathrm{Re}\varepsilon^{-1}$ spectra.

The methods we used to calculate the complete set of optical functions and decompose the integral spectra of ε_2 and $-\mathrm{Im}\varepsilon^{-1}$ into elementary transverse and longitudinal components were described in detail in [9, 10] and were discussed in [11–14].

3. RESULTS AND DISCUSSION

Among all optical functions of BeSe, only the spectrum $\varepsilon_2(E)$ has been studied experimentally in the range of 2.5–25 eV [4, 5]. The spectra were measured using a special unique ellipsometer and synchrotron radiation.

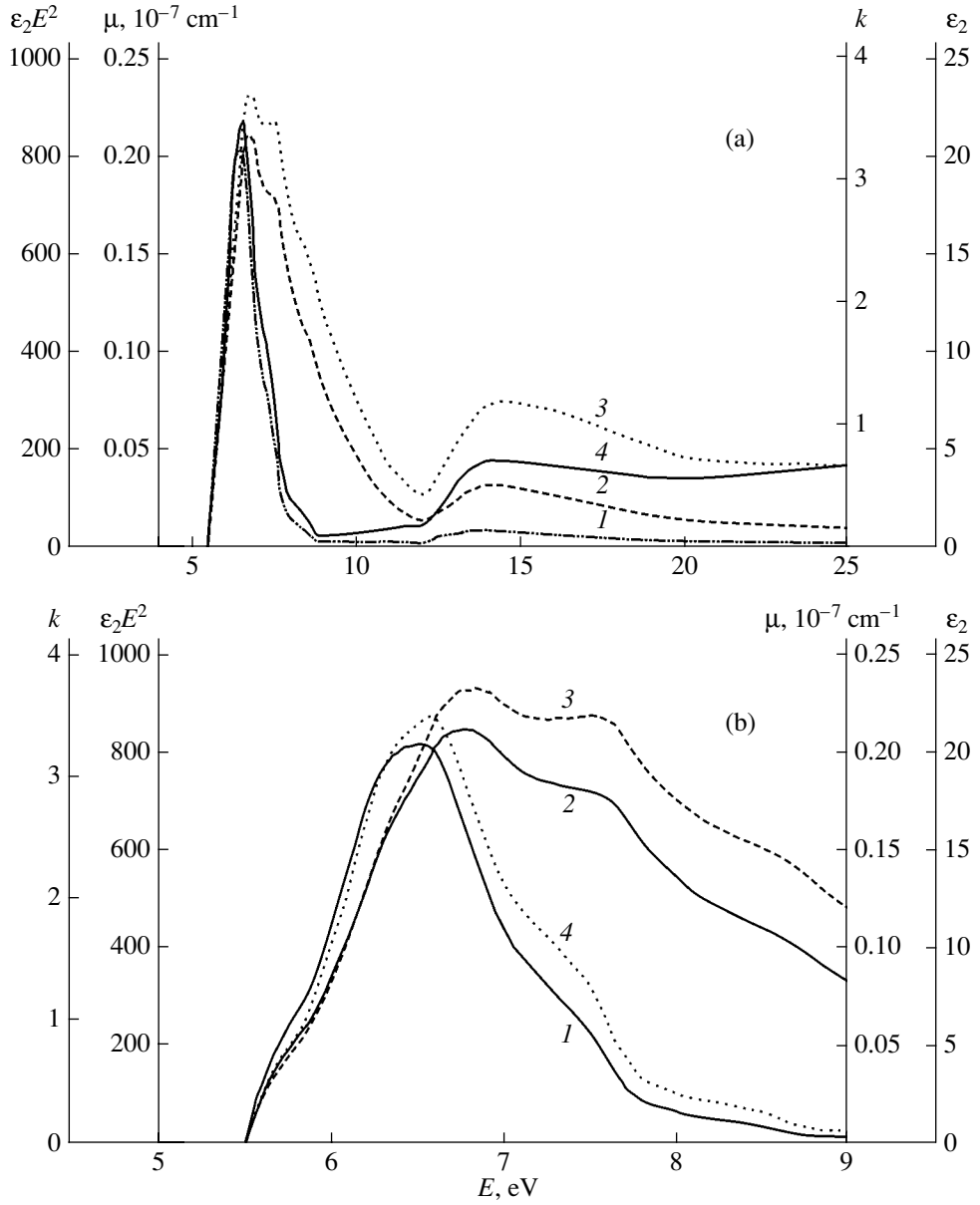

Fig. 1. (*1*) Experimental spectrum of ε_2 and calculated spectra of (*2*) k, (*3*) μ, and (*4*) $E^2\varepsilon_2$ for a beryllium selenide crystal in the energy ranges of (a) 5–25 eV and (b) 5–9 eV.

The samples were 0.8-μm-thick BeSe layers deposited onto GaAs substrate using molecular-beam epitaxy.

The BeSe energy bands were calculated *ab initio* using the self-consistent method of orthogonalized plane waves in the approximation of a nonrelativistic formalism [6], a combination of the methods of augmented plane waves and LCAO [7], and the *ab initio* GW approximation [8] for the points W, L, Γ, X, and K and for corresponding directions. On the basis of the calculated energy bands, the spectrum $\varepsilon_2(E)$ in the energy range of 5.5–9.0 eV [6] and the spectrum $E^2\varepsilon_2(E)$ for E = 5.5–26 eV [7] were derived.

We calculated the spectra of complete sets of fundamental optical functions for a BeSe crystal in the range of 0–25 eV using the $\varepsilon_2(E)$ spectrum [4, 5] (the experimental–calculated functions, $K1$) and theoretical data [6, 7] (theoretical functions, $K2$ [6] and $K3$ [7]).

The experimental spectrum $\varepsilon_2(E)$ of BeSe includes an intense broad band in the region of 6–7 eV with a poorly pronounced doublet feature (the peaks at ~6.3 and ~6.5 eV); a broad low-intensity peak at ~13.5 eV; and three shoulder features at ~5.7, ~7.3, and ~8.15 eV. In the calculated $k(E)$ and $\mu(E)$ spectra, an analogue of the ε_2 band at ~6.5 eV was shifted to higher energies by ~0.3 eV, while an analogue of the shoulder feature at ~7.3 eV became a high-intensity peak at ~7.5 eV (Fig. 1).

The calculated spectra of R, n, and ε_1 differ greatly from the spectrum of ε_2 (Fig. 2a). In the $R(E)$ spectrum,

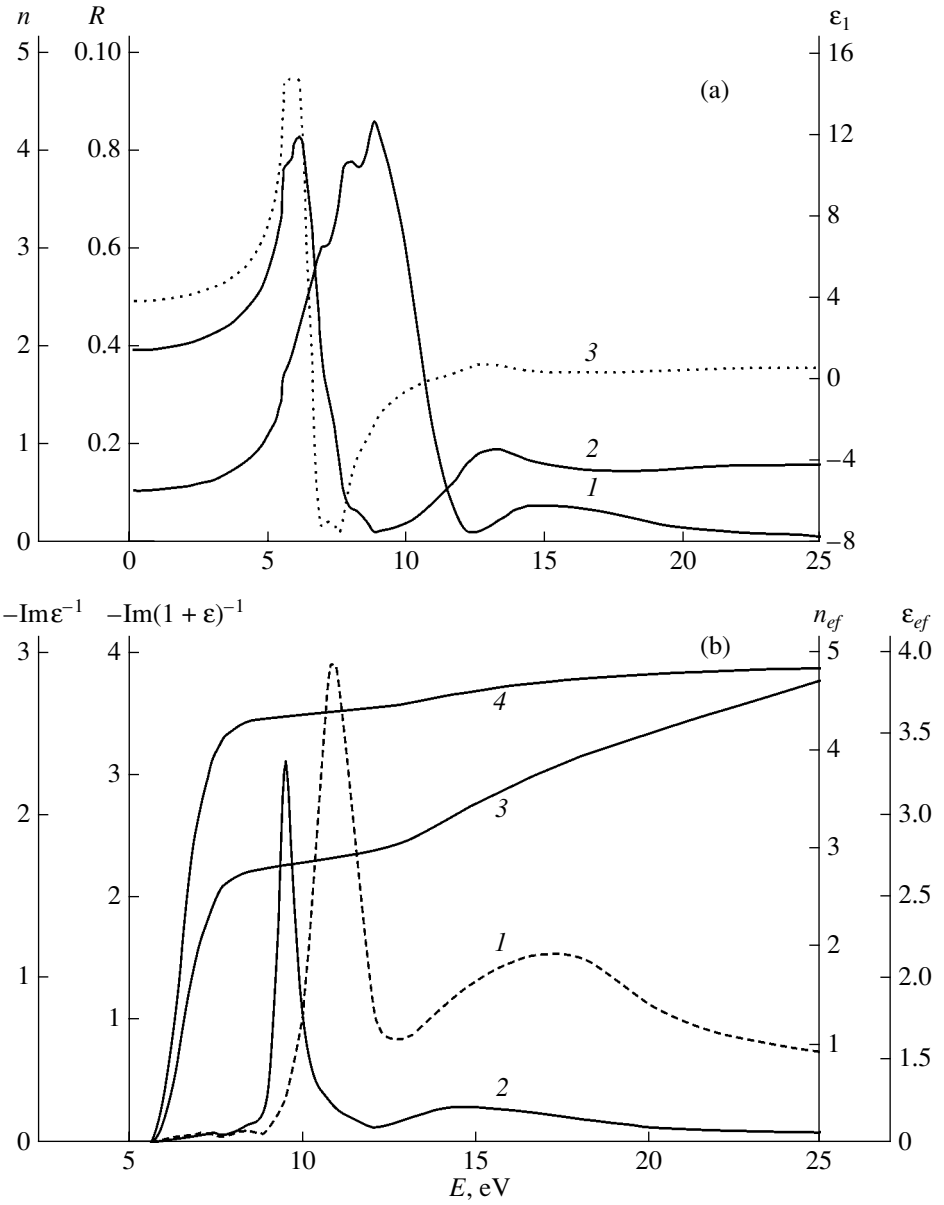

Fig. 2. (a) The spectra of (*1*) R, (*2*) n, and (*3*) ε_1 and (b) the spectra of (*1*) $-\mathrm{Im}\varepsilon^{-1}$, (*2*) $-\mathrm{Im}(1+\varepsilon)^{-1}$, (*3*) n_{ef}, and (*4*) ε_{ef} for a BeSe crystal.

we observe the most intense doublet band with peaks at ~7.5 and ~8.8 eV, a broad low-intensity band at ~14.5 eV, a poorly pronounced peak at ~6.95 eV, and a shoulder feature at ~5.6 eV. The curves $n(E)$ and $\varepsilon_1(E)$ closely resemble each other. They include an intense doublet band with peaks at ~5.6 and ~6.0 eV, a poorly pronounced peak at ~7.2 eV (ε_1) or a shoulder feature at ~7.1 eV (n), and a broad peak at ~12.8 eV.

In the spectra of characteristic energy losses of electrons, there are typical broad bands of the bulk ($-\mathrm{Im}\varepsilon^{-1}$, 18.55 eV) and surface ($-\mathrm{Im}(1+\varepsilon)^{-1}$, 15.25 eV) plasmons (Fig. 2b). In addition, two intense peaks at ~10.5 eV ($-\mathrm{Im}\varepsilon^{-1}$) and ~9.25 eV ($-\mathrm{Im}(1+\varepsilon)^{-1}$) are observed; these peaks are apparently related to the excitation of bound electrons from the highest valence bands, are located in the region of a broad band at 9–12 eV in the $\varepsilon_2(E)$ spectrum, and cannot be related to interband transitions.

We compared the experimental energy spectrum of ε_2 [4, 5] and the spectra of other optical functions calculated on the basis of $\varepsilon_2(E)$ with the theoretical spectra of ε_2 [6, 7] and the spectra of other optical functions derived on the basis on the latter spectra. For the sake of brevity, we will only show the data for ε_2 and R in Figs. 3 and 4. The theoretical data reported by Stukel [6] closely correspond to the experimental curve [4, 5] in the positions of the main peaks and shoulder features. The main difference between the theory and

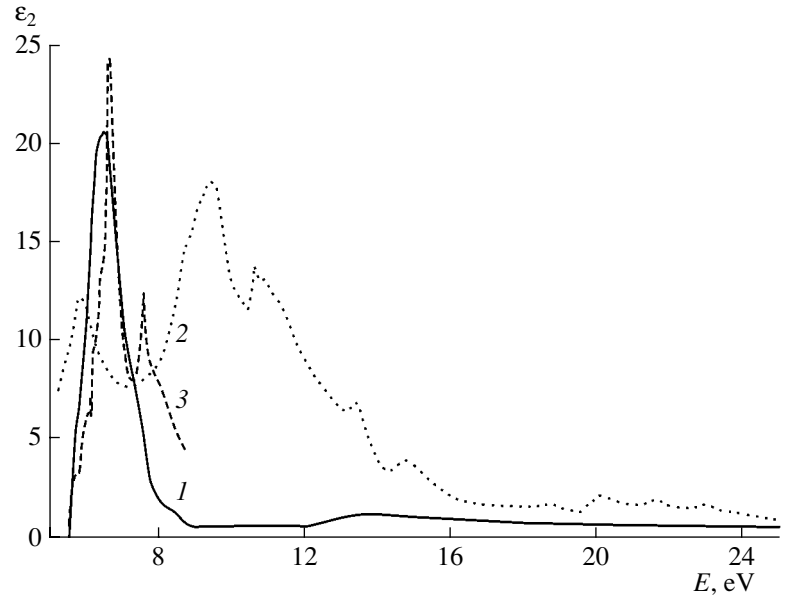

Fig. 3. (*1*) Experimental [4, 5] and theoretical (*2*) [7] and (*3*) [6] spectra $\varepsilon_2(E)$ for a beryllium selenide crystal.

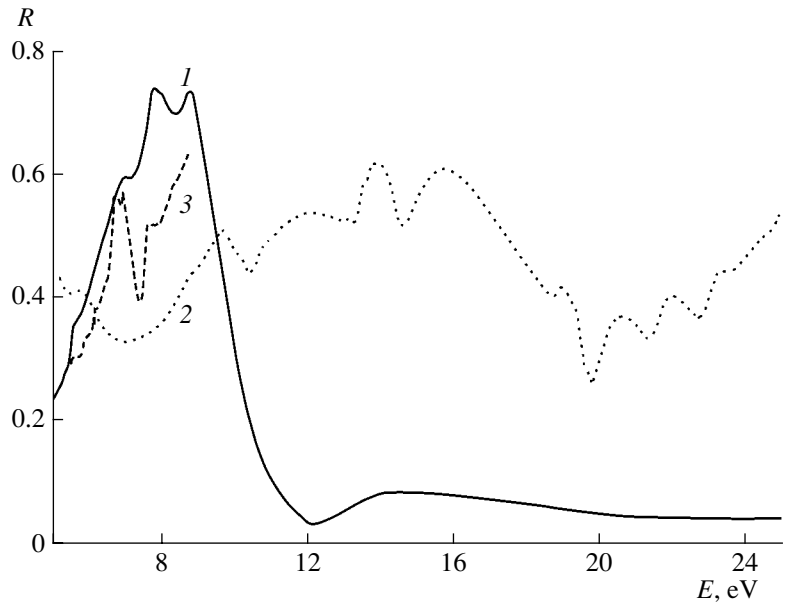

Fig. 4. The BeSe $R(E)$ spectra calculated using (*1*) experimental [4, 5] and (*2*, *3*) theoretical $\varepsilon_2(E)$ spectra (*2*) [7] and (*3*) [6].

experiment consists in the relative intensity of the spectrum features. This circumstance can apparently be attributed to conventional errors in theoretical calculations of the probabilities of interband transitions. The theoretical data obtained by Sarkar and Chatterjee [7] differ greatly from the experimental curve $\varepsilon_2(E)$ and calculated curve $R(E)$ in both the spectrum features and the distribution of intensities between the peaks in the energy range of 5–25 eV. This circumstance indicates that there are large errors in calculating the energy bands [7].

Using the spectra of two pairs of functions of ε_2 and ε_1 ($-\mathrm{Im}\varepsilon^{-1}$ and $\mathrm{Re}\varepsilon^{-1}$) and the combined Argand diagrams, we decomposed the spectra of ε_2 and $-\mathrm{Im}\varepsilon^{-1}$ into 6 transverse and 16 longitudinal components (see table). At energies E higher than that corresponding to the peak at 13.5 eV, the values of $\varepsilon_2(E)$ decrease drastically, which greatly hampers the determination of transverse components 10–16. In contrast, the values of $-\mathrm{Im}\varepsilon^{-1}$ are largest in this energy region, which makes it possible to determine with confidence the longitudinal components of the bands that correspond to transitions.

Energies corresponding to the peaks of the bands E_i and half-widths H_i of these bands (both expressed in eV), the band intensities I_i and areas S_i under the curves outlining these bands for transverse (ε_2) and longitudinal (ε^{-1}) components, and also the location at the points (Γ, L, X, W) of the Brillouin zone and energy (in eV) of the bands according to the theory [6, 8] for a beryllium selenide crystal

Component no.	E_i		H_i		I_i		S_i		[8]	[6]
	ε_2	ε^{-1}	ε_2	ε^{-1}	ε_2	ε^{-1}	ε_2	ε^{-1}		
1	5.71	5.70	0.21	0.20	2.80	0.03	0.92	0.01	Γ, 5.6	ΓL, 5.7
2	6.30	6.33	0.52	0.30	16.48	0.05	13.15	0.02	ΓX, 6.5	ΓX, 6.0, ΓL, 5.8
3	6.72	6.79	0.55	0.35	13.50	0.06	11.46	0.03	ΓL, 6.6	ΓX, 7.2
4	7.27	7.30	0.30	0.40	5.50	0.09	2.56	0.05	L, 7.1	ΓX, 7.2
5	–	7.85	–	0.35	–	0.07	–	0.04	ΓX, 8.1	ΓL, 7.6
6	8.15	8.35	0.40	0.45	1.10	0.13	0.68	0.09	ΓL, 8.3	ΓX, 8.3
7	–	10.45	–	1.35	–	1.50	–	3.06	X, 9.0	ΓL, 10.1
8	–	11.70	–	1.90	–	0.56	–	1.59	ΓL, 12.0	W, 10.9
9	13.50	13.90	1.00	2.20	1.35	0.39	2.61	1.28	ΓL, 14.0	ΓL, 15.1
10	–	15.90	–	2.50	–	0.67	–	2.51	XW, 16.0	ΓX, 16.5
11	–	18.00	–	2.20	–	0.67	–	2.23	X, 18.0	ΓL, 17.0
12	–	20.00	–	2.20	–	0.67	–	2.24	Γ, 20.2	ΓL, 19.0
13	–	22.00	–	2.20	–	0.63	–	2.11	Γ, 23.0	–
14	–	24.00	–	2.20	–	0.65	–	2.18	Γ, 23.0	–
15	–	26.00	–	2.20	–	0.65	–	2.19	Γ, 26.0	–
16	–	28.30	–	2.20	–	1.09	–	3.84	–	–

The areas under the curves S_i for the transverse components exceed the corresponding values for the longitudinal components by more than two orders of magnitude in the energy region $E < 8$ eV. This observation indicates that the probabilities of exciting the longitudinal components of the bands related to transitions in BeSe in the region $E < 8$ eV are negligible compared with the probabilities of transitions for the corresponding transverse analogues.

In the energy-band model, all the peaks and shoulder features in the spectra of optical functions and the components of decomposition of ε_2 and $-\mathrm{Im}\varepsilon^{-1}$ for a BeSe crystal are related to direct interband transitions. On the basis of analysis of theoretical energy bands [6, 8], we estimated the energies of the possible and most intense direct interband transitions at the points Γ, X, L, and W and along the directions ΓX, ΓL, and XW (see two uppermost columns in table).

According to the general theory of the optical properties of semiconductors [9], certain features in the spectra of ε_2 and $-\mathrm{Im}\varepsilon^{-1}$ in a BeSe crystal can be related to metastable excitons.

4. CONCLUSION

In this study, we calculated for the first time the spectra of a complete set of fundamental optical functions for a BeSe crystal in the energy range of 0–25 eV. The spectra of permittiviity and characteristic energy losses of electrons were decomposed into transverse and longitudinal components; the parameters of the latter were determined. We suggested a scheme for the specific origin of these components in the model of direct interband transitions. We ascertained that there was good agreement between the experimental [4, 5] and theoretical [6] spectra of $\varepsilon_2(E)$; the same was true for the spectra of other optical functions, which were calculated on the basis of the $\varepsilon_2(E)$ spectrum. This circumstance indicates that the results of calculating the energy bands of BeSe [6] are correct in the region of interband-transition energies $E < 8$ eV. The results we obtained make it possible to gain deeper insight into the optical properties and electronic structure of BeSe crystal in a wide energy range; they also serve as a firm basis for further theoretical calculations of energy bands and the $\varepsilon_2(E)$ spectrum with a higher accuracy.

ACKNOWLEDGMENTS

This study was supported by the Competitive Center for Fundamental Natural Science (St. Petersburg State University).

REFERENCES

1. W. M. Yim, J. P. Dismukes, E. J. Stofka, and R. A. Paff, J. Phys. Chem. Solids **33**, 501 (1972).

2. O. V. Nekrutkina, S. V. Sorokin, V. A. Kaĭgorodov, *et al.*, Fiz. Tekh. Poluprovodn. (St. Petersburg) **35**, 541 (2001) [Semiconductors **35**, 520 (2001)].
3. C. Chauvet, E. Tournie, and J.-P. Faurie, Phys. Rev. B **61**, 5332 (2000).
4. K. Wilmers, T. Wethkamp, N. Esser, and C. Cobet, Phys. Rev. B **59**, 10071 (1999).
5. K. Wilmers, T. Wethkamp, N. Esser, and C. Cobet, Phys. Status Solidi B **215**, 15 (1999).
6. D. J. Stukel, Phys. Rev. B **2**, 1852 (1970).
7. R. L. Sarkar and S. Chatterjee, J. Phys. C: Solid State Phys. **10**, 57 (1977).
8. A. Fleszar and W. Hanke, Phys. Rev. B **62**, 2466 (2000).
9. V. V. Sobolev and V. V. Nemoshkalenko, *The Methods of Computational Physics in the Theory of Solid State. Electronic Structure of Semiconductors* (Naukova Dumka, Kiev, 1988).
10. V. V. Sobolev, Zh. Prikl. Spektrosk. **63**, 143 (1996).
11. V. V. Sobolev, A. P. Timonov, and V. Val. Sobolev, Fiz. Tekh. Poluprovodn. (St. Petersburg) **34**, 940 (2000) [Semiconductors **34**, 902 (2000)].
12. V. V. Sobolev and A. I. Kalugin, Fiz. Tekh. Poluprovodn. (St. Petersburg) **36**, 155 (2002) [Semiconductors **36**, 148 (2002)].
13. V. Val. Sobolev, O. R. Zheltysheva, and V. V. Sobolev, in *Proceedings of III International Conference on Amorphous and Microcrystalline Semiconductors* (S.-Peterb. Gos. Pedagog. Univ., St. Petersburg, 2002), p. 92.
14. V. Val. Sobolev, O. R. Zheltysheva, and V. V. Sobolev, in *Proceedings of International Conference on Optics, Optoelectronics and Technology* (Ul'yan. Gos. Univ., Ul'yanovsk, 2002), p. 113.

Translated by A. Spitsyn

Semiconductors, Vol. 37, No. 7, 2003, pp. 757–762. Translated from Fizika i Tekhnika Poluprovodnikov, Vol. 37, No. 7, 2003, pp. 784–789.

CONFERENCE. ELECTRONIC AND OPTICAL PROPERTIES OF SEMICONDUCTORS

Optical Properties of Imperfect In_2Se_3

V. Val. Sobolev* and V. V. Sobolev

Udmurt State University, ul. Studencheskaya 7, Izhevsk, 426034 Russia

**e-mail: sobolev@uni.udm.ru*

Submitted December 23, 2002; accepted for publication December 27, 2002

Abstract—Spectra of complete sets of optical functions for α- and β-In_2Se_3 in the range of 0–20 eV were calculated using experimental reflection spectra and the Kramers–Kronig relation. Special features in the spectra of optical functions for both In_2Se_3 phases were analyzed. The spectra of both permittivity and characteristic electron energy losses were decomposed into elementary transverse and longitudinal components using the combined Argand diagrams. The main parameters of the electron transitions for these components were determined. The structure of the components was compared with the structure of the expected spectrum of interband transitions. © *2003 MAIK "Nauka/Interperiodica".*

1. INTRODUCTION

One-third of cationic sites in $A_2^{III}B_3^{VI}$ compounds are vacant. As a result, these compounds differ greatly from other binary semiconductors by the nature and forces of interatomic bonds. Several modifications with ordered or unordered vacancies are known for many of $A_2^{III}B_3^{VI}$ compounds [1]. The unit cell of some of these compounds contains a large number of atoms; for example, the number of atoms in a unit cell of the hexagonal phases of In_2Se_3 is equal to 32 and 6 in the α- and β-phases, respectively.

Intrinsic imperfection, possible large deviations from stoichiometry, high concentrations of extraneous impurities and various structural imperfections, and polytypism to a great extent hamper the identification of the energy levels and optical spectra of $A_2^{III}B_3^{VI}$ phases. Therefore, the study of optical spectra in a wide range of fundamental-absorption energies is especially important for $A_2^{III}B_3^{VI}$ compounds.

The most complete information about the special features of electronic structure can be gained from a wide set of numerous optical functions [2]; these include the reflection (R) and absorption (μ) coefficients; the indices of refraction (n) and absorption (k); the real (ε_1) and imaginary (ε_2) parts of permittivity; the real and imaginary parts of the bulk ($-\mathrm{Im}\varepsilon^{-1}$, $\mathrm{Re}\varepsilon^{-1}$) and surface ($-\mathrm{Im}(1+\varepsilon)^{-1}$, $\mathrm{Re}(1+\varepsilon)^{-1}$) energy losses of electrons; and so on.

The aim of this study is to obtain the spectra of a complete set of fundamental optical functions for α- and β-In_2Se_3 crystals, determine complete sets of transitions and their parameters, and theoretically analyze the data obtained.

2. METHODS OF CALCULATIONS

The most widely used method for obtaining a set of optical functions is based on using special software, the well-known experimental reflectance spectrum in a wide energy range, the Kramers–Kronig integral relations, and simple analytical formulas.

The problem of determining the parameters of a fine structure in the spectra of transverse optical transitions (the energies E_i, half-widths H_i, and amplitudes I_i of the peaks; the areas under the spectral curves S_i; and the oscillator strengths f_i) is conventionally solved using either of two methods: (i) by approximating the integrated spectral curve $\varepsilon_2(E)$ using a set of N Lorentzian oscillators with a large number of adjustable parameters $3N$, which can be as large as 30 for $N = 10$; and (ii) by using the combined Agrand diagrams also in the classical model of Lorentzial oscillators, however without employing the adjustable parameters from the simultaneous analysis of the $\varepsilon_2(E)$ and $\varepsilon_1(E)$ spectra. The longitudinal components of transitions are calculated similarly on the basis of the $-\mathrm{Im}\varepsilon^{-1}$ and $\mathrm{Re}\varepsilon^{-1}$ spectra.

The methods used in this study to calculate a complete set of optical functions and to decompose the integral spectra of ε_2 and $-\mathrm{Im}\varepsilon^{-1}$ into elementary transverse and longitudinal components have been described in detail in [2, 3] and have been discussed in [4–7].

3. RESULTS OF CALCULATIONS AND DISCUSSION

The long-wavelength edge absorption of In_2Se_3 single crystals was measured in the ranges of 1–1.3 eV [8] and 1.2–1.4 eV [9]. The direct-transition energies E_{gd} were reported to be equal to 1.22 eV (for α-In_2Se_3) and 1.17 eV (β-In_2Se_3) in [8] and to 1.31 eV (α) and 1.35 eV (β) in [9] at 300K; thus, $\Delta E = E_{gd}(\alpha) - E_{gd}(\beta) \approx 0.05$ eV.

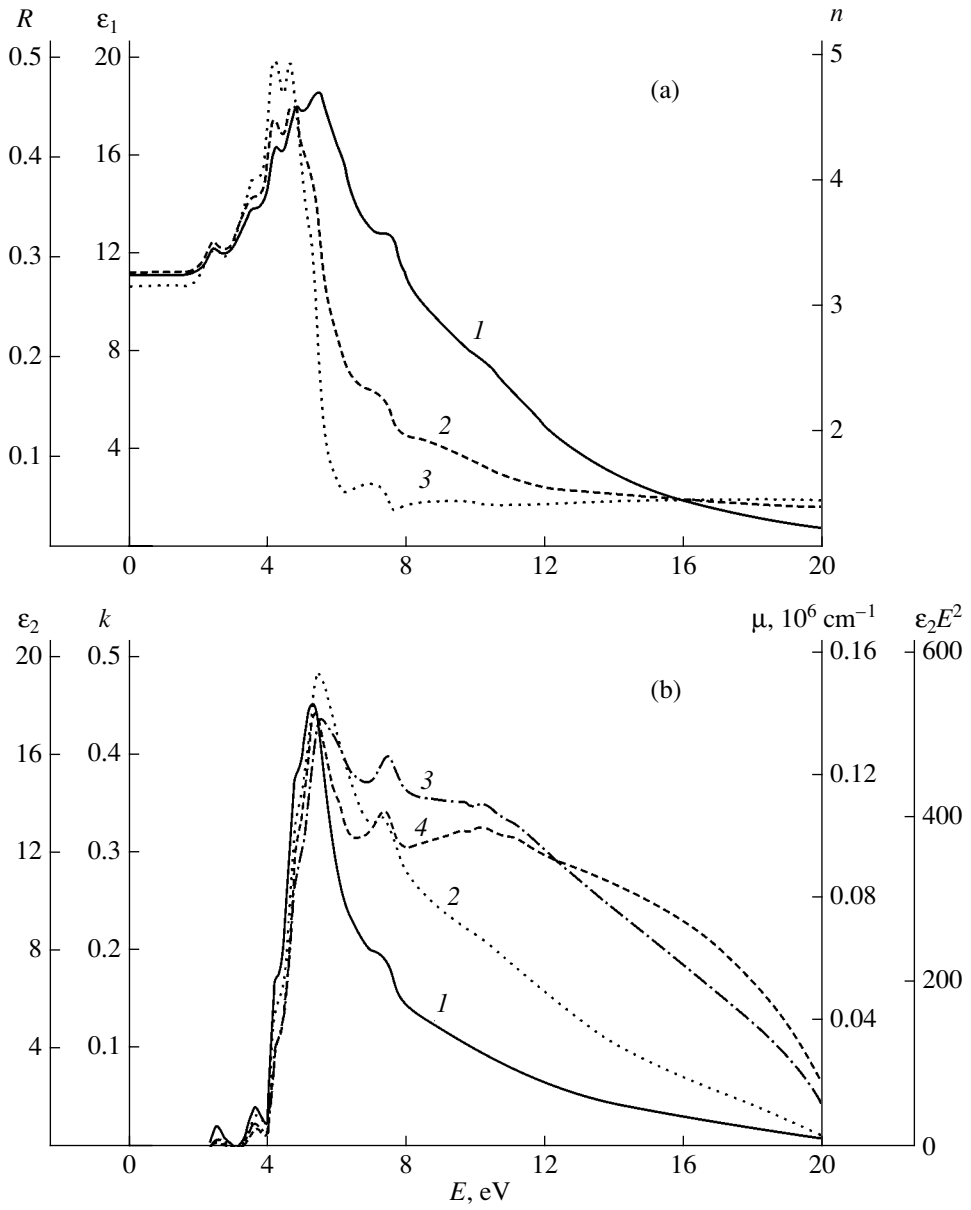

Fig. 1. (a) (*1*) Experimental spectrum of R and calculated spectra of (*2*) n and (*3*) ε_1; and (b) calculated spectra of (*1*) ε_2, (*2*) k, (*3*) μ, and (*4*) $E^2\varepsilon_2$ for an α-In_2Se_3 crystal.

The reflection spectra $R(E)$ of cleaved surfaces at 300 K have been studied in the ranges of 1–12.5 eV [10–14] and 1–5.7 eV [8]. The data obtained in [8] and [10–14] are in satisfactory agreement in the range of 1–5.7 eV.

We used the experimental spectra $R(E)$ for α- and β-In_2Se_3 [10–14] to calculate complete sets of fundamental optical functions in the range of 0–20 eV; in the range of 12.5–20 eV, we used the most widely accepted extrapolation $R(E) = R(12.5\text{ eV})\left(\frac{12.5}{E}\right)^p$, where the adjustable parameter $p \approx 4$. The spectra of seven optical functions are shown in Figs. 1 and 2.

The experimental reflection spectrum of α-In_2Se_3 includes five peaks and two features (shoulders) (Fig. 1, Table 1). In the calculated spectra of n and ε_1, the energy positions of the first two features coincide with those of the spectra for R; the next spectral features are shifted to lower energies by ~0.1 eV (features 3, 7), by 0.1–0.2 eV (feature 4), and by 0.3–0.4 eV (features 5, 6). Notably, the intensities in the $n(E)$ and $\varepsilon_1(E)$ spectra decrease drastically in the region $E > 4.6$ eV. All special features characteristic of $R(E)$ are observed in the k, μ, ε_2, $E^2\varepsilon_2$, $-\mathrm{Im}\varepsilon^{-1}$, and $-\mathrm{Im}(1+\varepsilon)^{-1}$ spectra, with the exception of feature 4 for $\mu(E)$. The energy positions for all features in the spectra of k, μ, and ε_2 are identical and are shifted to higher energies by $\Delta E \le 0.1$ eV with

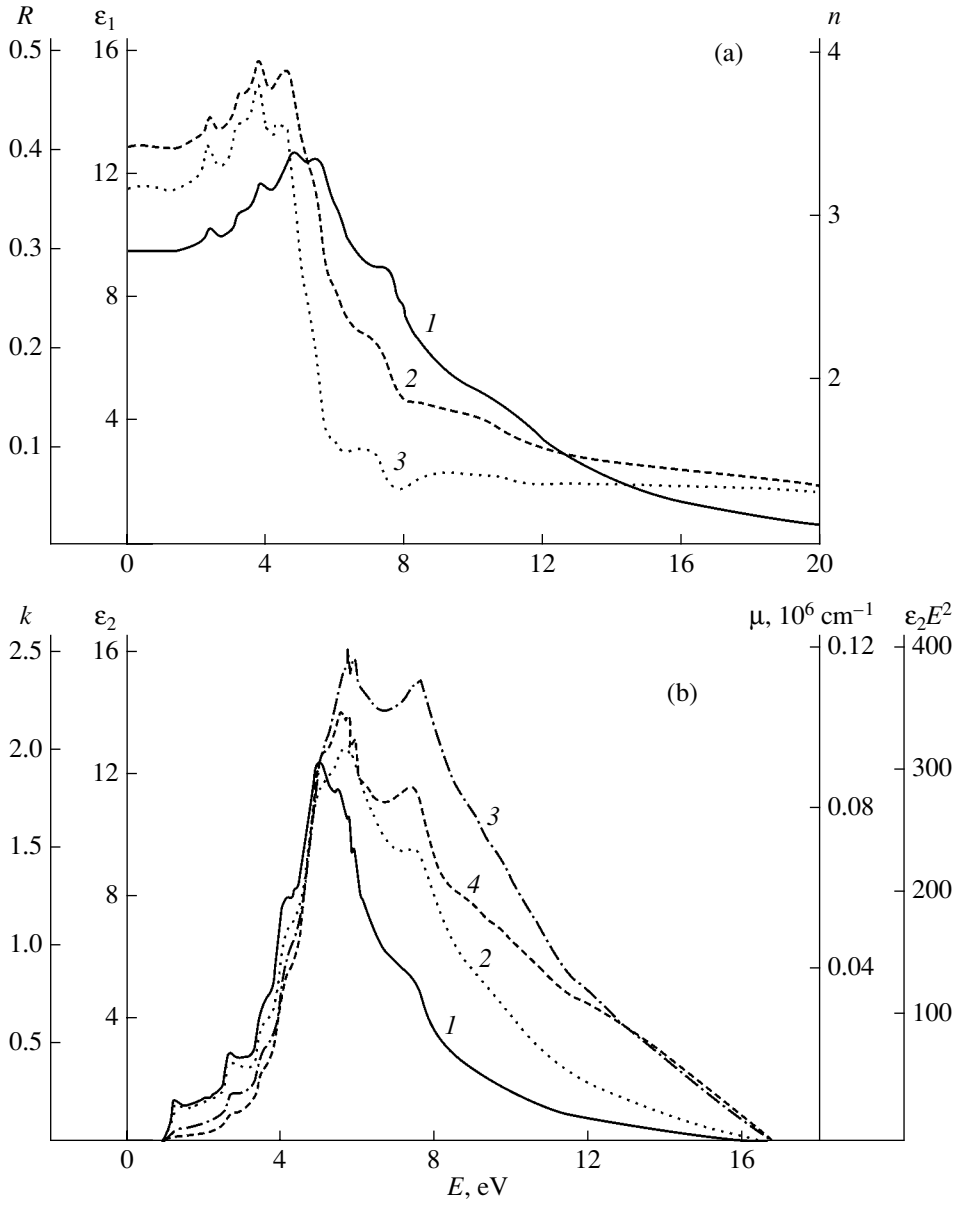

Fig. 2. (a) (*1*) Experimental spectrum of R and calculated spectra of (*2*) n and (*3*) ε_1; (b) calculated spectra of (*1*) ε_2, (*2*) k, (*3*) μ, and (*4*) $E^2\varepsilon_2$ for a β-In_2Se_3 crystal.

respect to $R(E)$. A shift in the electron-energy loss relative to ε_2 is very small for features 1–4 and 7; in contrast, this shift is equal to ~0.6 eV for feature 6 and 1.5 eV for feature 5.

In the transparency region, $R \approx 0.28$, $n \approx 3.27$, and $\varepsilon_1 \approx 10.7$, whereas $R \approx 0.03$, $n \approx 1.4$, and $\varepsilon_1 \approx 1.99$ at $E = 20$ eV; the largest values of these parameters are attained at peaks 5 ($R \approx 0.47$) and peaks 3 and 4 ($n \approx 4.7$, $\varepsilon_1 \approx 20$). The largest values of k, μ, and ε_2 are observed at peak 5: $k \approx 2.4$, $\mu \approx 1.4 \times 10^6$ cm^{-1}, and $\varepsilon_2 \approx 17$.

The peaks of very broad and intense bands of the bulk and surface plasmons are located at ~12.6 and ~11.5 eV, respectively.

The experimental spectrum $R(E)$ and other optical functions of a β-In_2Se_3 crystal, which were calculated on the basis of this spectrum, are similar to the spectra of optical functions for an α-In_2Se_3 crystal (Fig. 2, Table 1). The features of the $R(E)$ spectrum for β-In_2Se_3 are shifted to lower energies in reference to those of $R(E)$ for α-In_2Se_3; this shift amounts to ~0.3–0.4 eV only for three main components, 2, 3, and 7. An additional peak with a very low intensity is observed at ~1.22 eV (i.e., ~0.05 eV higher than E_{gd}) in the spectra of k, μ, ε_2, $-\mathrm{Im}\varepsilon^{-1}$, and $-\mathrm{Im}(1+\varepsilon)^{-1}$ for β-In_2Se_3.

A close resemblance between the spectra of optical functions for two In_2Se_3 phases can be attributed to an

Table 1. The energies (expressed in eV) of peaks and steplike features (in parantheses) in the spectra of optical functions, and also the energies (expressed in eV) and locations of transitions at the Γ, *M*, *L*, *A*, *K*, and *H* points of the Brillouin zone in the α- and β-In_2Se_3 crystals according to [15, 16]

N	1		2		3		4		5		6		7	
	α	β	α	β	α	β	α	β	α	β	α	β	α	β
R	2.53	2.55	(3.7)	3.35	4.32	3.90	4.90	4.90	5.55	5.50	7.4	(7.35)	(10.3)	(9.6)
n	2.51	2.50	(3.7)	3.40	4.20	3.90	4.77	4.65	(5.2)	(6.0)	(7.15)	(7.2)	(10.3)	(9.5)
ε_1	2.51	2.50	(3.7)	3.35	4.25	3.85	4.72	4.55	(5.2)	(5.3)	7.0	6.9	(10.2)	(9.6)
k	2.65	2.67	3.80	(3.5)	(4.40)	(4.10)	(4.9)	5.2	5.6	5.8	7.48	7.45	(10.2)	–
μ	2.65	2.67	3.80	(3.5)	(4.40)	(4.10)	–	5.1	5.7	5.8	7.6	7.55	(10.2)	(10.0)
ε_2	2.65	2.67	3.80	(3.5)	(4.40)	(4.10)	(4.9)	4.95	5.45	5.4	7.4	(7.3)	(10.2)	–
$-\mathrm{Im}\varepsilon^{-1}$	2.67	2.5	3.80	3.53	4.35	4.15	(5.0)	(5.3)	(6.9)	(6.4)	(8.0)	–	(10.2)	–
[15]	Γ, *M*, *A*		*M*, *L*		*H*		Γ, *K*		Γ, *M*, *K*, *H*		*K*, *L*		*K*, Γ	
	3.0		3.8		4.3		4.9		5.6		7.5		10.2	
[16]	Γ, *M*		Γ, *K*, *M*		Γ, *K*		Γ, *K*		Γ, *K*		Γ, *K*		Γ, *K*	
	2.7		3.8		4.4		4.9		5.8		7.4		10.0	

Table 2. Energy positions of the band peaks E_i and the bands' half-widths H_i (expressed in eV), intensities of bands I_i, and areas under the bands' spectral curves S_i for decomposed spectra of ε_2 and $-\mathrm{Im}\,\varepsilon^{-1}$, and also the energies (expressed in eV) and location of the bands at the Γ, *M*, *K*, and *L* points of the Brillouin zone for an α-In_2Se_3 crystal according to the theory [15, 16]

Component no.	E_i		H_i		I_i		S_i		[15]	[16]
	ε_2	$-\mathrm{Im}\,(1/\varepsilon)$	ε_2	$-\mathrm{Im}\,(1/\varepsilon)$	ε_2	$-\mathrm{Im}\,(1/\varepsilon)$	ε_2	$-\mathrm{Im}\,(1/\varepsilon)$		
1	1.46	1.5	0.54	0.98	1.90	0.01	1.44	0.01	–	Γ, 1.6
2	2.66	2.74	0.89	0.35	3.46	0.01	4.37	0.01	Γ, 2.4, 2.8	*M*, 2.7
2'	3.17	–	0.42	–	1.47	–	0.92	–	Γ, 3.0, 3.2	Γ, 3.1
3	3.54	3.58	0.35	0.28	4.08	0.01	2.15	0.01	Γ, 3.4	Γ, *M*, *K*, 3.6
3'	3.8	–	0.40	–	1.85	–	1.12	–	Γ, *M*, *L*, 3.9	Γ, *K*, 4.0
4	4.28	4.44	0.54	0.47	7.06	0.02	5.77	0.01	*M*, 4.4	Γ, *K*, *M*, 4.5
5	4.84	5.04	0.87	0.61	13.51	0.02	17.38	0.02	Γ, *M*, *K*, 4.8	Γ, *K*, *M*, 4.7
6	5.42	5.6	0.60	0.36	7.07	0.02	6.39	0.01	*K*, 5.3; Γ, 5.6	Γ, *K*, 5.4
7	6.2	6.4	0.83	1.24	6.57	0.08	8.19	0.15	Γ, 6.2	Γ, *K*, *M*, 6.1
8	7.18	7.04	0.75	0.35	4.75	0.02	5.43	0.01	*M*, *L*, 7.5	Γ, *K*, *M*, 7.2
9	7.7	8.06	0.41	1.66	1.35	0.15	0.85	0.36	*M*, *L*, 7.6	Γ, *K*, 7.7
10	8.26	8.66	0.74	0.47	3.12	0.04	3.53	0.03	Γ, *L*, 8.0	*M*, 8.0
11	–	9.2	–	0.50	–	0.06	–	0.04	Γ, *M*, *K*, 8.5	Γ, 9.2
11'	9.32	9.44	0.91	0.96	2.52	0.01	3.49	0.02	*M*, *L*, 9.2	*M*, 9.6
12	–	9.66	–	0.66	–	0.03	–	0.02	*M*, 9.7	*M*, 9.6
12'	–	9.9	–	0.20	–	0.01	–	0.01	*K*, 10.0	Γ, *K*, 10.0
13	10.4	10.44	0.72	1.42	1.76	0.13	1.96	0.29	*K*, *L*, 10.4	Γ, *K*, 10.4
14	11.44	11.36	0.65	0.75	1.44	0.05	1.45	0.05	*K*, *M*, 11.4	Γ, *K*, *M*, 11.7
14'	–	12.56	–	3.15	–	0.24	–	1.09	Γ, *M*, 12.6	–
15	–	14.06	–	1.04	–	0.06	–	0.09	Γ, *K*, 13.7	Γ, 14.0
16	–	15.6	–	2.92	–	0.17	–	0.74	Γ, *M*, *K*, 15.5	Γ, 15.6
17	–	16.84	–	0.65	–	0.04	–	0.04	*M*, 16.8	Γ, 17.1
18	–	17.68	–	1.56	–	0.11	–	0.26	Γ, 17.5	–

Table 3. Energy positions of the band peaks E_i and the bands' half-widths H_i (expressed in eV), intensities of bands I_i, and areas under the bands' spectral curves S_i for decomposed spectra of ε_2 and $-\mathrm{Im}\varepsilon^{-1}$, and also the energies (expressed in eV) and location of the bands at the Γ, *M*, *L*, and *K* points of the Brillouin zone for a β-In_2Se_3 crystal according to the theory [15, 16]

Component no.	E_i		H_i		I_i		S_i		[15]	[16]
	ε_2	$-\mathrm{Im}(1/\varepsilon)$	ε_2	$-\mathrm{Im}(1/\varepsilon)$	ε_2	$-\mathrm{Im}(1/\varepsilon)$	ε_2	$-\mathrm{Im}(1/\varepsilon)$		
1	2.66	2.74	0.82	0.43	2.23	0.02	2.63	0.01	Γ, 2.4, 2.8	*M*, 2.7; Γ, 3.0
2	3.5	3.59	0.23	0.72	0.93	0.02	0.33	0.02	Γ, 3.4	Γ, *M*, *K*, 3.5
3	4.0	4.00	0.99	0.41	4.53	0.02	6.52	0.01	Γ, *M*, *L*, 3.8	Γ, *K*, 4.0
4	4.98	5.06	0.90	0.68	7.08	0.05	9.44	0.05	Γ, *M*, *K*, 4.8	Γ, *K*, *M*, 4.7
5	5.76	5.90	1.43	0.81	8.47	0.06	17.62	0.07	*M*, *K*, 5.8	Γ, *K*, *M*, 5.8
6	6.6	6.92	0.76	1.27	3.05	0.12	3.54	0.23	*L*, 6.6; Γ, *K*, 6.9	*M*, 6.4
7'	7.52	–	0.89	–	5.37	–	7.20	–	Γ, *M*, *L*, 7.5	Γ, *K*, 7.6
7	8.05	8.02	0.35	0.79	1.24	0.08	0.66	0.10	Γ, *L*, 8.0	*M*, 8.0
8	8.64	8.88	0.88	1.35	3.90	0.17	5.20	0.34	Γ, *M*, *K*, 8.5	Γ, *K*, 8.6
9	9.74	9.67	0.87	0.43	3.18	0.04	4.23	0.02	*M*, *K*, 9.8	*M*, 9.6
10	10.76	10.48	0.65	1.47	2.80	0.13	2.82	0.29	Γ, *K*, 10.7	Γ, *K*, 10.4
11	11.5	11.22	0.59	0.46	2.35	0.03	2.14	0.02	Γ, *K*, 11.6	Γ, *K*, *M*, 11.7
11'	12.36	12.24	0.58	2.31	2.10	0.22	1.89	0.75	Γ, *M*, 12.6	Γ, 12.5
12	–	13.78	–	1.47	–	0.09	–	0.21	Γ, *K*, 13.7	Γ, 14.0
13	–	15.50	–	2.37	–	0.16	–	0.58	Γ, *M*, *K*, 15.5	Γ, 15.6
14	–	17.26	–	1.35	–	0.07	–	0.15	Γ, 17.5	Γ, 17.1

insignificant difference in the detailed structure of the hexagonal lattices in these phases. The optical axis *C* of In_2Se_3 single crystals is perpendicular to the plane of cleaved surfaces. Therefore, all spectra of the optical functions for the α- and β-phases were obtained for the $\mathbf{E} \perp \mathbf{c}$ polarization.

The experimental reflection spectrum and spectral curves of other optical functions calculated on the basis of this spectrum represent the result of summation of numerous separate transitions from occupied states to unoccupied states throughout the entire Brillouin zone.

We used the obtained $\varepsilon_2(E)$ and $\varepsilon_1(E)$ spectra for both In_2Se_3 phases to decompose $\varepsilon_2(E)$ into elementary components; we also determined the parameters E_i, H_i, I_i, and S_i. Altogether, we ascertained 15 (for the α phase) and 13 (for the β phase) transverse components for the bands corresponding to transitions in the range of 1–13 eV (Tables 2, 3). All components are comparatively broad: their half-widths range from 0.4 to 0.9 eV for the α phase and from 0.4 to 1.4 eV for the β phase. Component 5 is most intense. Components 7, 4, and 8 (for the α phase) and components 4, 7', 3, and 8 (for the β phase) are weaker by a factor of about 2–3. The bands 9, 2', and 3' (for the α phase) and bands 2 and 7 (for the β phase) were weakest.

Similarly, we used the combined Agrand diagrams to analyze simultaneously the pair of functions $-\mathrm{Im}\varepsilon^{-1}$ and $\mathrm{Re}\varepsilon^{-1}$ and decomposed the spectra of $-\mathrm{Im}\varepsilon^{-1}$ into longitudinal components for both phases of In_2Se_3; we determined the parameters E_i, H_i, I_i, and S_i for these components (Tables 2, 3). Altogether, we ascertained 21 (for the α phase) and 15 (for the β phase) components. Only bands 2' and 3' for the α phase and band 7' for the β phase were missing in the decomposition of electron-energy losses; these bands are analogues of transverse components. Among longitudinal components, components 14' (for the α phase) and 11' stand out as having the largest values for the area under the curves, half-widths, and intensities; these two components are related to bulk plasmons. The energy positions for the plasmon bands in the two In_2Se_3 phases differ by a mere ~0.3 eV, which amounts to about a tenth of the bands' half-widths. All other components in the spectrum of electron-energy losses are related to direct interband transitions.

In accordance with general theory, all longitudinal components are shifted to higher energies (although, insignificantly in certain cases) relative to the corresponding transverse components; this shift is equal to the energy of longitudinal–transverse splitting ΔE_{lt} for the components of the bands corresponding to interband transitions: ΔE_{lt} is approximately 0.04 eV (for components 1, 3, 13), 0.08–0.17 eV (components 2, 11', 4–7), and 0.4 eV (components 9, 10) for α-phase In_2Se_3. Notably, only two components have negative values of ΔE_{lt}; these are components 14 (ΔE_{lt} = –0.08 eV) and 8 (ΔE_{lt} = –0.14 eV). The magnitudes of these negative values amount to ~0.1 (component 14) and ~0.2 (component 8) of the corresponding half-widths. Similar special features of ΔE_{lt} are observed for

the second phase of In_2Se_3. The peak of transverse component 11 (for the β phase) is accidentally located in the vicinity of the peak of an intense and very broad band related to plasmons. As a result, the longitudinal analogue of the above transverse component was not ascertained.

The areas S_i under the spectral curves for many longitudinal components for the bands corresponding to transitions are smaller than those for transverse analogues by several hundred times. This observation indicates that the probabilities of excitation for many longitudinal components are lower than the probabilities of transitions for corresponding transverse analogues by several hundred times.

The energy bands in In_2Se_3 were calculated theoretically using the LCAO method for directions Γ*MK*Γ and *ALHA* [15] and the pseudopotential method in the local-density approximation [16] along the directions *K*Γ*M* and Γ*A*. We analyzed the data reported in [15, 16] and determined the energies of the most intense allowed direct interband transitions at the points Γ, *M*, and *K*. The transition energies are listed in the uppermost columns of Tables 2 and 3 and in the lower rows of Table 1. These data are estimative. In order to perform a theoretical detailed analysis of the peaks in the spectra of optical functions and the components of the complex fine structure of transverse and longitudinal bands, which correspond to transitions, one has to theoretically calculate the spectra of permittivity.

4. CONCLUSION

In this study, we calculated for the first time the spectra of complete sets of fundamental optical functions for the α- and β-In_2Se_3 crystals in the energy range of 0–20 eV. We decomposed the spectra of permittivities and electron-energy losses into transverse and longitudinal components, determined the parameters of these components, and suggested a scheme of their specific origin in the model of direct interband transitions. These results make it possible to gain deeper insight into the optical properties and electronic structure of the two phases in the imperfect In_2Se_3 compound in a wide energy range and form a radically new basis for further, more exact theoretical calculations of energy bands.

ACKNOWLEDGMENTS

This study was supported by the Competitive Center for Fundamental Natural Science (St. Petersburg State University).

REFERENCES

1. N. Kh. Abrikosov, V. F. Bankina, L. V. Poretskaya, E. V. Skudnova, and S. N. Chizhevskaya, *Semiconductor Chalcogenides and Chalcogenide-Based Alloys* (Nauka, Moscow, 1975).
2. V. V. Sobolev and V. V. Nemoshkalenko, *The Methods of Computational Physics in the Theory of Solid State. Electronic Structure of Semiconductors* (Naukova Dumka, Kiev, 1988).
3. V. V. Sobolev, Zh. Prikl. Spektrosk. **63**, 143 (1996).
4. V. Val. Sobolev, O. A. Makarov, and V. V. Sobolev, in *Proceedings of III International Conference on Amorphous and Microcrystalline Semiconductors* (S.-Peterb. Gos. Pedagog. Univ., St. Petersburg, 2002), p. 162.
5. V. Val. Sobolev, O. A. Makarov, and V. V. Sobolev, in *Proceedings of International Conference on Optics, Optoelectronics and Technology* (Ul'yan. Gos. Univ., Ul'yanovsk, 2002), p. 27.
6. V. V. Sobolev and A. I. Kalugin, Fiz. Tekh. Poluprovodn. (St. Petersburg) **36**, 155 (2002) [Semiconductors **36**, 148 (2002)].
7. V. V. Sobolev, A. P. Timonov, and V. Val. Sobolev, Fiz. Tekh. Poluprovodn. (St. Petersburg) **34**, 940 (2000) [Semiconductors **34**, 902 (2000)].
8. V. P. Mushinskiĭ and M. I. Karaman, *Optical Properties of Gallium and Indium Chalcogenides* (Shtiintsa, Chisinau, 1973).
9. C. Julien, A. Chevy, and D. Siapkas, Phys. Status Solidi A **118**, 533 (1990).
10. V. V. Sobolev and N. N. Sverbu, Fiz. Tverd. Tela (Leningrad) **6**, 2539 (1964) [Sov. Phys. Solid State **6**, 2020 (1964)].
11. V. V. Sobolev and S. G. Kroktoru, in *Proceedings of Conference on Physical Properties of III–V and III–VI Semiconductors* (Akad. Nauk AzSSR, Baku, 1967), pp. 76–80.
12. V. V. Sobolev, Phys. Status Solidi B **43**, K71 (1971).
13. V. V. Sobolev, Izv. Akad. Nauk SSSR, Neorg. Mater. **82**, 26 (1972).
14. V. V. Sobolev, *Bands and Excitons in Gallium, Indium, and Thallium Chalcogenides* (Shtiintsa, Chisinau, 1982).
15. N. Narita, S. Nagai, Sh. Saito, and K. Nakao, J. Phys. Soc. Jpn. **64**, 1622 (1995).
16. M. Ishikawa and T. Nakayama, Jpn. J. Appl. Phys. **36**, L1576 (1997).

Translated by A. Spitsyn

Semiconductors, Vol. 37, No. 7, 2003, pp. 763–765. Translated from Fizika i Tekhnika Poluprovodnikov, Vol. 37, No. 7, 2003, pp. 790–792.

CONFERENCE. SEMICONDUCTOR STRUCTURES, INTERFACES, AND SURFACES

Spectral Photosensitivity of *a*-SiGe:H/*c*-Si Heterostructures

A. A. Sherchenkov

Moscow Institute of Electronic Engineering (Technological University), Moscow, 124498 Russia

**e-mail: budaguan@ms.miee.ru*

Submitted December 23, 2002; accepted for publication December 27, 2002

Abstract—Characteristics of *a*-SiGe:H/*c*-Si heterostructures produced by rapid plasma-chemical low-frequency (55 kHz) deposition are studied. High photosensitivity of *a*-SiGe:H films is established. The spectral position of the maximum of photosensitivity of a *a*-SiGe:H/*c*-Si heterostructure can be varied from 830 to 920 nm by increasing the content of germanium in an *a*-SiGe:H alloy and decreasing its band gap. © *2003 MAIK "Nauka/Interperiodica"*.

INTRODUCTION

At present, the production of inexpensive photoelectric devices is one of the most important applications of amorphous hydrogenated silicon (*a*-Si:H) films [1]. By introducing Ge into *a*-Si:H, it is possible to vary the mobility gap in a wide range, thus changing the spectral range of the device sensitivity. This paper outlines the results of a pioneering study of the properties of *a*-SiGe:H/*c*-Si heterostructures produced for the first time by rapid low-frequency (55 kHz) plasma-chemical deposition.

Heterostructures were formed by the deposition of *a*-SiGe:H layers on single-crystal silicon substrates with a resistivity of 10 Ω cm. The temperature of the substrate, the discharge power, and the pressure in the reactor were 225°C, 150 W, and 70 Pa, respectively. The content of germanium in its mixture with monosilane (R_{Ge} = ([GeH_4]/[SiH_4] + [GeH_4])100%) was varied from 0 to 44.5%. The content of Ge in the films was determined by X-ray microprobe analysis. The properties of illuminated heterostructures were studied in the wavelength range from 500 to 1100 nm.

The results of investigations of the optical and electrical properties of *a*-SiGe:H alloys formed at different R_{Ge} are listed in Table 1. It is seen that low-frequency plasma-chemical deposition enables one to obtain an appreciably higher growth rate of *a*-SiGe:H films as compared to conventional plasma-chemical deposition at a frequency of 13.56 MHz (3.3 Å/s) [2]).

For the *a*-SiGe:H films obtained, the values of the $\eta\mu\tau$ product were calculated from the photoconductivity data and the Urbach energy E_0 was estimated by the direct-photocurrent method. These quantities are plotted versus the band-gap width (E_g) in Fig. 1. It is seen that, with a decrease in E_g, the Uhrbach energy increases and the $\eta\mu\tau$ product diminishes. The increase in E_0 indicates an increase in the density of states in the *a*-SiGe:H mobility gap. In turn, the increase in the density of states with increasing germanium content increases the number of recombination centers and reduces the $\eta\mu\tau$ product. According to IR spectroscopy data, an increase in E_0 and a decrease in $\eta\mu\tau$ correlate with the replacement of Si–H bonds by Ge–H bonds, which leads to the formation of Ge-related defects. Table 1 shows that, at E_g = 1.63 and 1.54 eV, the ratio σ_{ph}/σ_d is of the same order of magnitude as that for *a*-Si:H [1]. Therefore, the *a*-SiGe:H films produced by low-frequency plasma-chemical deposition have a high photosensitivity and comply with the requirements of device fabrication.

The spectral characteristics of *a*-SiGe:H/*c*-Si structures were studied by illuminating the samples from the side of the deposited amorphous alloy. Figure 2 shows the spectrum of the relative quantum efficiency of pho-

Table 1. Optical and electrical properties of *a*-SiGe:H alloys obtained at different R_{Ge}

Sample no.	R_{Ge}, %	V_d, Å/s	E_g, eV ± 0.01	E_F, eV ± 0.01	σ_d, Ω^{-1} cm^{-1}	σ_{ph}, Ω^{-1} cm^{-1}	σ_d/σ_{ph}
YG6-11	0	11.1	1.70	0.75	3.46×10^{-10}	3.42×10^{-5}	9.90×10^{4}
YG6-24	9.1	8.9	1.63	0.78	5.10×10^{-11}	1.40×10^{-5}	2.75×10^{5}
YG6-310	16.7	12.5	1.54	0.77	2.75×10^{-10}	4.60×10^{-6}	1.67×10^{4}
YG6-42	27.5	12.5	1.37	0.69	1.26×10^{-9}	1.90×10^{-6}	1.51×10^{3}
YG6-52	37.5	9.4	1.31	0.65	3.99×10^{-9}	5.28×10^{-7}	1.32×10^{2}
YG6-65	44.5	11.4	1.25	0.66	1.41×10^{-8}	7.00×10^{-7}	4.97×10^{1}

1063-7826/03/3707-0763$24.00

Table 2. Positions of photosensitivity peaks for *a*-SiGe:H/*c*-Si heterostructures at different reverse bias voltages

Sample no.	R_{Ge}, %	Photosensitivity peak position, nm							
		2.5 V	1.5 V	1.0 V	0.5 V	0 V	–0.5 V	–1.5 V	–2.5 V
YG6-1	0	830	830	830	830	830	830	830	830
YG6-2	9.1			810	830	830	830	830	830
YG6-3	16.7	830	830	830	830	830	830	840	830
YG6-4	27.5	860	860	880	870	870	870	870	870
YG6-5	37.5	940	920		930	890	930	940	930
YG6-6	44.5					920	920	920	920

toconversion η in *a*-SiGe:H/*c*-Si as obtained from expression [3]:

$$\eta(h\nu) = \frac{I_{sc}(h\nu)}{h\nu},$$

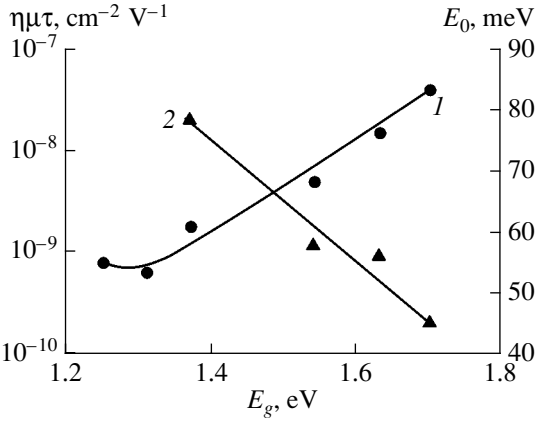

Fig. 1. The dependences of (*1*) the ημτ product and (*2*) the Uhrbach energy E_0 on the optical width of the band gap.

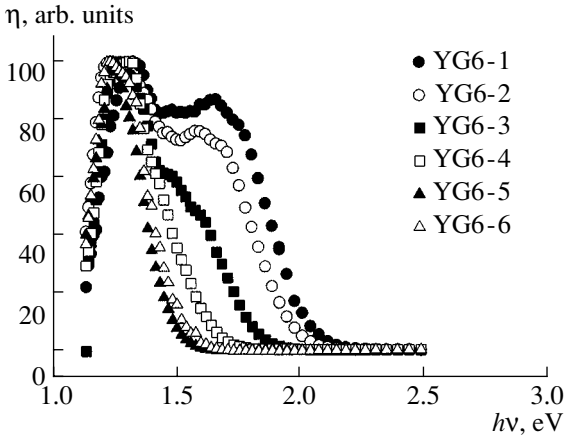

Fig. 2. Spectra of the relative quantum efficiency of photoconversion in *a*-SiGe:H/*c*-Si heterostructures formed at different R_{Ge}.

where I_{sc} is the short-circuit current and $h\nu$ is the energy of incident photons.

As can be seen from Fig. 2, the long-wavelength edge of the dependence $\eta(h\nu)$ is governed by the absorption of photons with energies $E \le 1.12$ eV in the narrow-gap *c*-Si material. The short-wavelength edge of absorption is controlled by the band gap of an *a*-SiGe:H alloy and shifts towards longer waves with an increase in the germanium content in the alloy and a decrease in E_g. As a result, a peak of η is observed in a narrow wavelength range with a maximum between 1.23 and 1.30 eV in the samples with high Ge content ($R_{Ge} \le 27.5\%$). For the heterostructures that were formed at $R_{Ge} \ge 27.5\%$, the quantum efficiency of photoconversion has a broadband character, which is indicative of a high quality of the heterostructure interface and a low intensity of the recombination at the interface. The high quality of the interface may be attributed to the presence of hydrogen in *a*-SiGe:H films and to the passivation of dangling bonds at the interface, as well as to the ion bombardment of the growth surface, which is characteristic of a low-frequency discharge.

Figure 3 shows a typical spectral dependence of the specific photosensitivity *S* for the *a*-SiGe:H/*c*-Si heterostructures, which was calculated as the ratio of the photoconductivity to the intensity of incident radiation. Table 2 lists the spectral positions of the photosensitivity peaks at different reverse biases applied to the studied structures. Only a slight dependence of the peak position of *S* on the applied voltage is observed. At the same time, the position of the photosensitivity peak changes from 830 to 920 nm when R_{Ge} increases from 0 to 44.5%. The appreciable red shift of the photosensitivity peak observed at $R_{Ge} \ge 27.5\%$ can be explained by narrowing of the band gap of the *a*-SiGe:H alloy and increasing long-wavelength absorption of the incident radiation.

Thus, the results obtained indicate that the *a*-SiGe:H films produced by rapid low-frequency plasma-chemical deposition have a high photosensitivity and, at E_g = 1.63 and 1.54 eV, the ratio σ_{ph}/σ_d is of the same order of magnitude as that for *a*-Si:H (1.67×10^4–2.75×10^5). By way of reducing the band-gap width via increasing

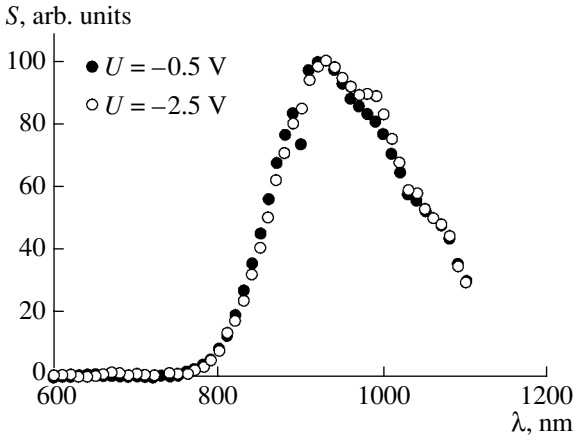

Fig. 3. Spectra of the specific photosensitivity of *a*-SiGe:H/*c*-Si heterostructures formed at R_{Ge} = 37.5%.

the Ge content in *a*-SiGe:H films, one can shift the photosensitivity peak in *a*-SiGe:H/*c*-Si heterostructures in the range between 830 and 920 nm and, thus, change the spectral range of sensitivity of photoelectric devices.

REFERENCES

1. R. E. I. Schropp and M. Zeman, *Amorphous and Microcrystalline Silicon Solar Cells: Modeling, Materials and Device Technology* (Kluwer Academic, Boston, 1998), p. 207.
2. B. G. Budaguan, A. A. Sherchenkov, A. A. Berdnikov, and A. A. Aivazov, in *Proceedings of International 196th Meeting of Electrochemical Society and 1999 Fall Meeting of Electrochemical Society of Japan* (Hawaii, 1999), p. 1449.
3. Yu. A. Nikolaev, V. Yu. Rud', Yu. V. Rud', and E. I. Terukov, Fiz. Tekh. Poluprovodn. (St. Petersburg) **34**, 685 (2000) [Semiconductors **34**, 658 (2000)].

Translated by A. Sidorova

Semiconductors, Vol. 37, No. 7, 2003, pp. 766–768. Translated from Fizika i Tekhnika Poluprovodnikov, Vol. 37, No. 7, 2003, pp. 793–795.

CONFERENCE. AMORPHOUS, VITREOUS, AND POROUS SEMICONDUCTORS

Photoinduced Conductivity Change in Erbium-Doped Amorphous Hydrogenated Silicon Films

A. G. Kazanskii*, H. Mell, E. I. Terukov***, and P. A. Forsh***

**Moscow State University, Moscow, 119899 Russia*

e-mail: Kazanski@phys.msu.ru

***Philipps-Universität Marburg, Fachbereich Physik, D-35032, Marburg, Germany*

****Ioffe Physicotechnical Institute, Russian Academy of Sciences, St. Petersburg, 194021 Russia*

Submitted December 23, 2002; accepted for publication December 27, 2002

Abstract—Changes in the dark conductivity of erbium-doped amorphous hydrogenated silicon (*a*-Si:H(Er)) films after their preliminary illumination at room temperature have been studied. The effect of a compensating boron impurity on the photoinduced change in the conductivity of *a*-Si:H(Er) films is analyzed. It is established that the magnitude and the sign of the change in conductivity depend on the duration of illumination and position of the Fermi level in the mobility gap. Possible mechanisms leading to a photoinduced change in the conductivity of *a*-Si:H(Er) films are discussed. © *2003 MAIK "Nauka/Interperiodica".*

Electroluminescence and photoluminescence (PL) from rare-earth ions embedded in a solid matrix is of interest for designing optoelectronic devices [1]. Er^{3+} ions luminesce at a wavelength of 1.54 μm, which falls within the transparency window of fiber-optical communication lines. Use of silicon as a material containing Er^{3+} ions allows integration of electronic and optoelectronic devices in a single matrix. In recent years, special attention has been given to films of Er-doped amorphous hydrogenated silicon, *a*-Si:H(Er). It has been shown [2, 3] that the Er^{3+}-related luminescence in *a*-Si:H is much stronger, and its temperature quenching, much weaker, compared with Er^{3+} luminescence in crystalline silicon.

Despite the considerable number of publications devoted to luminescence in *a*-Si:H(Er) (see, e.g., [3]), there are no studies concerned with photoinduced changes in the parameters of this material (Staebler–Wronsky effect). At the same time, such studies are important for the development of optoelectronic devices based on *a*-Si:H(Er). Therefore, it is of interest to study the influence exerted by prolonged illumination on the conductivity of erbium doped *a*-Si:H films.

a-Si:H(Er) films obtained by high-frequency glow-discharge decomposition of monosilane (SiH_4) were studied. Films with a thickness of ~0.8 μm were deposited onto quartz substrates heated to 250°C. The films were doped with erbium through sublimation at 105°C of an organometallic compound, $Er(C_5H_7O_2)$, placed in the vacuum line connected to the reaction chamber [4]. The films obtained exhibited PL at 1.54 μm. To change the Fermi level (E_F) position within the mobility gap, boron was introduced, in addition to erbium, into some of the films. Doping with boron was carried out by introducing diborane (B_2H_6) into the reaction chamber. The volume ratio of the gases, $k = [B_2H_6]/[SiH_4]$, was 10^{-5} and 3×10^{-5}. The films obtained were characterized by *n*-type conduction. With increasing *k*, the Fermi level position relative to the conduction band bottom ($E_c - E_F$) changed from 0.35 eV at $k = 0$ to 0.5 eV at $k = 3 \times 10^{-5}$ [4]. Measurements were done in a vacuum after annealing the films at 200°C for 15 min.

For all of the *a*-Si:H(Er) films, a long-term component of photoconductivity relaxation ($\Delta\sigma_{ph}$) was observed after their short-term (for a matter of seconds) illumination at photon energies $h\nu = 1.25$–1.8 eV. Figure 1 shows, as an example, the relaxation with time *t* of the photoconductivity of a film with $k = 3 \times 10^{-5}$. The long-term component of the photoconductivity decay is

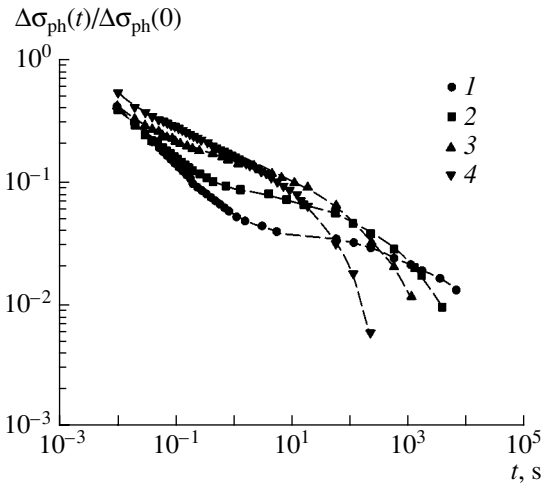

Fig. 1. Relaxation of the photoconductivity of *a*-Si:H(Er,B) film ($k = 3 \times 10^{-5}$) at different temperatures. *T*: (*1*) 300, (*2*) 330, (*3*) 360, and (*4*) 390 K.

1063-7826/03/3707-0766$24.00

satisfactorily described by a stretched exponential $\Delta\sigma_{ph}(t) \propto \exp[-(t/\tau)^{\beta}]$, where τ and β are temperature-dependent parameters of the stretched exponential.

It is known that persistent photoconductivity is observed in compensated *n*-type *a*-Si:H films [5], *a*-Si:H films with a heterogeneous structure [6], and multilayer *a*-Si:H *p–n–p–n* structures [7]. All of the above materials are characterized by the presence of potential fluctuations, which must separate nonequilibrium carriers, electrons and holes. At the same time, according to [8], carrier separation by potential fluctuations cannot lead to relaxation times as long as tens of hours at room temperature. In the opinion of Kakalios [8], the persistent photoconductivity in an *n*-type material based on *a*-Si:H may be due to charge separation and capture of holes by acceptor-like centers, with the subsequent rearrangement of the local configuration of these centers. It may be assumed that the model of persistent photoconductivity, which was suggested in [8], is valid for *a*-Si:H(Er) films. The nonuniform distribution of Er atoms and(or) their complexes with oxygen, ErO_{δ}, which are centers of the donor ($\delta < 1.5$) or acceptor type ($\delta > 1.5$) [9], and with defects must give rise to internal fields and lead to carrier separation. The appearance of acceptor centers that change their local configuration on capturing nonequilibrium carriers, i.e., holes, is also possible.

Figure 2 shows the kinetics of the relative change in dark conductivity, $\sigma_d(B)/\sigma_d(A)$, of Er-doped *a*-Si:H films exposed to the light of an incandescent lamp (incident power density $P = 50$ mW/cm^2) at room temperature; $\sigma_d(A)$ and $\sigma_d(B)$ are the σ_d values, respectively, before (in the annealed state) and after illumination for t_{ill}. The values of $\sigma_d(B)$ were measured 3 min after film illumination was terminated. It can be seen from the figure that, at short illumination times, $\sigma_d(B)/\sigma_d(A) > 1$ and weakly depends on the illumination time. With increasing illumination time, $\sigma_d(B)/\sigma_d(A)$ decreases to become less than unity at long t_{ill}. The observed kinetics of the change $\sigma_d(B)/\sigma_d(A)$ points to the occurrence of two processes which are responsible for changes in $\sigma_d(B)$ at short and long illumination times. Presumably, the increase in σ_d after illumination for short t_{ill} is associated with persistent photoconductivity, which was considered above. At the same time, the decrease in σ_d at long t_{ill} occurs because of an increase in the density of states in the middle of the mobility gap. It may be assumed that these states appear as a result of the restructuring of centers that capture nonequilibrium holes and give rise to persistent photoconductivity. In this case, the rate at which $\sigma_d(B)$ changes with illumination time must depend on the density-of-states distribution in the range through which the Fermi level travels and, correspondingly, on the level of compensation of the films with boron [10].

The temperature dependences of the dark conductivity of films in the annealed state, $\sigma_d \equiv \sigma_d(A)$, and those after illumination, $\sigma_d \equiv \sigma_d(B)$, (exposure to light of intensity $P = 50$ mW/cm^2 from an incandescence lamp for 2 h) are shown in Fig. 3. The temperature dependences of the dark conductivity of the degraded films, $\sigma_d(B)$, were measured 10 min after the illumination was terminated, with the temperature raised at a rate of 2 deg/min. Also shown in the figure is the temperature dependence of $\sigma_d(B)$ for a boron-free *a*-Si:H(Er) film illuminated for 20 s. The arrows show

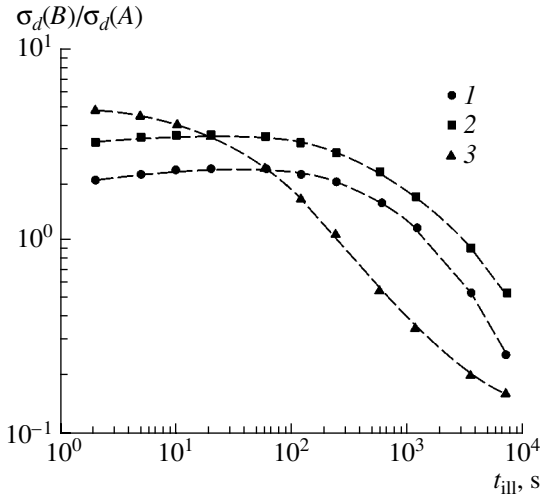

Fig. 2. Relative changes in the dark conductivity of the films under study vs. the time of their exposure at room temperature to light from an incandescent lamp (incident power density $P = 50$ mW/cm^2). k = (*1*) 0, (*2*) 10^{-5}, and (*3*) 3×10^{-5}.

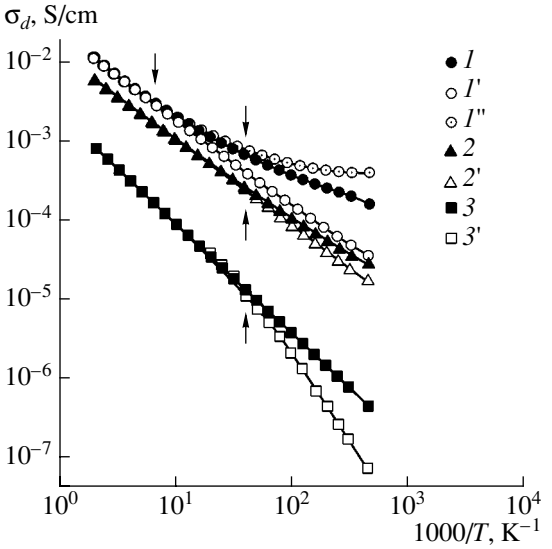

Fig. 3. Temperature dependences of the dark conductivity (σ_d) of films under study (*1–3*) in the annealed state and after exposure to light from an incandescent lamp (incident power density $P = 50$ mW/cm^2) at room temperature for (*1'–3'*) 2 h and (*1"*) 20 s. Arrows show characteristic temperatures at which photoinduced changes in dark conductivity are annealed out. k = (*1*, *1'*, *1"*) 0, (*2*, *2'*) 10^{-5}, and (*3*, *3'*) 3×10^{-5}.

characteristic temperatures at which illumination-induced changes in conductivity disappear. As seen from the figure, changes in the σ_d of a *a*-Si:H(Er) film containing no boron, which are caused by illumination at short t_{ill}, disappear at much lower temperatures (80–90°C) than do changes (decrease in σ_d) upon prolonged illumination (140–150°C). Additional introduction of boron also makes the temperatures lower at which changes in conductivity, induced by prolonged illumination, are annealed out. Presumably, this is due to an increase in the mobility of hydrogen atoms involved in the annealing-out of photoinduced defects in films containing boron atoms [11].

Thus, the study performed demonstrated that illumination of Er-doped *n*-type *a*-Si:H films leads to changes in conductivity whose magnitude and sign depend on the time of illumination and position of the Fermi level within the mobility gap. The intricate structure of defects and complexes contained in *a*-Si:H(Er) films presently gives no way of identifying the states responsible for photoinduced changes in conductivity. Additional introduction of boron into *a*-Si:H(Er) films substantially lowers the characteristic temperature for annealing-out the photoinduced change in conductivity.

ACKNOWLEDGMENTS

This study was supported by the program "Universities of Russia 2002."

REFERENCES

1. *Rare Earth Doped Semiconductors*, Ed. by G. S. Pomrenke, P. B. Klein, and D. W. Langer (Materials Research Society, Pittsburgh, 1993), MRS Symp. Proc., Vol. 301.
2. W. Fuhs, I. Ulber, G. Weiser, *et al.*, Phys. Rev. B **56**, 9545 (1997).
3. H. Kühne, G. Weiser, E. I. Terukov, *et al.*, J. Appl. Phys. **86**, 896 (1999).
4. A. G. Kazanskii, H. Mell, G. Weiser, and E. I. Terukov, J. Non-Cryst. Solids **299–302**, 704 (2002).
5. J. K. Rath, W. Fuhs, and H. Mell, J. Non-Cryst. Solids **137–138**, 279 (1991).
6. S.-H. Choi, G.-L. Park, C. Lee, and J. Yang, Solid State Commun. **59**, 177 (1986).
7. J. Kakalios and H. Fritzsche, MRS Symp. Proc. **37**, 29 (1985).
8. J. Kakalios, Philos. Mag. B **54**, 199 (1986).
9. C. Piamonteze, A. C. Iníguez, L. R. Tessler, *et al.*, Phys. Rev. Lett. **81**, 4652 (1998).
10. A. G. Kazanskii, Fiz. Tekh. Poluprovodn. (Leningrad) **24**, 556 (1990) [Sov. Phys. Semicond. **24**, 349 (1990)].
11. W. Beyer, J. Herion, and H. Wagner, J. Non-Cryst. Solids **114**, 217 (1989).

Translated by M. Tagirdzhanov

Semiconductors, Vol. 37, No. 7, 2003, pp. 769–774. Translated from Fizika i Tekhnika Poluprovodnikov, Vol. 37, No. 7, 2003, pp. 796–801.

CONFERENCE. AMORPHOUS, VITREOUS, AND POROUS SEMICONDUCTORS

On Studying Nanoporous-Carbon-Based Composites by Small-Angle X-Ray Scattering

É. A. Smorgonskaya

Ioffe Physicotechnical Institute, Russian Academy of Sciences, Politekhnicheskaya ul. 26, St. Petersburg, 194021 Russia

Submitted December 23, 2002; accepted for publication December 27, 2002

Abstract—Possible intensity variations arising in small-angle X-ray scattering as a result of filling nanopores in nanoporous carbon with extraneous impurities were analyzed in terms of a simple monodispersed system of electron-density fluctuations. Systems with various ratios between the electron density of the carbon skeleton and that of noncarbon nanoclusters incorporated in the skeleton were considered; these systems correspond to the composites with clusters of hexagonal or amorphous selenium, as well as those of rhombic or amorphous sulfur. The partial contributions to the intensity variation in scattering from unfilled nanopores, carbon and noncarbon nanoclusters, and also the total variation were calculated as functions of nanopore filling factor β for various degrees of initial-nanoporosity α of the carbon skeleton. It was shown that, depending on α and β, both an increase and a decrease in scattering is possible. The data obtained may be useful for controlling the filling efficiency of nanopores during the formation of a composite. *© 2003 MAIK "Nauka/Interperiodica".*

1. INTRODUCTION

Nanoporous carbon (np-C) in the form of bulk material with a high degree of nanoporosity (up to 40–45% for a total porosity of up to 70–75%) can be obtained using the original technology of high-temperature chlorination of carbide compounds [1–3]. As a result of a physical-chemistry study [1] and structural investigations [4–6], which have shown, in particular, a high size uniformity of np-C nanopores, the idea emerged that this uniformity could be used to create a new class of composites by filling the pores with extraneous materials. It is expected that introducing guests of various nature, along with choosing an np-C (host) source with certain structural and physical parameters, will make it possible to control the properties of the obtained composites in a wide range. In creating similar composites by the "host–guest" technology, the problem arises of controlling the efficiency of filling the nanopores and determining the dimensional parameters of incorporated impurity nanoclusters. A promising approach to solving this problem seems to be the method of small-angle X-ray scattering (SAXS), which was previously used particularly for investigating the processes of adsorption, desorption, and mass transport in porous carbon adsorbents [7, 8]. SAXS has been used for studying the structure of nanodimensional inhomogeneities in np-C prepared from various carbides [4–6]. Recently, data were obtained for the first time for SAXS from the np-C–sulfur nanocomposite as well [9]. The introduction of guests whose density is comparable with that of the carbon skeleton (contrary to those investigated in [7, 8]) considerably modifies the SAXS intensity and its angular distribution; as a result, the unambiguous interpretation of the experimental results becomes quite a complicated problem.

In this study, we analyze possible variations in the scattering power during SAXS, which can be expected if the np-C nanopores are filled with solid guests of various density d and, therefore, of various electron density ρ_i. The analysis is performed in terms of a simple model of a inhomogeneous monodisperse system, which involves subsystems of nanoclusters and nanopores of identical sizes in the context of the Guinier approximation [10]. Numerical calculations were performed for values of ρ_i corresponding to crystalline and amorphous selenium and sulfur, which are of interest as np-C guests and began to be studied experimentally [9]. It should be noted that we consider only the variations which are directly related to scattering. Variations (increase) in the losses associated with radiation absorption in a material are not considered here; however, they have to be taken into account in every particular case when processing experimental data as, for example, in [9].

2. GENERAL RELATIONSHIPS FOR VARIATIONS IN THE SAXS INTENSITY WHEN FILLING NANOPORES

We consider a hypothetical model of a system of spatial fluctuations $\Delta\rho \equiv \rho - \bar{\rho}$ in the electron density ρ relative to its mean value $\bar{\rho}$ over the whole system. Let an identical Guinier radius, or a radius of gyration R_g—a parameter characterizing the spatial size of fluctuations in a monodisperse system—be assigned to these fluctuations. In this case, if scattering angles 2ϑ are small, a SAXS intensity $i(s)$ per unit scattering volume

1063-7826/03/3707-0769$24.00

(scattering power) is conveniently described using the Guinier model [10]:

$$i(s) \propto |\Delta\rho|^2 N v^2 \exp[-(sR_g)^2/3]. \quad (1)$$

Here, $sR_g \ll 1$, $s = 4\pi\sin\vartheta/\lambda$ is the magnitude of the scattering vector, λ is the X-ray wavelength, $v \propto R_g^3$ is the fluctuation volume, and N is the number of electron-density fluctuations per unit volume of the system. We assume that the electron-density fluctuations are produced by the nanoclusters and nanopores with an identical radius of gyration R_g and certain values of internal electron density ρ_C (carbon skeleton) and ρ_{np} (nanopores). We also assume that filling of pores does not lead to "swelling" (increasing R_g) [4, 5]. In this case, the variations δi in the SAXS intensity associated with filling depend only on the variation $\Delta\rho$ in the value of fluctuations and on their total volume $V_{fl} = vN$ per unit volume of the system [preexponential factor in expression (1)]. Further, the variations δi are calculated in relation to the nanopore filling factor $\beta \equiv V_i/V_{np}$; here, V_{np} and V_i are the initial total volume of nanopores and the volume of filled nanopores, respectively ($0 \le \beta \le 1$). The dependences $\delta i(\beta)$ are calculated for systems with various degrees of initial porosity $\alpha \equiv V_{np}/V$ ($0 < \alpha \le 0.5$, and V is the sample volume).

The variation in the SAXS intensity associated with fluctuations of a certain type in the material (nanopores, nanoclusters of the carbon skeleton, or incorporated impurity nanoclusters) can be written as

$$\delta i \propto |\Delta\rho_2|^2 V_{2fl} - |\Delta\rho_1|^2 V_{1fl}. \quad (2)$$

From here on, subscript *1* refers to the host nanoporous system and subscript *2* refers to the nanocomposite. In the general case, the mean value of the electron density of a material is

$$\bar{\rho}_{1,2} = (1-\alpha)\rho_C + \alpha\rho_{np}. \quad (3)$$

In the initial system, $\rho_{np} = 0$ for unfilled pores and

$$\bar{\rho}_1 = (1-\alpha)\rho_C. \quad (3a)$$

If a certain volume fraction β of the pores is filled with an impurity, the mean electron density of the material increases depending on the electron density ρ_i in the impurity nanocluster:

$$\bar{\rho}_2 = (1-\alpha)\rho_C + \alpha\beta\rho_i. \quad (3b)$$

For the sake of definiteness, let the fluctuations under consideration be empty nanopores of identical volume v_{np}. Their scattering powers i_{1ep} and i_{2ep} in the host material and in the nanocomposite, respectively, are specified by the electron-density fluctuations

$$\Delta\rho_{1,2} = -\bar{\rho}_{1,2} \quad (4)$$

and by the fluctuation volumes $V_{1fl} \propto \alpha$ and $V_{2fl} \propto \alpha(1-\beta)$ in both cases, respectively. Here, the variation $\delta i_{ep} \equiv i_{2ep} - i_{1ep}$ in the scattering power of a material due to empty pores can be derived from (2) by simple transformations:

$$\delta i_{ep} \propto \left\{\left[1-\alpha\left(1-\beta\frac{\rho_i}{\rho_C}\right)\right]^2(1-\beta) - (1-\alpha)^2\right\}. \quad (5)$$

Expression (5) describes a variation in the scattering by empty nanopores, a fraction of which remains unfilled even after introducing the guest.

Similarly, we can find the contribution to the SAXS-intensity variation $\delta i_C \equiv d_{2C} - i_{1C}$ associated with nanoclusters of the carbon skeleton. In this case, it is clear that the volume of clusters does not vary when the nanopores are filled and variation in their contribution to scattering occurs due only to an increase in the mean electron density of the medium. Instead of (5), for such a variation we have

$$\delta i_C \propto \alpha^2(1-\alpha)\left[\left(1-\beta\frac{\rho_i}{\rho_C}\right)^2 - 1\right]. \quad (6)$$

For the variation $\delta i_i \equiv i_{2i}$ in scattering by impurity nanoclusters filling the nanopores, it is easy to find that

$$\delta i_i \propto \alpha\beta\left[(1-\alpha\beta)\frac{\rho_i}{\rho_C} - (1-\alpha)\right]^2. \quad (7)$$

From (7), it can be seen that the scattering by impurity clusters increases with β for small filling factors β.

The resulting variation δi_{tot} in the scattering with filling of the pores in a monodisperse system is specified by the sum of contributions of nanoinhomogeneities of all of the above types:

$$\delta i_{tot} = \delta i_{ep} + \delta i_C + \delta i_i. \quad (8)$$

In the following sections, general expressions (5)–(8) are used as applied to np-C-based nanocomposites with specific guests (selenium or sulfur) for which, as is easy to show, the electron density ρ_i in the solid state substantially exceeds the electron density ρ_C of the carbon skeleton (for hexagonal or amorphous selenium) or is close to this density (for orthorhombic or amorphous sulfur).

3. NANOCOMPOSITE CONSISTING OF NANOPOROUS CARBON AND HEXAGONAL SELENIUM

In Figs. 1a–1d, we illustrate the behavior of the scattering intensity for all types of inhomogeneities in the model nanocomposite obtained by the introduction of a guest with an electron density $\rho_i = 2\rho_C$. Approximately the same relationship between ρ_i and ρ_C can take place if hexagonal selenium (*c*-Se) is formed in nanopores. This can be easily shown on the basis of the known values of the c-Se density ($d_{c\text{-Se}} = 4.81$ g/cm^3) and that of

the carbon skeleton (d_C = 2.1 g/cm^3), as well as by using the relationship

$$\rho = (d/A)n, \quad (9)$$

which is valid for a monatomic medium with a density d, where A is the atomic weight, and n is the number of electrons in an atom. From Fig. 1, it can be seen that, for a low initial nanoporosity ($\alpha \lesssim 0.2$), the scattering at empty nanopores (Fig. 1a) is weakened if one introduces a guest ($\delta i_{ep} < 0$) because their volume decreases. For larger values of α ($\alpha > 0.2$), a rather wide range of filling factors β appears, which widens with increasing α, and the scattering by nanopores is increased in this interval: $\delta i_{ep} > 0$. This takes place because the effect of increasing the contrast between empty nanopores and the medium as a whole dominates in the scattering over the influence of a decreasing relative number of empty pores.

For the ratio between ρ_i and ρ_C under consideration, the scattering by skeleton clusters (Fig. 1b) always decreases with filling, which is associated with a decrease in the contrast between the skeleton and the medium. It is of interest to note that the greatest drop in intensity i_C takes place when exactly half of the nanopore volume ($\beta = 0.5$) is filled. If all of the nanopores are filled ($\beta = 1$), no variation in scattering by the skeleton should be observed; i.e., $\delta i_C = 0$, as expected. Actually, in this case, the corresponding electron-density fluctuations only change sign but remain equal in magnitude to the initial fluctuations without a guest.

The scattering by incorporated impurity nanoclusters first naturally increases as the nanopores are filled: $\delta i_{c\text{-Se}} \equiv i_{c\text{-Se}} > 0$, because the volume of these clusters increases (Fig. 1c). However, for a reasonably high initial nanoporosity α ($\alpha \gtrsim 0.3$) and high β, the quantity δi_i begins to decrease with increasing β. This occurs due to a decreasing contrast between dense clusters and the medium, whose density increases significantly with the content of guests.

As can be seen from Fig. 1d, the resulting SAXS intensity in the model nanocomposite under consideration turns out to be higher than in the host material for any value of the filling factor ($0 < \beta < 1$). In this case, an increase in the scattering manifests itself more obviously the higher the initial nanoporosity α. For the given value of α, the greatest increase in the scattering power is attained for $\beta = 0.5$, and the intensities of scattering by the nanocomposite and by the host coincide for $\beta = 1$, so that $\delta i_{tot} = 0$.

4. NANOCOMPOSITE CONSISTING OF NANOPOROUS CARBON AND AMORPHOUS SELENIUM

If selenium is amorphous in incorporated clusters of the nanocomposite, i.e., in the form of *a*-Se with a density $d_{a\text{-Se}}$ = 4.28 g/cm^3, its electron density ρ_i will be somewhat lower than in hexagonal *c*-Se, as follows from estimate (9): $\rho_i = 1.74\rho_C$. In Figs. 2a–2d, we show the variations in the SAXS intensity from all types of nanoinhomogeneities when introducing a guest with the aforementioned ratio between ρ_i and ρ_C. It can be seen that all these dependences of the SAXS intensity on the filling factor β are similar to those considered in Section 3. However, there are marked quantitative distinctions. In particular, the range of values of β for which the scattering by empty pores increases is narrower (Fig. 2a) and the scattering by the skeleton clusters is not suppressed even for $\beta = 1$ (Fig. 2b). The increase in the scattering by the *a*-Se nanoclusters (Fig. 2c) is less pronounced compared with *c*-Se (Fig. 1c).

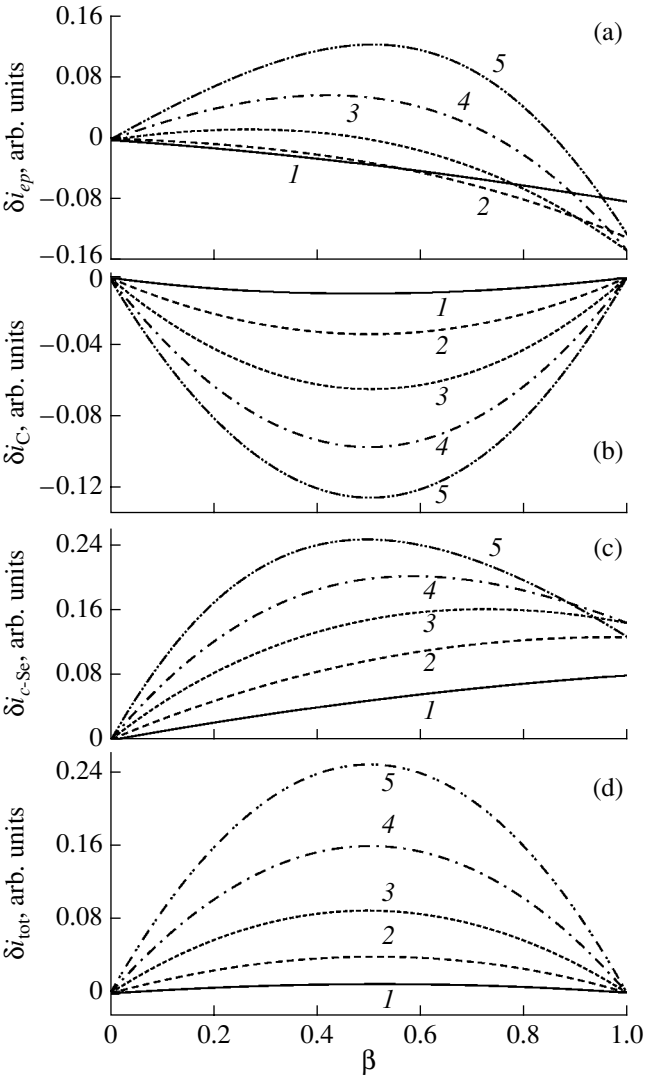

Fig. 1. Variation in the scattering power of a nanocomposite with incorporated nanoclusters of crystalline selenium ($\rho_i/\rho_C = 2$) for SAXS (a) by unfilled nanopores, (b) by carbon-skeleton nanoclusters, (c) by incorporated impurity nanoclusters, and (d) the resulting variation, in relation to the nanopore filling factor β for various degrees of initial nanoporosity α. α = (*1*) 0.1, (*2*) 0.2, (*3*) 0.3, (*4*) 0.4, and (*5*) 0.5.

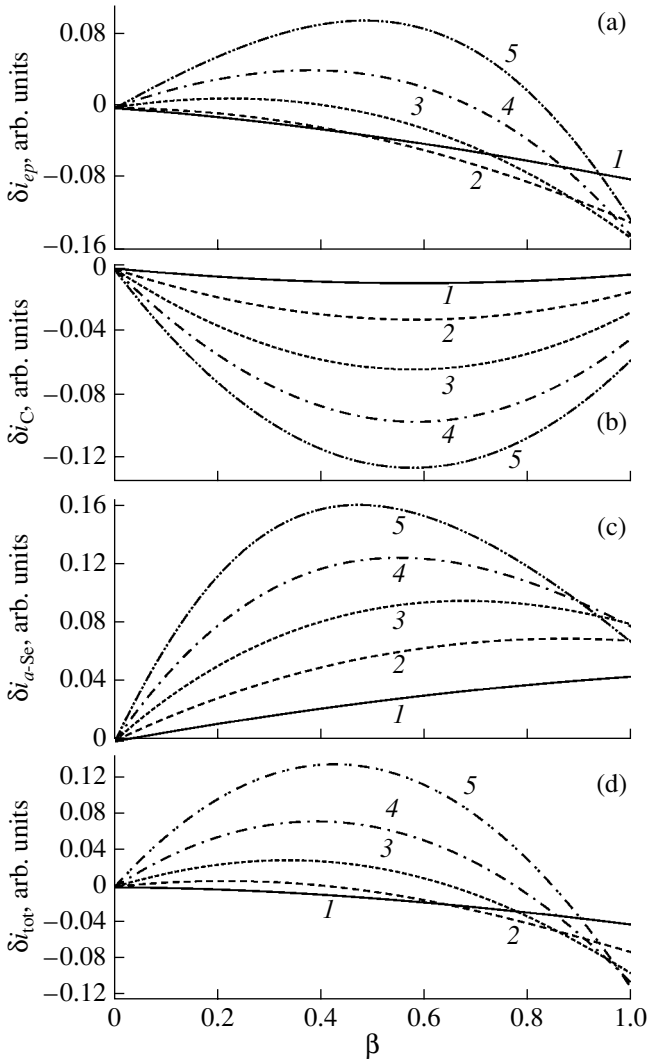

Fig. 2. The same as in Fig. 1 but for a nanocomposite with incorporated nanoclusters of amorphous selenium (ρ_i/ρ_C = 1.74).

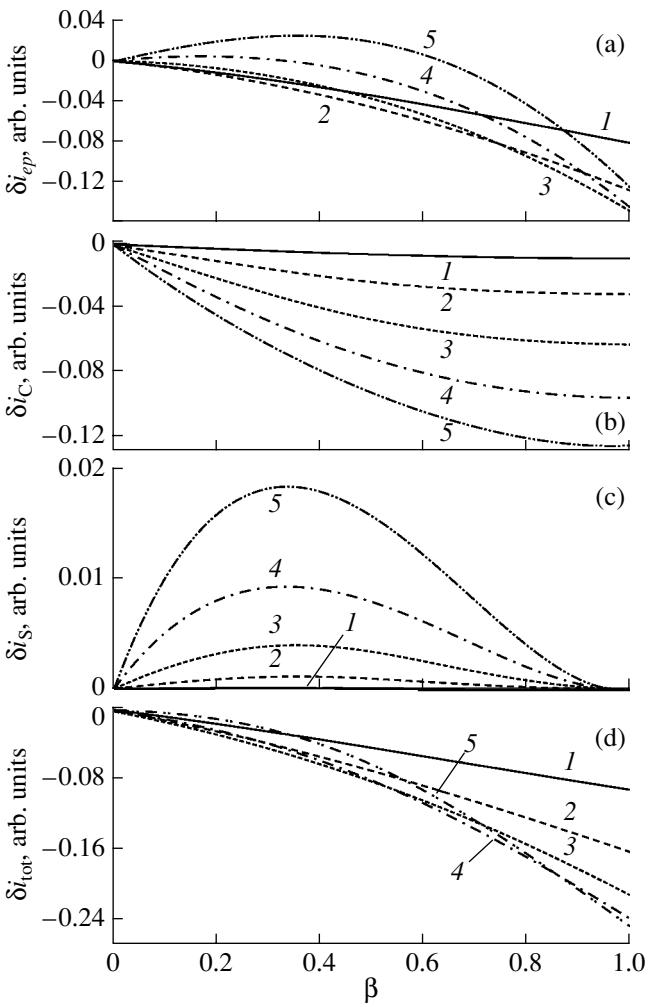

Fig. 3. The same as in Fig. 1 but for a nanocomposite with incorporated nanoclusters of amorphous sulfur (ρ_i/ρ_C = 1).

As a result, the net effect of nanopore filling (Fig. 2d) amounts to an increase in SAXS in a restricted interval of moderate values of the filling factor: $\delta i_{tot} > 0$ for $\beta < \beta_0$. From Fig. 2d, it can also be seen that the boundary value $\beta = \beta_0$, which separates the regions with opposite signs of δi_{tot} (i.e., with a different type of the SAXS behavior with filling of the nanopores) is shifted to larger values of β with increasing initial porosity α. This means that the reduction in the scattering power in the case of forming a-Se nanoclusters in the nanocomposite on the basis of a highly porous np-C with $\alpha \gtrsim 0.4$ can be expected only for reasonably large nanopore filling factors ($\beta \gtrsim 0.8$). For smaller values of β, the SAXS increases. Thus, the SAXS intensity can characterize the efficiency of nanopore filling. However, for this purpose, it is necessary to know, as accurately as possible, the state of incorporated nanoclusters and the corresponding values of electron densities.

5. NANOCOMPOSITE CONSISTING OF NANOPOROUS CARBON AND SULFUR

The nanocomposite in which $\rho_i = \rho_C$ is of special interest from the viewpoint of SAXS analysis; this situation, as follows from (9), takes place if the np-C pores are filled by amorphous or rhombic sulfur, whose densities ($d_S \approx 2$ g/cm^3) are close to the carbon-skeleton density. In this case, the SAXS difference curve $\delta i_{tot}(s)$ found from experiment for the composite and the host describes the scattering by sulfur nanoclusters. From an analysis of this curve, it is possible to derive the dimensional characteristics of these nanoclusters, in other words, those of the sulfur-filled nanopores in the host [9]. Figures 3a–3d, similarly to Figs. 1 and 2, show the contributions to the SAXS-intensity variation when forming the composite; different curves correspond to the scattering (a) at unfilled nanopores δi_{ep}, (b) at carbon nanoclusters δi_C, and (c) at sulfur nanoclusters δi_S, and also (d) to the resulting total variation δi_{tot} in relation to the filling factor β for various values of α. It can

be seen that, if sulfur is introduced instead of selenium, the scattering by empty nanopores can increase only for np-C with a high initial porosity α ($\alpha \gtrsim 0.4$). In this case, the scattering by the carbon nanoclusters decreases rather abruptly with increasing β (Fig. 3b). The scattering by the sulfur nanoclusters first increases due to the increasing total volume of these clusters and, then, decreases to zero for $\beta = 1$ (Fig. 3c), because the magnitude of the corresponding electron-density fluctuations vanishes. As a result, the introduction of sulfur into the carbon system with identical sizes of nanoclusters and nanopores ($v_{np} = v_i$) leads to a decrease in the total scattering power, i.e., $\delta i_{tot} < 0$ (Fig. 3d). This effect is in fact observed experimentally in a wide interval of scattering angles [9]. It should be noted that, for $v_{np} > v_i$ and large values of α and moderate values of β, a weak growth in i_{tot} is also possible ($\delta i_{tot} > 0$) [9], which continues to depend on the mean electron density of the medium against the background of which the empty pores scatter more strongly. In actual fact, the SAXS intensity in the np-C–sulfur nanocomposite turns out to be somewhat higher than in the host [9], according to the experiment performed in a narrow angular region corresponding to the finest nanopores. This fact can be associated either with the difficulties sulfur has penetrating into the finest nanopores (with the radius of gyration $R_g \lesssim 0.8$ nm) if the conventional method for introducing impurities is used or with an increasing concentration of fine nanopores accompanied by the partial filling of the pore space in individual large-size nanopores.

6. RELATIVE SCATTERING-POWER VARIATIONS

In Figs. 4a–4c, we compare the relative variations in the scattering power $\delta i_{tot}/i_{tot\,0}$ of nanocomposites in relation to the filling factor β when introducing the above guests into np-C with varying initial porosity α. Here, $i_{tot\,0} \propto \alpha(1-\alpha)$ is the scattering power of the host. In all of the cases considered, i.e., for $1 \le \rho_i/\rho_C \le 2$, it turns out that $-1 \le \delta i_{tot}/i_{tot\,0} \le 1$. As noted above (Section 5), if $\rho_i / \rho_C = 1$ (Fig. 4a), the scattering power of a composite should be lower than of the host for arbitrary degrees of filling and initial porosity; strictly speaking, SAXS in the composite should not occur at all without nanopores remaining empty ($\beta = 1$): $\delta i_{tot} = -i_{tot\,0}$. It should be noted that, in this case, for the given degree of filling from the interval $0 < \beta < 1$, the modulus of relative scattering-power variation $|\delta i_{tot}/i_{tot\,0}|$ always decreases with increasing initial porosity; this is not true for the magnitude of the variation $|\delta i_{tot}|$, which increases with α for reasonably high β (Fig. 3d). For $\rho_i/\rho_C = 2$ (Fig. 4c), on the contrary, the scattering power of the composite is always higher than that of the host (Section 3) and increases with the initial nanoporosity for an arbitrary value of β. If only half of the nanopores are filled the largest increase becomes twofold for $\alpha = 0.5$: $\delta i_{tot} = i_{tot\,0}$. In the intermediate case (Section 4),

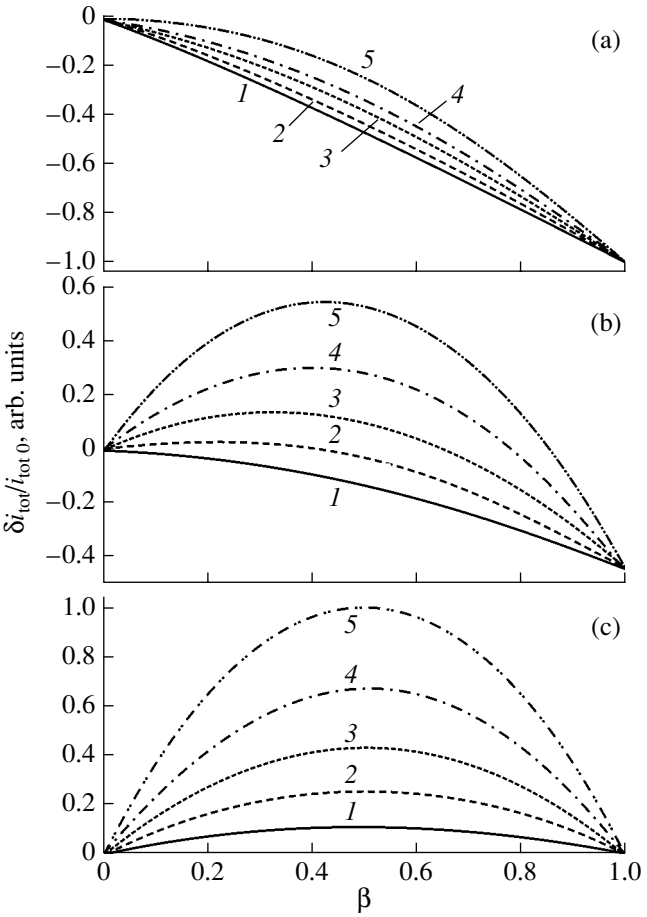

Fig. 4. Relative variations in the scattering power of a nanocomposite compared with hosts having various degrees of nanoporosity α in relation to the filling factor β for ρ_i/ρ_C = (a) 1, (b) 1.74, and (c) 2. α = (*1*) 0.1, (*2*) 0.2, (*3*) 0.3, (*4*) 0.4, and (*5*) 0.5.

both an increase and a decrease in the scattering power are possible during formation of the nanocomposite; however, all of the possible variations are less than the scattering power of the host (Fig. 4b). Notably, a degree of filling β_0 exists for nanopores (increasing with α) in np-C with an arbitrary initial nanoporosity α, so that $\delta i_{tot}/i_{tot\,0} = 0$ for $\beta = \beta_0$. In other words, the corresponding composite and the host are indistinguishable with respect to the SAXS intensity for an identical scattering volume.

7. CONCLUSION

Thus, in terms of a simple monodisperse model of a nanocomposite, it is possible to reveal the basic pattern of variations in the SAXS intensity induced by filling nanopores of the nanoporous material of the host. In polydisperse systems, in particular, np-C and nanocomposites based on it, the angular distribution of the SAXS intensity is not described by a single exponential function (1) but depends on the size distribution of

nanoinhomogeneities. In turn, the nanopore filling factor β, as was shown by the example of sulfur introduced in np-C [9], can depend on the nanopore size. In this case, the observed variations in the SAXS-curve shape during formation of the composite are governed by the "differential" parameters α and β related to nanopores of various sizes, and also by the state of a guest in nanoclusters and, therefore, can have a rather complicated character. Nevertheless, the above results may be useful for interpreting SAXS data at a qualitative level if it is assumed, for example, that a certain region *s* in the SAXS curve is primarily defined by a contribution from nanoinhomogeneities of a certain size (radius of gyration). For quantitative analysis of SAXS data, it is necessary to use independent data derived, for example, from adsorption experiments or from diffraction measurements.

ACKNOWLEDGMENTS

I am grateful to INTAS (grant no. 00-761) and to the Ministry of Industry and Science of the Russian Federation (State contract "Controlled Synthesis of Fullerenes and Other Atomic Clusters") for supporting this study.

REFERENCES

1. S. K. Gordeev and A. V. Vartanova, Zh. Prikl. Khim. (St. Petersburg) **66**, 1080 (1994); Zh. Prikl. Khim. (St. Petersburg) **66**, 1375 (1994).
2. S. K. Gordeev, A. V. Vartanova, S. G. Zhukov, *et al.*, RF Patent No. 2,026,735, Byull. No. 2 (1995).
3. R. G. Avarbz, A. V. Vartanova, S. K. Gordeev, *et al.*, U.S. Patent No. 5,876,787 (1999).
4. R. N. Kyutt, É. A. Smorgonskaya, S. K. Gordeev, *et al.*, Fiz. Tverd. Tela (St. Petersburg) **41**, 891 (1999) [Phys. Solid State **41**, 808 (1999)]; Fiz. Tverd. Tela (St. Petersburg) **41**, 1484 (1999) [Phys. Solid State **41**, 1359 (1999)].
5. É. A. Smorgonskaya, R. N. Kyutt, A. V. Shchukarev, *et al.*, Fiz. Tekh. Poluprovodn. (St. Petersburg) **35**, 690 (2001) [Semiconductors **35**, 661 (2001)].
6. E. Smorgonskaya, R. Kyutt, A. Danishevskii, *et al.*, J. Non-Cryst. Solids **299–302**, 810 (2002).
7. G. M. Plavnik, T. P. Puryaeva, and M. M. Dubinin, Izv. Ross. Akad. Nauk, Ser. Khim., No. 7, 628 (1993).
8. G. M. Plavnik and T. P. Puryaeva, in *Proceedings of I National Conference on Use of X-Rays, Synchrotron Radiation, and Neutrons and Electrons for Studying Materials, RSNÉ'97* (Dubna, 1997), Vol. 2, p. 149.
9. É. A. Smorgonskaya, R. N. Kyutt, V. B. Shuman, *et al.*, Fiz. Tverd. Tela (St. Petersburg) **44**, 1908 (2002) [Phys. Solid State **44**, 2001 (2002)].
10. D. N. Svergun and L. A. Feĭgin, *X-Ray and Neutron Small-Angle Scattering* (Nauka, Moscow, 1986).

Translated by V. Bukhanov

Semiconductors, Vol. 37, No. 7, 2003, pp. 775–783. Translated from Fizika i Tekhnika Poluprovodnikov, Vol. 37, No. 7, 2003, pp. 802–810.

CONFERENCE. AMORPHOUS, VITREOUS, AND POROUS SEMICONDUCTORS

Fullerene Single Crystals as Adsorbents of Organic Compounds

V. I. Berezkin*, I. V. Viktorovskiĭ*, A. Ya. Vul', L. V. Golubev**, V. N. Petrova*, and L. O. Khoroshko***

**Research Center for Environmental Safety, Russian Academy of Sciences, St. Petersburg, 197110 Russia*
e-mail: v.berezkin@inbox.ru
***Ioffe Physicotechnical Institute, Russian Academy of Sciences, Politekhnicheskaya ul. 26, St. Petersburg, 194021 Russia*
Submitted December 23, 2002; accepted for publication December 27, 2002

Abstract—The results of investigations of the adsorption properties of fullerenes are presented. Fullerenes acting as adsorbents are compared with soot and activated carbon. From its adsorption properties, soot is similar to activated carbon. Fullerenes do not manifest themselves in the composition of soot material. As an independent adsorbent, fullerenes are considerably more effective than activated carbon. Possible mechanisms of fullerene adsorption are discussed. It is concluded that the adsorptivity of fullerenes is realized mainly through dispersion interactions. Certain theoretical estimates are presented. *© 2003 MAIK "Nauka/Interperiodica".*

1. INTRODUCTION

Carbon adsorbents in the form of active (activated) carbons (grained or powderlike) are widely used in various branches of industry: the food industry, water purification and conditioning, gas purification, medicine and pharmaceutics, production of catalysts, and so on. Active carbons are obtained from wood, peat, nutshell, fossil coal, carbon-resin slurry, soot-pitch stock, organic resin, etc. Annual global production constitutes several hundred thousand tons.

Another disperse solid carbon which is also used in industry is soot. As an adsorbent, it has been considerably less investigated and is not usually used for this purpose in the disperse form. It is used primarily for the reinforcement of caoutchouc in rubber production, for the fabrication of printer ink, plastics, carbon electrodes, expendable materials for office equipment, etc. Global production amounts to several million tons per annum.

Finally, fullerenes, which are obtained from soot by extraction and the production of which is limited to research laboratories, have, as of yet, no industrial applications, in spite of the universal recognition that this form of solid carbon is promising. Although the physics and chemistry of fullerenes have been investigated rather intensively in recent decades, their adsorption properties have remained poorly understood.

In this study, we investigate the adsorption activity of fullerenes and compare it with the activity of activated carbon and soot.

2. EXPERIMENTAL

2.1. Initial Materials

Samples of natural river water and wastes from a pharmaceutical plant were used. Reference solutions of certain organic substances with a concentration no higher than the limits of their solubility in water were also investigated.The reference solutions were specially prepared in distilled water. The following substances were chosen as adsorbents:

(i) milled industrial grained active carbon BAU-A based on birch wood;

(ii) fullerene-containing soot;

(iii) the same soot after fullerene extraction;

(iv) total fullerene extract, which evolved from this soot.

Carbon of the grade mentioned is intended for the adsorption of organic substances from water solutions. It is considered to be one of the most effective adsorbents for these purposes. Soot was obtained in an electric arc chamber according to conventional technology for fullerene production; approximately 5% of the fullerenes were extracted from it. Fullerenes were preliminarily milled into a finely disperse powder.

2.2. Preparation of the Samples

Charges of activated carbon (0.5 g), fullerene-containing soot (0.5 g), soot containing no fullerenes (0.475 g), and fullerenes (0.025 g) were added to 500 ml aliquots of water. The mixtures, which were periodically stirred, were kept in dark, closed glass vessels at room temperature for two weeks. After that, water was filtered and extracted in a diluted funnel. Methylene chloride and diethyl ether were used as extractants–solvents.

2.3. Analysis of the Samples

The samples were investigated using a QP-5000 Shimazu (Japan) chromatographic mass spectrometer

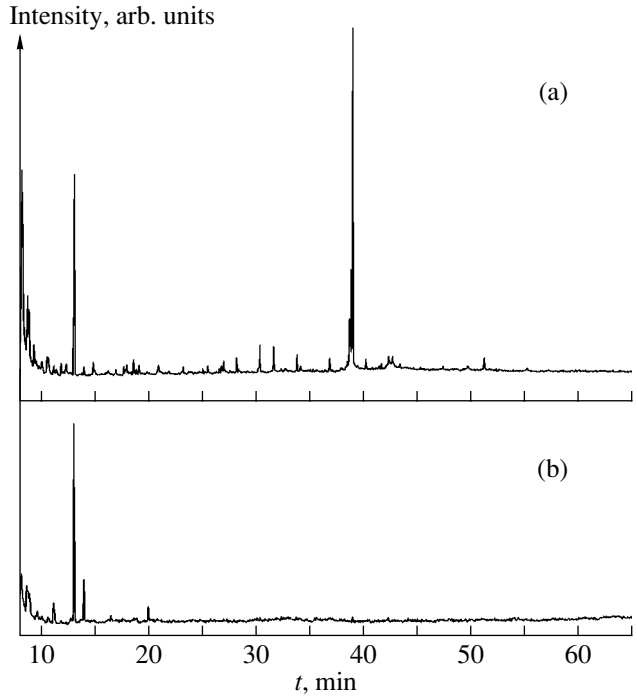

Fig. 1. Complete chromatograms of the samples of natural river water: (a) the initial sample; (b) the same sample after treatment with fullerene-containing soot.

in the mass range from 33 to 450 au and with a retention time of 8–65 min. A 60m-long capillary column with an inner diameter of 0.25 mm was used. The temperature of the column was increased to 290°C according to a specified program. The carrier gas was He. The volume of the sample introduced was 1 μl. The concentration of sample components was estimated by the internal-standard method of an internal standard, which was used as a known reference point. Decane was typically used for this purpose.

The specific surface of the fullerene samples was measured using a Micro Sizer 201 VA Instruments (Russia) laser analyzer; the measurement range was 0.2–600 μm.

3. RESULTS

Chromatograms of natural water ((a) initial and (b) treated with fullerene soot) are shown in Fig. 1. The results are summarized in Table 1. It can be clearly seen that the soot adsorbent effectively purifies the relatively pure water of practically all impurities contained in this water sample and which belong to various classes of organic compounds. The peaks with retention times of 8.2 (toluene), 8.7 (chloroalcane), 8.8 (butyl acetate), 10.5 (dichloropropyl acetate), 11.2 (tetrachloropropane), and 14.0 and 20.0 min (chloroalkenes) belong to impurities of the extractant, in this case, methylene chloride. The peak with a retention time of 13.0 min is attributed to introduced decane.

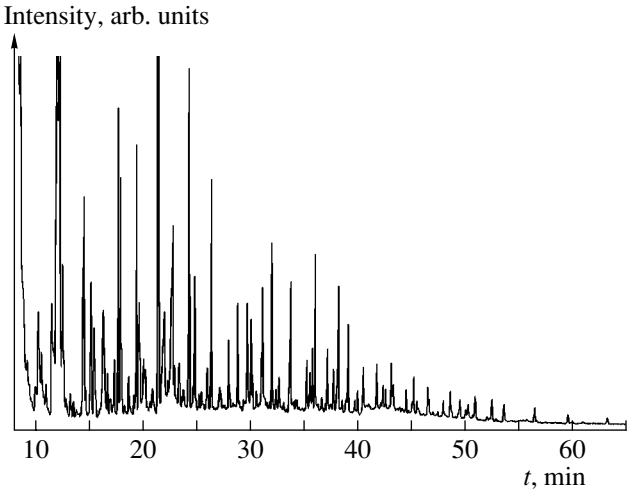

Fig. 2. Complete chromatogram of the initial sample of industrial sewage of the pharmaceutical plant.

Industrial sewage was used to obtain a quantitative estimate of the efficiency of water purification by various components of soot and for comparing their action with the standard adsorbent. A general initial chromatogram of the water used is shown in Fig. 2. About 150 peaks, which belong to various aliphatic, cyclic, and aromatic compounds, are observed. Among them, alkanes, acids, ethers, phosphates, ketones, nitrogen-containing compounds, and many other compounds were identified. The overwhelming majority of organic impurities were chlorine-containing compounds. Since it was inexpedient to investigate the chromatogram as a whole, we restricted ourselves to the portion with retention times of 22–40 min, where the general impurity concentration was 222.5 μg/l. From this amount, the concentration of chlorine-containing compounds was 215.5 μg/l. These substances were chosen for further analysis.

A corresponding portion of the chromatogram of the initial water is shown in Fig. 3a. The activity of adsorbents is illustrated in Fig. 3b by the example of fullerenes. The quantitative data on water purification are listed in Table 2.

From the experiments carried out, it was found that all substances used are efficient adsorbents and their action is approximately identical qualitatively. Fullerenes, as well as soot and active carbon, adsorbed virtually no alkanes, ethers, acids, ethers, and certain other impurities in industrial sewage. In quantitative terms, judging by the separate impurity components and by the total impurity concentration in treated water, in our experiments carbon was a somewhat more efficient adsorbent than soot. Two circumstances should be noted:

(i) The activity of components which comprise the soot material (soot itself and fullerenes) is obviously nonadditive.

Table 1. Results of chromatographic analysis of the samples of natural river water corresponding to the data of Fig. 1. Identified organic compounds, their retention times, and concentrations are given

No.	Compound	Retention time	Impurity concentration	
			prior to purifying	after purifying
		min	μg/l	
1	Alkanes	16–30	0.4	–
2	Alkadienes			
	Diethyl-dimethyl-3.5-octadiene	26.3	0.8	–
3	Fatty acids			
	Caproic	12.3	1.0	–
	Enanthic	15.0	1.0	–
	Caprylic	18.0	0.5	–
	Palmitic	38.6	14.2	–
	Stearic	42.6	0.7	–
	Others	23.7	0.4	–
4	Alkenols			
	Alkyl heptenol	17.7	0.6	–
5	Ethers of fatty acids			
	Methyl ethyl propyl propanoate	30.3	2.0	–
	Diethyl ether of adipinic acid	31.6	2.0	–
6	Ethers of phthalic acid			
	Diethyl	30.3	0.4	–
	Diisobutyl	36.7	1.0	–
	Dibutyl	38.9	43.5	–
	Dioctyl	51.2	1.1	–
7	Substituted 1.3-dioxanes			
		19.1	0.7	–
		26.7	0.5	–
		28.2	1.3	–
8	Chlorine-containing compounds			
	Chloroalkane*	8.7	8.1	4.0
	Dichloropropyl acetate*	10.5	2.3	1.5
	Tetrachloropropane*	11.2	1.0	1.0
	Chloroalkene*	14.0	0.6	4.0
	Chloroalkene*	20.0	–	1.2
9	Other compounds			
	Toluene*	8.2	37.2	21.3
	Butyl acetate*	8.8	6.5	–
	Epijuvabione*	40.1	1.0	–
	Total concentration of organic impurities:		125.0	33.0

* Impurities of solvent (methylen chloride).

(ii) As a self-dependent adsorbent, in these samples of industrial sewage fullerenes are an order of magnitude more efficient than active carbon in terms of their mass content in corresponding experiments.

To verify the latter assertion, reference solutions of benzene were prepared, in to which identical charges of fullerenes and carbon were introduced. The residual amounts of benzene in the treated solutions were either

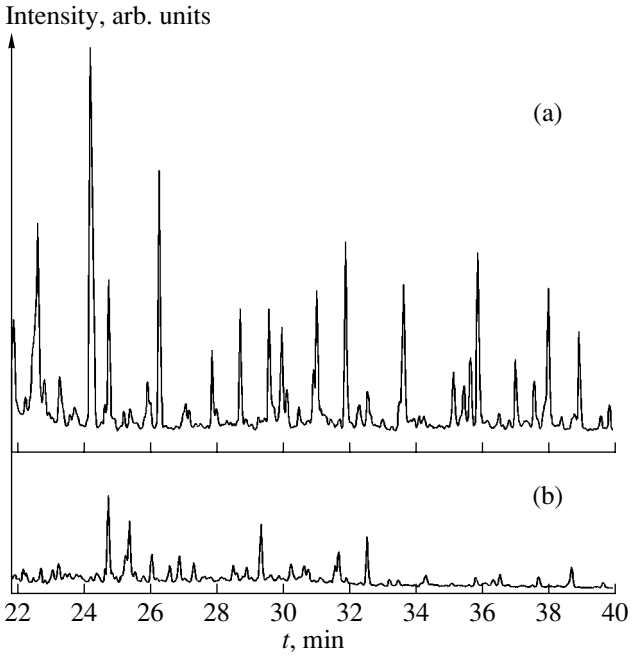

Fig. 3. Portions of chromatograms of the samples of pharmaceutical industrial sewage corresponding to retention times from 22 to 40 min: (a) the chromatogram of the initial sample of industrial sewage; (b) a typical chromatogram of the same sample after treatment with fullerenes.

approximately identical in both cases or the benzene content in the fullerene-treated solutions was lower by a factor of 1.5–2.

Attention should be also drawn to the following circumstances. Poorly water-soluble organic impurities, despite being solvated, could, in principle, gradually rise to the surface if they are lighter than water, and sink in the opposite case. The particles of activated carbon in solution gradually sink to the bottom, remaining partially at the surface or in a suspended state in the sample bulk. In contrast, particles of fullerene microcrystals, the overwhelming majority of which (~99%) were 0.5–150 μm in size, largely remained at the surface, partially sank to the bottom, or were in a form of suspension. These factors could distort the results of measurements. To clarify this situation, control solutions of 1.4-dioxane were investigated. For this substance, the adsorbent position is not important, since it can be mixed with water in any proportion. In this case, an increased (and equal) content of fullerenes and carbon was used, since dioxane is only slightly adsorbed by them. The residual content of this substance in the solution after treatment with activated carbon was approximately a factor of 2 lower than after treatment with the fullerene extract.

4. DISCUSSION

In the initial material, fullerenes are bound by soot particles and aggregates which are not dissociated in water. Therefore, fullerenes do not manifest themselves as an individual component and no additive activity of the soot components is observed. Components are separated in organic solvents, and it is well known that 5–10% of fullerenes are usually extracted from soot obtained in an electric arc chamber. However, it is believed that there are far more fullerenes in such soot, since the soluble fraction can be as large as 37% [1]. Thus, the greater portion of fullerenes remain in a bound state and are completely inseparable from soot even in organic solvents.

The adsorption properties of fullerenes released from the soot matrix correlate with the specific features of their solubility. Specifically, fullerenes are virtually insoluble in polar solvents, weakly soluble in alkanes, and relatively well-soluble in aromatic hydrocarbons and their derivatives [2]. The fact that, in our experiments, fullerenes manifest themselves as adsorbents in a specific manner is not surprising since, in both cases, the same intermolecular interaction forces are in effect. The main difference consists in the fact that, in our experiments, the solvents were strongly diluted with a third medium (water) and were treated as impurities.

For the direct qualitative verification of the consistency of fullerene adsorption efficiency with their solubility in various organic substances, different reference solutions of toluene, benzene, nitrobenzene (aromatic hydrocarbons and their derivatives), hexane (alkane), and dioxane (polar solvent) were used. The solubility of C_{60} in these substances, according to the data of various authors, is equal to 2.15–2.90, 0.88–1.70, 0.80, 0.040–0.052, and 0.041 mg/ml [3]. Therefore, in this experiment, almost all toluene (99%), 27–87% of benzene, and 10% of nitrobenzene were adsorbed. Hexane was adsorbed weakly, and dioxane was virtually un adsorbable.

The efficiency of adsorbents is determined by the efficiency of adsorption mechanisms and the specific surface. One of the main adsorption mechanism, which is realized in physical adsorbents, is the formation of van der Waals bonds between the particles (atoms, molecules, or their aggregates) of the adsorbent and the adsorptive(i.e., the substance adsorbed) at the *solid–liquid or gas* interface. Depending on the intensity of the force field at the adsorbent surface, adsorption layers, one or several molecules thick, may form under various external conditions (monomolecular and polymolecular adsorption). Therefore, the real specific surface of physical adsorbents may be considerably less than the effective specific surface, which is measured experimentally from the adsorption of reference substances.

Due to their high porosity, active carbons possess a developed internal surface with a pore size from tenths of a nanometer or larger. They are efficient physical adsorbents of hydrocarbons and many of their derivatives. It is well known that activated carbons extremely weakly adsorb polar molecules, e.g., lower alcohols, ammonium, and especially water [4].

Table 2. Summary results of the chromatographic analysis of industrial sewage samples of the pharmaceutical plant, which correspond to chlorine-containing organic compounds with retention times of 22–40 min. The retention times and impurity concentrations for the initial sample and the samples after treatment with fullerene-containing soot, soot without fullerenes, fullerenes, and activated carbon are given

No.	Retention time	Impurity concentration				
		water prior to purifying	water after purifying			
			fullerene-containing soot	soot without fullerenes	fullerenes	activated carbon
	min	μg/l				
1	22.7	31.0	6.0	3.5	1.0	2.0
2	22.8	5.0	–	–	0.6	–
3	24.2	30.0	5.5	8.0	2.0	3.0
4	24.8	10.0	1.5	2.0	5.0	0.6
5	25.9	3.5	1.5	2.0	–	–
6	26.3	16.5	5.0	1.5	2.0	1.0
7	27.9	5.0	1.5	1.0	1.0	0.4
8	28.8	8.0	2.5	4.0	4.0	1.5
9	29.7	8.0	1.0	1.0	1.5	–
10	30.0	9.0	1.5	1.0	1.0	3.0
11	30.2	2.5	0.5	0.7	0.7	–
12	30.9	3.5	1.0	1.5	1.0	0.4
13	31.0	9.0	1.0	1.5	2.5	0.5
14	31.9	12.5	3.0	4.0	3.5	1.5
15	33.7	10.5	0.5	0.5	1.5	–
16	35.2	4.5	0.7	1.0	0.7	–
17	35.5	3.0	2.0	0.5	–	–
18	35.7	5.0	1.5	0.2	0.5	–
19	35.9	12.0	4.5	1.5	1.0	0.6
20	37.0	5.0	–	–	0.8	–
21	37.6	3.5	0.5	–	–	–
22	38.0	12.0	1.0	0.7	1.5	0.5
23	39.0	6.5	0.6	–	0.7	–
Total impurity concentration		215.5	42.0	35.5	32.5	15.0

As can be seen from the data presented above, disperse carbon in a the form of soot also exhibits high adsorption activity relative to various organic compounds. The main structural units of soot and carbon are graphite-like nanocrystallites in the form of imperfect and distorted stacks of hexagonal carbon networks [5–7]. The length of the crystallites is 2–3 nm or more with a thickness of 1.0–1.7 nm; the layers are 0.34–0.37 nm apart. Amorphous carbon and heteroatoms are also present. The main distinction between soot and carbon is in the character of crystallite packing. In carbons, crystallites form turbostrate layers, and, in soot, mainly spherical particles with a diameter of approximately 5–10 nm or more are formed from them. In their turn, soot particles can form aggregates of various shapes (chains, spirals, bunches, etc). In this context, it is apparently possible to assume that the mechanisms of adsorption for soot and carbons, in general, have the same nature.

It is well known that soot has a large specific surface (tens and hundreds of m^2/g [8]), which is comparable with the specific surface of active carbons (a general range of $0.1–10^3$ m^2/g; the most characteristic range is also tens and hundreds of m^2/g [5]). Therefore, with the proviso that the specific surfaces are approximately equal, the efficiency of soot as an adsorbent should not differ strongly from the efficiency of activated carbons, which was observed in our experiments. The specific surface of the carbon used by us is rather large, although it may vary in a rather wide range, for example, from 258 m^2/g [9] to 915 m^2/g [10].

The activity of fullerenes can be related to both the larger effective specific surface and the more productive sorption. Taking into account that the diameter of a C_{60} molecule is equal to 0.71 nm [11], the overall real specific surface of these fullerenes is estimated as 1.34×10^3 m^2/g. However, the fullerenes in our experiments were microcrystals rather than separate molecules. Therefore, their real specific surface was substantially smaller. For various samples it varied in the range of 0.45–1.43 m^2/g. Let us assume that in our experiments the amount of organic substances adsorbed by fullerenes per mass unit and the same amount for active carbon are of the same order of magnitude. In this case, the mechanisms of adsorption by fullerenes should be recognized as much more productive.

As for the mechanisms of sorption by fullerenes, three possibilities can generally exist. The first possibility is absorption, which may be thought of as intercalation, i.e., the filling of the intermolecular spaces in the crystal lattice of fullerites. The second possibility is the breaking of the carbon–carbon bonds in the fullerene molecule, which is accompanied by chemisorption. The third possibility is physical adsorption.

The intercalation for both graphite [12] and fullerites [13] calls for temperatures of several hundred °C. As for the introduction of foreign atoms or molecules into the fullerene cell, endohedrals, as it is known, may form simultaneously with the formation of fullerenes, and this process calls for temperatures of ~1000°C.

The energy of C–C or C=C bonds is quite high, and it is equal to 344 and 615 kJ/mole, respectively [14]. Therefore, chemisorption by fullerenes requires large energy consumption. At the same time, the interaction with substances with an increased chemical activity may proceed relatively easily. However, elevated temperatures are also required in this case. For example, in the presence of O_2, fullerenes begin to be oxidized at 250°C and, with further rise in temperature, they decompose completely into CO and CO_2 [15]. As chemical adsorbents, carbon and soot behave identically, and in both cases, CO and CO_2 rather than O_2 leave the surface [4, 7].

Since adsorption was carried out at room temperature in our experiments, physical adsorption most likely occurred. In this case, fullerene molecules should be treated as chemically inert particles which conserve their individuality in interactions with other molecules.

The attractive forces of physical adsorption as is well known, are divided into electrostatic and dispersion forces. The former are effective if the molecules are electric dipoles (polar molecules), quadrupoles, or, in general, multipoles; these multipoles are caused by the nonuniform distribution of electron density in generally electroneutral molecules. The dipole interactions may be both intrinsic and induced. The latter ones emerge when the dipole moment is induced in a nonpolar molecule during its interaction with a molecule with a constant dipole moment. Therefore, dipole interactions are divided into orientation- and polarization-related ones.

The extremely low solubility of fullerenes in polar solvents poins to the insignificant role of dipole–dipole interactions, which might be expected since molecules are symmetric and have no dipole moment. The dipole-induced interaction also should not play a noticeable role, which is confirmed, for example, by the following circumstances. With increasing molecular dipole moments in the sequence of: fluorobenzene (its dipole moment is equal to 1.57D, where $D = 3.34 \times 10^{-30}$ C m), chlorobenzene (1.69D), bromobenzene (1.70D), and nitrobenzene (4.22D [16]), the solubility of C_{60} in these substances varies as 0.59, 7.00, 3.30, and 0.80 mg/ml, respectively [2], with no correlation with the dipole moment of the solvent.

Certain aromatic molecules (benzene, naphthalene, and anthracene) possess a considerable quadrupole moment [17]. Fullerene molecules may be considered as three-dimensional analogues of aromatic molecules, whose hexagonal fragments are similar to the benzene molecule, so that the fullerene fragments may possess quadrupole electric moments. Therefore, in theoretical calculations of intermolecular interactions, the corresponding expressions are modified taking into account quadrupole moments of surface fragments of the fullerene molecule. These moments are caused also by the inequality of bonds between carbon atoms and the local anisotropy in charge distribution [18]. The total quadrupole moment of molecules is equal to zero [19]. At temperatures above the temperature of orientation phase transition, 249–260 K for C_{60} or 280 K for C_{70} [20], the molecules rotate in the lattice. Therefore, fixed quadrupole interactions are absent under these conditions.

An assumption exists stating that the rather high solubility of fullerenes in solvents, which contain six-membered carbon rings, may be caused by the magnetic interaction of closed ring electron currents in corresponding fragments of the fullerene structure and aromatic solvent [3].

The molecules of chemically saturated substances, as a rule, have no magnetic moments. For an overwhelming majority of organic molecules with covalent bonds, in which unpaired electrons are absent, the magnetic moment is absent completely. Aromatic molecules are unusual substances. Although their molecular formula corresponds to a high degree of unsaturation, they do not enter into an addition reaction, which is characteristic of unsaturated compounds. Instead of an addition reaction, these substances, as a rule, enter into an electrophilic substitution reaction [21]. In the aromatic system, the π electrons are not located at a single atom; rather, they occupy molecular orbitals which envelop the molecule as a whole; i.e., they are delocalized. Therefore, aromatic compounds, including fullerenes, are diamagnetic substances. In this case, allowance should not be made for second order effects,

which are associated with the moments of atomic nuclei. Therefore, no basis exists for the realization of the magnetodipole interaction mechanism.

Thus, at sufficiently high temperatures, the adsorption mechanism with the predominance of dispersion interaction forces should be preferable for fullerenes. The dispersion forces are universal; they are not associated with the existence of steady-state electric or magnetic moments. They act between the atoms and molecules of any nature irrespective of their structure and emerge due to the synchronization of instant dipoles inherent to the interacting particles.

In investigations of physical interactions between a pair of spherically symmetric atoms or molecules which are spaced at a distance r the Lennard-Jones potential is used quite often. This potential has the form

$$u(r) = 4\varepsilon\left[\left(\frac{\sigma}{r}\right)^{12} - \left(\frac{\sigma}{r}\right)^{6}\right], \quad (1)$$

where the second term corresponds to the attractive forces of the particles, the first term corresponds to the repulsive forces of the particles, and ε and σ are the constants of this substance. The Lennard-Jones potential for carbon atoms can be quite successfully applied to the investigation of physical interactions of fullerene molecules by the methods of molecular dynamics for the calculation of various characteristics of fullerites [17, 22, 23]. Let us calculate the energy of adsorption interaction U of a C_{60} molecule with a single aromatic ring C_6, which is equivalent to the benzene molecule in the absence of chemical interactions. For this purpose, it is necessary to calculate the sum of van der Waals potentials of interaction for all carbon atoms of one molecule with all carbon atoms of a second molecule. At a sufficiently high temperature, fullerene molecules rotate almost freely. Therefore, they may be approximated as a sphere that has a uniformly distributed density of carbon atoms, and integration may be substituted for summation [23]. Let the C_{60} molecule be located at the origin of coordinates, while the hexagon is located at a distance a from the center of the fullerene molecule in a plane normal to the radius, which connects the centers of molecules. The expression for $U(a)$ can be written in the following form:

$$U(a) = d_1 d_2 \int_{1,2} u(r)\, d\Sigma_1 d\Sigma_2. \quad (2)$$

Here, r is the distance between the center of the C_6H_6 molecule and an arbitrary point on the surface of the C_{60} molecule, and $d_1 = 60/4\pi R^2$ and $d_2 = 6/1.5\sqrt{3}\,\rho^2$ are the corresponding surface densities of carbon atoms. Integration is carried out over the surface of the C_{60} molecule (Σ_1 is the sphere with a radius R) and over the plane of the C_6H_6 molecule (Σ_2 is the hexagon with a side length ρ). As a result, for expression (2), where $u(r) = r^{-n}$, we derive

$$d_1 d_2 \int_{1,2} r^{-n} d\Sigma_1 d\Sigma_2 = -\frac{3\sqrt{3}\pi R\rho^2}{2a^2} \times \left[\frac{r_0(r_0+2R)^{2-n} - r_0^{2-n}(r_0+2R)}{n-1} + \frac{(r_0+2R)^{3-n} - r_0^{3-n}}{n-3}\right], \quad (3)$$

where $r_0 = a - R$ is the distance between the carbon atoms of interacting molecules. Applying this to potential (1), using for carbon atoms the constants $\varepsilon = 28.0$ K and $\sigma = 0.34$ nm, which were obtained from graphite compressibility [24], and assuming $r_0 = 0.335$ nm, we derive $U = -1245.5$ K $= -0.107$ eV. If we use the recommendation of Cheng and Klein [22] and increase ε by 15% to achieve better agreement between the results of calculations and experimental data, then $U = -1432.3$ K $= -0.123$ eV.

Fullerites, by virtue of their molecular structure and bond organization in the crystal lattice, are the only soluble form of solid carbon. Since fullerenes in solutions are able to form aggregates (clusters) which consist of several molecules, the energies of interaction of fullerene molecules with each other and with solvent molecules (as well as with adsorptive molecules) should not differ strongly.

Cheng and Klein [22] estimated the bonding energy for two C_{60} molecules as 2200–2900 K (0.19–0.25 eV). The heat of dissolution of fullerenes, which was calculated for benzene, toluene, and CS_2, is equal to approximately 10 kJ/mol (0.104 eV) [3]. In our opinion this value can also serve as an indicator of the bonding energy of fullerenes with the soot matrix. The cohesion energy of C_{60} in the crystal lattice, which was calculated per molecule with allowance made for the 12 nearest neighboring C_{60} molecules, is equal to 1.6 eV [25]. The experimentally measured energy of sublimation of C_{60} at 400°C is equal to 40 kcal/mol (1.74 eV) [15]. Therefore, we can assume that the estimate from formula (3) is in good agreement with the known data for fullerenes.

On the other hand, for active carbons, the characteristic energy of adsorption relative to the standard vapor (benzene) has virtually the same values 10–15 kJ/mol [26] (0.104–0.156 eV). However, here allowance should be made for the fact that in any porous adsorben, adsorption proceeds mainly in pores no larger than 2 nm in size. In this case, the pores may be considered as three-dimensional, since practically all of the atoms which constitute the pore interact with the adsorptive molecule as the pore and the molecule adsorbed are comparable in size [27]. In other words, the adsorption potential of active carbon may be lower than the poten-

tial of fullerene if the interaction area is taken into consideration.

If we nevertheless assume the energies of adsorption for active carbons and fullerenes to be of the same order of magnitude, other factors should be taken into account for explaining the more productive activity of fullerenes.

The molecules of organic compounds, especially high-molecular, as a rule, are far from spherically symmetric in shape, which leads to the anisotropy of physical properties. For example, for an aromatic molecule, the diamagnetic susceptibility in the ring plane is less than in the normal direction by several times. In the limiting case of graphite, which is a giant two-dimensional molecule, this difference becomes as large as almost two orders of magnitude [28]. The anisotropy may lead to the dependence of the adsorption potential and the potential well depth on the mutual orientation of the adsorbent and adsorptive molecules.

Fullerene molecules, unlike molecules with an elongated or plane shape, interact with their surroundings independently of their orientation. Such "molecules" in the form of carbon networks exist in soot and activated carbon. They are the outer layers of crystallites interacting directly with the molecules of adsorptives or solvents. In other words, the adsorbent and adsorptive molecules interact most efficiently only for a certain mutual orientation. In contrast, in the case of a spherical molecule of fullerene, the adsorptive molecule will find any orientation of the fullerene molecule surface relative to itself (including the required one) by approaching the molecule of this adsorbent closely enough. At room temperature, the energy of interaction of fullerene molecules both with each other in the crystal and with molecules of adsorptives should not be sensitive to the mutual orientation of fullerene molecules.

One more circumstance should be noted. In fullerene carbon rings, defects are absent, whereas the rings of carbon and soot have a large number of defects. This may affect the efficiency of emergence of instantaneous electric moments and the magnitude of the adsorption force field at the interface.

5. CONCLUSION

By its adsorbing properties, soot is on the same level as activated carbon. This result is not surprising, since both of these substances apparently have the same adsorption mechanism and a comparable specific surface.

Fullerenes do not manifest themselves in soot material as an adsorbent since they are linked to the soot matrix. In the form of a separate fraction, they are physical adsorbents under normal conditions. Let us correlate the amount of substance adsorbed for all of our experiments and the effective surfaces of adsorbents used. From this correlation, it is possible to conclude that the adsorption mechanism of organic substances by fullerenes is far more productive than by active carbon or soot.

All of the adsorbents investigated are formed of identical structural units, specifically, carbon rings, although these rings are packed differently. Therefore, three circumstances may cause the higher adsorption efficiency of fullerenes. First, the adsorption potential of active carbons per interaction area may be lower than that of fullerenes. Second, the problem of orientation of absorptive molecules relative to fullerene molecules is nonexistent. Third, structural defects are absent in the fullerene structure. All of these factors probably also affect the level of polymolecularity of adsorption.

The adsorption properties of fullerenes correlate with specific features of their solubility due to the action of the same intermolecular forces upon the interaction with the same molecules of adsorptives or solvents. The similarity of the adsorption properties of fullerenes with analogous properties of active carbon and soot, as well as the commonness of structural elements, allows us to assume that the adsorption mechanisms of the carbon investigated sorbents possess common features. Under normal conditions, dispersion interactions are realized between the fullerene molecules and adsorbed substances.

REFERENCES

1. C. Smart, B. Eldridge, W. Reuter, *et al.*, Chem. Phys. Lett. **188**, 171 (1992).
2. R. S. Ruoff, D. S. Tse, R. Malhorta, and D. C. Lorents, J. Phys. Chem. **97**, 3379 (1993).
3. V. N. Bezmel'nitsyn, A. V. Eletskiĭ, and M. V. Okun', Usp. Fiz. Nauk **168**, 1195 (1998) [Phys. Usp. **41**, 1091 (1998)].
4. *Concise Chemical Encyclopedia*, Ed. by I. L. Knunyants (Sovetskaya Entsiklopediya, Moscow, 1961), Vol. 1.
5. V. B. Fenelonov, *Porous Carbon* (Inst. Kataliza Sib. Otd. Ross. Akad. Nauk, Novosibirsk, 1995).
6. V. I. Berezkin, Phys. Status Solidi B **226**, 271 (2001).
7. H. von Kienle and E. Bader, *Aktivkohle und Ihre Industrielle Anwendung* (Enke, Stuttgart, 1980; Khimiya, Moscow, 1984).
8. *Production and Properties of Carbon Blacks*, Ed. by V. F. Surovikin (Zap.-Sib. Knizh. Izd., Omsk, 1972).
9. F. E. Keneman, O. P. Potapov, P. V. Ryabinin, and É. A. Sokolov, in *Carbon Adsorbents and Their Application in Industry*, Ed. by T. G. Plachenov (Nauka, Moscow, 1983), p. 84.
10. A. D. Smirnov, *Sorption Purification of Water* (Khimiya, Leningrad, 1982).
11. Q.-M. Zhang, J.-Y. Yi, and J. Bernholc, Phys. Rev. Lett. **66**, 2633 (1991).
12. M. S. Dresselhaus and G. Dresselhaus, Adv. Phys. **30**, 139 (1981).
13. O. Gunnarson, Rev. Mod. Phys. **69**, 575 (1997).
14. L. Pauling, *General Chemistry* (Freeman, San Francisco, 1958; Mir, Moscow, 1964).

15. H. S. Chen, A. R. Kortan, R. C. Haddon, and D. A. Fleming, J. Phys. Chem. **96**, 1016 (1992).
16. V. A. Rabinovich and Z. Ya. Khavin, *Concise Chemical Handbook* (Khimiya, Leningrad, 1977).
17. A. Cheng and M. L. Klein, Phys. Rev. B **45**, 1889 (1992).
18. W. I. F. David, R. M. Iberson, J. C. Matthewman, *et al.*, Nature **353**, 147 (1991).
19. E. Burgos, E. Halac, and H. Bonadeo, Phys. Rev. B **49**, 15544 (1994).
20. A. V. Eletskiĭ and B. M. Smirnov, Usp. Fiz. Nauk **165**, 977 (1995) [Phys. Usp. **38**, 935 (1995)].
21. R. T. Morrison and R. M. Boyd, *Organic Chemistry* (Allyn and Bacon, Boston, 1970; Mir, Moscow, 1974).
22. A. Cheng and M. L. Klein, J. Phys. Chem. **95**, 6750 (1991).
23. L. A. Girifalco, J. Phys. Chem. **96**, 858 (1992).
24. W. A. Steele, *The Interaction of Gases with Solid Surfaces* (Pergamon, New York, 1974).
25. S. Saito and A. Oshiyama, Phys. Rev. Lett. **66**, 2637 (1991).
26. *Activated Carbon: A Catalog*, Ed. by S. L. Glushakov, V. V. Konopleva, and N. G. Lyubchenko (Pravda, Cherkassy, 1990).
27. A. Dąbrowski, Adv. Colloid Interface Sci. **93**, 135 (2001).
28. P. J. Wheatley, *The Determination of Molecular Structure*, 2nd ed. (Clarendon Press, Oxford, 1968; Mir, Moscow, 1970).

Translated by N. Korovin

Semiconductors, Vol. 37, No. 7, 2003, pp. 784–788. Translated from Fizika i Tekhnika Poluprovodnikov, Vol. 37, No. 7, 2003, pp. 811–815.

CONFERENCE. AMORPHOUS, VITREOUS, AND POROUS SEMICONDUCTORS

X-Raying Studies of the Nanoporous Carbon Structure Produced from Carbide Materials

R. N. Kyutt*, A. M. Danishevskiĭ*, É. A. Smorgonskaya*, and S. K. Gordeev**

**Ioffe Physicotechnical Institute, Russian Academy of Sciences, Politekhnicheskaya ul. 26, St. Petersburg, 194021 Russia*

***Central Research Institute for Materials, St. Petersburg, 121014 Russia*

Submitted December 23, 2002; accepted for publication December 27, 2002

Abstract—X-raying is used to study the structure of nanoporous carbon particles produced from carbides of various materials (SiC, TiC, Mo_2C, and B_4C) by chemical removal of carbide-forming elements. The X-ray diffraction patterns exhibit reflections in the double reflection angle ranges $2\theta = 23°–26°$ and 42°–44°. An analysis of the angular position, half-widths, and intensities of these peaks shows that the former peak is a reflection from basal planes of distorted graphite-like crystalline fragments, and the latter reflection can be caused by two-dimensional diffraction $(10\bar{1})$ from graphene plane fragments in the sample bulk. The amount of graphite-like crystallites depends on the sample preparation method. Their size varies within 40–100 Å, and the volume fraction is from 5 to 12% for various samples. © *2003 MAIK "Nauka/Interperiodica".*

1. INTRODUCTION

Recently, many new nanocarbon modifications characterized by unique properties have been discovered. Their structure depends, first and foremost, on the initial object and the preparation method. One method for producing nanocarbon material from carbide compounds is based on the chemical removal of carbide-forming noncarbon atoms [1, 2]. As a result, a nanopore system with a high (about 65% or above) total porosity is formed. Structural studies of this type of bulk material carried out using small-angle X-ray scattering have shown rather high uniformity of nanopores (0.8–2.5 nm in size depending on the initial carbide) and nanoparticles (1–3 nm) representing quasi-amorphous structures with partial absence of long-range order [3, 4]. However, the results of these studies have also shown larger particles (5–6 nm and larger) in the samples studied. The structure of these particles can be revealed by measuring and analyzing X-ray diffraction reflections. This paper is devoted to this problem.

2. MEASURING TECHNIQUE

An X-ray diffraction pattern from polycrystalline samples, measured by 2θ- or $(\theta–2\theta)$-scanning, includes all of the allowed *hkl* reflections of the phases existing in the material under study. The angular position of the peaks is controlled by the corresponding interplane spacing. The peak half-width in the X-ray diffraction pattern depends on polycrystal grain sizes. Taking into account probable size anisotropy in various directions, the reflection half-width on the scale 2θ is given by

$$w(2\theta) = \lambda/\tau\cos\theta, \quad (1)$$

where τ is the average crystallite size in the direction of the diffraction vector and λ is the wavelength.

The integrated reflectivity for polycrystals is written as

$$J = \frac{pzt}{2\pi x\sin(2\theta)}Q, \quad (2)$$

where t is the sample thickness, p is the multiplicity factor for reflecting planes, z is the counter slit height, x is the sample–detector distance, and Q is the integral reflectivity of a unit volume,

$$Q = \frac{F^2\lambda^3}{v^2\sin(2\theta)}r_e^2 \quad (3)$$

F is the structure factor, v is the unit cell volume, and $r_e = 2.818 \times 10^{-13}$ cm is the classical electron radius). At the same time, experimental reflectivity is given by

$$R_i = A/I_0R_s, \quad (4)$$

where A is the area under the diffraction peak, I_0 is the intensity of the direct beam passed through the sample, and R_s is the resolution of the detector entrance slit. The ratio of experimentally determined R_i to calculated J is equal to the volume fraction of crystallites causing a given reflection (needless to say under the condition of grains uniformly distributed over orientations).

3. SAMPLE PREPARATION

We studied bulk samples of nanoporous carbon (NPC) produced from powdery polycrystalline SiC, TiC, Mo_2C, and B_4C carbides. Two methods were used to prepare NPC. According to one method (hereafter designated as type *B*), polycrystalline carbide α-SiC, TiC, Mo_2C, and B_4C powders with grain sizes from 2 to

40 μm were pressed into pellets. Pyrolitic carbon (pyrocarbon), playing the role of binding material, was synthesized in pellet macropores through high-temperature annealing in methane. The samples were then annealed at 900–950°C in chlorine. The chemical reaction between chlorine and carbides produced gaseous chlorides of carbide-forming metals, which were removed from the samples. Eventually, bulk carbon samples were prepared in the shape of disks ~1 mm thick with a high total porosity (up to 65–70%) and nanoporosity (up to 35%). As a rule, their pyrocarbon fraction did not exceed 10–12%. In the samples prepared from SiC powders by the second method (type *A*), β-SiC was synthesized from pyrocarbon inclusions using high-temperature siliconization. Only then was silicon removed by chlorination. The nanopore volume was no less than 45–50% of the total volume.

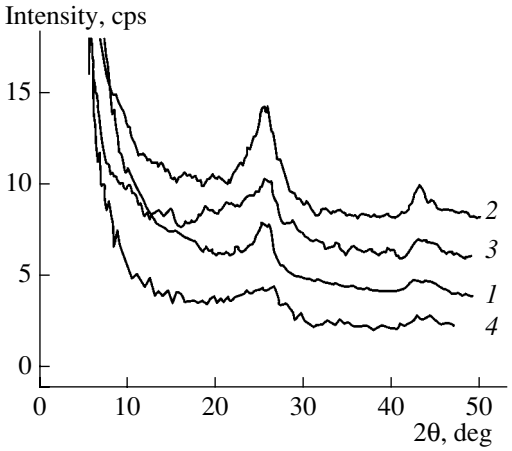

Fig. 1. X-ray diffraction patterns of nanoporous carbon prepared by method *B* from polycrystalline SiC (*1*), Mo_2C (*2*), TiC (*3*), and B_4C (*4*).

4. EXPERIMENTAL

X-raying measurements were carried out using a two-crystal diffractometer with a crystal monochromator made of a perfect Ge crystal (reflection (111)), which ensured that angular divergence of the incident beam was as small as 20″. A 0.5-mm entrance slit in the counter provides a resolution of 0.16° over the angle 2θ. Scattering in the angle range 2θ = 0°–50° was measured in the beam transmission geometry. The (θ–2θ scanning mode was used, which yielded an intensity distribution in the scattering plane in the direction of the scattering vector $\mathbf{S} = \mathbf{k}_1 - \mathbf{k}_0$ parallel to the sample surface.

5. RESULTS AND DISCUSSION

The X-ray diffraction patterns measured for the NPC samples produced from various carbides are shown in Fig. 1. They do not reveal the diffraction reflections of an initial carbide material. Broad peaks are observed in the angular range 2θ = 23°–26° and 40°–45°. The first peak is close to the reflection (0002) from the graphite basal planes. The angular region of the second peak location covers the Bragg angles of graphite reflections $(10\bar{1}0)$ and $(10\bar{1}1)$ (from planes normal and inclined to the basal plane, respectively) and the diamond reflection (111). As follows from the general view of the X-ray diffraction patterns, nanoporous samples contain fragments of the carbon structure with a short-range order close to that of graphite. The parameters of the peaks in the X-ray diffraction patterns (angular positions and half-widths) for some of the samples are listed in Tables 1 and 2.

We can see from Tables 1 and 2 that the angular positions of the peaks slightly vary from sample to sample. However, for the most part, these variations are within measurement error and are independent of the initial material. We note that silicon, titanium, molybdenum, and boron carbides fall into different structural types. However, the X-ray diffraction reflections in the samples produced from different carbide materials are similar.

For most of the samples, the reflection in the angular range of 23°–26° is distinctly shifted to smaller angles in comparison with the double Bragg angle of the graphite reflection (0002) (2θ = 26.6°). This can be caused by the distortion of graphite planes. It seems that the detected crystallites have a structure referred to as "turbostratum" and are characterized by graphite planes (0001) irregularly packed along the *c* axis and randomly rotated about it. This structure is also encountered in other carbon compositions. In this case, the interplane spacing *d* (0002) is within 3.40–3.49 Å for materials produced under various technological conditions [5–7]. This value is much larger than that of graphite, *d* = 3.35 Å. The average position of the peak (0002) in the X-ray diffraction patterns of the structures under study corresponds to $d = (3.46 \pm 0.03)$ Å, which is within the above-mentioned limits. In specific cases, the corresponding peak has a more intricate shape and it can be resolved into several peaks. Such samples

Table 1. Angular position and half-width (in degrees of arc) of the diffraction peak in the range of 23°–26°

Sample type	From SiC(*B*)	From TiC(*B*)	From Mo_2C (*B*)	From B_4C(*B*)	Graphite	Pyrocarbon (experiment)
2θ	25.8	25.8	25.7	25.5	26.6	26.44
w	2.5	3.2	3.5	4.7		0.61

Table 2. Angular position and half-width (in degrees of arc) of the diffraction peak in the range of 40°–45°

Sample type	From B_4C		From SiC(*A*)		From SiC(*B*)		From TiC	From Mo_2C	Graphite $(10\bar{1}0)$	Graphite $(10\bar{1}1)$	Diamond (111)
Index	1	2	22	25	19	32					
2θ	43.7	44.4	43.4	43.5	43.1	43.4	43.3	43.3	42.3	44.5	44.2
w	4.1	4.6	3.7	3.2	2.5	4.5	4.7	3.6			

probably contain various graphite-like fragments with various degrees of distortion in planes (0001). We also note other probable types of graphene plane distortions, e.g., a great number of vacancies, which might be reasonably expected for a high-porous material. This should also cause an increase in the corresponding interplane spacing.

The peak half-width varies from 1.3° to 3.5° and from 2.5° to 5.5° for the peaks in the regions of 26° and 40°–44°. We can see that the second reflection is distinctly broader than the first one. Expression (1) yields the average size of graphite-like crystallites: from 3.0 to 8.0 nm for peak (0002). In the case of the samples produced from TiC and Mo_2C, the crystallite sizes are, on average, smaller than those for the samples produced from SiC.

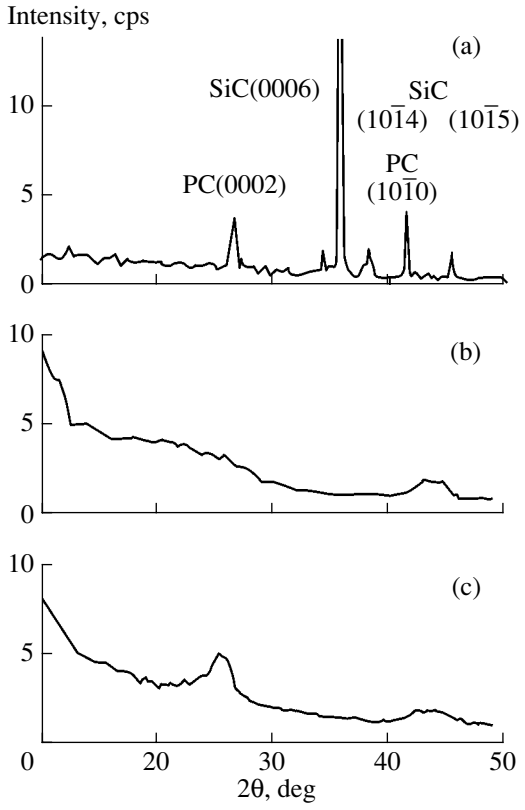

Fig. 2. X-ray diffraction patterns of nanoporous carbon prepared by methods (b) *A* and (c) *B* from polycrystalline SiC, as well as from the initial SiC sample with pyrocarbon (a).

The samples whose X-ray diffraction patterns are shown in Fig. 1 were prepared by method *B*. For type-*A* samples, the diffraction pattern appreciably changes. Figure 2 displays the X-ray diffraction patterns for the samples prepared from polycrystalline SiC powders by both methods. It is evident that no appreciable peak is detected in the region of graphite reflection (0002) for type-*A* wafers. Instead of a peak, we observe a smooth intensity increase in the range of smaller angles, 18°–23°. Mathematical processing allows separation of a very broad peak with a half-width larger than 5°. However, measurements in the angular range 2θ = 40°–45° exhibit distinct peaks for all of the samples produced by both methods. The angular position of the peak in these curves is almost identical for all of the samples, ~43.5°. Although the half-width varies from sample to sample, it is independent of the preparation method.

Thus, there are no significantly extended fragments with graphene planes in the type-*A* samples, which radically distinguishes them from type-*B* samples. We note that the disappearance of the graphite reflection (0002) also takes place in some of the other cases described previously (in particular, for powdery samples of nanoporous carbon produced from very fine SiC powders [8]).

The difference in the behavior of the two peaks (in the angular ranges of 23°–26° and 42°–45°) suggests that they are related to different particles. This fact may be considered with greater confidence by comparing the intensities of two reflections. If we assume that these reflections are caused by diffraction from the same graphite particles, the ratio of the integral intensities of two peaks for polycrystalline samples (taking into account that the second peak consists of two reflections $(10\bar{1}0)$ and $(10\bar{1}0)$) should be given by

$$I_1/I_2 = \frac{p_1F_1^2/\sin^2(2\theta_1)}{p_2F_2^2/\sin^2(2\theta_2) + p_3F_3^2/\sin^2(2\theta_3)},$$

where F_1, F_2, and F_3 are the structure factors of graphite reflections (0002), $(10\bar{1}0)$, and $(10\bar{1}1)$; and θ_1, θ_2, and θ_3 are the corresponding Bragg angles. The structure factors of the graphite reflections are $F_1 = 52.4$, $F_2 = 9.4$, and $F_3 = 15.7$. Taking into account the multiplicity factors, the integrated intensity of the first reflection should be higher than the sum of the integrated intensities of the two others by a factor of 4.1. This value is valid for a perfect structure of graphite crystal. As for

Table 3. Ratio of the integral intensities of the peaks in X-ray diffraction patterns and the volume fraction V of graphite fragments calculated from the integrated intensity of reflection (0002)

Sample type	From SiC(B)	From SiC(B)	From Mo_2C	From TiC	From B_4C
Index	19	32			
$I(0002)/\{I(10\bar{1}0) + I(10\bar{1}1)\}$	2.0	1.3	1.8	0.9	1.5
V from (0002)	0.053	0.091	0.07	0.05	0.10

distorted graphite fragments, which exist in the case under consideration, this value should be even greater, since the reflection $(10\bar{1}1)$ is much more sensitive to any distortions of the graphene planes than to direct reflection from them. All experimental values of this ratio (see Table 3) are smaller than the calculated value. Thus, it may be unambiguously concluded that the peaks in the ranges of 25° and 43° are caused by different particles.

In this case, the peak observed in the range of 41°–45° can be caused by the two-dimensional diffraction (10) from graphene plane fragments, which form the basis of the quasi-amorphous fraction of carbon material. This inference is confirmed (see [9]) by the characteristic asymmetry of this peak with a less steep decrease in intensity in the range of large angles, which was observed for some samples produced mainly from SiC and Mo_2C. The finite size of such structures is responsible for the peak intensity shift to larger angles with respect to the Bragg angle of the (10) reflection (θ = 42.3°). Estimations of the average diameter of such plane fragments according to the formulas of [9] yield values from 40 to 60 Å. However, the integrated intensity of the peak in the range of 41°–45° for most of the samples turned out to be higher than that calculated using the expressions given in [9] for two-dimensional reflection (10), even under the condition that the entire material volume of the sample consists of such structures. Furthermore, the corresponding peak is symmetric for a number of samples, in particular, those produced from TiC. This observation suggests that the NPC samples under study also contain other particles, e.g., those characterized by a long-range order close to that of diamond, whose reflection (111) is also in the angular range under study (2θ = 44.2°). This assumption is confirmed by Raman scattering and photoelectron spectroscopy data [10, 11], which show the probable existence of diamond sp^3 bonds in such objects, along with sp^2 bonds characteristic of graphite. The diffraction peak observed in the range of 40°–45° is most probably caused by the total contribution of different particles.

Since the major part of the peak in the range of 40°–45° is not caused by graphite-like fragments, we can estimate the sizes of these only on the basis of an analysis of reflection (0002). However, in this case, we obtain an effective size in the direction normal to these planes, i.e., the average thickness of a stack of graphene planes. Therefore, the diffraction data we obtained do not provide a conclusion on the graphite-like crystallite sizes in axial directions.

The volume fractions V of graphite-like particles estimated using expressions (2)–(4) from the integrated intensity of reflection (0002) are listed in Table 3. One can see that this value does not exceed 10% of the total volume for most of the samples under study and is close to the volume concentration of pyrocarbon introduced as a binding material during preparation. It is the pyrocarbon contained in initial (before chlorination) wafers which constitutes the major difference between type-B and type-A samples. Figure 2a shows the X-ray diffraction pattern of such an initial sample from SiC powder bound by pyrocarbon. In addition to the reflections from SiC, we can see a narrow "graphite" peak from pyrocarbon inclusions at 2θ = 26.44°. Chlorination results in the disappearance of the reflections of both initial carbide and initial pyrocarbon. This suggests that the chlorine treatment distorts (or destructs) the pyrocarbon 3D lattice as well, although the pyrocarbon–chlorine chemical interaction is not strong at the temperature indicated. It seems that the observed broad reflections of graphite-like crystallites in NPC are caused by precisely this transformation. In this case, the absence of reflection (0002) in the X-ray diffraction patterns of type-A samples is to be expected. However, it would be incorrect to completely relate the formation of graphite-like grains solely to pyrocarbon, since they have been detected (as shown previously) in the samples produced by chlorination from SiC single crystals, as well as in powder samples of nanoporous carbon [8], prepared from SiC powders.

The data obtained allow certain assumptions on the kinetics of NPC formation during chemical treatment with chlorine. The presence or absence of graphite-like fragments obviously depends on the features of chlorination in various initial samples. The major factor affecting the result of this process is the reaction front velocity. In the case of samples from rather coarse initial carbide powders with macropores, through which gaseous reaction products are freely released during chlorination, the carbide-to-carbon transformation rate is quite high (moreover, the role of the reverse reaction has only minor importance in this case). As a result, rather large graphite-like particles have no time to form, and the material rapidly transforms into a mainly quasi-amorphous phase, which mostly consists of small

graphene fragments. In the case of fine powders and a significant volume fraction of pyrocarbon inclusions, the reaction front velocity during chlorination of a carbide sample is much lower due to the complicated release of reaction gases, and there is a tendency for rather large (10–15 nm) graphite clusters to form.

6. CONCLUSIONS

(i) X-ray diffraction patterns of samples of nanoporous carbon produced from carbides of various materials were measured and analyzed.

(ii) The dependence of the structure on sample preparation method was studied. It was shown that the samples grown by the type-*B* method contain microcrystalline fragments with a graphite-like structure.

(iii) The sizes and volume fraction of these crystalline fragments were estimated. It was ascertained that the volume fraction is a small portion of the sample mass. It was shown that the major differences in the X-ray diffraction patterns of *A*- and *B*-type samples are caused by pyrocarbon inclusions in *B*-type samples, despite the fact that these inclusions are significantly modified during the high-temperature reaction with chlorine.

ACKNOWLEDGMENTS

This study was supported by the federal program "Fullerenes and Atomic Clusters" and INTAS Grant 00-761.

REFERENCES

1. N. F. Fedorov, G. K. Ivakhnyuk, and D. N. Gavrilov, Zh. Prikl. Khim. (Leningrad) **55**, 272 (1981).
2. S. K. Gordeev and A. V. Vartanova, Zh. Prikl. Khim. (St. Petersburg) **66**, 1080 (1994).
3. R. N. Kyutt, É. A. Smorgonskaya, A. M. Danishevskiĭ, *et al.*, Fiz. Tverd. Tela (St. Petersburg) **41**, 891 (1999) [Phys. Solid State **41**, 808 (1999)].
4. R. N. Kyutt, É. A. Smorgonskaya, S. K. Gordeev, *et al.*, Fiz. Tverd. Tela (St. Petersburg) **41**, 1484 (1999) [Phys. Solid State **41**, 1359 (1999)].
5. Y. Chen, J. E. Gerald, L. T. Chadderton, and L. Chafton, Appl. Phys. Lett. **74**, 2782 (1999).
6. Y. Yu and E. G. Wang, Appl. Phys. Lett. **74**, 2948 (1999).
7. A. W. Moore, S. L. Strong, G. L. Doll, *et al.*, J. Appl. Phys. **65**, 5109 (1989).
8. É. A. Smorgonskaya, R. N. Kyutt, A. M. Danishevskiĭ, *et al.*, Fiz. Tekh. Poluprovodn. (St. Petersburg) **35**, 690 (2001) [Semiconductors **35**, 661 (2001)].
9. B. E. Warren, Phys. Rev. **59**, 693 (1941).
10. Yu. G. Gogotsi, I.-D. Jeon, and M. J. McNallen, J. Mater. Chem. **7**, 1841 (1997).
11. A. M. Danishevskiĭ, É. A. Smorgonskaya, S. K. Gordeev, and A. V. Grechinskaya, Fiz. Tverd. Tela (St. Petersburg) **43**, 132 (2000) [Phys. Solid State **43**, 137 (2000)].

Translated by A. Kazantsev

Semiconductors, Vol. 37, No. 7, 2003, pp. 789–794. From Fizika i Tekhnika Poluprovodnikov, Vol. 37, No. 7, 2003, pp. 816–821.

CONFERENCE. AMORPHOUS, VITREOUS, AND POROUS SEMICONDUCTORS

The Influence of Deposition Conditions and Alloying on the Electronic Properties of Amorphous Selenium[1]

S. O. Kasap, K. V. Koughia, B. Fogal, G. Belev, and R. E. Johanson

Department of Electrical Engineering, University of Saskatchewan, Saskatoon, S7N 5A9, Canada

e-mail: Kasap@engr.usask.ca

Submitted December 23, 2002; accepted for publication, December 27, 2002

Abstract—Electronic properties of *a*-Se as a function of the source (boat) temperature and as a function of As (up to 0.7%) and Cl (up to 40 wt ppm) concentrations have been experimentally studied by carrying out conventional and interrupted field time-of-flight (IFTOF) transient photoconductivity measurements that provide accurate determinations of the drift mobility and the deep trapping time (lifetime). No variation in electron and hole lifetimes and mobilities for pure *a*-Se was observed with the source temperature, that is, no dependence was observed either on the deposition rate or on the vapor composition. The addition of As reduces the hole lifetime but does not change the hole mobility. At the same time, As addition increases the electron lifetime while reducing the electron mobility. The electron range $\mu\tau$, however, increases with the As content, which means that the overall concentration of deep electron traps must be substantially reduced by the addition of As. Cl addition in the ppm range increases the hole lifetime but reduces the electron lifetime. The drift mobility of both carriers remains the same. We interpret the results in terms of a shallow-trap-controlled charge transport in which deep traps are due to potential under- and overcoordinated charged defects that can exist in the structure. *© 2003 MAIK "Nauka/Interperiodica".*

1. INTRODUCTION

Renewed interest in amorphous selenium (*a*-Se) is motivated by its use as an X-ray sensitive photoconductor in recently developed direct-conversion flat-panel X-ray image detectors [1, 2]. In these devices, a layer (thick film) of *a*-Se is deposited over a thin-film transistor array. X-ray irradiation generates mobile charge carriers in the selenium layer that separate and drift due to a large applied electric field. With positive bias applied to the radiation-receiving electrode, electrons are collected by the pixel storage capacitors. The amount of charge stored on each pixel is proportional to the radiation received by that pixel and represents a "pixel" of the X-ray image. Sense amplifiers periodically read the stored charge row by row through the array's transistors thus forming the X-ray image. For more detail refer to the review articles by Kasap and Rowlands [1, 2]. Amorphous selenium satisfies three conditions that are necessary for its use as an X-ray photoconductor in such an imaging system. First, it has good X-ray photosensitivity, thus producing a strong signal. Second, its very high resistivity limits the background (dark) current. Third, it is easily evaporated to form large-area thick films comparable in size to typical objects to be X-rayed, e.g., a human chest.

A large electric field is necessary because the amount of collected charge per unit of absorbed radiation is a strongly increasing function of the field. Although the intrinsic dark conductivity of *a*-Se is small, the large field that is needed for good X-ray sensitivity tends to cause injection of charge from the metallic electrodes, which leads to a significant dark current. One way to minimize this undesired dark current is by adding thin layers that have small carrier lifetimes in order to trap the injected carriers, creating an analog of a *p–i–n* structure [3]. In these advanced detector structures, control over the carrier mobilities and lifetimes is crucial.

There are a number of parameters that can potentially influence the structure and electronic properties of *a*-Se prepared by thermal evaporation such as the boat (or source) temperature, evaporation rate, and the substrate temperature. Postdeposition treatments such as annealing can also modify the sample's properties. In addition, the *a*-Se that is used in actual X-ray photoconductor applications is not simply "pure" *a*-Se but *stabilized a*-Se, that is, *a*-Se that has been alloyed with a small amount of As and doped with Cl in the parts per million (ppm) range. Over time, pure *a*-Se tends to crystallize even at room temperature, but this process is greatly retarded by the addition of As, which forms crosslinks between the selenium chains [4, 5]. However, As addition also produces deep hole traps that reduce the hole lifetime. In order to obtain acceptably long hole lifetimes, Cl is added (or another halogen) [5–8]. In this paper, we systematically examine how the hole and electron drift mobility μ, the lifetime τ, and the product called the carrier *range* $\mu\tau$ depend on the amount of As and Cl added to *a*-Se. The carrier range $\mu\tau$ is an important technological parameter that closely con-

[1] This article was submitted by the authors in English.

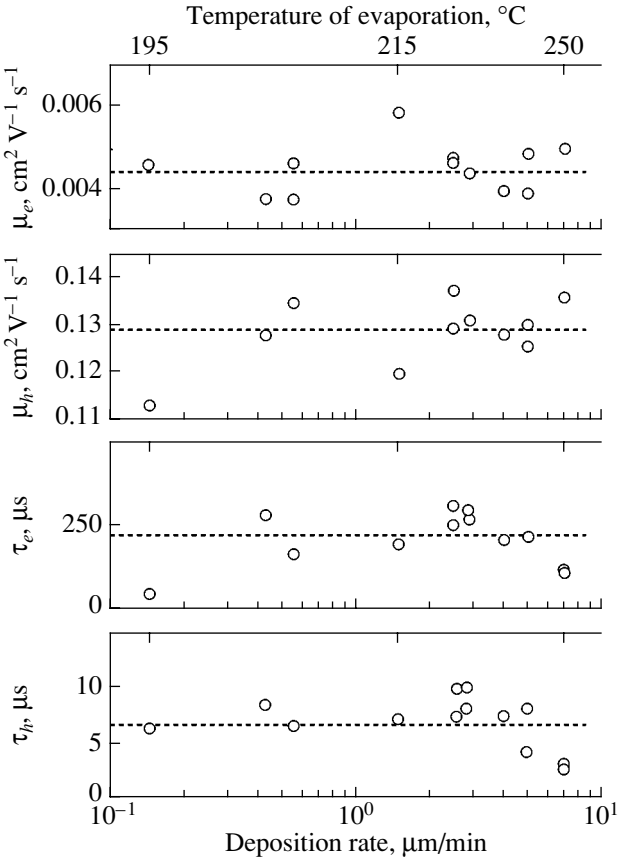

Fig. 1. The influence of the evaporation temperature and deposition rate on the electronic properties of *a*-Se. The source material is high purity photoreceptor grade selenium.

trols the sensitivity of the X-ray photoconductor [2]. It is therefore highly desirable to understand not only the experimental dependence of $\mu\tau$ on the exact composition of stabilized *a*-Se but also the reasons why such effects are observed.

2. SAMPLE PREPARATION AND EXPERIMENTAL DETAILS

Samples of *a*-Se were prepared by thermal evaporation of selenium pellets from a molybdenum boat using a Norton NRC3117 vacuum system with a base pressure of $(5–9) \times 10^{-7}$ Torr. The deposition rate was measured by a Sigma Instruments SQM-160 rate monitor. A shutter protected the substrates until steady evaporation conditions had been established and also during cooldown following deposition. For depositions using boat temperatures lower than the melting point of selenium, the pellets were first melted at 230°C and then cooled to the desired temperature. Numerous samples were prepared with the boat temperature T_B kept constant at a value in the range of 190–250°C. The substrate temperature was typically 60–65°C, above the glass transition temperature of pure and stabilized *a*-Se. The pellets used for the starting material were either high-purity (photoreceptor grade) selenium or high-purity selenium alloyed with various concentrations of arsenic and chlorine. In referring to alloyed samples below, the concentration listed is that of the starting material; because of fractionation, the concentration of particular vacuum deposited films will be somewhat different than the bulk material. Substrates were either intentionally oxidized aluminum plates or Corning 7059 glass with predeposited aluminum, platinum, or gold electrodes. The top electrodes were semitransparent films of sputtered gold or platinum. Samples were aged at least 24 h before depositing the top electrode. Sample thicknesses ranged from 50 to 200 μm and were measured by a precision micrometer (to 0.1 μm).

Electron and hole drift mobilities and deep-trapping lifetimes were determined by time-of-flight (TOF) and interrupted-field time-of-flight (IFTOF) transient photoconductivity experiments [9, 10]. The samples were aged at least 24 h in the dark prior to measurement. To avoid the buildup of trapped charge within the selenium film, a measurement consisted of a single light pulse rather than an average over multiple pulses. The samples were shorted and rested in the dark between measurements.

3. RESULTS AND DISCUSSION

Evaporation of pure selenium avoids the issue of fractionation which can occur with alloys, leading to a nonuniform composition across the thickness of the sample (this effect, for example, has been well studied and modeled for Se–Te alloys [11]). For pure *a*-Se, the relevant deposition parameters include the temperature of the substrate T_S and the temperature of the evaporating boat T_B. Most samples were prepared with T_S in the range of 60–65°C, just above the glass transition temperature, which is known to lead to electronic quality *a*-Se films [5]. T_B influences the deposition in two ways. Firstly, T_B simply controls the rate of deposition, and, secondly, T_B also determines the composition, that is, the distributions of different molecular species, in the vapor phase [12]. For selenium, increasing T_B from 190 to 250°C causes Se_5 to increase and be the predominant species in the gas-phase instead of Se_6 [12]. We have investigated pure *a*-Se samples deposited by using various boat temperatures in this range. Figure 1 summarizes the mobility and lifetime values as a function of T_B and shows that the lifetimes and mobilities of both electrons and holes are relatively independent of T_B, even though the deposition rate varied by nearly two orders of magnitude. The lack of any change in the electronic properties despite the change in the vapor-phase composition implies that all arriving species are either decomposed or incorporated into the growing film in a uniform way regardless of the particular vapor-phase composition. Maintaining T_S above the glass transition temperature during film deposition enhances the surface atomic mobility of deposited species and allows them to find optimal positions. In contrast, our attempt

to deposit *a*-Se at room temperature led to samples with very poor electronic properties that improved only marginally with subsequent annealing.

The structure of *a*-Se is believed to consist of ringlike and chainlike molecular regions [5]. Ringlike Se regions are various fragments of Se_8-rings found in α-monoclinic Se, which has good electron transport but exhibits poor hole transport. Chainlike Se regions are fragments of Se_n chains found in trigonal Se, which has good hole transport but poor electron transport. There is an intuitive argument that the relative fraction of atoms in chainlike and ringlike regions may control the relative importance of hole and electron transport in *a*-Se, respectively. The fact that we see no dependence of electronic properties on the Se vapor composition implies that the deposited *a*-Se structure does not seem to depend on the vapor-phase molecular species.

In the past, the effects of adding As and Cl had been studied by either xerographic measurements or by conventional TOF experiments. Xerographic experiments involve measuring the first residual potential V_{r1} that results from the complete photodischarge of an electrostatically charged *a*-Se film. V_{r1} can only provide a value for the product μτ, and the determination of μτ depends on the actual model used to interpret V_{r1} [13, 14]; hence, μτ values tend to be only estimates. Further, since *a*-Se cannot always be charged negatively to high voltages, xerographic measurements provide μτ for holes only. In conventional TOF measurements, one relies on decreasing the electric field until the carrier transit time t_t ($t_t = L/\mu E$; E is the field) is comparable with the lifetime τ and the photocurrent decays exponentially with a time constant τ that represents the deep trapping time, i.e., the lifetime. (This method was used previously to measure τ in stabilized *a*-Se [6, 7].) There are various problems with this technique as well. First, in *a*-Se alloys, photogeneration depends on the field and if we reduce the field too much we effectively extinguish the photocurrent. Long lifetimes, therefore, cannot be measured reliably. Secondly, the composition of alloyed *a*-Se is not completely uniform across the film, which means that the shape of the photocurrent will be influenced by this fractionation effect. Further, any net bulk space charge in the sample due to trapped carriers will result in a nonuniform field profile $E(x)$ which will lead to a photocurrent shape $i(t)$ that depends on this field profile rather than on trapping. Thus, the determination of τ from the shape $i(t)$ of the conventional TOF photocurrent is not reliable. In IFTOF experiments, on the other hand, the drift of photoinjected carriers is suddenly halted at a time t_1 corresponding to a particular location x_1, usually near the middle of the sample, by removing the field. The carriers then gradually become trapped at x_1, and the concentration of free carriers decreases exponentially with a time constant τ equal to the lifetime. When the field is reapplied at a time t_2, the carriers begin to drift again and give rise to a photocurrent i_2 that is less than the photocurrent i_1 at time t_1 just before interruption. The lifetime τ is obtained from the slope of the $\ln(i_2/i_1)$ vs. $(t_2 - t_1)$ plot. This technique has been widely used by Kasap and coworkers to obtain accurate measurements of τ for both electrons and holes in a wide range of *a*-Se alloys [15].

We have used the IFTOF technique to investigate the effects of adding As (up to 0.7%) and Cl (up to 40 wt ppm) to *a*-Se. The results for hole transport are presented in Fig. 2. It is apparent from the latter figures that the hole lifetime and also the hole range both decrease with As addition irrespective of the Cl content. Every time the Cl content is increased, there is a corresponding increase in τ and μτ. Every time the As content is increased, there is a corresponding decrease in τ and μτ. The As and Cl additions have *opposite* effects on the hole lifetime and range. The hole drift mobility is unaffected by either the addition of As or Cl. The most important technological conclusion from these two figures is that by appropriately choosing the relative amounts of As and Cl, we can control the hole range. There is some latitude in choosing the composition of stabilized *a*-Se for a given μτ product. For example, the hole range for 20 ppm of doped *a*-Se:0.3% As is about the same as that for 40 ppm of doped Se:0.5% As. Approximately 20 ppm Cl is needed to compensate for the addition of 0.2% As.

We also investigated the influence of As and Cl on the electron lifetime and drift mobility. The electron mobility μ_e in *a*-Se depends on the applied electric field [16]. In order to get comparable values for different samples, we measured the dependences of μ_e versus the electric field, as shown in Fig. 3, and determined the values corresponding to the same electric field, which was chosen to be 4 V/μm. Figure 4 shows the effects of As and Cl on electron transport parameters. It is apparent that the behavior of the electron lifetime τ_e is opposite to that of holes. Increasing the concentration of As increases the electron lifetime, whereas increasing the Cl content decreases the lifetime. The electron mobility tends to decrease as the As content is increased, but the increase in the lifetime is greater and thus the electron range μτ increases by adding As, which is a distinct technological advantage. The electron mobility is not affected by Cl doping, which is as apparent from Fig. 4.

The influence of As and Cl doping on the properties of *a*-Se. Double arrows are used to stress the strength of influence

	Holes			Electrons		
	τ	μ	μτ	τ	μ	μτ
As	↓	0	↓	↑	↓	↑
Cl	↑↑	0	↑↑	↓↓	0	↓↓

The results are qualitatively summarized in the table. It is interesting that only small amounts of Cl

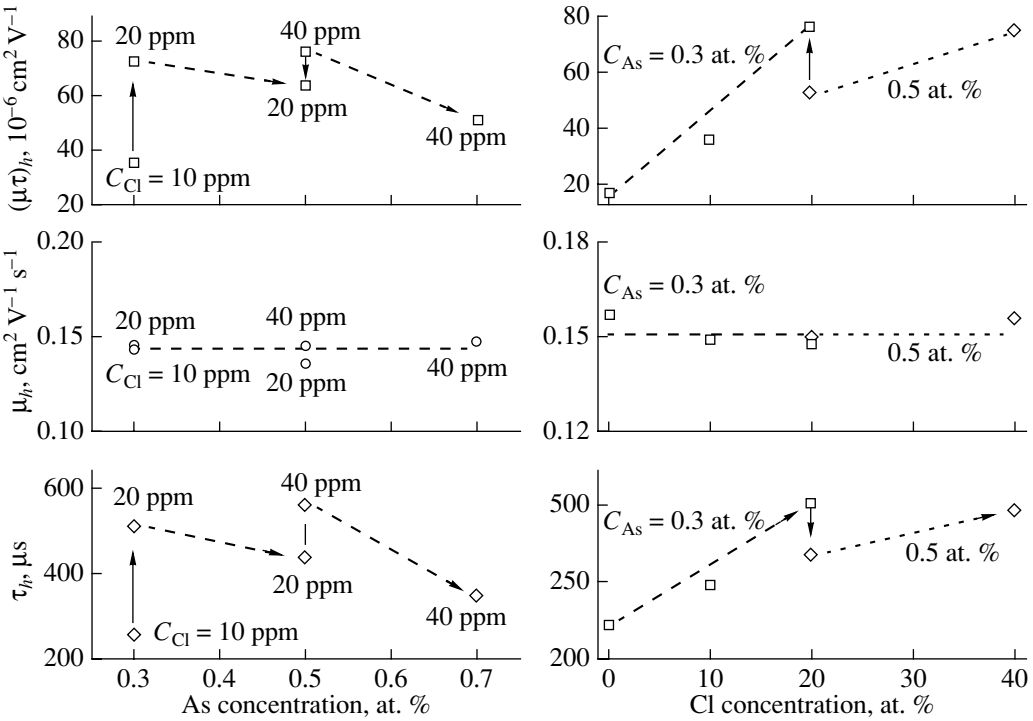

Fig. 2. The influence of As and Cl doping on hole lifetime, mobility, and hole range in *a*-Se.

(typically in the ppm range) are needed to observe large changes in the properties compared with the amount of As (typically, 0.1–1%) needed for similar changes. For example, the reduction in hole lifetime induced by an increase of the As concentration from 0.3 to 0.5 at. % may be compensated by the addition of only 20 ppm of Cl (see Fig. 2).

The accepted density of states distribution for *a*-Se shows clearly defined shallow traps and deep traps [5, 17] for both types of carriers. Within the shallow-trap-controlled transport model, the measured carrier range $\mu\tau$ is given by

$$\mu\tau = \mu_0\tau_0 = \frac{\mu_0}{C_t N_t},$$

where μ_0 is the microscopic mobility (in the transport band), τ_0 is the intrinsic deep trapping time in the absence of shallow traps, C_t is the capture coefficient, and N_t is the concentration of deep traps. Thus, the improvement in the hole product $\mu\tau$ with small additions of Cl, as in Figs. 2a and 2b, implies that the hole population in deep traps, N_t, is *reduced* with Cl addition; we make the reasonable assumption that there is no substantial change in the microscopic mobility and C_t. It is generally believed that the deep localized states are connected with under- or overcoordinated defects; that is, the deep traps in *a*-Se are Se_3^+ and Se_1^- overcoordinated and undercoordinated charged defects [5]. One possible interpretation for the observed effect is that since Cl is highly electronegative it will tend to capture an electron within the structure when it interacts with an Se chain or with charged defects, so we may expect

$$Se_2^0 + Cl_1^0 \longrightarrow Se_3^+ + Cl_0^-$$

and

$$Se_1^- + Cl_1^0 \longrightarrow Se_2^0 + Cl_0^-,$$

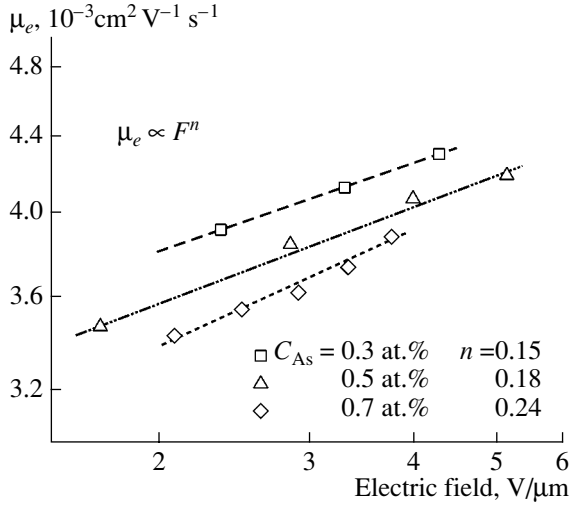

Fig. 3. The dependence of electron mobility versus applied electric field F in *a*-Se:As:Cl (both scales are logarithmic).

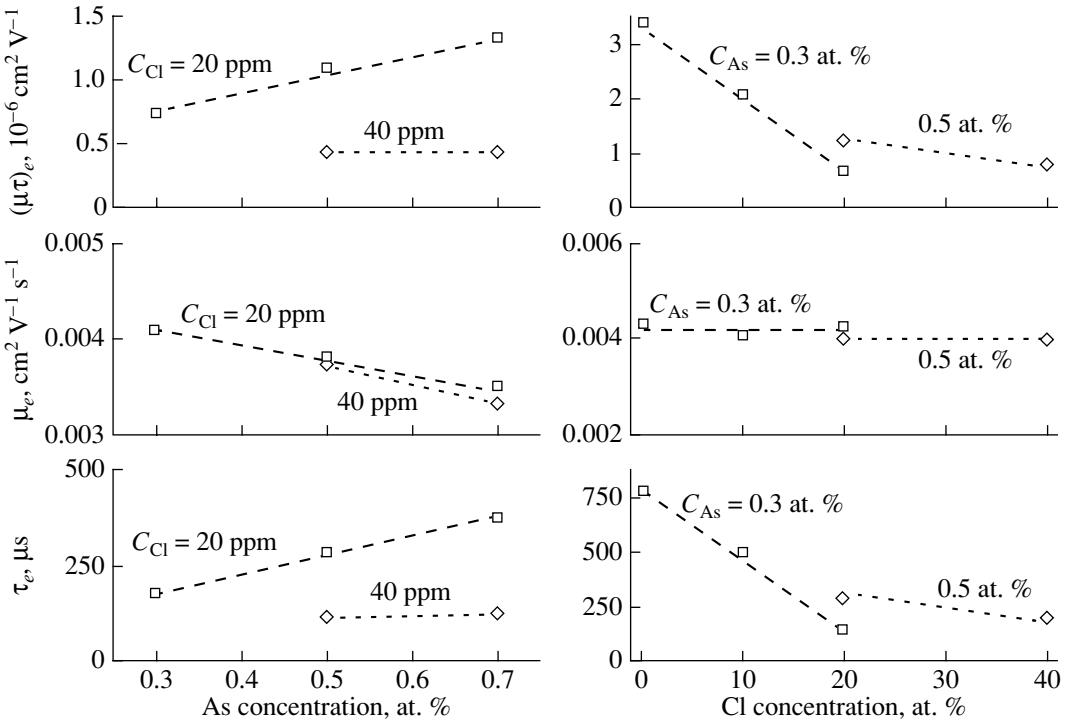

Fig. 4. The influence of As and Cl doping on electron lifetime, mobility, and electron range in *a*-Se.

in which the number of primary bonds is conserved. In the first reaction, Cl generates Se_3^+ defects and there is an increase in the electron trap concentration. In the second reaction, Cl eliminates Se_1^- defects and thus decreases the hole trap concentration. We assume that Cl_0^- centers do not act as deep hole traps. Unlike As, Cl does not seem to affect the electron and hole drift mobilities in *a*-Se:As, which implies that Cl does not modify the concentration of shallow traps in the presence of As in *a*-Se. In stabilized *a*-Se, the Cl doping effect is limited only to the deep trapping time. (It should be mentioned that Cl doping of pure *a*-Se, on the contrary, has been reported to reduce the drift mobility [18], i.e., affect the shallow hole traps.)

It is more difficult to explain the effects of As in terms of simple defect-forming reactions. Experiments indicate that As addition reduces the hole lifetime but increases the electron lifetime. The hole mobility remains the same, but the electron mobility is decreased. The electronegativity of As differs only slightly from Se, which implies the formation of both As_2^- and As_4^+ charged defects. Normally bonded As_3^0 atoms can react with Se_3^+ defects to create As_4^+ by the structural reaction

$$Se_3^+ + As_3^0 \longrightarrow Se_2^0 + As_4^+.$$

This process can explain the electron transport results because it reduces the Se_3^+ (electron trap) concentration, which means longer electron lifetimes. The resulting As_4^+ defects act as shallow traps, thereby reducing only the electron drift mobility. The decrease in the hole lifetime can be interpreted by the structural reaction

$$Se_2^0 + As_3^0 \longrightarrow Se_1^- + As_4^+,$$

which increases the Se_1^- (hole trap) concentration, and As_4^+ acts as a shallow electron trap, as postulated above. One would expect that As_2^- type centers will also be formed within the *a*-Se:As structure. Such centers can also trap holes. Thus, it is difficult to unambiguously explain the role of As. On an intuitive level, the formation of As_4^+ should require somewhat greater energy than As_2^- because As_4^+ must spatially connect with four neighbors (more lattice distortion will be needed to find four neighbors), whereas As_2^- simply fits into a chain. Although we do not yet have a complete model for the compensation effects of As and Cl in the *a*-Se structure, we can nonetheless speculate that under- and overcoordinated charged defects play an important role. There have been other discussions in the literature on the compensation mechanism between As and Cl in stabilized *a*-Se [19] though, to date, there is no accepted final model that can explain all the observations.

4. CONCLUSION

The electronic properties of *a*-Se as a function of the source (boat) temperature and as a function of As (up to 0.7%) and Cl (up to 40 wt ppm) concentrations have been experimentally studied by carrying out conventional and interrupted field time-of-flight (IFTOF) transient photoconductivity measurements that provide accurate determinations of the drift mobility and the deep trapping time (lifetime). No variation in electron and hole lifetimes and mobilities for pure *a*-Se was observed with the source temperature, that is, no dependence was observed on the deposition rate or on the vapor composition. The composition of the vapor in terms of different relative amounts of various Se molecular species does not influence the electronic properties of the resulting *a*-Se films deposited at a substrate temperature above the glass transition temperature. The addition of As reduces the hole lifetime but does not change the hole mobility. Arsenic addition increases the electron lifetime while reducing the electron mobility. The electron range $\mu\tau$, however, increases with the As content, which is a technologically desirable result for X-ray photoconductors that have a radiation receiving electrode negatively biased. The increase in the electron $\mu\tau$ with the As content means that the overall concentration of deep electron traps must be substantially reduced by the addition of As. Arsenic is less effective in increasing the electron lifetime when the structure has more Cl present. Cl addition in the ppm range increases the hole lifetime but reduces the electron lifetime. The drift mobility of both carriers remains the same. Cl is less effective in decreasing the electron lifetime when there is more As present in the structure. We interpret the results in terms of potential under- and overcoordinated charged defects that can exist in the structure.

ACKNOWLEDGMENTS

We thank the Natural Sciences and Engineering Research Council of Canada (NSERC) and Anrad (Montreal, Quebec, Canada) for funding this project. We thank S. O'Leary (University of Regina) for his interest in the project.

REFERENCES

1. J. A. Rowlands and S. O. Kasap, Phys. Today, No. 11, 24 (1997).
2. S. O. Kasap and J. A. Rowlands, Proc. IEEE **90**, 591 (2002) and references therein.
3. Z. Shukri, B. Polischuk, C. Coia, and H. Rougeot, in *Proceedings of 6th International Symposium on the Uses of Selenium and Tellurium, Scottsdale, AZ, 1998* (STDA, Grimbergen, Belgium, 1998), p. 25.
4. S. V. Nemilov and G. T. Petrovskiĭ, Zh. Prikl. Khim. (Leningrad) **36**, 932 (1963).
5. S. O. Kasap, in *Handbook of Imaging Materials*, 2nd ed., Ed. by A. S. Diamond and D. S. Weiss (Marcel Dekker, New York, 2002), Chap. 9 and references therein.
6. M. D. Tabak and W. J. Hillegas, J. Vac. Sci. Technol. **9**, 387 (1972).
7. S. O. Kasap and C. Juhasz, Photogr. Sci. Eng. **26**, 239 (1982).
8. L. P. Kazakova, E. A. Lebedev, N. B. Zakharova, *et al.*, J. Non-Cryst. Solids **167**, 65 (1994).
9. S. O. Kasap, B. Polischuk, and D. Dodds, Rev. Sci. Instrum. **61**, 2080 (1990).
10. B. Polischuk and S. O. Kasap, Meas. Sci. Technol. **2**, 75 (1991).
11. C. Juhasz, V. Gembala, and S. O. Kasap, J. Mater. Sci.: Mater. Electron. **10**, 1 (1999).
12. V. V. Illarionov and L. M. Lapina, Dokl. Akad. Nauk **114**, 1021 (1957).
13. S. O. Kasap, V. Ajyah, B. Polischuk, *et al.*, Phys. Rev. B **43**, 6691 (1991).
14. S. O. Kasap, J. Phys. D: Appl. Phys. **25**, 83 (1992).
15. S. O. Kasap and B. Polischuk, Can. J. Phys. **73**, 96 (1995).
16. C. Juhasz, S. M. Vaezi-Nejad, and S. O. Kasap, J. Imaging Sci. **29**, 144 (1985).
17. M. A. Abkowitz, Philos. Mag. Lett. **58**, 53 (1988).
18. S. O. Kasap and J. Juhasz, J. Phys. D: Appl. Phys. **18**, 703 (1985).
19. D. M. Pai, J. Imaging Sci. Technol. **41**, 135 (1997).

Semiconductors, Vol. 37, No. 7, 2003, pp. 795–799. Translated from Fizika i Tekhnika Poluprovodnikov, Vol. 37, No. 7, 2003, pp. 822–826.

CONFERENCE. AMORPHOUS, VITREOUS, AND POROUS SEMICONDUCTORS

Synthesis and Physical Properties of Si(Ge)–Se–Te Glasses

L. A. Kulakova, B. T. Melekh, V. I. Bakharev, and V. Kh. Kudoyarova

Ioffe Physicothechnical Institute, Russian Academy of Sciences, Politekhnicheskaya ul. 26, St. Petersburg, 194021 Russia
e-mail: L.Kulakova@pop.ioffe.ru

Submitted December 23, 2002; accepted for publication December 27, 2002

Abstract—Ternary $Si_{15}Ge(Ga)_5Te_{80}$, $Si_{19.7}Te_{78.7}Se_{1.6}$, $Si_{19.2}Te_{76.8}Se_4$, and $Ge_{19}Te_{72}Se_9$ telluride glasses were synthesized. Electrical, acoustic, acoustooptical properties, and the dispersion of optical transmittance of these films were studied in a wide range of temperatures and frequencies. Comparative analysis of the results obtained is performed. Possible mechanisms of the observed phenomena are discussed. It is shown that $Ge_{19}Te_{72}Se_9$ alloy is quite competitive with $Si_{20}Te_{80}$ alloy for the fabrication of highly efficient acoustooptical devices with a wide range of applications in the middle IR spectral region (2–12 μm). © *2003 MAIK "Nauka/Interperiodica".*

1. INTRODUCTION

The discovery [1] of high values of the acoustooptical figure of merit M_2 in the binary Si–Te system stimulated similar studies of ternary systems of glasses by using the replacement of silicon by germanium (or by gallium) or the anionic replacement of tellurium by selenium. The glasses with the composition $Si_{15}Ge(Ga)_5Te_{80}$ with high glass-formation ability were synthesized. They were obtained by air quenching in conical cells ≥ 15 mm in diameter. It was found that partial replacement of tellurium by selenium reduces the glass-formation ability in melts of the Si–Se–Te system; therefore, only glasses of the compositions $Si_{19.7}Te_{78.7}Se_{1.6}$ and $Si_{19.2}Te_{76.8}Se_4$ were obtained. The alloy $Si_{18.7}Te_{74.6}Se_{6.7}$ was crystalline and unstable in air because of high hydration.

Taking into consideration the structural similarity of Si–Te and Ge–Te glasses, one may expect that the glasses of the latter system should also exhibit high acoustooptical characteristics. However, high glass-formation ability is restricted by the possibility of obtaining a vitreous state for the composition $Ge_{18}Te_{82}$ by cold-water quenching in conical cells 5–6 mm in diameter. If tellurium is partially replaced by selenium (specifically, for the composition $Ge_{19}Te_{72}Se_9$ corresponding [2] to ternary eutectic), one should expect an appreciable increase in the glass-formation ability with retention of a glass structure close to that observed in $Si_{20}Te_{80}$. Experiments confirmed the high glass-formation ability of this composition synthesized in conical cells with ≥15 mm diameter.

A complex study of density ρ_0, refractive index n, temperature dependence of conductivity, and the dispersion of optical transmittance of various alloys ($Si_{15}Ge(Ga)_5Te_{80}$, $Si_{19.7}Te_{78.7}Se_{1.6}$, $Si_{19.2}Te_{76.8}Se_4$, and $Ge_{19}Te_{72}Se_9$) has been performed.

2. RESULTS AND DISCUSSION

Technological aspects of the preparation of alloys and measurement details are described in [1].

2.1. Electrical Properties

Temperature dependences of resistivity $\rho(T)$ of $Si_{15}Ge(Ga)_5Te_{80}$, $Si_{19.7}Te_{78.7}Se_{1.6}$, $Si_{19.2}Te_{76.8}Se_4$, and $Ge_{19}Te_{72}Se_9$ are shown in Figs. 1–3. It can be seen that the partial replacement of tellurium by selenium in $Si_{19.7}Te_{78.7}Se_{1.6}$ and $Si_{19.2}Te_{76.8}Se_4$ results (Fig. 1), in

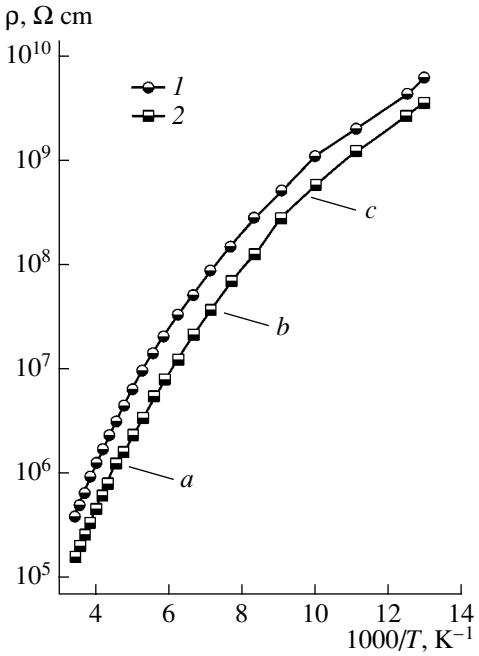

Fig. 1. Temperature dependence of resistivity of glasses: (*1*) $Si_{19.7}Te_{78.7}Se_{1.6}$ and (*2*) $Si_{19.2}Te_{76.8}Se_4$. Activation energy E = (*a*) 0.15, (*b*) 0.10, (*c*) 0.06 eV.

1063-7826/03/3707-0795$24.00 © 2003 MAIK "Nauka/Interperiodica"

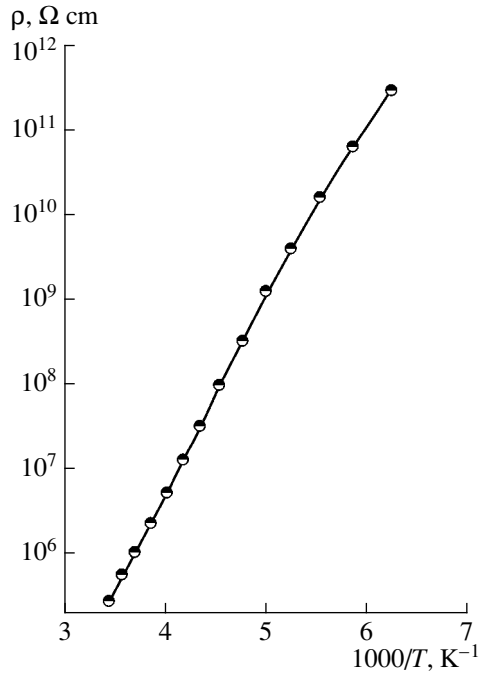

Fig. 2. Temperature dependence of resistivity of $Ge_{19}Te_{72}Se_9$ glass. Activation energy E = 0.44 eV.

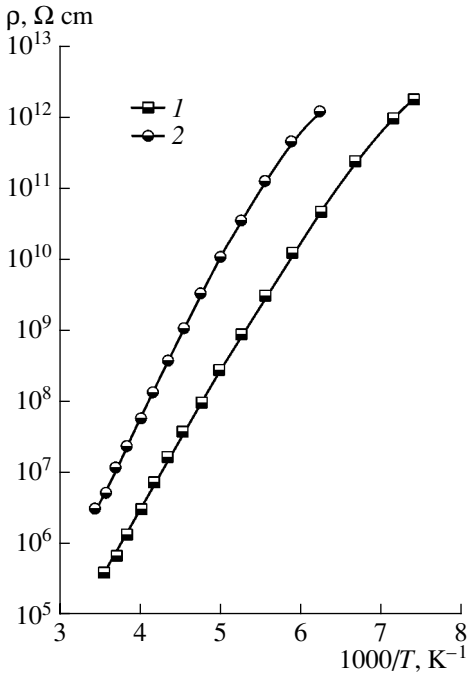

Fig. 3. Temperature dependence of resistivity of glasses: (*1*) $Si_{15}Ga_5Te_{80}$, E = 0.37 eV; (*2*) $Si_{15}Ge_5Te_{80}$, E = 0.42 eV.

contrast to $Si_{20}Te_{80}$ glasses, in the appearance of three ranges where the activation energy E decreases with decreasing temperature, which may be indicative of the increasing role of structural imperfections in alloys. The partial replacement of tellurium with selenium in germanium-containing glass $Ge_{19}Te_{72}Se_9$ essentially increases its glass-formation ability: in this case, the $\rho(T)$ dependence in the entire temperature range is characterized by a single activation energy, which is significantly higher than the values for $Si_{19.7}Te_{78.7}Se_{1.6}$ and $Si_{19.2}Te_{76.8}Se_4$ glasses (Fig. 2). The partial replacement of silicon by germanium or gallium in $Si_{15}Ge(Ga)_5Te_{80}$ glasses does not profoundly affect the glass-formation ability in these glasses, which is consistent with the existence of a single linear part in the $\rho(T)$ dependence (Fig. 3). However, the optical transmittance of these glasses is appreciably (by an order of magnitude) lower than that of $Si_{20}Te_{80}$; therefore, primary emphasis in studying optical and photoelastic properties is placed on the $Ge_{19}Te_{72}Se_9$ alloy and, to a lesser degree, on the $Si_{19.7}Te_{78.7}Se_{1.6}$ and $Si_{19.2}Te_{76.8}Se_4$ alloys.

Table 1. Main elastic parameters of alloys under investigation at T = 300 K

Composition	v, 10^5 cm/s	ρ_0, g/cm^3	C_{11}, 10^{12} dyn/cm^2
$Ge_{19}Se_9Te_{72}$	2.06	5.41	0.230
$Si_{19.7}Te_{78.7}Se_{1.6}$	2.05	5.1	0.214
$Si_{19.2}Te_{76.8}Se_4$	2.05	5.0	0.210
$Si_{15}Ge_5Te_{80}$	2.04	5.25	0.218
$Si_{15}Ga_5Te_{80}$	2.10	5.29	0.233
$Si_{20}Te_{80}$	2.03	5.03	0.207

2.2. Acoustic Properties

We measured the velocities of longitudinal sound υ in the glasses synthesized (see Table 1). From the data listed in Table 1, it is seen that the basic matrix of tellurium is predominant in determining the elastic properties of telluride glasses.

The dependence of the sound absorption coefficient α_{ac} on frequency f (Fig. 4) and the dependence of the velocity of sound on temperature (Fig. 5) were obtained only for the $Ge_{19}Te_{72}Se_9$ alloy, because, as will be shown below, this alloy is of greatest interest from the scientific standpoint, and it is also a promising material for the fabrication of acoustooptical devices. In contrast to the $Ge_{19}Te_{72}Se_9$ alloy, $Si_{15}Ge_5Te_{80}$ and $Si_{15}Ga_5Te_{80}$ alloys are found to be fragile (stressed), which is most likely the consequence of high mechanical imperfection.

Comparison of the magnitude and the frequency dependences of the sound absorption coefficient of the $Ge_{19}Te_{72}Se_9$ alloy with the previously studied $Si_{20}Te_{80}$ alloy allows two main conclusions to be made. In $Ge_{19}Te_{72}Se_9$ the sound absorption at low frequencies is less and the frequency dependence is steeper, approaching a quadratic low typical of crystals.

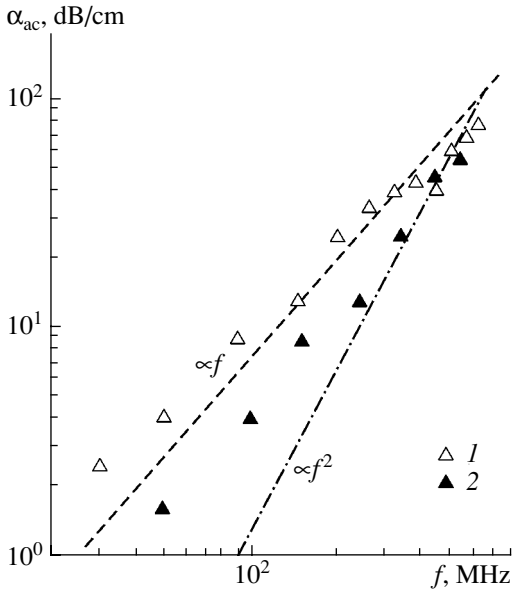

Fig. 4. Coefficient of sound absorption as a function of frequency in glasses: (*1*) $Si_{20}Te_{80}$, (*2*) $Ge_{19}Te_{72}Se_9$.

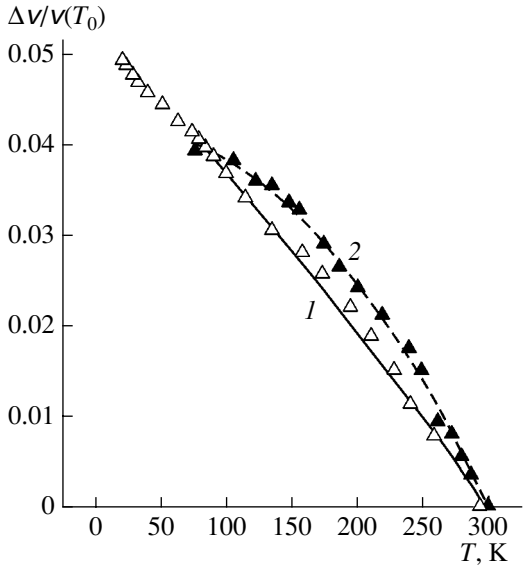

Fig. 5. Temperature dependence of relative change of the sound velocity in glasses: experiment (triangles), theory (lines): (*1*) $Si_{20}Te_{80}$, (*2*) $Ge_{19}Te_{72}Se_9$.

Previously, we showed [3] that the large value of the sound absorption coefficient observed in $Si_{20}Te_{80}$, which differs by two orders of magnitude from the values in crystals, and its linear frequency dependence (Fig. 4) are the consequences of a specific structure of glasses having a system of two-well structural defects with a broad, almost uniform, distribution of relaxation times. Therefore, the observed value of the absorption coefficient and the character of its frequency variation in the $Ge_{19}Se_9Te_{72}$ alloy under investigation can be attributed to the higher structural quality of this alloy.

With the aim of studying the effect of composition on elastic properties of glasses, we measured the velocity of sound in them and showed that the magnitudes of the modulus of elasticity C_{11} (see Table 1) in $Ge_{19}Te_{72}Se_9$ are larger than in $Si_{20}Te_{80}$. Temperature dependences of the relative change of velocity of sound in these alloys (Fig. 5) also differ. The calculation of the contribution of anharmonicity due to the interaction of a sound wave with thermal phonons by the formula [3]

$$\frac{(\Delta v)^{\text{anh}}}{v(T_0)} = \frac{\bar{\gamma}^2 T_0 C_p(T_0)}{3v^2(T_0)}\left\{1 - \frac{TC_p(T)}{T_0 C_p(T_0)}\right\} \qquad (1)$$

showed (Fig. 5, curve *1*) that it is this interaction which is responsible for the observed temperature dependences of the velocity of sound in $Si_{20}Te_{80}$, provided that the value of the averaged Grüneisen constant (anharmonicity of bonding forces) is $\bar{\gamma} = 1.45$. The quantities T and C_p in formula (1) are the temperature and heat capacity at constant pressure, respectively; $T_0 = 300$ K. The calculation by formula (1) for $Ge_{19}Te_{72}Se_9$ at $\bar{\gamma} \sim 1.39$ (Fig. 5, curve *2*) shows that attainment of agreement with the experimental data on $v(T)$ requires the temperature behavior of heat capacity C_p^1 in this alloy to be different from that in $Si_{20}Te_{80}$. Specifically, the slope of this dependence should be steeper at lower temperatures; i.e., $C_p^1(T)/C_p^1(T_0) \approx (T/T_0)^n C_p(T)/C_p(T_0)$, where $n = 0.9$. This means that the temperature behavior of heat capacity qualitatively approaches the temperature dependences of heat capacity in crystals. This is consistent with the features of frequency dependences of absorption in this alloy. As was shown above, the frequency dependences of absorption in $Ge_{19}Te_{72}Se_9$ differ from the linear dependences typical of glasses observed in $Si_{20}Te_{80}$ and qualitatively approach the quadratic dependences typical of the crystals in the low-frequency region [3]. This is surprising if one takes into consideration that the increase in the number of components in alloy (as happens in the $Ge_{19}Te_{72}Se_9$ alloy in contrast to $Si_{20}Te_{80}$) is more often than not the prerequisite for the formation of defects, including two-well defects which are responsible for the specific behavior of the thermal and elastic properties of glasses. However, it is evident that the abovementioned increase in the glass-formation ability induced by the combination of selenium and germanium in tellurium alloy is not the only attractive consequence of this structural ensemble. Most likely, a reduction in the number of defects occurs in such a structure.

2.3. Optical Properties

The low optical transmittance T_0, which is only slightly greater than several percent in the transparent region at a wavelength of ~2–20 μm, observed in

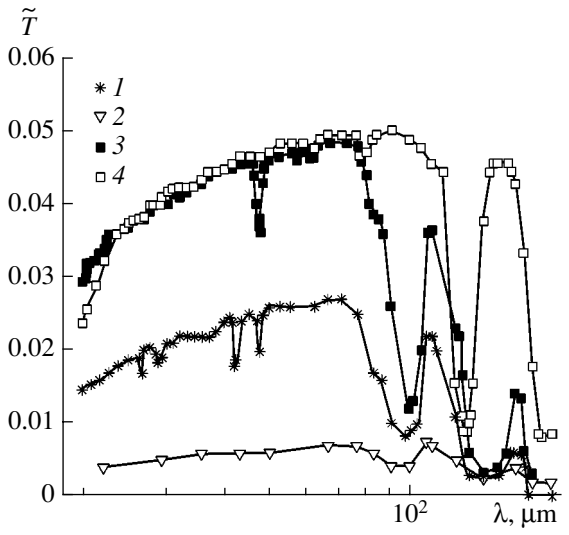

Fig. 6. Dispersion of the optical transmittance coefficient of glasses: (*1*) $Si_{19.7}Te_{78.7}Se_{1.6}$, (*2*) $Si_{19.2}Te_{76.8}Se_4$, (*3*) $Si_{20}Te_{80}$, and (*4*) $Ge_{19}Te_{72}Se_9$. The thickness of glasses is 6 mm.

$Si_{15}Ge(Ga)_5Te_{80}$ glasses is, in our opinion, the consequence of the inhomogeneity of mechanical properties.

The transmittance of Si–Te allays doped with Se is shown in Fig. 6 (curves *1*, *2*). It is seen that the optical transmittance of these appreciably decreases with increasing Se content. Such transmittance behavior can be explained by the scattering of light by defects which affect the temperature dependence of resistivity ρ(*T*) (Fig. 1).

The study of the optical properties of the $Ge_{19}Te_{72}Se_9$ alloy showed that minimization of the amount of structural defects observed through acoustic measurements (see above) also manifests itself in this case. First, this alloy exhibits much higher optical homogeneity. Second, within the entire spectral range, the transmittance of this alloy (Fig. 6, curve *4*) is higher than in $Si_{20}Te_{80}$ (Fig. 6, curve *3*). This is most clearly pronounced at the wavelengths corresponding to the radiation of a CO_2 laser (10.6 μm), i.e., in the atmospheric transparency window (which is of prime importance).

The value of the refractive index $n = 3.4 \pm 0.02$ for the alloy under study is obtained from the reflection coefficient. The value obtained is higher than that in the $Si_{20}Te_{80}$ alloy ($n = 3.3$).

2.4. Acoustooptical Properties

It is known that the efficiency of Bragg diffraction of light by ultrasound waves is determined by the acoustooptical figure of merit M_2. In linear mode (low sound intensity), the interaction of light with sound is described as

$$I_1 = (1/2)I_0M_2P[\pi d/(\lambda\cos\theta)]^2, \quad (2)$$

$$(M_2)_{ik} = n_i^6 p_{ik}^2/(\rho_0 v_k^3), \quad (3)$$

where I_1 and I_0 are the intensities of diffracted and incident light, respectively; P is the sound intensity; λ is the wavelength of light; d is the width of the acoustic beam; θ is the angle of incidence; n_i is the refractive index; p_{ik} is the component of the photoelastic tensor; ρ_0 is the density of a crystal; v_k is the velocity of a sound wave; $i, k = 1, 2, 3, 4, 5, 6$; i is the index of light polarization; and k is the index of deformation in matrix representation.

We showed previously that the $Si_{20}Te_{80}$ alloy has the highest acoustooptical efficiency of Bragg diffraction in a wide range in the near and medium IR region of the spectrum (Table 2). However, the existence of a noticeable optical inhomogeneity in this material called for a further search for ways to optimize its optical properties. An appreciable improvement of the acoustic parameters (lower sound absorption at the operating

Table 2. Acoustooptical parameters of the system of Si(Ge)–Se–Te alloys and other IR materials at $T = 300$ K

Material	Transparency range Δλ, μm	α, cm^{-1}	α_{ac}, dB/cm ($f = 100$ MHz)	λ, μm	Polarization of light with respect to the direction of sound propagation	$(M_2)'$
				10.6	∥	3500
$Si_{20}Te_{80}$	1.7–13	0.1	8	3.39	∥	3200
				1.87	∥	2800
$Ge_{19}Se_9Te_{72}$	2–18		4	3.39	∥	3150
Ge	2–20	0.06	0.3	10.6	∥	540
As_2Se_3	0.9–11			1.15	∥	700
a-Se	1–20			1.15	⊥	776
				10.6	⊥	692

Note: $(M_2)' = M_2/(M_2)''$, where $(M_2)'' = 1.56 \times 10^{-18}$ s^3/g (M_2 is given for quartz glass); α is the coefficient of optical absorption.

acoustooptical frequencies in the region of about 100 MHz; see Table 2) and optical characteristics (lower light absorption, a large refractive index n, and optical homogeneity; see Table 2) observed in the $Ge_{19}Te_{72}Se_9$ alloy makes this alloy very attractive for studying acoustooptical properties. Preliminary data (Table 2) on the acoustooptical figure of merit M_2 obtained for $\lambda = 3.39$ μm show that acoustooptical efficiency in this spectral region is no worse than in $Si_{20}Te_{80}$. From this fact it follows that the new $Ge_{19}Te_{72}Se_9$ alloy is quite promising for the fabrication of new acoustooptical devices. Therefore, more detailed acoustooptical studies in a wider optical spectral range are needed.

3. CONCLUSION

Thus, the comparative analysis of properties of ternary telluride Si–Ge(Ga)–Te and Si(Ge)–Te–Se glasses yielded the following results:

(i) It is shown that the basic tellurium matrix governs, to a great extent, the elastic properties of telluride glasses.

(ii) $Ge_{19}Te_{72}Se_9$ is found to be the highest quality alloy and exhibits a number of advantages in comparison to the promising acoustooptical $Si_{20}Te_{80}$ alloy studied previously [1]. Having a rather high optical homogeneity, the new alloy is more transparent, particularly in the range of the atmospheric transparency window $\lambda \approx 10$–11 μm (CO_2 laser, $\lambda = 10.6$ μm). Owing to these properties, and also because of lower acoustic attenuation, the $Ge_{19}Te_{72}Se_9$ alloy is a worthy competitor of the $Si_{20}Te_{80}$ alloy in the fabrication of modulators for the medium IR region of the spectrum.

4. ACKNOWLEDGMENTS

This study was supported in part by the Russian Foundation for Basic Research, project no. 98-03-18305.

REFERENCES

1. L. A. Kulakova, B. T. Melekh, É. Z. Yakhkind, *et al.*, Fiz. Tekh. Poluprovodn. (St. Petersburg) **35**, 658 (2001) [Semiconductors **35**, 630 (2001)].
2. A. Feltz, *Amorphe und Glasartige Anorganische Festkörper* (Akademie, Berlin, 1983; Mir, Moscow, 1986).
3. L. A. Kulakova, Fiz. Khim. Stekla **26**, 839 (2000).

Translated by A. Zalesskiĭ

Semiconductors, Vol. 37, No. 7, 2003, pp. 800–802. Translated from Fizika i Tekhnika Poluprovodnikov, Vol. 37, No. 7, 2003, pp. 827–829.

CONFERENCE. AMORPHOUS, VITREOUS, AND POROUS SEMICONDUCTORS

Effect of Rare-Earth Impurities on the Photoluminescence of Ge_2S_3 Glass

A. A. Babaev*, I. K. Kamilov*, Z. V. Vagabova*, S. M. Sultanov*, A. M. Askhabov*, E. I. Terukov, and I. N. Trapeznikova****

**Institute of Physics, Dagestan Scientific Center, Russian Academy of Sciences, Makhachkala, 367003 Russia*
e-mail: kamilov@datacom.ru

***Ioffe Physicotechnical Institute, Russian Academy of Sciences, St. Petersburg, 194021 Russia*

Submitted December 23, 2002; accepted for publication December 27, 2002

Abstract—The photoluminescence properties of Ge_2S_3 glass doped with rare-earth elements La, Ce, Gd have been studied in the temperature range of 4.2–300 K. It has been shown that these impurities do not form new levels responsible for emission. The variation in the principal parameters of the excitation and emission spectra with the concentration and nature of impurities has been estimated. © *2003 MAIK "Nauka/Interperiodica".*

The effect of impurities on the photoluminescence (PL) of chalcogenide glass semiconductors has been studied experimentally [1–3] in attempts to reveal the energy spectrum of localized states and the nature and mechanisms of radiative recombination. However, the diversity and, occasionally, inconsistency of the available data indicate insufficient clarity in the understanding of the problem and, thus, provides an impetus for further studies.

Presently, intense effort is being made in the field of the technology and study of the rare-earth impurities in amorphous hydrogenated films, sulfides, and oxysulfides of rare earths.

These studies are aimed at creating a new class of active media for optoelectronic devices operating in the IR spectral range in different pumping modes. Progress in this field is assisted by the study of correlations between the composition of a material, the nature of centers responsible for radiative recombination, and the quantum efficiency of luminescence.

Here, we report on the study of the effect of rare-earth impurities on the PL of chalcogenide glass semiconductors. One might expect that, owing to their specific electronic structure, rare-earth atoms would give rise to impurity-related emission centers, as happens in crystalline chalcogenides, rare-earth oxychalcogenides, and amorphous hydrogenated films.

Undoped and doped Ge_2S_3 glass was synthesized by the direct fusion of necessary amounts of elementary components, Ge and S, with La, Gd, and Ce of B-5 purity in evacuated quartz ampules under vibrational agitation. To prevent an ampule from exploding, the synthesis was performed in two stages. At the first stage, ampules were heated in a tubular furnace to a temperature of 1223 K at a rate of 0.1–0.2 K s^{-1} and kept for 50 h at this temperature. At the second stage, the furnace was heated to the melting temperature of the higher-melting element at a rate of ~ 0.1 K s^{-1} and kept constant for 20–25 h. Finally, the melt was quenched in salt water with ice. To relieve mechanical strain, all the synthesized glasses were annealed at 500–530 K for 20 h. The atomic content of La, Gd was 0.1–0.2 at. % and that of Ce, 0.1–1.0 at. %.

The criteria for the glassy state of a material were the absence of lines in the Debye powder patterns, diffuse X-ray scattering, and the absence of micro-inclusions and heterogeneities on the polished and cleaved surfaces upon examination with a Neofot microscope.

The steady-state luminescence was excited with an Xe lamp of 1000 W power. To exclude possible distortions of the emission spectra due to self-absorption, the emission was recorded from the illuminated side of a sample. The power density of the exciting beam did not exceed 5 mW cm^{-2}. A Ge photodiode was used as a detector. The PL excitation spectra were recorded in the peak of a PL spectrum, and the PL, under excitation with photons corresponding to the peak in the excitation spectrum. In view of the long-term decay of PL under steady excitation (PL fatigue), the spectra presented here were recorded after a quasi-steady state was reached, i.e., when fatigue during the time of spectrum recording could be neglected.

The excitation and emission spectra at T = 4.2 K, temperature quenching of PL, and the PL fatigue were studied in relation to the nature and concentration of a rare-earth impurity. Figure 1 shows the obtained emission and PL excitation (*A* and *B*, respectively) spectra of Ge_2S_3 glass—both the initial one and that doped with a rare-earth impurity to 0.2 at. %. As can be seen, doping with a rare-earth element leads to PL quenching relative to the initial sample. The degree of quenching depends on the nature of a rare-earth impurity, being the highest for Gd. The emission spectra of rare-earth-doped samples (Fig. 1, spectra *A*) shift to higher ener-

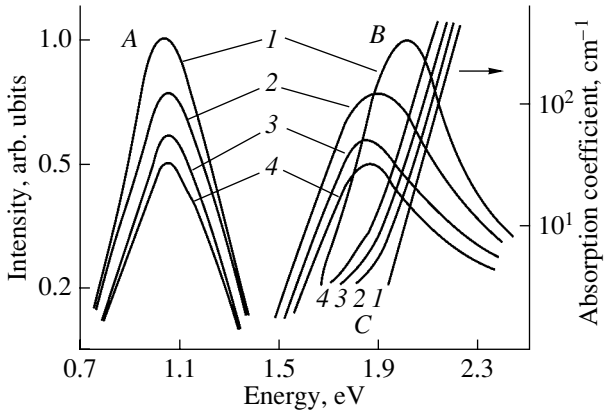

Fig. 1. (*A*) emission and (*B*) PL excitation spectra and (*C*) absorption edge of Ge_2S_3 glass at T = 4.2 K for (*1*) an undoped sample and samples doped with a rare-earth element: (*2*) La, (*3*) Ce, and (*4*) Gd.

gies, and the excitation spectra (Fig. 1, *B*), to lower energies relative to undoped samples; the emission band FWHM decreases.

The listed changes in the luminescence characteristics are enhanced as the dopant concentration increases (Fig. 2). The study of the optical absorption edge of rare-earth-doped glasses has shown that the slope of the optical absorption edge decreases with doping and the edge shifts slightly to lower energies (Fig. 1, *C*). Since the slope of the absorption edge decreases, a small shift to lower energies in the range $\alpha < 10^2$ cm^{-1} cannot be attributed to the band gap decreasing.

The study of the fatigue effect (Fig. 3) at T = 4.2 K has shown that the rare-earth doping of Ge_2S_3 glass accelerates this process in direct proportion to the size of the ionic radius R_i.

Rare-earth impurities occupy the dangling bonds of the chalcogen (centers with negative correlation energy) and reduce their density, so that the intensity and FWHM of the emission spectrum decrease. The low-energy shift of the PL excitation spectra is related to the shift of the optical absorption edge in chalcogenide glass semiconductors doped with rare-earth elements, which is in agreement with the data obtained in [4], where the effect of rare-earth doping on the absorption edge of As_2S_3 and As_2Se_3 glasses was studied. It is worth noting that the introduction of rare earths markedly reduces the glass-forming ability of chalcogenide glasses, which, in turn, enhances the nonuniformity of the rare-earth distribution in the glass bulk. Introduction of an impurity by an amount exceeding 1 at. % results in the formation of crystal blocks of rare-earth chalcogenides with a cubic structure ~ 0.5 mm in size on the surface of Ge_2S_3 glass.

The temperature quenching of PL (Fig. 4) is more pronounced for the rare-earth impurity with the smallest R_i. A material can be characterized by the values of parameter T_0 in the dependence $I = I_0\exp(-T/T_0)$; for the

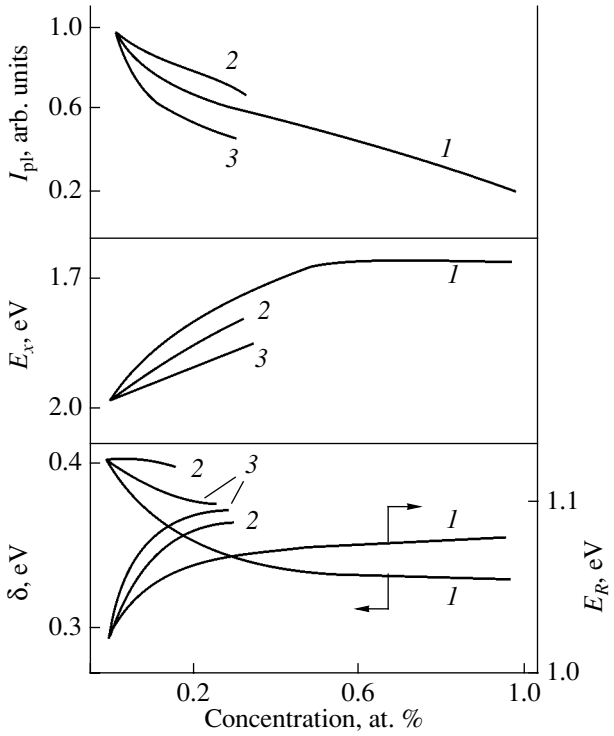

Fig. 2. Main PL characteristics of glassy Ge_2S_3: (I_{pl}) PL intensity; (E_x) and (E_R) peak energies for excitation and emission spectra, respectively; (δ) FWHM of the PL band for samples doped with (*1*) Ce, (*2*) La, and (*3*) Gd.

initial glass and samples doped with 0.1 at. % La, Ce, or Gd, the values of T_0 are 35, 34, 33, and 28 K, respectively. The direct proportionality between the changes in T_0 and R_i may be indicative of the charge interaction of a rare-earth impurity with the Ge_2S_3 glass matrix.

The obtained data show that rare-earth doping of Ge_2S_3 glass does not give rise to new PL emission

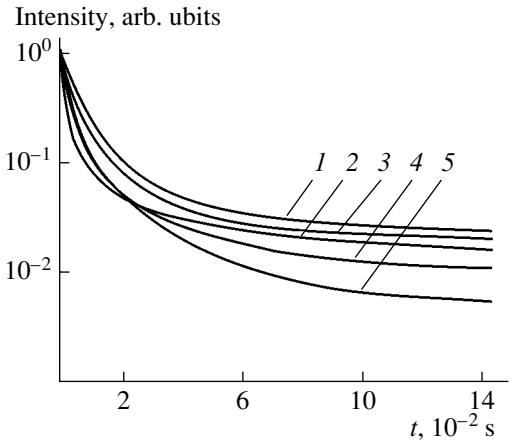

Fig. 3. Long-term PL decay under steady excitation (fatigue) in (*1*) undoped samples and those doped with a rare-earth element: (*2*) La, 0.1; (*3*) Gd, 0.1; (*4*) Ce, 0.5; (*5*) Ce, 1.0 at. %.

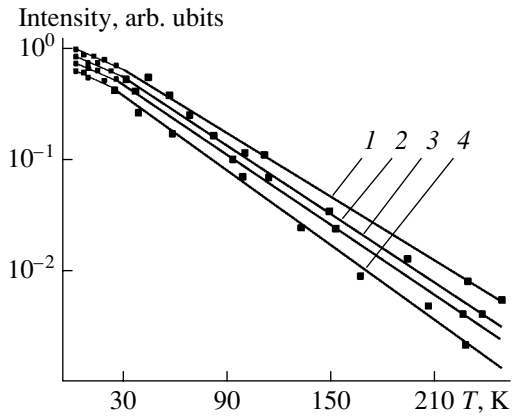

Fig. 4. Temperature dependence of PL intensity for (*1*) an undoped sample and samples doped (0.1 at. %) with (*2*) La, (*3*) Ce, and (*4*) Gd.

bands that might be attributed to impurity states or defect–impurity complexes. Changes in the PL band, which is inherent in initial undoped Ge_2S_3, upon rare-earth doping are indicative of the changing local structure in the vicinity of the native emission centers.

ACKNOWLEDGMENTS

This study was supported by the Russian Foundation for Basic Research (project no. 00-05-72031), and the Russian Federal program “Integration” (research area 3.2, project no. 96 (2001)).

REFERENCES

1. B. T. Kolomiets, T. N. Mamontova, and A. A. Babaev, J. Non-Cryst. Solids **8–10**, 1004 (1972).
2. T. N. Mamontova and V. A. Vasil’ev, in *Proceedings of International Conference on Amorphous Semiconductors-80* (Chisinau, 1980), p. 183.
3. S. G. Bishop, V. Strom, E. J. Friebele, and P. C. Taylor, J. Non-Cryst. Solids **32**, 359 (1979).
4. E. M. Raspopova, V. A. Masloboev, and L. I. Polezhaeva, in *Proceedings of International Conference on Amorphous Semiconductors-78* (Pardubitse, 1978), p. 162.

Translated by D. Mashovets

Semiconductors, Vol. 37, No. 7, 2003, pp. 803–806. Translated from Fizika i Tekhnika Poluprovodnikov, Vol. 37, No. 7, 2003, pp. 830–834.

CONFERENCE. AMORPHOUS, VITREOUS, AND POROUS SEMICONDUCTORS

Influence of the Order–Disorder Transition in the Crystal Electron Subsystem on the Electron Density at Lattice Sites

N. P. Seregin*, T. R. Stepanova, Yu. V. Kozhanova**, V. P. Volkov**, P. P. Seregin**, and N. N. Troitskaya****

**Institute of Analytical Instrument Making, Russian Academy of Sciences, Rizhskii pr. 26, St. Petersburg, 198103 Russia*

***State Technical University, St. Petersburg, 195251 Russia*

Submitted December 23, 2002; accepted for publication December 27, 2002

Abstract—The temperature dependence of the Mössbauer spectrum centroid S of $^{67}Zn^{2+}$ impurity atoms at the copper and yttrium sites of $YBa_2Cu_3O_{6.9}$, $YBa_2Cu_3O_{6.6}$, $YBa_2Cu_4O_8$, $Nd_{1.85}Ce_{0.15}CuO_4$, $La_{1.85}Sr_{0.15}CuO_4$, $HgBa_2CuO_4$, $HgBa_2CaCu_2O_6$, $Bi_2Sr_2CaCu_2O_8$, and $Tl_2Ba_2CaCu_2O_8$ compounds at temperatures $T > T_c$ (T_c is the superconducting transition temperature) is controlled by a second-order Doppler shift. The value of S in the temperature range $T < T_c$ is affected by the energy-band mechanism associated with the formation of Cooper pairs and their Bose condensation. A relationship between the electron density at the metal site of the crystal and its superconducting transition temperature is found. In the case of compounds containing two structurally nonequivalent sites for copper atoms, a change in the electron density caused by the Bose condensate of Cooper pairs is shown to be different for these sites. The experimental temperature dependence of the superconducting electron fraction conforms to a similar dependence following from the Bardeen–Cooper–Schrieffer theory for all the sites under study. © *2003 MAIK "Nauka/Interperiodica"*.

1. INTRODUCTION

The superconducting transition of a crystal is a second-order phase transition. The Landau theory interprets it as a transition with a change in symmetry: at temperatures above the transition temperature T_c, the crystal electronic subsystem is characterized by a higher symmetry than at $T < T_c$ (the transition from Bloch wave functions of the metal to a single coherent wave function of the superconductor). Therefore, the electron density distribution at lattice sites of superconducting and normal phases should differ, and this difference can be measured using Mössbauer spectroscopy [1].

In this study, $^{67}Cu(^{67}Zn)$ and $^{67}Ga(^{67}Zn)$ emission Mössbauer spectroscopy was used to measure electron changes in density at copper and yttrium lattice sites of $YBa_2Cu_3O_{6.9}$ (T_c = 90 K), $YBa_2Cu_3O_{6.6}$ (T_c = 50 K), and $YBa_2Cu_4O_8$ (T_c = 80 K) compounds during their superconducting transition. Copper atoms in the structure of these compounds occupy two structurally nonequivalent sites, Cu(1) and Cu(2) [2, 3]. It was not ruled out that the change in the electron density in these sites could be different. The change in the electron density was also studied in the copper lattice sites of $Nd_{1.85}Ce_{0.15}CuO_4$ (T_c = 22 K), $La_{1.85}Ce_{0.15}CuO_4$ (T_c = 37 K), $HgBa_2CuO_4$ (T_c = 79 K), $HgBa_2CaCu_2O_6$ (T_c = 93 K), $Bi_2Sr_2CaCu_2O_8$ (T_c = 80 K), and $Tl_2Ba_2CaCu_2O_8$ (T_c = 60 K) compounds, where copper occupies a single site [4–6].

2. TECHNIQUE AND RESULTS

Mössbauer sources of superconducting samples were prepared by the diffusion of radioactive carrier-free ^{67}Cu and ^{67}Ga into polycrystalline compounds in evacuated quartz cells at 450°C for 2 h. As reference samples (in which a superconducting transition was not observed), we took materials produced by 2-h annealing of superconducting samples in air at 600°C. The Mössbauer spectra were measured with a ^{67}ZnS absorber. The absorber temperature was 10 ± 1 K, and the source temperature varied from 10 ± 2 to 90 ± 2 K.

The $^{67}Cu(^{67}Zn)$ Mössbauer spectra of compounds characterized by single sites of copper atoms constituted quadrupole triplets; the spectra of compounds incorporating two copper sites represented a superposition of two quadrupole triplets.

The isomer shift ([I.S.]) in all of the spectra corresponds to $^{67}Zn^{2+}$ ions ([I.S.] ≈ 67–77 μm/s with respect to the spectrum of the ^{67}Ga-in-copper source). Therefore, it was assumed that parent ^{67}Cu atoms occupy copper sites during diffusion doping; hence, the $^{67}Zn^{2+}$ probe produced after ^{67}Cu decay is at copper sites as well.

The $^{67}Ga(^{67}Zn)$ Mössbauer spectra of $YBa_2Cu_3O_{6.9}$, $YBa_2Cu_3O_{6.6}$, $YBa_2Cu_4O_8$, and $La_{1.85}Ce_{0.15}CuO_4$ compounds represented quadrupole triplets whose [I.S.] corresponds to $^{67}Zn^{2+}$ ions ([I.S.] ≈ 100–107 μm/s). It was assumed that parent ^{67}Ga atoms occupy yttrium or lanthanum sites during diffusion doping; hence,

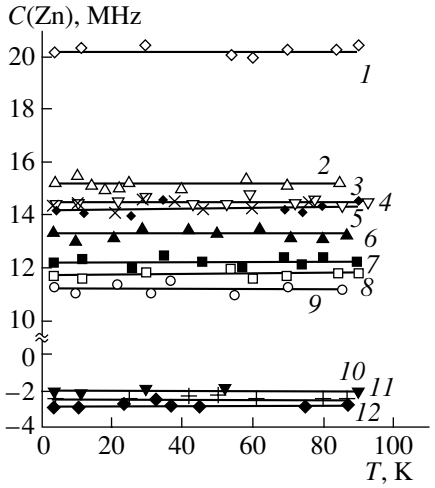

Fig. 1. Temperature dependences of the constants of the quadrupole interaction of $^{67}Zn^{2+}$ probe ions at the sites of (*1*) Cu(1) in $YBa_2Cu_3O_{6.9}$, (*2*) Cu in $Nd_{1.85}Ce_{0.15}CuO_4$, (*3*) Cu in $Tl_2Ba_2CaCu_2O_8$, (*4*) Cu(1) in $YBa_2Cu_4O_8$, (*5*) Cu in $HgBa_2CaCu_2O_6$, (*6*) Cu in $Bi_2Sr_2CaCu_2O_8$, (*7*) Cu(2) in $YBa_2Cu_4O_8$, (*8*) Cu(2) in $YBa_2Cu_3O_{6.9}$, (*9*) Cu in $La_{1.85}Ce_{0.15}CuO_4$, (*10*) Y in $YBa_2Cu_4O_8$, (*11*) Y in $YBa_2Cu_3O_{6.9}$, and (*12*) Y in $La_{1.85}Ce_{0.15}CuO_4$.

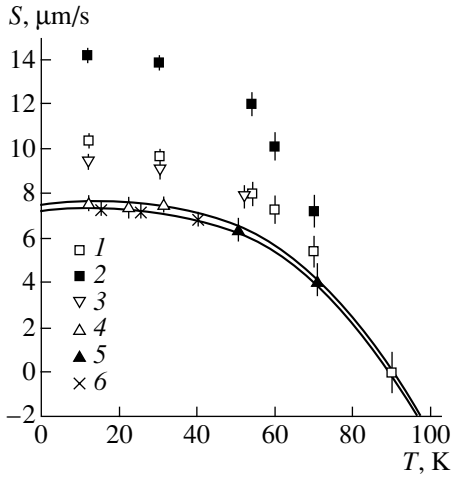

Fig. 2. Temperature dependences of the centroid *S* of the $^{67}Zn^{2+}$ Mössbauer spectra at the Cu(1) (*1*, *4*), Cu(2) (*2*, *5*), and Y (*3*, *6*) sites measured with respect to their values at 90 K for $YBa_2Cu_3O_{6.9}$ (*1*–*3*) and $YBa_2Cu_3O_{6.5}$ (*4*–*6*). The solid line is the temperature dependence of *S* calculated for the secon-order Doppler shift at $\theta = 420$ K.

$^{67}Zn^{2+}$ probe atoms produced after ^{67}Ga decay are at corresponding sites as well.

The quadrupole interaction constants *C* for $^{67}Zn^{2+}$ centers in both copper and yttrium (lanthanum) sites are virtually independent of temperature (see Fig. 1). This is explained by the fact that the electric field gradient in ^{67}Zn nuclei for Zn^{2+} probe ions is preferentially caused by lattice ions, and the changes in the lattice constants of the compounds under study are very small in the temperatures range of 4.2–90 K [2–6].

3. DISCUSSION

The temperature dependence of the centroid *S* of the ^{67}Zn Mössbauer spectrum at a fixed pressure *P* is given by (see [7])

$$(\delta S/\delta T)_P = (\delta[\text{I.S.}]/\delta \ln V)_T(\delta \ln V/\delta T)_P + (\delta D/\delta T)_P + (\delta([\text{I.S.}])/\delta T)_V. \quad (1)$$

The first term on the right-hand side of expression (1) accounts for the dependence of the [I.S.] on the volume *V*; it manifests itself at structural phase transitions. The second term represents the temperature dependence of the second-order Doppler shift *D* written in the Debye approximation as (see [7])

$$(\delta D/\delta T)_P = -(3k_0E_0/2Mc^2)F(T/\theta), \quad (2)$$

where k_0 is the Boltzmann constant, E_0 is the isomeric transition energy, *M* is the probe nucleus mass, *c* is the speed of light in free space, θ is the Debye temperature, and $F(T/\theta)$ is the Debye function. Finally, the third term in Eq. (1) describes the temperature dependence of the [I.S.]; it allows for a change in the electron density at Mössbauer nuclei, which is expected as the host converts to the superconducting state.

Typical dependences $S(T)$ for Cu(1), Cu(2), and Y sites in the $YBa_2Cu_3O_{6.9}$ lattice are shown in Fig. 2. It turns out that the temperature dependence of the spectrum centroid *S* measured with respect to its value at T_c for reference samples is adequately described by formula (2) in the temperature range of 10–90 K if one uses the Debye temperatures determine from specific heat measurements [8–11]. In other words, the [I.S.] changes due to both volume and temperature changes almost have no effect on the dependence $S(T)$ for non-superconducting samples. Since there are no structural phase transitions for the compounds under study in the temperature range of 10–90 K, this $S(T)$ run is quite expected.

The dependence $S(T)$ at $T > T_c$ for all of the superconducting samples is also described by a second-order Doppler shift (see formula (2)), and the Debye temperatures remain unchanged in comparison with reference samples. In the temperature range $T < T_c$, the quantity *S* depends more heavily on temperature than follows from formula (2), and both the second and third terms should be taken into account in expression (1). The latter describes the temperature dependence of the [I.S.].

For quantitative determination of [I.S.], we introduce the following quantities.

(i) The isomer shift $[\text{I.S.}]_T$ at a given temperature *T*, which is defined as $[\text{I.S.}]_T = S_T - D_T$ (where S_T and D_T are the spectrum centroid and Doppler shift at the temperature *T*).

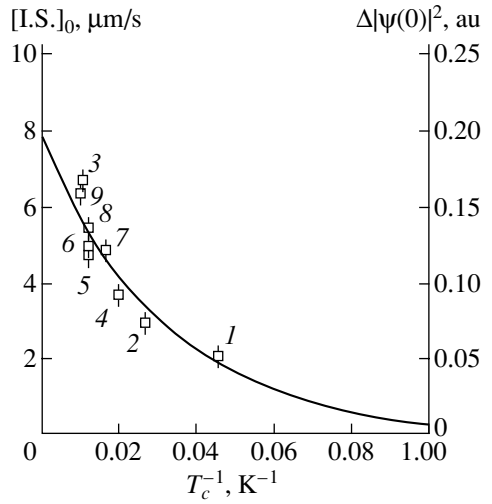

Fig. 3. Dependences of $[I.S.]_0$ and $\Delta|\Psi(0)|^2$ on T_c^{-1}. Squares are the data on (*1*) Cu in $Nd_{1.85}Ce_{0.15}CuO_4$, (*2*) Cu in $La_{1.85}Ce_{0.15}CuO_4$, (*3*) Cu(1) in $YBa_2Cu_3O_{6.9}$, (*4*) Cu(2) in $YBa_2Cu_3O_{6.6}$, (*5*) Cu(2) in $YBa_2Cu_4O_8$, (*6*) Cu in $Bi_2Sr_2CaCu_2O_8$, (*7*) Cu in $Tl_2Ba_2CaCu_2O_8$, (*8*) Cu in $HgBa_2CuO_4$, and (*9*) Cu in $HgBa_2CaCu_2O_6$.

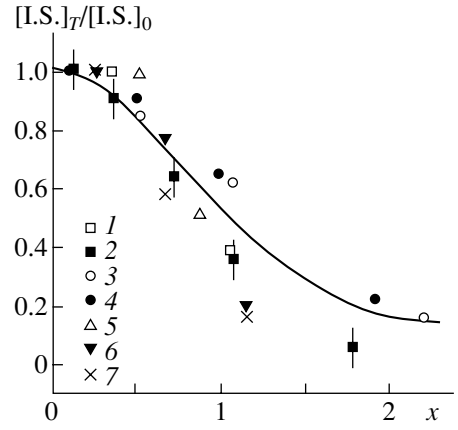

Fig. 4. Dependence of $[I.S.]_T/[I.S.]_0$ on the parameter $x = 1.76kT/\Delta$. The solid curve is the calculated dependence of the effective density of superfluid electrons on the parameter x. Symbols correspond to the data on (*1*) Cu in $Tl_2Ba_2CaCu_2O_8$, (*2*) Cu in $Bi_2Sr_2CaCu_2O_8$, (*3*) Cu in $HgBa_2CuO_4$, (*4*) Cu in $Hg_2Ba_2CaCu_2O_6$, (*5*) Cu in $Nd_{1.85}Ce_{0.15}CuO_4$, (*6*) Cu in $La_{1.85}Ce_{0.15}CuO_4$, and (*7*) Y in $La_{1.85}Ce_{0.15}CuO_4$.

(ii) The limiting value of the isomer shift [I.S.] at $T \longrightarrow 0$ K, determined as $[I.S.]_0 = S_0 - D_0$ (where S_0 and D_0 are the spectrum centroid and Doppler shift at $T \longrightarrow 0$ K).

We can see from Fig. 3 that $[I.S.]_0$ increases with the superconducting transition temperature of a compound. The value of $[I.S.]_0$ also depends on the site at which the Mössbauer probe is localized: the value is highest for Cu(2) sites, much lower for Cu(1) sites, and lowest for Y sites, if we compare the shifts for sites in the same lattice. For example, in the $YBa_2Cu_3O_{6.9}$ lattice, $[I.S.]_0$ = 6.6, 2.9, and 1.9 μm/s for Cu(2), Cu(1), and Y sites, respectively.

The isomer shift of the Mössbauer spectra is directly related to the change in the electron density of ^{67}Zn nuclei; the values of $[I.S.]_0$ characterize the electron density caused by the Bose condensate under conditions where all the conduction electrons have formed Cooper pairs. Figure 3 shows the dependence of $\Delta|\Psi(0)|^2$ on T_c^{-1}; the calibration of [12] was used in this case. The parameter $\Delta|\Psi(0)|^2 = |\Psi_c(0)|^2 - |\Psi_0(0)|^2$ increases with T_c, which indicates that the electron density at ^{67}Zn nuclei increases as a result of a superconducting transition. The quantities $|\Psi_0(0)|^2$ and $|\Psi_c(0)|^2$ are the electron densities at ^{67}Zn nuclei of the nonsuperconducting and superconducting phases, respectively.

The dependence of $\Delta|\Psi(0)|^2$ on T_c can be understood if it is taken into account that the standard correlation length ξ_0 (the Cooper pair "size" at $T \longrightarrow 0$ K) in the Bardeen–Cooper–Schrieffer (BCS) theory is defined as $\xi_0 \propto T_c^{-1}$. Thus, Fig. 3 displays the dependence of $[I.S.]_0$ and $\Delta|\Psi(0)|^2$ on T_c^{-1}, i.e., on the standard correlation length ξ_0. This dependence is exponential,

$$\Delta|\Psi(0)|^2(\text{au}) = 0.2(\text{au})\exp[(-31.4/T_c)].$$

It is evident that the greatest possible change in the electron density at ^{67}Zn nuclei during the superconducting transition is $\Delta|\Psi(0)|^2 = 0.2$ au, which corresponds to the smallest possible "size" $\xi_0^{\min}$ of the Cooper pair. The existence of such a minimum size is probably caused by the physical impossibility of a Cooper pair existing with the distance between components shorter than a certain critical length. Assuming the dependence of $\Delta|\Psi(0)|^2$ on ξ_0 to be linear, we find that $\xi_0^{\min} \approx 2.5$ Å, which conforms with the conventional values $\xi_0^{\min} \approx$ 0.5–30 Å [13].

We note that, if the Cooper pair "size" is large (significantly larger than the atomic scale), the change in the electron density at ^{67}Zn nuclei is insignificant and it is hardly possible to reliably observe a change in the electron density for materials with $T_c < 10$ K using ^{67}Zn spectroscopy.

Within the BCS theory, the temperature dependence $\rho(T)$ of the effective density of superfluid electrons can be determined [14]; at the same time, it would be expected that $\rho(T) \propto [I.S.]_T/[I.S.]_0$. Therefore, the theoretical dependence of ρ on the parameter $x = 1.76(k_0T/\Delta)$ is shown in Figs. 4 and 5 (where k_0 is the Boltzmann constant and Δ is the energy gap in the spectrum of elementary excitations of the superconductor,

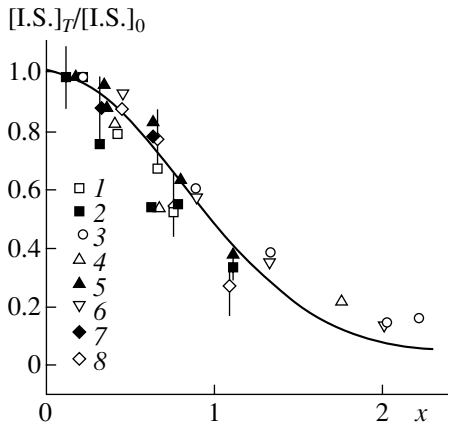

Fig. 5. Dependence of [I.S.]$_T$/[I.S.]$_0$ on the parameter $x = 1.76kT/\Delta$. The solid curve is the calculated dependence of the effective density of superfluid electrons on the parameter x. Symbols correspond to the data on (*1*) Cu(1) in $YBa_2Cu_3O_{6.6}$, (*2*) Cu(1) in $YBa_2Cu_3O_{6.9}$, (*3*) Cu(1) in $YBa_2Cu_4O_8$, (*4*) Cu(2) in $YBa_2Cu_3O_{6.6}$, (*5*) Cu(2) in $YBa_2Cu_3O_{6.9}$, (*6*) Cu(2) in $YBa_2Cu_4O_8$, (*7*) Y in $YBa_2Cu_3O_{6.9}$, and (*8*) Y in $YBa_2Cu_4O_8$.

taken from [14]) along with the data on the dependence of [I.S.]$_T$/[I.S.]$_0$ on the parameter x, which we measured for various compounds. Figures 4 and 5 show data on lattices containing a single-type sites and two structurally nonequivalent sites for copper atoms, respectively. We can see a satisfactory fit between the calculated and experimental temperature dependences of the effective density of superfluid electrons. Apparently, this agreement should be considered as evidence that the formation of Cooper pairs and their Bose condensation should necessarily be taken into account in any theory of high-temperature superconductivity. The special feature of the compounds presented in Fig. 5 lies in the fact that the values of [I.S.]$_0$ are found to be different for Cu(1), Cu(2), and Y sites. This is probably caused by the spatial nonuniformity of the electron density due to the Bose condensate of Cooper pairs. Nevertheless, satisfactory agreement between the calculated and experimental temperature dependences of the effective density of superfluid electrons has been found for Cu(1), Cu(2), and Y sites.

4. CONCLUSION

It was ascertained that the temperature dependence (at $T > T_c$) of the centroid S of the $^{67}Zn^{2+}$-probe Mössbauer spectrum is controlled by a second-order Doppler shift for $YBa_2Cu_3O_{6.6}$, $YBa_2Cu_3O_{6.9}$, $YBa_2Cu_4O_8$, $Nd_{1.85}Ce_{0.15}CuO_4$, $La_{1.85}Ce_{0.15}CuO_4$, $HgBa_2CuO_4$, $HgBa_2CaCu_2O_6$, $Bi_2Sr_2CaCu_2O_8$, and $Tl_2Ba_2CaCu_2O_8$ compounds. In the region $T < T_c$, the quantity S depends on the formation of Cooper pairs and their Bose condensation. In the case of $YBa_2Cu_3O_{6.6}$, $YBa_2Cu_3O_{6.9}$, and $YBa_2Cu_4O_8$ crystals containing two structurally nonequivalent sites for copper atoms, the change in the electron density, caused by the Bose condensation of Cooper pairs, was shown to be different for these sites, and for yttrium sites as well. The maximum change in the electron density was highest for Cu(2) sites, much lower for Cu(1) sites, and lowest for Y sites. The experimentally observed temperature dependence of the fraction of superconducting electrons satisfactorily agreed with a similar dependence following from the BCS theory for all of the Cu(1), Cu(2), and Y sites under study. A dependence between the change in the electron density at the metal crystal site and its superconducting transition temperature was found. In this case, the greatest possible change in the electron density exists at ^{67}Zn nuclei during the superconducting transition. It was assumed that this value corresponds to the smallest possible "size" of the Cooper pair, ~2.5 Å.

ACKNOWLEDGMENTS

This study was supported by the Russian Foundation for Basic Research, project no. 02-02-17306.

REFERENCES

1. N. P. Seregin and P. P. Seregin, Zh. Éksp. Teor. Fiz. **118**, 1421 (2000) [JETP **91**, 1230 (2000)].
2. J. Capponi, C. Chaillout, A. Hewat, *et al.*, Europhys. Lett. **3**, 1301 (1987).
3. E. Kaldis, P. Fischer, A. W. Hewat, *et al.*, Physica C (Amsterdam) **159**, 668 (1989).
4. O. Chmaissem, Q. Huang, S. N. Putilin, *et al.*, Physica C (Amsterdam) **212**, 259 (1993).
5. E. V. Antipov, J. J. Capponi, C. Chaillout, *et al.*, Physica C (Amsterdam) **218**, 348 (1993).
6. J. M. Tarascon, W. R. McKinnon, P. Barboux, *et al.*, Phys. Rev. B **38**, 8885 (1988).
7. D. L. Nagy, in *Mössbauer Spectroscopy of Frozen Solutions*, Ed. by A. Vértes and D. L. Nagy (Akadémiai Kiado, Budapest, 1990; Mir, Moscow, 1998).
8. T. Sasaki, N. Kobayashi, O. Nakatsu, *et al.*, Physica C (Amsterdam) **153–155**, 1012 (1988).
9. H. M. Ledbetter, S. A. Kim, and R. B. Goldfarb, Phys. Rev. B **39**, 9689 (1989).
10. A. Junod, T. Craf, D. Sánchez, *et al.*, Physica C (Amsterdam) **165–166**, 1335 (1990).
11. S. J. Collocott, R. Driver, C. Audrikidis, and F. Pavese, Physica C (Amsterdam) **156**, 292 (1989).
12. A. Svane and E. Antoncik, Phys. Rev. B **34**, 1944 (1986).
13. *Physical Properties of High Temperature Superconductors*, Ed. by D. M. Ginsberg (World Sci., Singapore, 1989; Mir, Moscow, 1990).
14. J. R. Schrieffer, *Theory of Superconductivity* (Benjamin, New York, 1964; Nauka, Moscow, 1970).

Translated by A. Kazantsev

Semiconductors, Vol. 37, No. 7, 2003, pp. 807–815. Translated from Fizika i Tekhnika Poluprovodnikov, Vol. 37, No. 7, 2003, pp. 835–843.

CONFERENCE. AMORPHOUS, VITREOUS, AND POROUS SEMICONDUCTORS

Organic Materials for Photovoltaic and Light-Emitting Devices

T. A. Yourre*, L. I. Rudaya*, N. V. Klimova*, and V. V. Shamanin**

**St. Petersburg State Technological Institute (Technical University), St. Petersburg, 198013 Russia*
e-mail: rudi@mail.avmgroup.ru
***Institute of Macromolecular Compounds, Russian Academy of Sciences, St. Petersburg, 199004 Russia*
Submitted December 23, 2002; accepted for publication December 27, 2002

Abstract—Materials for organic photovoltaic cells and light-emitting devices are reviewed. Dye-sensitized systems represent the most studied of these materials as they offer high efficiency of photoelectric energy conversion. Systems demonstrating efficient luminescence were identified; they are based on conjugated polymers, complexes of rare-earth elements with organic ligands, and dyes. To achieve efficient photoelectric conversion, different types of sensitizing dyes will be tested. Phthalocyanines and pentacenes are of special interest. Phthalocyanines are the most promising materials: they are easily synthesized and nontoxic, and their electric characteristics are widely investigated. Harnessing the unique electron-acceptor properties of the C_{60} molecule, one can attain considerable enhancement in the efficiency of solar-energy conversion into electricity. Organic photovoltaic cells are often made on the basis of aromatic and heterocyclic polymers—poly(*p*-phenylene-vinylene), polyanilines, polypyrroles, and polythiophenes. Organic photoconducting materials offer high photosensitivity and low dark current. They are readily available and can be easily deposited on a substrate, which make them suitable for the fabrication of relatively cheap photovoltaic cells. © *2003 MAIK "Nauka/Interperiodica".*

Photoconducting organic materials of a very diversified chemical nature are currently being used for the fabrication of photovoltaic systems. The goal of the numerous researchers working in the still immature scientific field of chemical photonics is the creation of ordered molecular assemblies, built around aromatic and heteroaromatic compounds with electron-donor and electron-acceptor properties, capable of forming charge-transfer complexes (CTCs) that strongly absorb ultraviolet, visible, and infrared radiation. It is these assemblies that form the basis for the materials of molecular electronics, photovoltaic units, and phototransducers with good electrical and optical characteristics and long service life.

Conformationally nonrigid heteroaromatic systems, where photochemical and photophysical processes are related to photoinduced structural changes, form the basis of "intelligent" or "smart" molecular assemblies with the properties of bistability used for information storage and processing. In these systems, general electronic properties typical of molecules with C–X groups (where X stands for O, N, S, etc.) combine advantageously with high structural stability, which is clearly manifested in the formation of the spectral, luminescent, and photochemical properties.

In a supramolecular assembly, molecules of different types form an integral *D*–π–*A* system (here, *D* is an electron-rich donor, π is a conjugated polymer or oligomer, and *A* is an electron acceptor).

Among light-induced processes, photosynthesis is the one most important for all living species—including humans—and a perfect supramolecular assembly is involved here. Photosynthesis is based on the chlorophyll molecule (**I**). Chlorophyll is a derivative of aromatic porphyrin and includes conjugated five-member pyrrole rings with substituents in β-positions and Mg as the complexing agent.

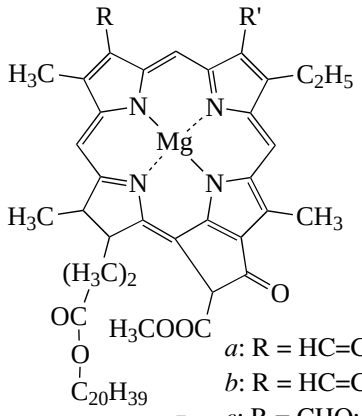

a: R = HC=CH$_2$; R' = CH$_3$
b: R = HC=CH$_2$; R' = CHO
c: R = CHO; R' = CH$_3$

I

Through a number of intermediate stages, chlorophyll molecules are organized into rather complex formations called chloroplasts. These are ordered formation aggregated in diskotics that are anisotropic and amorphous at the same time. Thus, an ordered supramolecular assembly is responsible for the efficiency of photosynthesis in all higher plants. In natural materials, the light-absorbing substance is incorporated in a layered polymer matrix, which to a large extent determines its properties. The oxidation of a chemically active photoexcited chlorophyll molecule and initiation of the chain of oxidation–reduction reactions is made possible due to the localization of the pigment in the ordered lipid–protein matrix. Native chlorophyll aggregates, where oxidation takes place, are considered in the literature as semiconductors. It is believed that the charge in the conduction band migrates to the acceptor

or donor electron-capture centers, where dissociation of oppositely charged carriers occurs.

Photosynthesis is remotely imitated in the systems suggested by Graetzel [1]. Mesocrystalline or nanocrystalline oxides (Ti, Sn, and Zn oxides etc.) are used to form thin-film electrodes, and the bipyridine complex of Ru (**II**) is used as a sensitizer. The band gap of TiO_2, which does not absorb visible light, is 3.2 eV. TiO_2 layers act as biological lipid membranes. Electrons are transferred from photoexcited complexes to effective electron acceptors, i.e., oxide particles.

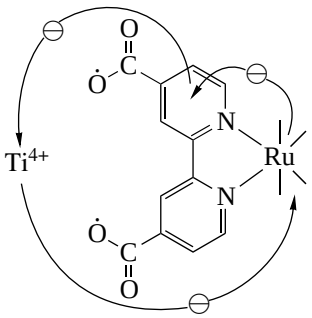

II

Mesocrystalline or nanocrystalline oxides (such as Ti and Zn oxides) are used to form thin-film electrodes that are self-organized into cubic arrangements. These systems are sensitized with bipyridine complexes of Ru (**II**). Electrons are transferred from photoexcited complexes, where organic ligands act as antennas, to oxide particles, which are effective electron acceptors. The photovoltaic and electrical characteristics of these systems are quite good: the short-circuit current I_{sc} = 18.3 mA/cm^2, the open-circuit voltage V_{oc} = 0.72 V, the filling factor FF = 0.73, and the quantum efficiency η = 10%. An oligomer variant of this design is also suggested; here, Ru polypyridine complexes are linked by ethynyl bridges to achieve better delocalization of electrons [2].

Ruthenium bipyridine complexes bonded chemically to polymers of the polystyrene structure were used to demonstrate stabilization of *n*-GaAs photoanodes, with the conversion efficiency of the photoelectrochemical solar cell being 12%. Such a polymer system should possess weak adhesion bonds. Nevertheless, a solid-state heterojunction in sensitized solar cells was patented in 2002 by the Graetzel team [3].

The application of photoconductive polymers in photovoltaics is the most attractive area of organic material research. Reviews [4–8] describe the properties of the main classes of polymers in use; for each of them, data on the band gap and the highest conductivity attained upon doping are given. The mechanisms of conductivity in novel organic polymers of the fourth generation are discussed in the reviews by Nobel laureates MacDiarmid [7] and Heeger [8].

A breakthrough in the field of conducting polymers was associated with the use of polyacetylene, which became renowned throughout the world due to the studies performed by Shirakawa. It was demonstrated that the soliton mechanism is responsible for the conductivity in this material, whose basic advantage is the significant delocalization of π electrons along the macromolecule [5].

Among various photoconductive polymers, polypyrrole (PPy) (**III**) and its derivatives are of special interest due to their high conductivity, stability in the oxidized state, and interesting redox properties. These materials are also attractive due to their simplicity and easy availability of corresponding pyrrole monomers. PPy is obtained through the polymerization of pyrrole [6]. There are chemical and electrochemical methods for its synthesis. Among all five-member aromatic heterocycles, nature chose pyrrole to build the "pigments of life"—chlorophyll and hemoglobin—along with other vitally important supramolecular structures (miscellaneous porphyrins, prodigiosines, vitamin B_{12}, etc.).

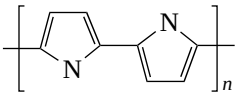

III

The conductivity of the starting polyconjugated polymer (**III**) is 10^{-10}–10^{-5} S/cm; doping results in the metallic or semiconducting conductivity ranging from 1 to 10^5 S/cm.

Studies of the origin of the electronic conduction in PPy indicated that neutral undoped PPy is an insulator with a band gap of 4 eV. Upon oxidation, a shift of the band edges occurs and the band gap decreases to $\lesssim$2.5 eV; i.e., the material becomes a semiconductor. Polarons (cation radicals) and bipolarons (dications) are usually spread over three–four monomeric units of the PPy polymer chain [8].

The choice of the anionic dopant (I_2, $FeCl_3$, etc.) is dictated by the requirements imposed on the properties of the polymer. The presence of hydrophobic anions leads to a lowered sensitivity of the PPy to moisture. In the presence of optically active anions (e.g., (±)-camphorsulfonic acid), the polymer also becomes optically active. To obtain flexible and smooth films that can be easily detached from the electrode, organic anions are used. Doping with aromatic and surface-active sulfonates provides for higher conductivity and stability of the polymer [6].

Polythiophene and its derivatives are popular photoconductive polymers with a very narrow band gap, from 1.0–1.2 eV to 0.58 eV. True enough, the band gap of condensed polypyrroles is still lower and amounts to 0.38 eV. Unlike other conductive polymers, PPy is used as a coating which prevents the passivation of the electrode surface. Simultaneously, PPy serves as a hole-transport layer. Systems of this design were developed on the basis of GaAs, CdS, and CdSe [6].

Polyanilines still attract interest in industry; this is due to the relative simplicity in synthesizing them, their low cost, and their stability under exposure to air. The conductivity of these materials can be efficiently increased by doping.

The fullerene (Fu) molecule proved to be a unique acceptor in supramolecular assemblies used in the design of photovoltaic cells. Its large size and spherical shape, as well as pyramidization of carbon atoms, causes high electron affinity. In photoexcited polymer–Fu composites, electron transfer to Fu occurs in less than 10^{-12} s; the formation of an excited complex with a subsequent transition to a state with separated charge carriers takes place [9].

In π-electron-rich polymers with conjugated bonds in the main chain and conjugated aromatic and heteroaromatic rings in the side chain (containing arylamino groups) charge carriers are generated upon irradiation. Currently, much attention is attracted to polyphenylenevinylenes (PPV) and their analogues, homopolymers and conjoint polymers (**IV–VI**) [10]. PPV derivatives are used as transport and emitting layers; depending on the substituents, emission—photoluminescence (PL) and electroluminescence (EL)—in the green and blue regions of the spectrum can be obtained. For example, in PPV, changing the substituents in the benzene rings leads to a shift of the EL peak wavelength by almost 80 nm [9].

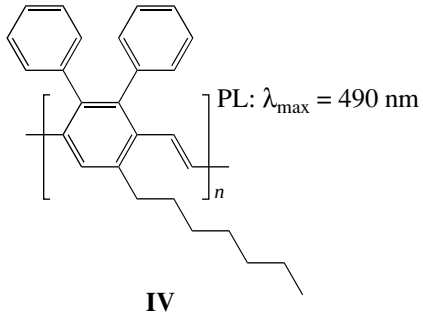

IV

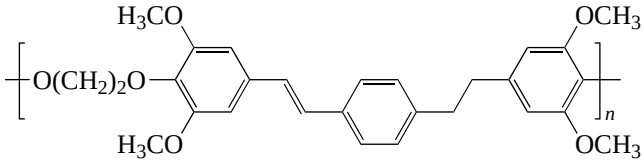

PL: λ_{max} = 464 nm

V

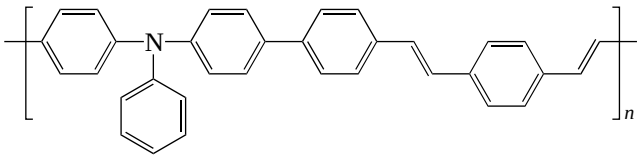

PL: λ_{max} = 550 nm; EL: λ_{max} = 600 nm

VI

In polymers with structure **IV**, intense luminescence in the green spectral region is observed, with a peak wavelength λ_{max} = 490 nm [11]. A thin film of soluble prepolymer is deposited and polymerized in vacuum, which results in the green EL.

The lasing properties of the chloroform-soluble conjugated polymer **V** were studied by Liu *et al.* [12]. The third harmonic of an Nd laser was used as a pump light. Stimulated emission with a linewidth of 15 nm was observed in the blue region, λ_{max} = 450 nm. The maximum power of the laser radiation was 40 kW, and the conversion efficiency reached 3.4%.

In 2000, polymers of structure **VI**, exhibiting blue EL, were suggested; their thermal stability is related to the presence of the triarylamino fragment. They feature high-brightness emission. The energy of the highest occupied molecular orbital is equal to 5.4 eV, which indicates that a sandwich light-emitting diode (LED) structure with a low barrier for holes can be formed if this polymer is used as an active layer. The maximum current density is 140 mA/cm^2 at 20 V [13].

A number of conjugated polymers with EL from the blue to the infrared spectral regions were suggested by researchers from Hoechst AG [4]. In LEDs based on these materials, a brightness of $\gtrsim$1000 cd/m^2 at <3 V and an emission duration >5000 h were obtained. Because of the poor solubility of high–molecular substances, one has to use oligomers with a much lower molecular mass; however, in this case, a hypsochromic shift of the peak luminescence wavelength takes place. In this respect, the use of spiro-6-paraphenylenes (**VII**) seems to be of particular interest [4].

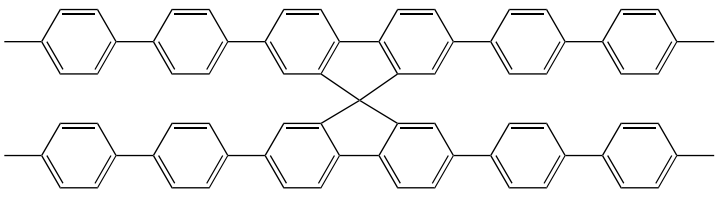

VII

A team from Cavendish Laboratory (Cambridge) used polymers with PPV segments containing nitrile groups; mixtures of compounds **VIII** and **IX** with CdSe nanocrystals of different sizes (3.3, 4.0, and 2.5 nm) were studied.

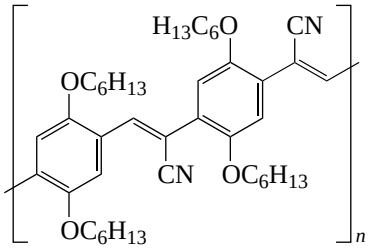

VIII

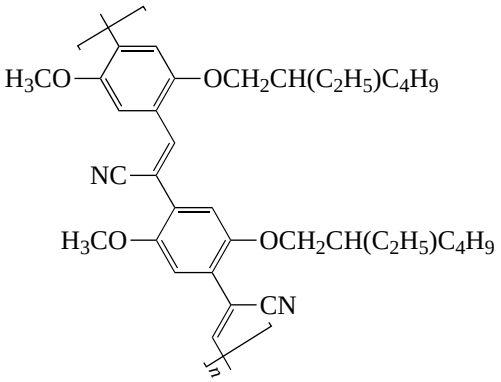

IX

Efficient charge separation was attained and high-intensity PL was observed [14]. The company Cambridge Display Technology announced that, in 2002, it will present a full-color display based on this kind of PPV polymer with CN substituents [15].

In 1991, Ohmory and coworkers suggested using polymers containing a fluorene fragment (**X**) as the luminescent layers in LEDs [16]. These systems exhibit blue luminescence with λ_{max} = 470 nm. Five years later, the same team fabricated a three-layer LED with red and blue emission [17].

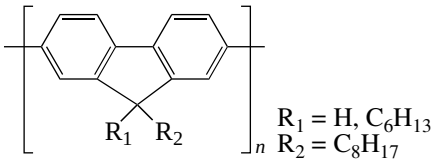

X

In 1987 in Austria, Tasch and his coworkers proposed a white-light LED based on a mixture of a polymer having a very rigid fluorene structure and a perylene oligomer [18]. In Cambridge, Millard and coworkers developed a material also based on polyfluorenes with monomeric units providing for emission variability. Its performance is quite good: a high stability of white-light emission is achieved, the emission persists at 70–80°C, and the operation lifetime is 1000 h. The design has commercial potential [19].

The fluorene macromolecule network is three-dimensional, which impedes molecule rotation around the chain axis. The higher degree of crystallinity leads to an enhancement in the charge transport due to higher uniformity in chromophore unit spacing and increased overlap between them.

In 2000, Fletcher and coworkers reported on a system where the hole-transport layer is combined with fluorene [20]. Based on this design, Dow Chemical Co., Midland, developed green-emission diodes with a brightness in excess of 25000 cd/m^2; under a pulsed voltage of 100 V, the peak brightness was as high as 2000000 cd/m^2.

After PPV—the first polymer that found extensive use in LEDs—interest was drawn to poly(9,9-dioctylfluorene), which is capable of blue emission with a fluorescence quantum yield of 45% in the solid state. The brightness of the EL with λ_{max} = 436 nm is 0.25 cd/m^2 and 600 cd/m^2 in a device [21].

In another design variant, the transport amine layer is combined with perylene fragments; in this way, red luminescence (λ_{max} = 580 nm) with a brightness of 4800–8700 cd/m^2 is obtained [22]. The use of substituted perylene derivatives provides for intense red emission. Columnar liquid-crystal derivatives of perylene (**XI**, **XII**) find applications as hole-transport layers (for electron-rich perylenes) and electron-transport layers (for electron-deficient perylenes).

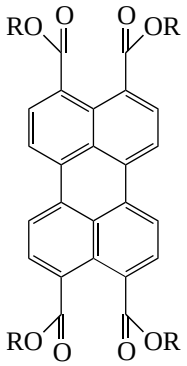

XI

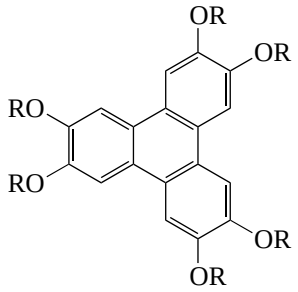

XII

Both derivatives are liquid crystals at room temperature and can be used in LEDs [23]. Columnar liquid crystals or the columnar crystal phase of diskotics based on aromatic compounds represent very good charge-transport media due to their π-electron system, which is enhanced by electron-rich alkoxy substituents. Most of them exhibit high-intensity fluorescence; owing to this, two-layer LEDs based on perylene-tetracarboxylate and hexabutoxy-triphenylene were developed by the research centers at the universities of Toulouse and Bordeaux. The peak wavelength of the PL is λ_{max} = 620 nm, and the band width is 80 nm.

The choice of material is determined by two factors. First, it is convenient that the hexagonal columnar crystal phase has a melting point at 244°C, with isotropism appearing at 313°C. Second, short-chain perylene possesses high conductivity. In combination with aluminum tris(hydroxyquinolinate) (**XIII**) (Alq_3), perylene serves as both emitter and electron-transport layer; the EL brightness is 15 cd/m^2 at 0.03 A/cm^2 and 30 V. The luminescence intensity remains unchanged for 18 h of operation and drops twice during the next 22 h. The characteristics of these LEDs are comparable to those of conventional LEDs based on Alq_3 and diamines [23].

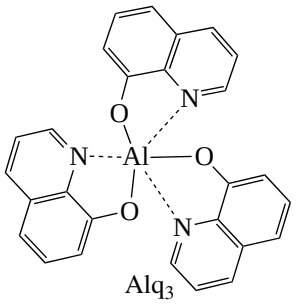

XIII

Polyheteroarylenes are polymers with high photosensitivity; the presence of an unshared pair of electrons at the nitrogen atom is favorable for deep collectivization of π-conjugated bonds. The conductivity equals 10^{-10}–10^{-13} S/cm. The photosensitivity does not depend on the length of the molecular chain; however, it does depend on the degree of ordering in a supramolecular structure and increases by an order of magnitude upon the transition from the amorphous to the crystalline state.

Polyimides are characterized by a combination of photovoltaic properties with good electrical and mechanical parameters. Their photosemiconductor properties are determined by donor–acceptor interactions between the structural elements of polyimide chain—diimide fragments and arylene groups. In aromatic polyimides, whose chains contain alternating electron–acceptor diimide fragments and electron-donor arylene fragments, interchain donor–acceptor interaction between these structural elements takes place with the formation of a kind of a charge-transfer complex (CTC); the luminescence originates from charge-transfer excited states (exciplexes), which have the same nature as the CTC excited state [24]. The electroluminescent and transport properties of nonconjugated anthracene-containing polymers are reported in [25].

Continuing their study of this polymer [26], researchers from the Karpov Institute of Physical Chemistry in collaboration with the Napier University in Edinburgh demonstrated the existence of effective EL in single-layer LEDs upon incorporation of nanocrystalline *J* aggregates of carbocyanine dyes into the polymer layer. *J* aggregates play an important role in charge transport in composites. It was shown that a very narrow emission line appears in the red and infrared spectral regions. LEDs based on rigid perylene mesogens are excited by a He–Ne laser [27]. The He–Ne laser radiation is not absorbed by the layer of Alq_3 (**XIII**), but its spectral position coincides with the short-wave length absorption band of the perylene mesogen at 1.85 eV and with the shoulder of the main band at 2.3 eV. The emitting layer is formed by Alq_3 (**XIII**); typical EL can be observed even one week after irradiation. The diodes can be used in optical memory units or in liquid-crystal displays.

In aromatic molecules, π–π* is the only type of orbital overlap, which causes low mobility of the charge carriers. In organometallic and coordination compounds, *d*–*d* and *d*–σ orbital overlap can prove important. However, it is difficult to obtain infinite chains of metal atoms in organometallic complexes with aromatic ligands. The "thickness" of an aromatic molecule is just 3.4 Å, and strong bonds between the metal atoms cannot form when such molecules are arranged in a crystal. When ligands such as quinoline and imidazole are used, collectivization of the electron cores takes place due to *d*–π orbital overlap and the geometric restrictions are relaxed [28].

White-light luminescence was obtained by Gao and coworkers from Hong Kong in the following system [29]: ITO/HTL/Tb(acac)$_3$phen/Mg:Ag (here, "acac" stands for acetyl acetonate and "phen" stands for phenanthroline). The hole-transport layer (HTL) incorporated a mixture of poly(*N*-vinylcarbazole) and aryldiamines in different proportions, which had some effect on the EL spectrum.

Multilayer structures incorporating complexes of Tb, Eu, and Al with organic ligands exhibit intense luminescence, the brightness being up to 90 cd/m^2 under 14 V voltage. It is a rather low value in comparison with other white-emission systems, where a brightness of 2000–4000 cd/m^2 was achieved. One study [30] relates this to the possibility of the formation of exciplexes between a Tb complex and a tetraphenyldiamine (TPD) derivative, which results in a lowered quantum efficiency of the luminescence. Three discrete peaks were observed in the luminescence spectrum at 410–420, 545, and 615 nm, which correspond to TPD, Tb, and Eu complexes, respectively.

The Tb complex acts both as an electron-transport layer and emitting layer with green luminescence; in addition, its function is to prevent recombination of electrons and holes, which may occur in the hole-transport layer [30].

A breakthrough in the attained EL brightness occurred when structures utilizing green electrophosphorescence of tris(2-phenylpyridine) iridium were developed. A material with intense green luminescence was proposed by researchers at Princeton University. Tris(2-phenylpyridine)Ir complexes are used to dope the host matrix formed by 4,4'-dicarbazolediphenyl. The host itself exhibits blue luminescence with λ_{max} =

Table 1. Electroluminescent characteristics of complexes with heteroaromatic ligands

Complex	λ_{max}, nm	Color	Brightness, cd/m^2
$Zn(ODZ)_2$	449	Blue	11000 (18 V)
$Zn(TDZ)_2$	508	Blue-green	4020 (12 V)
$Zn(PhPy)_2$	485	Green-blue	11450 (15 V)
$Zn(BIZ)_2$	447	Blue	4100 (13 V)
$Alpq_3$	550	Yellow	26000 (14 V)
$Al(ODZ)_3$	447	Blue	3500 (18 V)

Note: $Zn(ODZ)_2$ stands for bis[2-phenyl-4(2-hydroxyphenyl)oxdiazolate]Zn; $Zn(TDZ)_2$ stands for bis[2-phenyl-4(2-hydroxyphenyl)thiadiazolate]Zn; $Zn(PhPy)_2$ stands for bis[(2,2'-hydroxyphenyl)pyridinate]Zn; $Zn(BIZ)_2$ stands for bis[*N*-phenyl-2(2-hydroxyphenyl)benzimidazolate]Zn; $Al(ODZ)_3$ stands for tris[2-phenyl-4(2-hydroxyphenyl)oxdiazolate]Al; and $Alpq_3$ stands for tris(2-hydroxy-5-phenylquinolinato)Al.

400 nm, and the Ir complex exhibits green luminescence. This system has an efficiency of 8% (26 cd/A, 19 lm/W at 4.3 V voltage). It is believed [31] that these high values arise due to the process of energy transfer from singlet *S** and triplet *T** excited states of the host to the Ir complex followed by efficient intramolecular radiative transitions. The short time of the phosphorescence of the Ir complex (<1 μs) limits source saturation at high conductivity. The barrier layer is formed by TPD. At the peak of emission, the brightness can be as high as 100000 cd/m^2 [31].

A number of novel benzoxazole and benzthiazole complexes of Al and Zn exhibiting strong luminescence from the yellow to blue-green regions (see Table 1) were studied at the Toyota Laboratories [32].

LEDs with polycyclic ligands exhibit blue luminescence with a quantum efficiency of 1.5–1.7% and a brightness of 300 cd/m^2 upon perylene doping. In the case of yellow luminescence, the quantum efficiency is lower than 0.8%. Layers incorporating $Zn(ODZ)_2$, $Al(ODZ)_3$, and $Zn(BIZ)_2$ demonstrate pure blue emission peaked at about 450 nm; the layers of $Zn(PhPy)_2$ and $Zn(TDZ)_2$ demonstrate green-blue and blue-green emission peaked at 485 and 508 nm, respectively. This observation indicates that structural changes affect electroluminescent properties. The newly synthesized $Alpq_3$ complexes (in which ligands are formed by phenyl substituted hydroxyquinolines) have less intense and less stable emission than Alq_3. Only for $Alpq_3$ does the EL duration exceed 500 h; in all other cases, it is only 5–10 h [32].

Low-molecular complexes of rare-earth elements with organic ligands are well suited for the fabrication of LEDs with red, green, and blue luminescence. Mixtures of these provide for bright white-light emission. The Alq_3 complex has found the most widespread application: it is incorporated both in low-molecular layers and in polymer composites (e.g., those with PPV).

A number of condensed aromatic and heteroaromatic compounds used in LEDs and solar cells incorporate 9-alkylfluoren and 9,9-dialkylfluoren, rubrene, pentacene, perylenes, coumarin, and derivatives of phenazines and thiazines. Dye-sensitized photovoltaic cells are quite promising at the moment, as are the subjects of a wide range of research and development efforts.

Variants of solar cells and LEDs based on the dye–redox system were developed at Jadavpur University in Calcutta [33]. Different dyes—derivatives of thiazines, phenazines, xanthenes, acridines, and triarylmethanes—were examined. Their photoelectrochemical parameters were investigated, and the feasibility of applying phenazine dyes in solar cells was demonstrated. The same team has shown that mixtures of dyes, phenosafranine (PSF) and methylene blue (thiazine derivative) or PSF and fluorescein acridine orange (a xanthene dye), have a considerably higher efficiency than individual dyes (see Table 2) [34]. Semitransparent SnO_2, In_2O_5, and ZnO electrodes were used.

The development of photovoltaic systems based on electron-rich phthalocyanines (Pc) (**XIV**) is now being widely carried out [35]. These compounds are ecologically safe, cheap, and easily synthesized; and their electrical properties are far from being fully exploited; this circumstance points to the potential for considerably broader use of these materials in electronics and for increased efficiency in future R&D products.

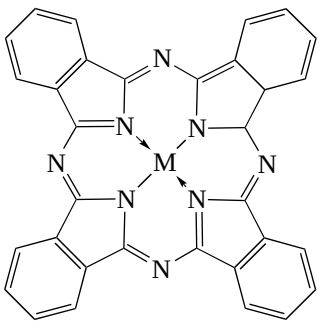

M = Cu, Ni, Co, Si, Ge

XIV

Metallocyanines are molecular crystals whose allowed energy bands have a small width (on the order of the thermal energy *kT*). They have been widely developed in recent years. Numerous phthalocyanines (Pc) used in photovoltaic cells incorporate cations of Cu, Co, Ni, Pd, VO, TiO, etc. The efficiency of the energy conversion in Pc is rather low; it depends strongly on the method used for the formation of layers with effective electron acceptors and on doping (see Table 3). As dopants, I_2 and tetracyanoquinonedimethane were described.

Two-layer $PcCu/C_{60}$ systems for solar batteries demonstrated a very high conversion efficiency η = 3.6%, with I_{sc} = 13 mA/cm^2, V_{oc} = 0.53 V, and FF = 0.52; the highest quantum efficiency, η = 18%, is

Table 2. Performance of the solar cells

Layer	V_{os}, mV	I_{sc}, μA	FF	P, μW/cm^2	η, 10^{-2}%
PSF	600	26.00	0.41	7.61	2.54
MB	425	7.92	0.64	1.79	0.10
AO	4	–	–	–	–
PSF + AO	685	24.00	0.33	9.04	4.50
PSF + MB	665	22.75	0.32	6.05	3.02

Note: PSF stands for phenosafranine, MB stands for methylene blue, and AO stands for acridine orange; η is the conversion efficiency; and P is the effective power.

Table 3. Performance of the solar cells incorporating macrocycles

Solar-cell structure	I_{sc}, μA/cm^2	V_{oc}, V	η, %	FF	Comments
Al/C_{60}/OEP/OOPPV/ITO	1.4	0.15	0.01	0.3	ITO side
	1.1	0.35	6	–	Al side
TiO_2/H_2Pc/NiPc	0.56	0.24	0.02	0.64	–
Al/CuPc/ITO	0.25	0.4	9	–	–
Al/CuPc/ITO	0.25	0.4	–	–	Ion implantation
SnO_2/CuPc/BP/Ag	0.5	0.47	0.66	–	White light
SnO_2/CuPc/BP/Ag	0.21	0.47	0.33	0.19	–

Note: OEP stands for octaethylporphin, OOPPV stands for poly(2,5dioctyloxy-*p*-phenylenevinylene), and BP stands for perylene Bordeaux.

attained at 620 nm. Fullerene C_{60} acts as an acceptor and serves as the electron transport layer [36].

Electroluminescent diodes containing substituted Pc were fabricated by vacuum deposition at the University of Tübingen. The peak position and the relative intensity of the luminescence are given in [37].

A type of bridge macrocyclic complexes is represented by cofacial poly(phthalocyanato)metallooxanes [PcMO]*n* (**XV**) (here, M = Si, Ge, or Sn). Their conductivity increases greatly upon stoichiometric doping with I_2. In recent years, conjugated ladder polymer systems were created on the basis of Pc.

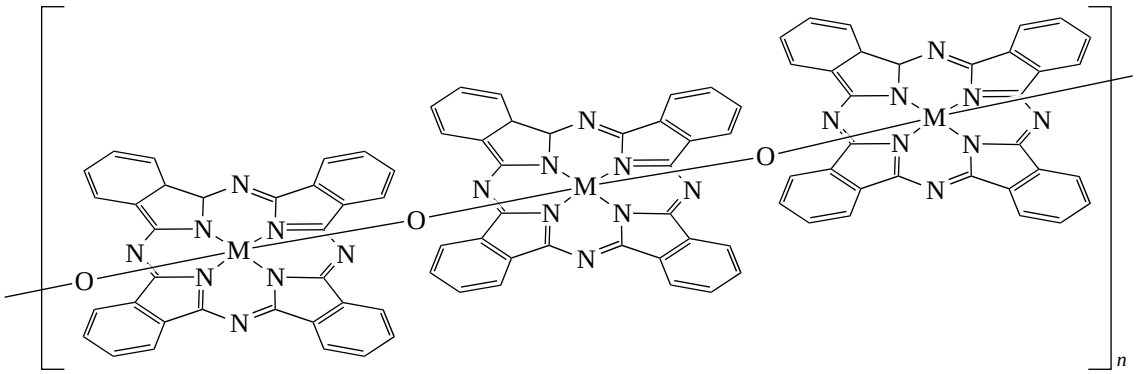

XV

It is conceivable that systems with efficient charge generation, separation, and transfer can be built around cofacial Pc, and this attracts interest to this class of materials [38]. The molecular structure of cofacial Pc has a core with C_2 symmetry and a planar Pc ring around this core. The Si–Si spacing is 3.32 Å (or 3.14 Å according to our own results). The Si–O–Si angle is 179°; the angle of the ring rotation (oscillation), which is close to that in PcNi and is very sensitive to the distance between the rings and the substituents, equals 36.6° (39.6°). The calculated value of the ionization potential of Si(Pc)(OR_2) agrees well with that determined exper-

imentally (6.8N and 6.46N, respectively). These results confirm that charge transport in [Si(Pc)O]*n* polymer occurs mainly via the π system of Pc and the contribution of polarons is of little importance [38]. In the case of metallomacrocyclic conductors with cofacial arrangement, a good transport layer may be formed by liquid-crystal oligomers or polymers with conjugated reactive mesogens [39].

As a variant, layers can be composed from *V*- or *T*-shape oligomers with a rigid aromatic triad containing a 2,5-benzophenone (**XVI**) or 3,4-benzophenone group at the center of the monomeric unit [40]; these oligomers have high photochemical activity, transparency, and capability for light-induced texture changes [41, 42].

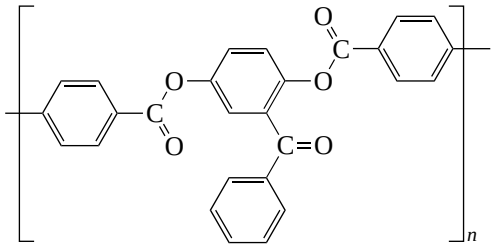

XVI

CONCLUSION

The application of photoconductive organic materials in photovoltaics has been widely investigated in recent years. However, the attractiveness of this approach is offset by the instability of the proposed organic materials, the difficulties in producing them, and problems in predicting the effect of doping on electrical characteristics.

The creation of high-efficiency solar cells based on organic composites requires (i) a modern approach to polymer synthesis (at the stages of both monomer synthesis and polymerization) and polymer design, and (ii) high precision in the selection of all elements of the complex organic composite system, with respect to their chemical nature (taking account donor–acceptor interactions) and optimization of the quantitative proportions between the polymer and the low-molecular complexes.

The possibility of choosing supramolecular assemblies combining several different types of molecules, which have the potential capability to function as microprocessors, along with the convenience in combining inorganic and organic components in one system, is responsible for the ongoing interest in using organic materials in photovoltaic devices.

The diversity of available molecular assemblies, the lack of a unified view of the energy structure of each system component, and the unordered nature of polymer matrices are factors preventing rapid progress towards favorable results. Research in the field of molecular electronics and nanotechnology is mainly directed at the creation of novel molecular systems for the accumulation of light and electric energy and the development of nanomaterials for LEDs. Almost every new study leads to an understanding of certain previously unknown properties and the development of methods for increasing the efficiency of LEDs and for organizing ordered states of matter—in particular, imitating the processes occurring in living species. It is conceivable that the utilization of organic photoconductive molecular materials will become one of the important means in the effort to overcome the energy crisis.

REFERENCES

1. M. Graetzel, in *Proceedings of 6th Sede Boquar Symposium on Solar Electricity Production* (1994), p. 32.
2. A. C. Benniston, V. Grosshenny, A. Harriman, and R. Liessel, Angew. Chem. **106**, 1956 (1994).
3. M. Graetzel, R. Plass, and U. Bach, Eur. Pat. Appl. EP 1.176.646 (cl H01L 51/20) 30.01.2002, Appl. 2000/810,681, 28.07.2000.
4. H. Sixl, H. Schenk, and N. Yu, Phys. Bl **54**, 225 (1998).
5. H. Shirakawa, Curr. Appl. Phys. **1**, 281 (2001).
6. T. V. Vernitskaya and O. M. Efimov, Usp. Khim. **66**, 489 (1997).
7. A. G. MacDiarmid, Curr. Appl. Phys. **1**, 269 (2001).
8. A. J. Heeger, Curr. Appl. Phys. **1**, 247 (2001).
9. K. Feldrapp, W. Brutting, M. Schwoerer, *et al.*, Synth. Met. **101**, 156 (1999).
10. C. J. Brabec, Monatsh. Chem. **132**, 421 (2001).
11. R. H. Bing, W. Ch. Wan, J. Yu, *et al.*, Macromolecules **31**, 631 (1998).
12. X. Y. Liu, S. M. Wang, L. J. Wang, *et al.*, Synth. Met. **111–112**, 571 (2000).
13. Xue Minzhao, Deyin Huang, and J. Lin, Synth. Met. **110**, 203 (2000).
14. D. S. Ginger and N. C. Greenham, Synth. Met. **104**, 425 (1999).
15. LEP-Monitors are Cheaper and Better. LCD Came to the End?, http://www.Membrana.ru/articles/technic 10.04.2002.
16. J. Ohmori, M. Uchida, and K. Muro, Jpn. J. Appl. Phys. **30** (11B), 1941 (1991).
17. J. Ohmori, N. Tada, and M. Yoshida, Appl. Phys. **29**, 2983 (1996).
18. S. Tasch, E. J. W. List, and O. Ekstrom, Appl. Phys. Lett. **71**, 2883 (1997).
19. I. S. Millard, Synth. Met. **111–112**, 119 (2000).
20. R. B. Fletcher, D. G. Lidzey, and D. D. C. Bradley, Synth. Met. **111–112**, 151 (2000).
21. L. C. Palilis, D. G. Lidzey, and M. Redecker, Synth. Met. **111–112**, 159 (2000).
22. S. Toguchi, J. Morioka, and H. Ischikawa, Synth. Met. **111–112**, 57 (2000).
23. I. Seguy, P. Destruel, and H. Bock, Synth. Met. **111–112**, 15 (2000).
24. G. V. Kapustin, V. Zh. Tilika, V. I. Berendyaev, *et al.*, Vysokomol. Soedin., Ser. B **30**, 653 (1988).

25. E. J. Mal'tsev, M. A. Brusentsova, D. A. Lypenko, *et al.*, Polym. Adv. Technol. **11**, 323 (2000).
26. E. J. Mal'tsev, D. A. Lypenko, and B. I. Shapiro, Appl. Phys. Lett. **75**, 1896 (1998).
27. M. Cölle and T. Tsutsui, Synth. Met. **111–112**, 95 (2000).
28. J. Simon and J.-J. Andre, *Molecular Semiconductors* (Springer, Berlin, 1985; Mir, Moscow, 1988).
29. Z. Q. Gao, C. S. Lee, L. Bello, and S. T. Lee, Synth. Met. **111–112**, 34 (2000).
30. J. Kido, W. Ikeda, and M. Kimura, Jpn. J. Appl. Phys., Part 2 **35** (38), L394 (1996).
31. M. A. Baldo, S. Lamansky, P. E. Burreus, *et al.*, Appl. Phys. Lett. **75**, 4 (1999).
32. Sh. Tokito, K. Noda, and H. Tanaka, Synth. Met. **111–112**, 393 (2000).
33. A. K. Jana, J. Photochem. Photobiol. A **123**, 1 (2000).
34. A. K. Jana and B. B. Bhowmik, J. Photochem. Photobiol. A **122**, 53 (1999).
35. T. A. Yourre, L. I. Rudaya, and N. V. Klimova, in *Polymers, Phosphors and Voltaics for Radioisotope Microbatteries*, Ed. by K. E. Bower *et al.* (CRC Press, New York, 2002), Chap. 9, p. 389.
36. J. Nelson, Solid State Mater. Sci. **6** (1), 20 (2002).
37. M. Ottmor, D. Hohnholz, and A. Wede, Synth. Met. **105**, 145 (1999).
38. E. Giliberto, K. A. Doris, and W. J. Pietro, J. Am. Chem. Soc. **106**, 7784 (1984).
39. A. Bacher, P. G. Bentley, and P. A. Glarvey, Synth. Met. **111–112**, 413 (2000).
40. M. N. Bol'shakov, L. I. Rudaya, N. V. Klimova, *et al.*, Zh. Org. Khim. **38** (10), 1591 (2002).
41. T. A. Yurre, L. I. Rudaya, and N. V. Klimova, Zh. Nauchn. Prikl. Fotogr. **47** (2), 14 (2002).
42. S. S. Skorokhodov, S. S. Bogolyubova, L. I. Rudaya, *et al.*, Zh. Prikl. Khim. (St. Petersburg) **73**, 268 (2000).

Translated by M. Skorikov

Semiconductors, Vol. 37, No. 7, 2003, pp. 816–817. Translated from Fizika i Tekhnika Poluprovodnikov, Vol. 37, No. 7, 2003, pp. 844–845.

CONFERENCE. AMORPHOUS, VITREOUS, AND POROUS SEMICONDUCTORS

Optical and Electrical Properties of Polyamide Acid and Metal–Polymer Complex Based on Terbium

É. A. Lebedev*, M. Ya. Goikhman, M. E. Kompan*, V. Kh. Kudoyarova*, I. V. Podeshvo**, E. I. Terukov*, and V. V. Kudryavtsev****

**Ioffe Physicotechnical Institute, Russian Academy of Sciences, St. Petersburg, 194021 Russia*

***Institute of Macromolecular Compounds, Russian Academy of Sciences, St. Petersburg, 199004 Russia*

Submitted December 23, 2002; accepted for publication December 27, 2002

Abstract—The basic optical and electrical properties of polyamide acid and its complex with Tb^{+2} have been studied. The occurrence of room-temperature photoluminescence (PL) with an emission peak at 520 nm is established. The activation energy of conductivity at temperatures above 350 K is 2.1 eV. Polyamide acid is comparable in PL intensity with an electroluminescent polymer, poly(*p*-phenylvinylene). © *2003 MAIK "Nauka/Interperiodica".*

Recently, electroluminescence from organic polymers have found increasingly wide and effective application. The best studied electroluminescent materials are polymers with conjugated bonds, poly(*p*-phenylvinylene) (PPV) and its derivatives [1]. Of interest is the search for other polymeric materials possessing a set of properties required for the effective use of these materials in optoelectronics. In particular, of interest are materials for creating hybrid organic–inorganic optoelectronic devices. The promise of this approach has already been demonstrated by examples of luminescence from erbium ions in a polymeric matrix [2] or emission from semiconductor quantum dots incorporated in an electroluminescent structure based on organic semiconductors [3].

With the above in mind, the study of optical and electrical properties of polyamide acid (PAA) and a metal–polymer complex based on Tb^{+2} (PAA + Tb^{+2}) was undertaken. PAA and (PAA + Tb^{+2}) polymers, polyamide acids with imide and biquinolyl units in their main chain (which are denoted by indices *n* and *m* in Fig. 1), are soluble, hydrolytically stable materials which can be used to obtain transparent films. These films possess good strength and deformational properties and thermal stability at temperatures up to 180°C. The presence of biquinolyl units in the main chain allows

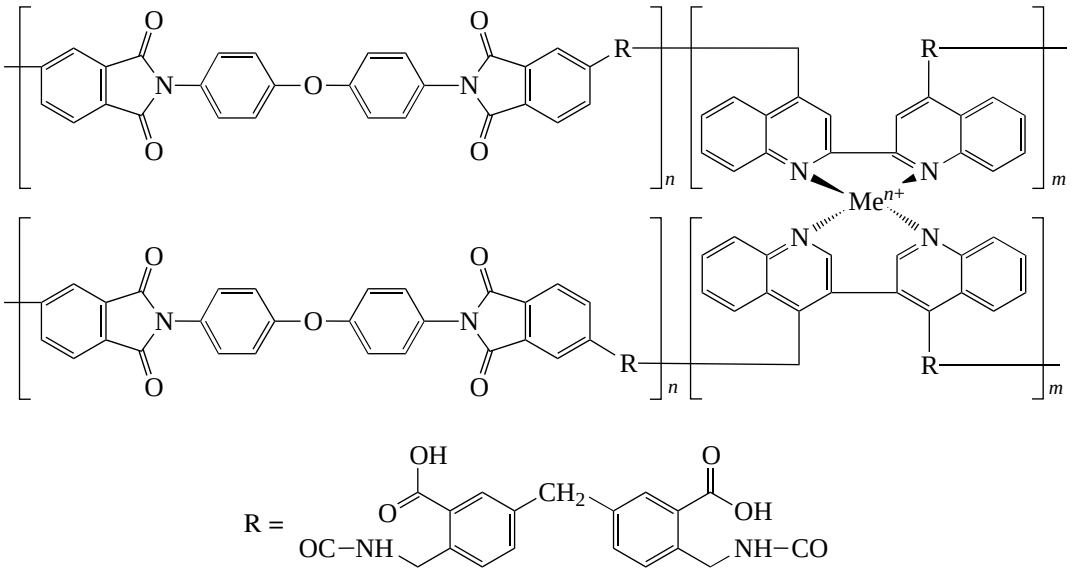

Fig. 1. Structural formula of the metal–polymer complex of polyamide acid.

1063-7826/03/3707-0816$24.00 © 2003 MAIK "Nauka/Interperiodica"

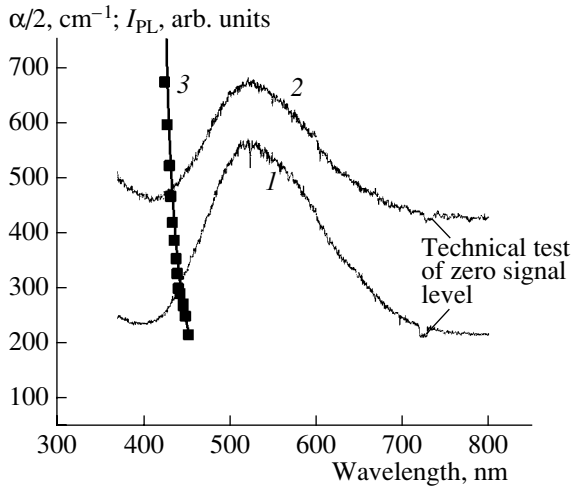

Fig. 2. PL spectra of (*1*) the terbium complex of polyamide acid (PAA + Tb^{+2}) and (*2*) polyamide acid (PAA), and also (*3*) the optical absorption spectrum of (PAA + Tb^{+2}).

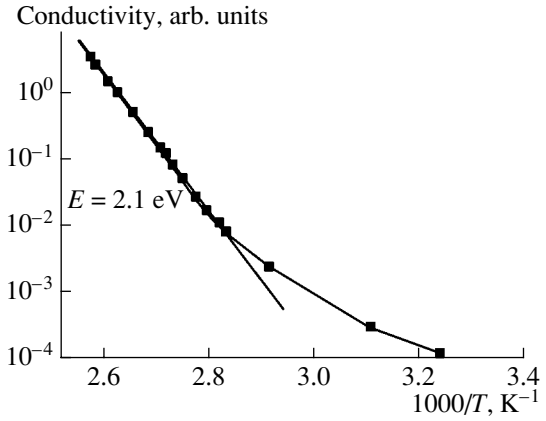

Fig. 3. Temperature dependence of conductivity for the terbium complex of polyamide acid (PAA + Tb^{+2}).

these polymers to form stable soluble complexes with transition metals (general formula is shown in Fig. 1).

The presence of sufficiently long segments with conjugated bonds and the high degree of π-hybridization of orbitals give reason to expect that electrical conduction and effective luminescence will be observed.

On being heated to 180–250°C, the polymers undergo cyclization, being converted into high-strength nonbrittle polybenzoxazinonimides [4]. The polymer solution obtained was used to deposit films by casting on glass substrates, after which the films were subjected to drying at 100°C to constant weight. The thickness of the films was in the range of 20–40 μm.

The following basic electrical and optical characteristics of the material were determined: absorption spectrum in the visible range, PL spectra, electrical conductivity at room temperature, and temperature dependence of conductivity.

The results obtained in studying the optical properties of PAA and (PAA + Tb^{+2}) are summarized in Fig. 2. The study of the long-wavelength optical absorption edge demonstrated that the absorption coefficient (α) changes by an order of magnitude, from 10^3 to 10^2 cm^{-1}, in the approximate wavelength range 410–450 nm (curve *3*), which corresponds to photon energies of 3 to 2.75 eV. On introduction of terbium, the absorption spectrum of the material shifts noticeably to longer wavelengths.

The PL from PAA and (PA + Tb^{+2}) was observed during excitation with 337-nm light. The PL intensity (I_{PL}) was on the same order of magnitude as that for films of the standard photoluminescent material PPV (recorded under identical conditions). The PL spectra, which are peaked at 520 nm (2.4 eV), are shown in Fig. 2. The PL peak positions virtually coincide with the wavelength of the PL peak for PPV. As in the case of PPV, the luminescence spectrum observed lies at much lower energies than the absorption edge [5, 6]. The metal–polymer complex (PAA + Tb^{+2}) shows no characteristic bands of terbium PL. The absence of intrinsic terbium luminescence can be attributed to insufficient electronegativity of the environment of the terbium ion in the metal–polymer complex.

The dark conductivity of PAA and (PAA + Tb^{+2}) is low: ~10^{-13} Ω^{-1} cm^{-1} at room temperature (T = 300 K). Figure 3 shows the temperature dependence of the electrical conductivity of this material. It can be seen that the conductivity is characterized by a constant activation energy (~2.1 eV) in a wide range of temperatures, from 350 to 400 K.

Since the material used in organic electroluminescent devices is in the form of thin films and a high current density is ensured by carrier injection from the contacts, the relatively low dark conductivity of the material is not an obstacle to its application in optoelectronic devices.

REFERENCES

1. J. H. Burroughes, D. D. C. Bradley, A. R. Brown, *et al.*, Nature **347**, 539 (1990).
2. S. I. Klink, G. A. Hebbink, L. Grave, *et al.*, J. Appl. Phys. **86**, 1181 (1981).
3. S. Coe, W.-K. Woo, M. Bawendi, and V. Bulovec, Nature **420**, 8003 (2002).
4. I. V. Podeshvo, M. Ya. Goĭkhman, E. L. Aleksandrova, *et al.*, in *Abstracts of 10th International Conference on Synthesis and Study of Properties, Modifications and Treatment of High-Molecular Compounds* (Kazan, 2001), p. 96.
5. M. Herold, J. Gmeiner, C. Drummer, and M. Schwoerer, J. Mater. Sci. **32**, 5709 (1997).
6. S. Barth, H. Bassler, H. Rost, and H. H. Horhold, Phys. Rev. B **56**, 3844 (1997).

Translated by M. Tagirdzhanov

Semiconductors, Vol. 37, No. 7, 2003, pp. 818–820. Translated from Fizika i Tekhnika Poluprovodnikov, Vol. 37, No. 7, 2003, pp. 846–848.

CONFERENCE. AMORPHOUS, VITREOUS, AND POROUS SEMICONDUCTORS

Photosensitivity of New Photoconductive Polymers Based on Ruthenium–Biquinolyl Complexes

E. L. Aleksandrova, M. Ya. Goĭkhman, I. V. Podeshvo, I. V. Gofman, and V. V. Kudryavtsev

Institute for High-Molecular Compounds, Russian Academy of Sciences, St. Petersburg, 199004 Russia

Submitted December 23, 2002; accepted for publication December 27, 2002

Abstract—A set of new metal–polymer complexes has been synthesized on the basis of polymers containing biquinolyl units in the main chain and $Ru(bPy_2)Cl_2$. The spectral and mechanical properties of these complexes were studied, as well as their photosensitivity in the temperature range from 20 to 150°C. It was shown that the photosensitivity of synthesized polymers is 2×10^4 cm^2 J^{-1} and the quantum yield of carrier photogeneration is $\eta = 0.025$. © *2003 MAIK "Nauka/Interperiodica".*

1. INTRODUCTION

In the context of the promising application of polymer–metal complexes (the possibility of implementing new physical principles for data recording and storing; the photoconductivity, self-assembly, and self-organization of polymer structures; etc.), much attention has been given to the synthesis of new polymers which allow functionalization of polymer matrices by transition-metal ions.

From the viewpoint of various physical applications, the most attractive are metal–polymer complexes based on divalent ruthenium. They feature a unique combination of chemical stability, redox properties, luminescence, and a long lifetime of the excited state [1]. Recording materials produced on the basis of such complexes are characterized by nonlinear optical and photorefractive properties (the optical yield is 200 cm^{-1} at the field $E = 0$, the quantum efficiency is 0.2% at $E = 10^6$ V cm^{-1}, the diffraction efficiency is ~1% [2]); high resolution, which is characteristic of molecular media; high carrier mobilities (~10^{-5} cm^2/(V s) [3]); and photosensitivity (~3×10^4 cm^2/J [4]). Concerning fabrication of electroluminescence devices [3], recording media based on metal–polymer complexes have a rather high luminescence efficiency (luminous emittance) at relatively low operating potentials.

In our opinion, it is of interest to obtain metal–polymer complexes on the basis of polymer matrices, featuring high thermal stability. Such complexes are characterized by the presence of biquinolyl units in the structure of thermostable polymers. As an object of study, we took polybenzoxazinoneimides, since (as shown previously [5]) these polymers exhibit a unique combination of hydrolytic stability of prepolymers and thermal stability of corresponding products of their cyclization.

2. EXPERIMENTAL

The objects of study were soluble metal–polymer complexes **I** (see Figs. 1a, 1c) produced by the interaction between polyamide acid **II** (PAA) and $Ru(bPy_2)Cl_2$ (where bPy is 2,2'-bipyridyl) in *N*-methylpyrrolidone (the method referred to as "assembling") (see Figs. 1b, 1c).

PAA containing biquinolyl units in its main chain was synthesized on the basis of 2,2'-biquinolyl-4,4'-dicarboxylic acid dichlorides, *N*,*N*-diphenyloxide-bis-(trimethylimido) acid, and methylene-bis-anthranil acid by low-temperature polycondensation.

The synthesis of 2,2'-biquinolyl-4,4'-dicarboxylic acid was carried out using the Pfitzinger reaction from isatin and acetoin (see [6]). The synthesis of *N*,*N*-diphenyloxide-bis-(trimethylimido) acid is described in [5]. The synthesis of dicarboxylic acid dichlorides, $Ru(bPy_2)Cl_2$ complex, and PAA was performed according to the procedures described in [5], [7], and [4], respectively. PAA–$Ru(bPy_2)Cl_2$ complex was synthesized at 190°C in *N*-methyl pyrrolidone according to [8]. The polymer solutions obtained were poured onto glass substrates to form films, which were dried at 80°C up to a contrast mass. The thickness of films designed for measuring the mechanical properties and photosensitivity was 30–40 μm and 1–3 μm, respectively.

The technique for studying the photosensitive properties included measurement of the spectra of the photosensitivity $S_{0.1}$ and the quantum yield of carrier photogeneration η. The photosensitivity $S_{0.1}$ was determined by such a criterion as the reduction of the surface potential by 10% of the initial value. The measurements were carried out in the electrophotographic mode in the spectral range of 400–800 nm under electric fields of 10^4–10^6 V cm^{-1} using the technique [4]. The thermalization length r_t and the quantum yield η_0 of bound-pair formation were determined by the field-dependence slope within the Onsager model.

1063-7826/03/3707-0818$24.00

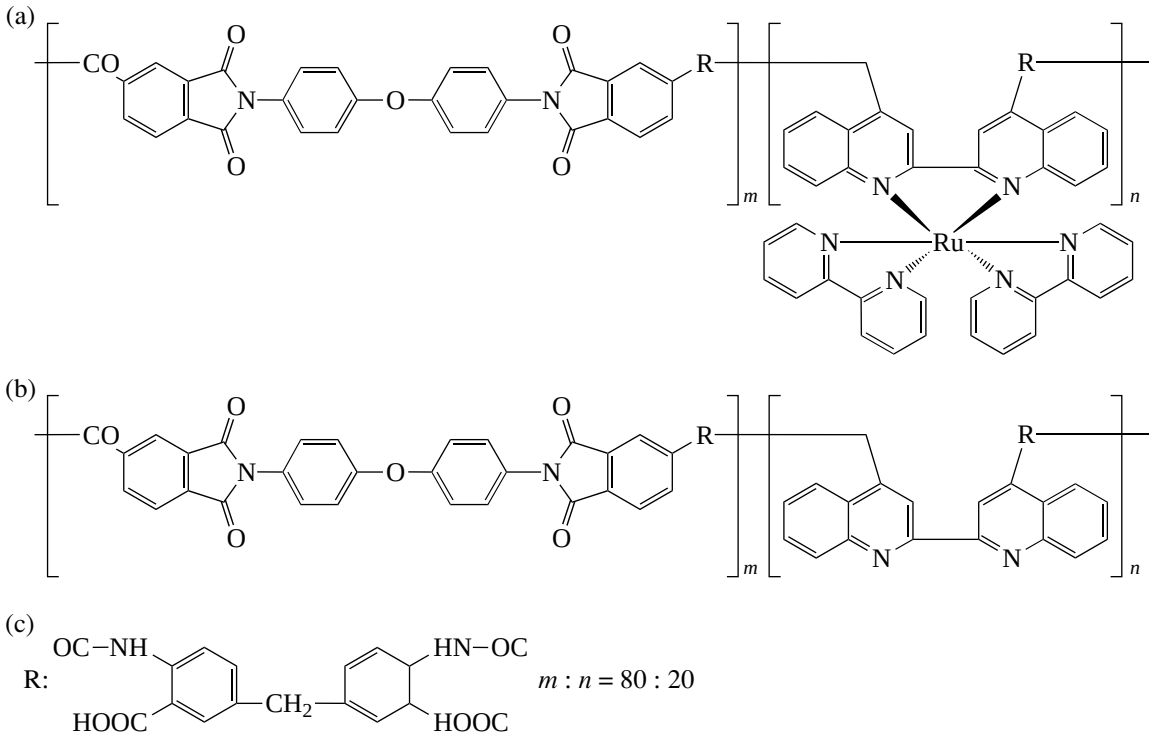

Fig. 1. (a) Metal–polymer complex **I**, (b) polyamide acid **II**, and (c) fragment *R* in Figs. 1a, 1b.

The mechanical characteristics of the films of metal–polymer complexes were measured using the technique [5].

3. RESULTS AND DISCUSSION

All of the synthesized polymers are characterized by rather good deformation–strength properties (E = 2.8–3.2 GPa, σ_p = 95–110 MPa, ε_p up to 20%). The presence of ruthenium has almost no effect on the mechanical properties of films. It is noteworthy that some decrease in the elastic modulus of metal–polymer complexes is observed, which is explained by the screening of hydrogen bonds by $Ru(bPy)_2^{2+}$ volume units.

Figure 2 shows the absorption spectra of synthesized model compounds: complexes of bivalent ruthenium with bipyridyl $Ru(bPy_2)Cl_2$, with bipyridyl and 2,2'-biquinolyl-4,4'-dicarboxylic acid (bqa) $Ru(bPy_2)Cl_2$; metal–polymer complex **I**; and the initial compounds: (bqa) and polymer **II**.

We can see from the spectra that polymer **I** (curve *4*) and bqa (curve *2*) virtually do not absorb in the range of 400–700 nm. The spectrum of the low-molecular complex $Ru(bPy_2)Cl_2$ (curve *1*) contains two intense peaks at 360 and 520 nm. The latter peak is caused by the metal-to-ligand charge transfer (referred to as MLCT [1]). The spectrum of $Ru(bPy)_2(bqa)Cl_2$ (curve *3*) has a similar shape, but its peaks are shifted to longer waves, which is caused by the influence of the biquinolyl ligand itself and its carboxyl groups. The spectrum of PAA + $Ru(bPy_2)Cl_2$ (curve *5*) exhibits a broad peak in the range of 470–560 nm, which indicates the formation of metal–polymer complex **II**.

Figure 3 shows the photosensitivity spectra of the synthesized materials. We can see that photosensitivity increases by almost an order of magnitude (curve *2*) in the case of ruthenium complex formation in comparison with the initial polymer (curve *1*) and is equal to

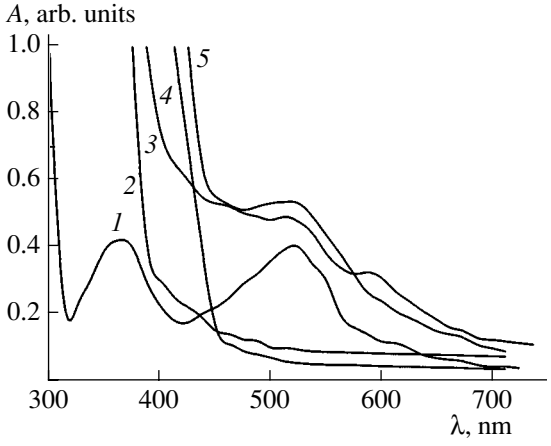

Fig. 2. Absorption spectra of the synthesized compounds: (*1*) $Ru(bPy_2)Cl_2$, (*2*) 2,2'-biquinolyl-4,4'-dicarboxylic acid (bqa), (*3*) $Ru(bPy)_2(bqa)Cl_2$, (*4*) polyamide acid (PAA), and (*5*) PAA + $Ru(bPy_2)Cl_2$.

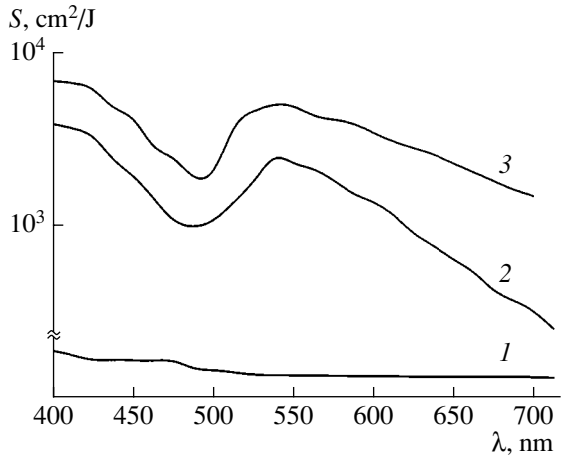

Fig. 3. Photosensitivity spectra of synthesized polymers: (*1*) PAA, (*2*) PAA + $Ru(bPy_2)Cl_2$, and (*3*) PAA + $Ru(bPy_2)Cl_2$ + fullerene.

2×10^4 cm^2 J^{-1}. In the case of incorporation of fullerene (a sensitizer increasing the electron mobility) into the metal–polymer complex, the photosensitivity further increases by a factor of 2–3 (curve *3*) in comparison with the complex without fullerene. The most significant increase is observed in the long-wave length spectral region. The quantum yield of carrier photogeneration η of the metal–polymer complex is constant within the absorption band and is equal to 0.025, which is somewhat lower than that of similar biquinolyl complexes with Cu [4]. The quantum yield of bound-pair formation is $\eta_0 = 0.06$, and the thermalization length r_t is 3.0 nm. This value is comparable to the value of r_t for complexes with copper. In the case of metal–polymer complexes with fullerene admixture, η is higher than that of complexes without fullerene by a factor of 1.5. Thermal treatment of the polymeric materials under study (heating up to 150°C) does not decrease their photosensitivity.

4. CONCLUSIONS

(i) New polyamide acids with biquinolyl units in the main chain and their complexes with $Ru(bPy_2)Cl_2$ have been synthesized. Their mechanical and physical properties were studied.

(ii) It was shown that the synthesized metal–polymer complexes are characterized by a rather high photosensitivity, which can be significantly increased by fullerene sensitization.

(iii) The developed method opens up wide opportunities for synthesizing metal–polymer complexes, which may be of practical importance for producing photoconductive systems.

REFERENCES

1. A. Juris, Coord. Chem. Rev. **84**, 85 (1988).
2. Z. Pend and A. R. Charavi, Appl. Phys. Lett. **69**, 4002 (1996).
3. Sze Chit Yu and Xiong Gong, Macromolecules **31**, 5639 (1998).
4. E. L. Aleksandrova, M. Ya. Goĭkhman, I. V. Podeshvo, and V. V. Kudryavtsev, Opt. Zh. **68** (11), 67 (2001) [J. Opt. Technol. **68**, 849 (2001)].
5. M. Ya. Goĭkhman, I. V. Gofman, L. Yu. Tikhonova, and V. V. Kudryavtsev, Vysokomol. Soedin., Ser. A **39** (2), 197 (1997).
6. S. D. Lesesne and H. R. Henze, J. Am. Chem. Soc. **64**, 1897 (1942).
7. B. P. Sullivan and T. J. Meyer, Inorg. Chem. **17**, 2211 (1987).
8. P. Belser and A. Zelewesky, Helv. Chim. Acta **63** (6), 176 (1980).

Translated by A. Kazantsev

Semiconductors, Vol. 37, No. 7, 2003, pp. 821–824. Translated from Fizika i Tekhnika Poluprovodnikov, Vol. 37, No. 7, 2003, pp. 849–852.

CONFERENCE. AMORPHOUS, VITREOUS, AND POROUS SEMICONDUCTORS

Optical and Photosensitive Properties of Comb-Shaped Polyamide-Imides

E. L. Aleksandrova, M. Ya. Goĭkhman, L. I. Subbotina, K. A. Romashkova, I. F. Gofman, V. V. Kudryavtsev, and A. V. Yakimanskiĭ

Institute for High-Molecular Compounds, Russian Academy of Sciences, St. Petersburg, 199004 Russia

Submitted December 23, 2002; accepted for publication December 27, 2002

Abstract—A new method for modifying polymers with side carboxyl groups by glycidyl ethers of hydroxyl-containing azobenzene dyes has been developed. The spectral, thermomechanical, and photosensitive properties of dye-modified polyamide-imides have been studied as a function of the dye content in a polymer. The films of polymers under study were shown to be almost transparent at wavelengths above 500 nm. The mobility of side chromophore groups is rather high, which makes these polymers promising for nonlinear optical applications. The polymers are characterized by a photosensitivity of 10^3–10^4 cm^2 J^{-1}, which can be significantly increased by doping with diphenylamide molecules, which transport charge carriers. © *2003 MAIK "Nauka/Interperiodica".*

1. INTRODUCTION

The development of polymers characterized by nonlinear optical properties is an urgent problem in the chemistry of polymers, since such materials play a decisive role in solving the fundamental problem of interaction between laser radiation and matter, during which the characteristics of the incident laser radiation change [1]. Among thermostable heterocyclic polymers used as matrices for photosensitive materials, polyamide-imides (PAI) have attracted attention. These polymers are widely used in microelectronics due to their solubility in amide solvents, as well as their rather good physicomechanical, thermal, and insulating properties [2, 3]. The possibility of introducing various functional groups characterized by rather high dipole moments μ_e in the excited state into the side chain, as well as optical homogeneity and transparency, make PAIs promising for new optical technologies, in particular, for the fabrication of photosensitive and nonlinear optical (NLO) media.

In this study, we investigated the optical properties of newly synthesized comb-shaped PAIs produced by etherification of carboxyl-containing PAIs by a glycidyl ether of an azo dye. Such dyes are characterized by efficient charge transport in the excited state, as well as by high values of μ_e.

2. EXPERIMENTAL

The studies were carried out using modified PAIs differing in main-chain rigidity. The modification was carried out according to the following schematic diagram:

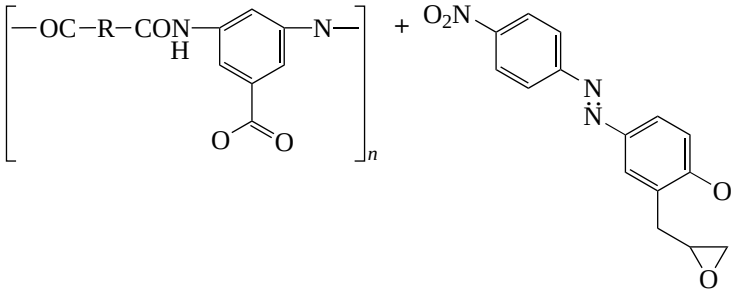

1063-7826/03/3707-0821$24.00 © 2003 MAIK "Nauka/Interperiodica"

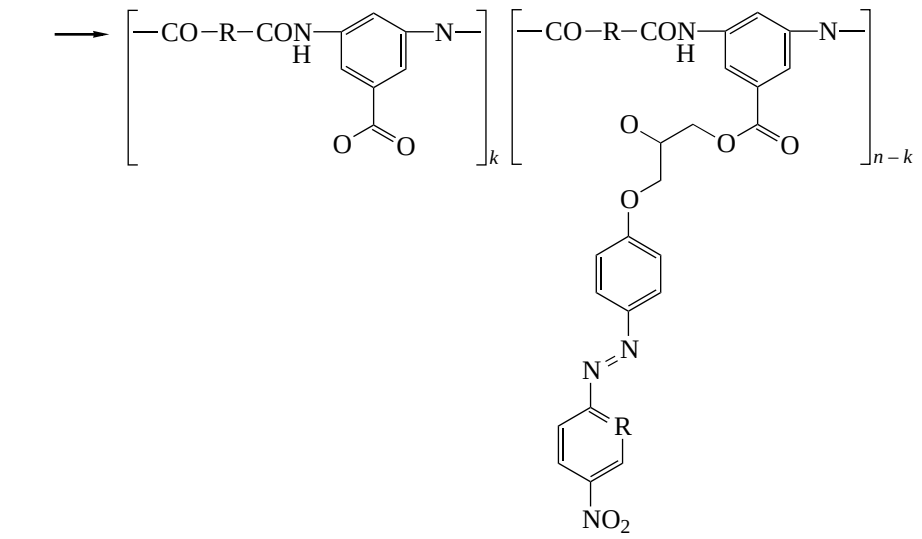

R = 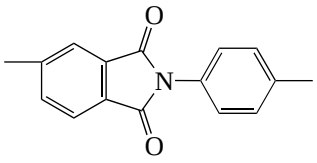 (PAI-K) 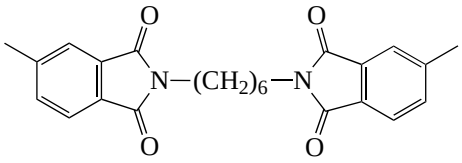 (PAI-A)

The PAI modification by glycidyl ether of azo dye was carried out using the technique of [4]. Hexa methylene diamine, phenol, *N*,*N*-dimethyl formamide (DMFA), and *N*-methyl-2-pyrrolidone (*N*-MP) were purified by distillation in vacuum. Thionyl chloride and epichlorohydrin were purified by simple distillation. 3,5-diaminobenzoic acid and dimethylbenzylamine (DMBA) were purified according to [5]. Initial PAIs were synthesized using the technique of [6]. 4-nitro-4'-hydroxyazobenzene and its glycidyl ether were produced using the technique described in [7]. PAI solutions in *N*-MP were deposited on glass substrates with a conductive coating. After drying, the polymer-layer thickness was 1–3 μm.

The degree of substitution of carboxyl groups (degree of etherification α) in PAI was determined by potentiometric titration of solutions of reprecipitated samples of etherified polymers in DMFA by an aqueous solution of KOH using a pH-121 millivoltmeter. Mechanical tests of the films were carried out using a universal UTS-10 system in the uniaxial-tension mode. The glass-transition temperature was determined thermomechanically using a UMIV-3 instrument under the sample load $\sigma = 0.01\sigma_p$.

When estimating the photosensitivity of modified polymers, we took into account the fact that introduced dye fragments are characterized by a high efficiency of charge separation within dye functional groups and do not provide carrier transport through the sample, which is necessary to attain a high photosensitivity. Therefore, an aromatic nitrogen-containing compound with a low ionization potential (I_D = 7.0 eV)—diphenylamine (DPA)—was added to the material. The DPA content was 3%, which corresponds to a distance of ~100 nm between DPA transport molecules, which provide transport of free carriers. This compound allows a carrier (hole) mobility of 10^{-4}–10^{-5} cm^2/(V s). The photosensitivity $S_{0.1}$ and the quantum yields of carrier photogeneration η and bound-pair formation η_0, as well as the thermalization lengths, were determined using the electrophotographic technique [8] in the spectral range of 400–700 nm.

3. RESULTS AND DISCUSSION

In the first stage of the study, optimum conditions for PAI modification were selected by varying the reaction temperature, the type of catalyst, and the dye–polymer molar ratio. The optimum etherification conditions correspond to a temperature of 60°C, DMBA as a catalyst, and a double molar excess of chromophore. Under these conditions, samples of modified polymers with various degrees of etherification (α = 20, 40, 60, and 80%) were obtained.

Figure 1 shows the absorption spectra of the PAI-A film (α = 80%) and a pure chromophore. Due to the self-absorption of the polymer matrix in the range of 300–380 nm, the spectrum of the modified polymer

exhibits only a shoulder of the chromophore-absorption maximum in this range. The absorption maximum of pure chromophore is observed at ~370 nm, which is characteristic of chromophores of this type [9]. The optical transparency of both chromophore and PAI-A films in the region above 500 nm ensures the promising application of these systems as NLO active media when using lasers with a wavelength of 1064 nm. This is also indicated by the data [9] on the NLO activity of polypeptides containing chromophores of this type in the side chain. Since the use of chromophore-containing polymers in NLO processes of the second-harmonic generation requires chromophore orientation, whose efficiency heavily depends on the thermomechanical properties of the polymer matrix, we carried out thermomechanical studies of the PAI-K and PAI-A films.

These studies showed that both initial PAI-K and its ethers have no pronounced transition into the high-elasticity region. This does not allow chromophore-group orientation, since such orientation is carried out at temperatures close to the glass-transition temperature. However, the thermomechanical curves of the modified PAI-A samples show that all of these polymers are softened in the temperature range of 115–125°C. This makes the PAI-A films promising for further studies of their NLO properties, which are we planning to conduct.

The spectra of photosensitivity $S_{0.1}$ are shown in Fig. 2. We can see that $S_{0.1}$ is maximum in the spectral region $\lambda < 550$ nm and steadily decreases at longer λ. The value of $S_{0.1}$ of modified PAI-K is higher than that of modified PAI-A by a factor of 2.5, which is caused by the high electron affinity E_A of the diimide fragment R_1. Therefore, the quantum yield of carrier photogeneration $\eta \propto \exp(E_A/kT)$ increases [10]; hence, $S_{0.1} \propto A\eta$ (A is the film absorptivity) increases too. The value of η was estimated to be about 5×10^{-3} for the permittivity $\varepsilon \approx 4.5$–5.0 [4]. The thermalization length was determined by the slope of the field dependence of η as $r_t \approx 1.5$ nm; the quantum yield of bound-pair formation η_0 is about 1.5×10^{-2}.

When DPA is introduced into modified PAI-K, the photosensitivity of the latter increases three times in comparison with $S_{0.1}$ of PAI-K with no DPA. This is probably caused by efficient transport of carriers (holes) via DPA molecules, since PAI-A layers (with no transport DPA molecules) are also photosensitive. Studies have shown that carboxyl groups in the PAI structures give rise to photosensivity even in the absence of DPA. Therefore, it may be concluded that the transport of free carriers in the absence of transport molecules also occurs and is most likely caused by electron transport via unsubstituted carboxyl groups.

As the content of side chromophore groups (the degree of etherification α) increases, $S_{0.1}$ increases (see Fig. 3, curve *1*) by a factor of 2–2.5 as α increases from 20 to 80%. In this case, the dark conductivity of the layer, characterized by the dark decay of the potential (see Fig. 3, curve *2*), increases by more than three times.

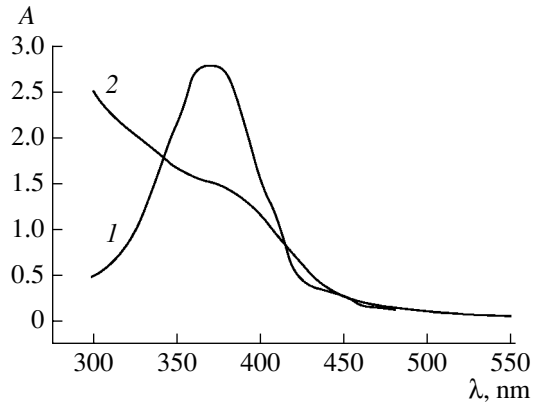

Fig. 1. Absorption spectra of (*1*) 4-nitro-4'-hydroxyazobenzene and (*2*) PAI-A film (α = 80%).

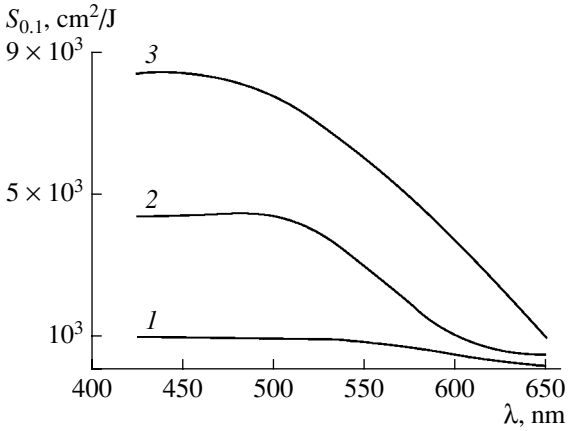

Fig. 2. Photosensitivity of (*1*) PAI-A (α = 40%), (*2*) PAI-K (α = 40%), and (*3*) (PAI-K (α = 40%) + 3% DPA) films versus the wavelength λ.

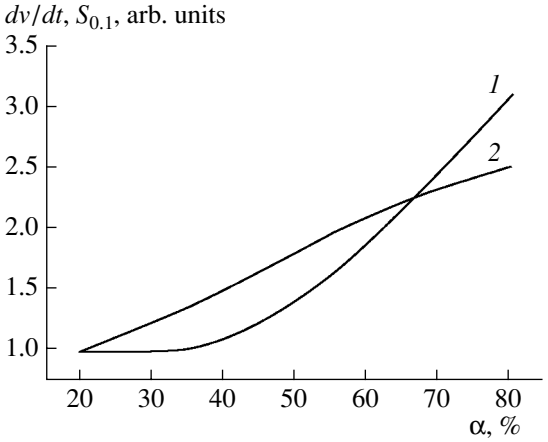

Fig. 3. (*1*) Photosensitivity of modified PAI-A films and (*2*) the rate of the dark decay of the potential versus the degree of etherification α.

4. CONCLUSIONS

(i) New polyamide-imides were synthesized which contain side chromophore groups of 4-nitro-4'-hydroxyazobenzene.

(ii) The relationship between the photosensitivity of synthesized PAIs and their structure was ascertained. It was shown that the photosensitivity is 10^3–10^4 cm^2 J^{-1} and increases threefold due to introduction of transport DPA molecules.

(iii) The optical and thermomechanical properties of these polymers make them promising for NLO applications.

REFERENCES

1. I. E. Kardash and A. V. Peblak, Itogi Nauki Tekh., Ser.: Khim. Tekhnol. Vysokomol. Soedin. **26**, 88 (1990).
2. B. Z. Motsenyat, V. A. Gusinskaya, and M. M. Koton, Plast. Massy **6**, 55 (1981).
3. V. A. Gusinskaya, S. S. Churganova, and M. M. Koton, Zh. Prikl. Khim. (Leningrad) **57**, 1819 (1984).
4. M. Ya. Goĭkhman and K. A. Romashkova, Zh. Prikl. Khim. (St. Petersburg) **72**, 473 (1999).
5. V. A. Gusinskaya and M. M. Koton, Vysokomol. Soedin., Ser. A **18**, 2681 (1976).
6. X. Jing, C. Yang, Y. Wang, and F. Wang, J. Synth. Met. **71**, 1727 (1995).
7. H.-R. Lee and Y.-D. Lee, J. Polym. Sci. Polym. Chem. **21**, 1481 (1989).
8. E. L. Aleksandrova and Yu. A. Cherkasov, Opt. Spektrosk. **64**, 1047 (1988) [Opt. Spectrosc. **64**, 624 (1988)].
9. T. Verbiest, C. Samyn, C. Bouton, *et al.*, Adv. Mater. **8**, 756 (1996).
10. E. L. Aleksandrova, Opt. Zh. **67** (3), 43 (2000) [J. Opt. Technol. **67**, 1034 (2000)].

Translated by A. Kazantsev

Semiconductors, Vol. 37, No. 7, 2003, pp. 825–831. Translated from Fizika i Tekhnika Poluprovodnikov, Vol. 37, No. 7, 2003, pp. 853–859.

CONFERENCE. AMORPHOUS, VITREOUS, AND POROUS SEMICONDUCTORS

A Study of the Effect of Oxygen on the Intensity of Erbium Photoluminescence in Amorphous SiO_x:(H, Er) Films Formed by DC Magnetron Sputtering

Yu. K. Undalov, E. I. Terukov*, O. B. Gusev, and V. Kh. Kudoyarova

Ioffe Physicotechnical Institute, Russian Academy of Sciences, Politekhnicheskaya ul. 26, St. Petersburg, 194021 Russia
**e-mail: eug.terukov@mail.ioffe.ru*

Submitted December 23, 2002; accepted for publication January 21, 2003

Abstract—The effect of oxygen on the intensity of erbium photoluminescence at $\lambda = 1.54$ μm in amorphous *a*-SiO_x:H(Er) films formed by dc magnetron sputtering was studied. The oxygen content in the gaseous phase ranged from 0.1 to 12 mol %, with other parameters of deposition remaining constant. Analysis of an *a*-Si:(H, Er, O) system showed that the range of homogeneity of amorphous *a*-SiO_x:H(Er) is retrograde (T = const). The range of homogeneity can be conventionally divided into two portions, each of which should contain either of two differently charged $[Er–O]^{n-}$ and $[Er–O–Si–O]^{m-}$ clusters ($m > n$). This inference is confirmed experimentally: in the range of oxygen concentrations amounting to 5.5–8 mol % in the plasma, unusual associative processes take place probably directly above the growing film surface; these processes are caused by the appearance of $[Er–O–Si–O]^{m-}$ clusters in the plasma and at the surface. It is these processes that account for the intensification of erbium photoluminescence as the oxygen content increases above 5.5 mol %.

1. INTRODUCTION

Erbium–oxygen clusters in amorphous hydrogenated silicon (*a*-Si:H) give rise to luminescence at a wavelength $\lambda = 1.54$ μm. The luminescence intensity depends on the content of Er in the amorphous host and on the amount both of Er and O atoms bonded to each other and the number of O atoms linked to Si atoms (we do not consider here the effect of other impurities).

The composition and structure of the atomic network in amorphous silicon, which is doped with erbium and contains oxygen (*a*-SiO_x:(H, Er)), are governed by the fact that, at comparatively low substrate temperatures ($T_s < 300$°C), the composition and geometric parameters of intrinsic and impurity (erbium) clusters existing in the gaseous phase of the plasma are reproduced to a great extent for the clusters formed in the film produced by magnetron sputtering. It is this circumstance (as well as the special physicochemical features of silicon, erbium, oxygen, and their clusters) that governs the metastable state of *a*-SiO_x:(H, Er) films formed by dc magnetron sputtering.

The aim of this study is to determine the relation between parameters of magnetron sputtering and composition and properties of formed *a*-SiO_x:(H, Er) films.

2. EXPERIMENTAL

In the course of investigations, we varied the content of oxygen C_{O_2} in the gas mixture (20%SiH_4 + 80%Ar) + O_2 within 0.1–12 mol %. In all experiments, the areas S of the Er target ($S_{Er} = 3.2$ mm^2) and Si target ($S_{Si} = 2830$ mm^2), the plasma current, magnetic field, and other parameters were kept constant. The erbium target had the shape of a platelet 4 mm long and 0.2 mm thick, was always positioned at the same site within the erosion zone of the silicon target, and was never outside this zone.

The erosion zone of the Si target had the shape of a ring with an inside diameter of ~29 mm and an area of ~490 mm^2.

The substrates made of borosilicate glass, Pyroceram, and single-crystal silicon (*c*-Si) were always positioned at the same site of the substrate holder. The substrates were heated by quartz lamps to $T_s = 265$°C (to 320°C during degassing).

The pressure (P_B^{tot}) of the SiH_4 + Ar + O_2 gas mixture was measured using a PMT-2 thermocouple vacuum gauge calibrated under atmospheric pressure. The measured total pressure P_B^{tot} was maintained constant in all experiments and was equal to either 7.5×10^{-3} Torr (the first run) or 4.5×10^{-3} Torr (the second run); the pressure of residual gases was equal to $\sim 4 \times 10^{-5}$ Torr. It was assumed that, at this pressure of residual gases in the sputtering chamber, the partial pressure of O_2 was equal to $P_{O_2} \approx 1.3 \times 10^{-5}$ Torr, which corresponded to $C_{O_2} \approx 0.15$ mol % if the SiH_4 + Ar mixture was inlet to a pressure of 7.5×10^{-3} Torr.

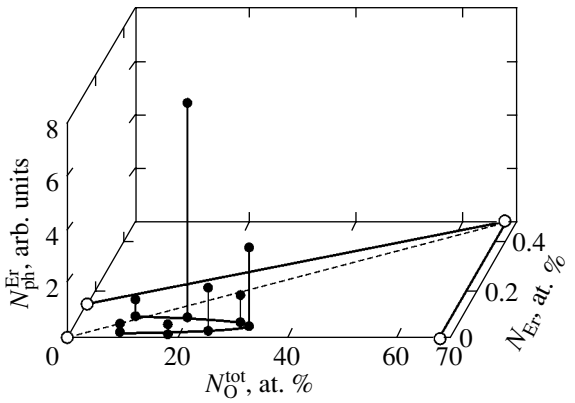

Fig. 1. Representation of a hypothetical homogeneity region for *a*-SiO_x:(H, Er) and the relation between the intensity of erbium photoluminescence I_{ph}^{Er} and the composition of *a*-SiO_x:(H, Er) films obtained at $P_B^{tot} = 7.5 \times 10^{-3}$ Torr and $T_s \approx 250$°C.

In each experiment, the oxygen pressure in the sputtering chamber was set before switching on the magnetron using a PMI-2 ionization gauge; the 20%SiH_4 + 80%Ar gas mixture was then introduced. Both gauges (of the thermocouple and ionization types) were positioned side by side in the sputtering chamber and as close as possible to the substrate.

The values of P_B^{tot} and C_{O_2} were related by the formula

$$C_{O_2}\ (\text{mol}\ \%) = 100P_{O_2}/(P_{SiH_4} + P_{Ar} + P_{O_2}). \quad (1)$$

Other parameters of the gas mixture in the initial state (before the plasma was ignited) were determined from the formulas below. In particular, the true value of the total pressure $P^{tot} = P_{SiH_4} + P_{Ar} + P_{O_2}$ was calculated using the formula

$$P^{tot} = qP_B^{tot}/(1 - k + kq); \quad (2)$$

the partial pressure of oxygen was defined by

$$P_{O_2} = kqP_B^{tot}/(1 - k + kq), \quad (3)$$

where

$$k(\text{arb. units}) = 0.01C_{O_2}. \quad (4)$$

The correction factor q for the 20%SiH_4 + 80%Ar gas mixture was defined as

$$q = q_{SiH_4}q_{Ar}/(0.2q_{Ar} + 0.8q_{SiH_4}) \approx 1.2, \quad (5)$$

where $q_{Ar} = 1.56$ [1] and $q_{SiH_4} \approx 0.6$.

Before each sputtering event, the surface of the silicon target was cleaned by plasma etching; to this end, an oxygen-free SiH_4 + Ar mixture was introduced into the sputtering chamber. The annular anode was then cleaned mechanically and was coated with an *a*-Si:H film in a SiH_4 + Ar plasma. The surface of the Er plate was cleaned mechanically before each sputtering process. The deposition time was equal to 1 h in all experiments.

The elemental composition of the films was studied using Rutherford backscattering (RBS) and nuclear resonance reactions (NRR).

The structure and content of hydrogen and oxygen that bonded to silicon were studied using infrared (IR) spectroscopy.

The photoluminescence of the films deposited on Pyroceram substrates was excited with an argon laser (λ = 514 nm) and was measured using a grating monochromator and a Ge photodetector.

The optical band gap E_g^{opt} was determined by extrapolating the experimental curve to the intersection with the horizontal axis in accordance with the dependence $(\alpha\hbar\omega)^{0.5} = B(\hbar\omega - E_g^{opt})$.

3. RESULTS AND DISCUSSION

In the *c*-Si–Al–P and *c*-Si–Al–Sb systems at equilibrium, the joint solubility of Al and P and of Al and Sb in *c*-Si at T = constant is retrograde [2]. This circumstance is attributed to the donor–acceptor interaction between the atoms of the doping impurity [2].

Similar behavior of the homogeneity-region boundary should also be observed in the *c*-Si–Er–O system at T = const. This inference is confirmed by an increase in the solubility of Er in *c*-Si when oxygen is added to the system [3].

On the basis of general considerations, a similar effect of joint solubility of Er and O_2 in *a*-Si:H, caused by chemical interaction of Er with O_2, should also be expected in the case of the metastable *a*-Si:H–Er–O system: when erbium is introduced into *a*-SiO_x:H, the solubility of oxygen in the system should increase. At the same time, the introduction of oxygen into *a*-Si:(H, Er) should also increase the solubility of erbium in the system. Each of the aforementioned processes in mutual influence on solubility should be characterized by two branches of the boundary of the homogeneity region for *a*-SiO_x:(H, Er) (Fig. 1). Both branches meet at the point that corresponds to the highest joint solubility of Er and O in *a*-Si:H. In this way, the retrograde property of joint solubility of Er and O in *a*-Si:H is specified (Fig. 1).

However, we should also take into account the difference between the factors that govern both the existence of homogeneity regions (which have retrograde boundaries in the equilibrium and metastable systems (*c*-Si–Er–O and *a*-Si–Er–O, respectively)), the extent of these regions, and the location of the point corresponding to the highest joint solubility of the doping elements.

Knowledge of the causes of the above differences will be conducive to gaining insight into the difference between erbium clusters in an equilibrium *c*-Si–Er–O system and those in the metastable *a*-Si:H–Er–O system.

In the equilibrium system, all of the above factors are controlled by the existence of fairly efficient diffusion of dopant atoms at high temperatures. As a result, conditions are provided for the more active aggregation of Er and O into clusters; for the buildup and association of the latter; and (if saturation is attained) for the appearance of inclusions of the second phase, for example, Er_2O_3.

If the equilibrium *c*-Si–Er–O system is represented using the Gibbs triangle, the composition with the highest joint solubility of Er and O in *c*-Si is most likely (in analogy with a *c*-Si–Al–P system [2]) located at the segment which links *c*-Si to Er_2O_3 (in a *c*-Si–Al–P system, this composition is located within the *c*-Si–AlP segment).

In the *a*-Si:H–Er–O metastable system, this sitiation cannot be realized since, at the low substrate temperatures ($T_s < 300$°C) used in the formation of *a*-Si, the diffusion of erbium [4], oxygen, and (even to a greater extent) their associations (clusters) is suppressed (except for the diffusion of hydrogen [5]). At the same time, in spite of low T_s, we may still assume that association- and rearrangement-related processes at the growing film surface can be promoted somewhat as the impurity concentration and the plasma parameters increase. However, it is most likely that the contribution of the above factors to the existence of clusters and their associations in an amorphous film should not be of primary importance.

From general considerations, we should accept the existence of a homogeneity region for *a*-SiO_x:(H, Er) (irrespective of the method for production). Deviation from homogeneity in an amorphous host can be caused by two factors.

1. The first factor is the saturation of the *a*-Si host with erbium associations. This saturation sets in when introduced impurities give rise (even at $T_s < 300$°C) to the spontaneous ordering of silicon–silicon and silicon–oxygen tetrahedra in the metastable system under consideration; simultaneously with this ordering, the second "erbium" phase precipitates, since this phase is soluble to a lesser extent in *c*-Si than in *a*-Si. Conceivably, the second phase is finely divided at the boundaries of *c*-Si grains, which precipitated from the amorphous host.

The above processes can be profoundly affected by the presence of a certain number of hydrogen atoms in the plasma and the film (in this study, the effect of hydrogen on experimental results and the processes under investigation is not considered).

2. The second factor is related to the specific features of physicochemical processes that occur in plasma. As a result, the second phase can appear even when the concentration of doping atoms is not sufficient for true saturation.

Indeed, an amorphous *a*-SiO_x:H film is a solid phase in which an unordered arrangement of distorted silicon–silicon and silicon–oxygen tetrahedra is fixed to certain extent [6, 7]. These tetrahedra likely form and associate in the gaseous phase in the immediate vicinity of the growing-film surface. Under certain conditions, the sizes of corresponding associations can be on the order of nanometers or micrometers in the plasma [8, 9]. The processes resulting in the growth of silicon clusters in plasma should also be similar to those for erbium clusters.

Thus, new properties of the substance appear as a result of the aggregation of clusters into nanoparticles [10]; this fact suggests that the composition and structure of erbium clusters, which are uniformly distributed in the amorphous host, cannot be identified with erbium-based inclusions in the form of the second phase.

Disorder in the *a*-Si:(H,Er,O) system implies that higher ultimate individual and joint solubilities of Er and O in the amorphous silicon host take place in the above system compared to the solubility in the equilibrium *c*-Si:(H, Er, O) system. Thus, for example, separate solubilities of Er and O (at $T_s = 250$°C) in *c*-Si are very low: lower than 0.0004 at. % ($<10^{16}$ cm^{-3}) [2, 11, 12]; according to our estimations, these solubilities in *a*-Si:H amount to ~0.14 at. % ($\sim 7 \times 10^{19}$ cm^{-3}) for erbium and to ~67 at. % (3.35×10^{22} cm^{-3}) for oxygen. The existence of a fairly extended homogeneity region in an *a*-Si:H–O system with the oxygen content as high as $N_O = 67$ at. % in combination with a relatively low solubility of erbium in *a*-Si:H drastically distinguishes the position of the composition with the highest joint solubility of Er and O in the Gibbs concentration triangle for an *a*-Si–Er–O system ($N_O \approx 68$ at. % and $N_{Er} \approx 0.5$ at. %) compared to that in a *c*-Si–Er–O system. For example, this composition should be found in the segment which connects *c*-Si and Er_2O_3 for a *c*-Si–Er–O system and in the segment which is adjacent to the *a*-Si:H–O axis and is sufficiently remote from *a*-Si:H in the O direction for an *a*-Si:H–Er–O system.

Therefore, we should expect not only differences in the composition of the host *c*-Si:(Er, O) and *a*-SiO_x:(H, Er) clusters but also in the composition of the oxygen-containing neighbors of erbium. The closest neighbors of an erbium atom should be treated as the main characteristic of an erbium cluster. For example, in *c*-Si:(Er,O) with $N_O = 10^{18}$ cm^{-3}, in Er_2O_3, and in *D*-type $Er_2Si_2O_7$, the nearest neighbors of an Er atom are six oxygen atoms [13, 14], with the Er–O interatomic spacing being equal to 2.25 ± 0.03, 2.27 ± 0.03 [13], and 2.26 ± 0.03 Å [14], respectively. In other words, the nearest neighbors of an Er atom in the above equilibrium crystalline hosts are almost the same.

The number of oxygen atoms neighboring an erbium atom is decreased to two–three and the Er–O

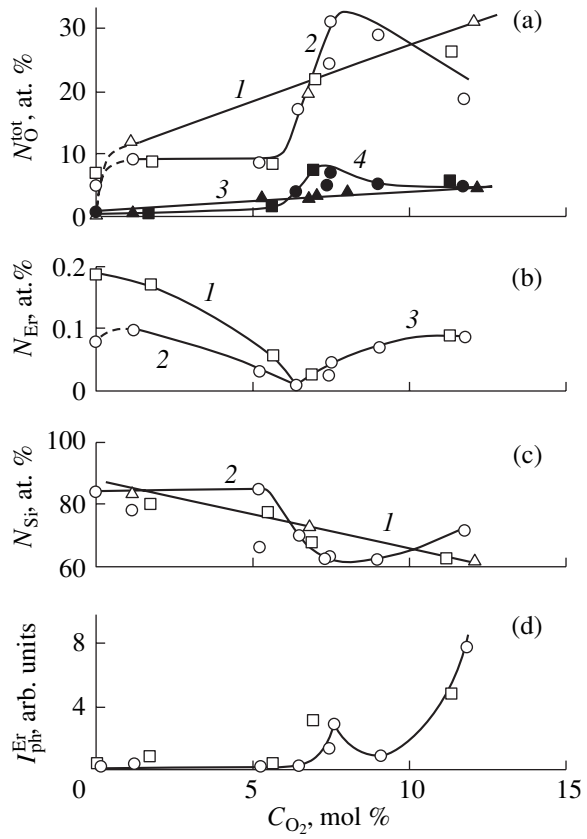

Fig. 2. Dependences of (a, b, c) composition of the *a*-SiO_x:(H, Er) and *a*-SiO_x:H films and (d) I_{ph}^{Er} for *a*-SiO_x:(H, Er) films on C_{O_2} at S_{Er} = 3.2 mm^2 according to (a) (*1*, *2*) NRR data and (*3*, *4*) IR spectroscopy and (b) and (c) RBS data; designations are the same as for curves *1* and *2* in Fig. 2a. For other details, see text.

spacing is reduced to (2.07–2.14) ± 0.02 Å [15, 16] in the amorphized *a*-SiO_x:(H, Er) host obtained using magnetron sputtering, at least for $x < 0.1$ and $N_{Er} \approx 0.1$–0.3 at. %. Furthermore, it was observed [15] that the second maximum in the electron pseudodistribution function in *a*-SiO_x:(H, Er) ($x < 0.1$) corresponds to an interatomic spacing of (3.10–3.17) ± 0.02 Å; this spacing most probably corresponds [15] to the Er–Si spacing in an erbium cluster which contains oxygen and silicon. Nevertheless, it was concluded [15] that erbium complexes which do not contain silicon exist in *a*-SiO_x:(H, Er) ($x < 0.1$).

However, in our opinion, the presence of plasma-activated Si atoms in the gaseous phase [17] suggests that both $[Er–O]^{n–}$ and $[Er–O–Si–O]^{m–}$ clusters can exist under certain conditions in the gaseous-phase zone, which is adjacent to the growing-film surface, and, consequently, in the *a*-SiO_x:(H, Er) film. In other words, we assume that erbium clusters exist in the second (silicon) and third (oxygen) coordination shells around the erbium atom in *a*-SiO_x:(H, Er). To a certain extent, this assumption is consistent with the data [18] on appearance of nanocrystalline inclusions in certain *a*-SiO_x:(H, Er) films; the structure of these inclusions resembles that of one of the erbium silicates.

Indeed, the segment connecting *a*-Si:H to *a*-SiO_x:(H, Er) in an *a*-Si:H–Er–O system and corresponding to the highest joint solubility of Er and O in *a*-Si:H divides the homogeneity region of *a*-SiO_x:(H,Er) into two parts (Fig. 1). Thus, one of these parts (region *1*), which is adjacent to the *a*-Si:H–Er axis, contains compositions that are enriched with erbium and are depleted in oxygen and silicon in comparison with the other (adjacent to the *a*-Si:H–O axis) region *2*. This inference can be easily verified if we compare the compositions of regions *1* and *2* at N_O = const, for example at 68 at. % > N_O > 67 at. % (or at N_{Er} = const in the range of 0.5 at. % > N_{Er} > 0.14 at. %).

If we assume that the concentration of optically active erbium is proportional to the total erbium concentration N_{Er}, then, in a sample with N_O^{tot} = const, the compositions in region *1* (Fig. 1) should ensure higher intensities of erbium photoluminescence (PL) I_{ph}^{Er} than in region *2*. This inference is true if erbium clusters of only a single type (composition) exist in both parts of the *a*-SiO_x:(H, Er) homogeneity domain. However, we experimentally observed the reverse situation: the PL intensity of the films with a composition corresponding to region *2* was higher than that of the films with compositions within region *1* (Fig. 1). We relate the latter observation to the possible existence of two or three types of erbium clusters in *a*-SiO_x:(H, Er); these include electroneutral clusters and two types of negatively charged clusters. Apparently, one of the latter, $[Er–O–Si–O]^{m–}$, exists in region *2*, whereas the other, $[Er–O]^{n–}$, exists in region *1* (where $m > n$). Apparently, electroneutral clusters exist at the interface between the aforementioned regions and also probably in each of these regions, although in combination with charged clusters in accordance with the domain of existence for the latter. As the composition recedes from the boundary, which conventionally divides the above regions, the relation between the numbers of neutral and charged erbium clusters changes apparently in favor of the latter.

The above hypothesis that two types of negatively charged clusters exist in *a*-SiO_x:(H, Er) is supported by the experimental observation of a drastic increase in N_O^{tot} at C_{O_2} > 5.5 mol % (S_{Er} = 3.2 mm^2) (see Fig. 2a and [18]). In addition, the magnitude of a jump in N_O^{tot} amounting to about 25 at. % cannot be attributed to the existence of a single (the first) oxygen-containing coordination sphere around an erbium atom (especially at N_{Er} = 0.01 at. % or 6×10^{18} cm^{-3}) in an erbium cluster; moreover, the aforementioned jump cannot be completely related either to an increase in the number of

oxygen atoms N_O^{Si-O} bonded to silicon atoms in an amorphous matrix (the data of IR spectroscopy) or to an increase in the concentration of OH groups [19].

In addition to the aforesaid, let us compare the content of oxygen (Fig. 2a) and E_g^{opt} (Fig. 3) in *a*-SiO_x:H films (triangles in Fig. 3) with that in *a*-SiO_x:(H, Er) films (circles in Fig. 3) obtained at $P_B^{tot} = 7.5 \times 10^{-3}$ Torr.

(i) In the *a*-SiO_x:H films (triangles in Fig. 2a), the dependences of N_O^{tot} (curve *1*) and N_O^{Si-O} (curve *3*) on C_{O_2} are monotonic in the entire range of variation C_{O_2} = 1–12 mol % at $P_B^{tot} = 7.5 \times 10^{-3}$ Torr.

(ii) In the case of *a*-SiO_x:(H, Er) films (the data are represented in Fig. 2a by circles for $P_B^{tot} = 7.5 \times 10^{-3}$ Torr and by squares for $P_B^{tot} = 4.5 \times 10^{-3}$ Torr) for C_{O_2} = 5.5–8 mol %, the dependence on C_{O_2} ceases to be monotonic: a drastic increase in N_O^{tot} by 25% is observed (curve *2*), whereas an increase in N_O^{Si-O} is much smaller (by 7.5%, see curve *4* in Fig. 2a).

(iii) In the ranges of C_{O_2} = 1–5.5 and 8–12 mol %, the dependences $N_O^{Si-O} = f(C_{O_2})$ are virtually the same for *a*-SiO_x:H and *a*-SiO_x:(H, Er) (Fig. 2a; curves *3* and *4*, respectively).

(iv) The curves $E_g^{opt} = f(N_O^{Si-O})$ increase monotonically and are virtually the same for the *a*-SiO_x:H and *a*-SiO_x:(H, Er) films (Fig. 3).

We may conclude from the above that introduction of erbium in combination with oxygen into plasma (in the ranges of C_{O_2} = 1–5.5 and 8–12 mol %), in general, affects insigificantly the content of oxygen in an amorphous (erbium-free) host.

(v) The value of the difference $N_O^{tot} - N_O^{Si-O}$ for *a*-SiO_x:H (Fig. 2a) indicates that oxygen introduced into plasma in our experiments (C_{O_2} = 0.1–12 mol %) not only increases the oxygen content monotonically (i.e., N_O^{Si-O}) in the silicon matrix but that is also involved in the formation of OH and other oxygen-containing groups.

However, in the case of *a*-SiO_x:(H, Er), these processes are supplemented with the formation of Er–O and Er–O–Si–O associations in the plasma (with subsequent transfer of these associations to the growing-film surface). Notably, as can be seen from Fig. 2a (curves *1*, *2*), variations in N_O^{tot} in *a*-SiO_x:(H, Er) differ from those observed in *a*-SiO_x:H obtained under the same conditions in the entire range of C_{O_2}.

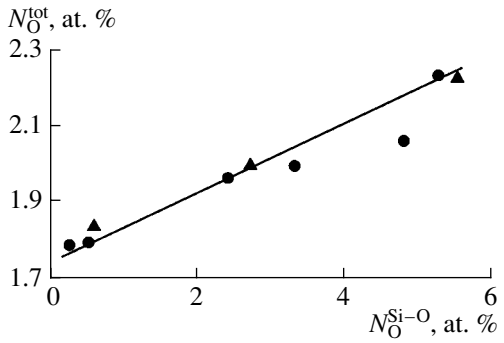

Fig. 3. Dependence of E_g^{opt} for the *a*-SiO_x:(H, Er) and *a*-SiO_x:H films on the concentration of oxygen bonded to silicon atoms N_O^{Si-O} (according to the data obtained using the IR spectroscopy).

If the content of oxygen in the plasma is low (C_{O_2} < 5.5 mol %), the $[Er–O]^{n-}$ clusters, which are relatively weakly accelerated by an electric field, are apparently formed in the gaseous phase; a fraction of these clusters are evacuated from the working chamber [16]. As a result of the above reasoning, the total concentration of oxygen N_O^{tot} in *a*-SiO_x:(H, Er) films increases relatively weakly (from 9 to 10 at. %) in comparison with that in *a*-SiO_x:H (from 10 to 20%); at the same time, N_{Er} (see Fig. 2b) decreases from ~0.1 to ~0.01 at. % (from ~5×10^{19} to ~5×10^{18} cm^{-3}) for $P_B^{tot} = 7.5 \times 10^{-3}$ Torr (curve *2*) and from ~0.2 to ~0.01 at. % (from ~1×10^{20} to ~5×10^{18} cm^{-3}) for $P_B^{tot} = 4.5 \times 10^{-3}$ Torr (curve *1*). The value of N_O^{Si-O} in *a*-SiO_x:H differs only slightly from that in *a*-SiO_x:(H, Er) (compare curves *3* and *4* in Fig. 2a). By comparing the difference between N_O^{tot} and N_O^{Si-O} for *a*-SiO_x:H and *a*-SiO_x:(H, Er), we can see that this difference is larger in *a*-SiO_x:H than in *a*-SiO_x:(H, Er) in the region of C_{O_2} < 6.5 mol %. The cause of this effect is probably the same as that outlined above.

Starting with C_{O_2} > 5.5 mol %, oxygen introduced into plasma ultimately brings about both a certain increase (by ~7.5 at. %) in its content in the amorphous silicon host (Fig. 2a, curve *4*) due to the Si–O interaction and the formation of oxygen-enriched and multiply charged $[Er–O–Si–O]^{m-}$ clusters. This process is accompanied by a drastic increase in both N_O^{tot} (from 10 to 35 at. %) and N_{Er} (from 0.01 to 0.1 at. %) in these films. Notably, the rate of the increase in the concentration of these clusters at C_{O_2} > 5.5 mol % is apparently much higher than that of OH groups (the latter reduce

I_{ph}^{Er}); as a result, the dependence $I_{ph}^{Er} = f(C_{O_2})$ suddenly becomes much steeper (Fig. 2d).

In all likelihood, the structure of an $[Er–O–Si–O]^{m-}$ cluster resembles that of a distorted fragment of a *D*-type $Er_2Si_2O_7$ structure; up to 18 atoms are present in the third coordination shell of oxygen in the latter structure [14]. We should also take into account the fact that oxygen in this shell is not of the bridge type [14]; bridge-type oxygen is characteristic of matrices consisting of amorphous silicon and silicon and of silicon and oxygen [20].

Taking into account the above reasoning, we believe that the drastic increase in N_O^{tot} is caused by the formation of erbium clusters with the third oxygen coordination shell $[Er–O–Si–O]^{m-}$; these clusters are formed at $C_{O_2} > 5.5$ mol %.

The onset of the drastic increase in N_O^{tot} (as C_{O_2} increases) (Fig. 2a, curve *2*) corresponds to the transformation of the film composition from region *1* to region *2* (Fig. 1) and is accompanied by a drastic increase in I_{ph}^{Er} (Fig. 2d) even if N_{Er} decreases to ~0.01 at. % (Fig. 2b, curves *1*, *2*). In our opinion, this observation is also indicative of the emergence of large-size erbium clusters enriched with oxygen owing to the appearance of the third oxygen coordination shell in these clusters. The fact that erbium clusters in region *2* are charged negatively to a greater extent than those in region *1* can also be attributed to enrichment of the former with oxygen when the size of the clusters increases. As a result, the flow of erbium clusters in region *2* is accelerated by an electric field of the magnetron to a greater extent than that in region *1* (for the plasma parameters maintained constant, including the current strength).

Thus, acceleration of erbium clusters from region *2*, which are large in size and enriched with oxygen, ensures an increase in the oxygen flow to the substrate; apparently, this increase brings about the drastic increase in N_O^{tot} at $C_{O_2} > 5.5$ mol %. This inference differs from that reported in [1], where a drastic increase in N_O^{tot} at $C_{O_2} > 5.5$ mol % was attributed solely to an increase in the concentration of OH groups. If this inference were valid, the value of I_{ph}^{Er} both for $P_B^{tot} = 4.5 \times 10^{-3}$ Torr (Fig. 2d, squares) and for $P_B^{tot} = 7.5 \times 10^{-3}$ Torr (Fig. 2d, circles) would decrease in this region of C_{O_2} (since the OH groups reduce I_{ph}^{Er}) rather than increase (as was observed experimentally, see Fig. 2d).

It is noteworthy that all dependences of N_O^{tot}, $N_O^{Si–O}$, N_{Si}, and I_{ph}^{Er} on C_{O_2} at $S_{Er} = 3.2$ mm^2 are virtually no different from each other and are rather weak (see Figs. 2a, 2c, 2d) in the entire range of C_{O_2} as P_B^{tot} decreases from 7.5×10^{-3} to 4.5×10^{-3} Torr. However, if $P_B^{tot} = 4.5 \times 10^{-3}$ Torr, the curve $N_{Er} = f(C_{O_2})$ runs higher (Fig. 2b, curve *1*) than that at $P_B^{tot} = 7.5 \times 10^{-3}$ Torr (Fig. 2b, curve *2*) in the range of $C_{O_2} = 0.1$–6.5 mol %. Notably, at $C_{O_2} \approx 0.1$ mol %, the value of N_{Er} at $P_B^{tot} = 4.5 \times 10^{-3}$ Torr is nearly twice as large as that at $P_B^{tot} = 7.5 \times 10^{-3}$ Torr. At the same time, the dependences $N_{Er}(C_{O_2})$ practically coincide for $C_{O_2} > 6.5$ mol % in the range of P_B^{tot} under consideration.

In our opinion, this observation indicates that, in the region $C_{O_2} < 6.5$ mol %, the concentrations of photoactive erbium centers are virtually the same notwithstanding the fact that the values of N_{Er} are larger at $P_B^{tot} = 4.5 \times 10^{-3}$ Torr than at $P_B^{tot} = 7.5 \times 10^{-3}$ Torr. This behavior can probably be attributed to a deficit of oxygen in the plasma and to the fact that oxygen-poor $[Er–O]^{n-}$ clusters exist predominantly in plasma.

In all likelihood, the observed decrease in the curve $N_{Er} = f(C_{O_2})$ at $C_{O_2} < 6.5$ mol % and its subsequent increase at larger values of C_{O_2} is also caused by changes in the composition of erbium clusters both in the plasma and in the film.

This reasoning is consistent with the hypothesis that, at $C_{O_2} < 6.5$ mol % and $P_B^{tot} = (4.5–7.5) \times 10^{-3}$ Torr, the oxygen-deficient $[Er–O]^{n-}$ clusters that form in the film have a low optical activity.

We should also add that, in the range $C_{O_2} = 5.5$–8 mol %, jumplike changes are characteristic of not only N_O and N_{Er} but also of N_{Si} (Fig. 2c) (and N_H, which is not shown in Fig. 2). In our opinion, these features conclusively demonstrate that unusual associative processes related to erbium occur in the plasma.

4. CONCLUSIONS

Analysis of the obtained experimental data allows the following conclusions:

(i) The homogeneity region of *a*-SiO_x:(H, Er) in an *a*-Si:H–Er–O system should be retrograde.

(ii) The features of dependences of N_{Er}, N_O^{tot}, $N_O^{Si–O}$, N_{Si}, and I_{ph}^{Er} on C_{O_2} at $C_{O_2} < 12$ mol %, $S_{Er} = 3.2$ mm^2, and $P_B^{tot} = (4.5–7.5) \times 10^{-3}$ Torr make it possible to conclude that oxygen-deficient $[Er–O]^{n-}$ clusters are formed in the plasma and in the film at $C_{O_2} < 5.5$ mol %,

whereas oxygen-enriched $[Er–O–Si–O]^{m–}$ clusters are formed if $C_{O_2} > 5.5$ mol % ($m > n$).

(iii) The largest values of I_{ph}^{Er} are observed for the samples whose composition corresponds to the part of a *a*-SiO_x:(H, Er) homogeneity region close to that of an *a*-Si:H–O system; we assume that the latter system involves $[Er–O–Si–O]^{m–}$-clusters, which have higher photoluminescent activity than $[Er–O]^{n–}$ clusters.

ACKNOWLEDGMENTS

This study was supported by the Russian Foundation for Basic Research, project no. 01-02-17825a.

REFERENCES

1. B. I. Korolev, *Fundamentals of Vacuum Engineering* (Énergiya, Moscow, 1964).
2. V. M. Glazov and V. S. Zemskov, *Physicochemical Principles of Semiconductor Doping* (Nauka, Moscow, 1967; Israel Program for Scientific Translations, Jerusalem, 1968).
3. R. Sema, J. H. Shin, M. Lohmeier, *et al.*, J. Appl. Phys. **79**, 35 (1966).
4. A. Polman, J. S. Custer, E. Snoens, and G. N. van den Hoven, Appl. Phys. Lett. **62**, 507 (1993).
5. V. Petrova-Koch, H. P. Zeinde, J. Herion, and W. Beyer, J. Non-Cryst. Solids **97–98**, 807 (1997).
6. G. B. Bokiĭ, *Crystal Chemistry* (Nauka, Moscow, 1971).
7. N. F. Mott and E. A. Davis, *Electronic Processes in Non-Crystalline Materials*, 1st ed. (Clarendon Press, Oxford, 1971; Nauka, Moscow, 1974).
8. K. Koga, Y. Matsuoka, K. Tanaka, and M. Shiratani, Appl. Phys. Lett. **77**, 196 (2000).
9. H. Fujishiro and S. Furukawa, Solid State Commun. **73**, 835 (1990).
10. I. P. Suzdalev, Usp. Khim. **70**, 203 (2001).
11. F. Y. Ren, J. Michel, Q. Sun-Paduano, *et al.*, Mater. Res. Soc. Symp. Proc. **301**, 87 (1993).
12. P. E. Freeland, K. A. Jackson, C. W. Lowe, and J. R. Patel, Appl. Phys. Lett. **30**, 31 (1977).
13. D. L. Adler, D. C. Jacobson, D. J. Eaglesham, *et al.*, Appl. Phys. Lett. **61**, 2181 (1992).
14. J. Felsche, Rare Earths **13**, 99 (1973).
15. C. Piamonteze, A. C. Iníguez, L. R. Tessler, *et al.*, Phys. Rev. Lett. **81**, 4652 (1998).
16. L. R. Tessler and A. C. Iniguez, J. Non-Cryst. Solids **266–269**, 603 (2000).
17. F. J. Kammpas, Semicond. Semimet. A **21**, 153 (1984).
18. E. I. Terukov, Yu. K. Undalov, V. Kh. Kudoyarova, *et al.*, J. Non-Cryst. Solids **299–302**, 699 (2002).
19. E. I. Terukov, V. Kh. Kudoyarova, Yu. K. Undalov, and O. B. Gusev, Izv. Ross. Akad. Nauk, Ser. Fiz. **66**, 268 (2002).
20. G. Lucovsky, J. Yang, S. S. Chao, *et al.*, Phys. Rev. B **28**, 3225 (1983).

Translated by A. Spitsyn

Semiconductors, Vol. 37, No. 7, 2003, pp. 832–837. Translated from Fizika i Tekhnika Poluprovodnikov, Vol. 37, No. 7, 2003, pp. 860–865.

CONFERENCE. PHYSICS OF SEMICONDUCTOR DEVICES

Splitting of Resonant Optical Modes in Fabry–Perot Microcavities

V. G. Golubev, A. A. Dukin*, A. V. Medvedev, A. B. Pevtsov, A. V. Sel'kin, and N. A. Feoktistov

Ioffe Physicotechnical Institute, Russian Academy of Sciences, Politekhnicheskaya ul. 26, St. Petersburg, 194021 Russia

**e-mail: dookin@gvg.ioffe.rssi.ru*

Submitted December 23, 2002; accepted for publication December 27, 2002

Abstract—Splitting of resonant optical modes in Fabry–Perot microcavities with distributed Bragg reflectors is studied experimentally. The splitting was detected in polarized light at large angles of incidence onto the external boundary of a microcavity. A theoretical model is developed which makes it possible to describe quantitatively all of the special features of the splitting observed. *© 2003 MAIK "Nauka/Interperiodica".*

INTRODUCTION

Recently, much attention has been focused on Fabry–Perot microcavities (MCs) because of their interesting physical properties [1]. Some examples of the phenomena that were observed in MCs are given by Rabi splitting due to the interaction of localized optical modes with excitons in quantum wells [2], the splitting of eigenmode frequencies in a system of two MCs coupled by a common mirror [3], and the polarization splitting of eigenfrequencies of optical TM and TE modes [4]. Most of the effects in MCs were studied at angles close to normal incidence of light.

The aim of this study is a detailed investigation of the optical eigenmode of a planar MC at large angles of incidence. As experimental samples, we used MCs on the basis of oxygen-saturated hydrogenated amorphous silicon (a-SiO_x:H) and tin oxide (SnO_x). The splitting of the optical-mode resonant frequency in one of the polarizations of light is revealed. The value of splitting and the polarization (TM or TE) in which it appears depend on the optical constants of the individual layers and the MC geometry.

EXPERIMENTAL

The microcavity under consideration is a thin-film structure comprised of alternating layers of oxygen-saturated hydrogenated amorphous silicon (a-SiO_x:H) and tin oxide (SnO_x).[1] A schematic of the MC structure is shown in Fig. 1. The upper (A) and the lower (B) distributed Bragg reflectors (DBRs) consist of two pairs of quarter-wave layers of SnO_x and a-SiO_x:H (the respective thicknesses are $\lambda/4n_1$ and $\lambda/4n_2$) with a high (n_1) and a low (n_2) refractive indices ($n_1 = 1.87$ for SnO_x and $n_2 = 1.46$ for a-SiO_x:H). A half-wave active layer of SnO_x with the thickness $\lambda/2n_1$ is placed between the two DBRs. The optical parameters of the layers were determined from the interference pattern recorded directly during the growth of the microcavity structure. The properties of each layer were independently obtained from ellipsometry measurements. The thicknesses of the layers were chosen so that the resonance wavelength (λ) in vacuum at normal incidence of light

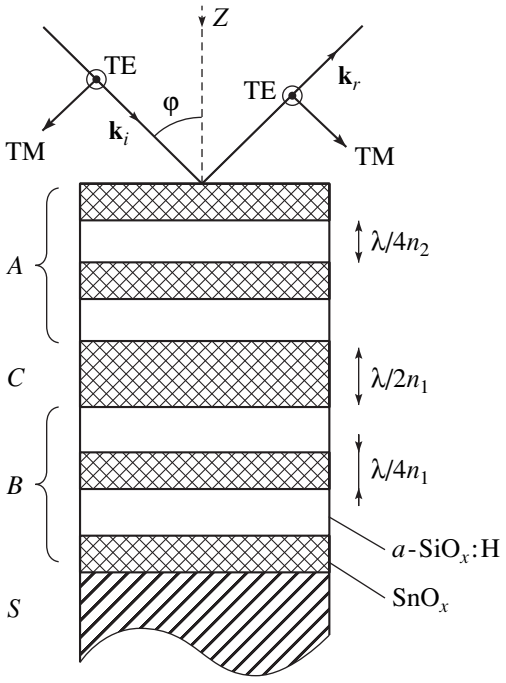

Fig. 1. Scheme of an SnO_x/a-SiO_x:H-based microcavity consisting of two quarter-wave distributed Bragg reflectors, the upper (A) and the lower (B), and a half-wave active SnO_x layer (C). S is the quartz substrate; $\mathbf{k}_i$ and $\mathbf{k}_r$ are the wave vectors of the incident and reflected waves, respectively; φ is the angle of light incidence; TM and TE are the polarizations of light; n_1 and n_2 are the refractive indices; and λ is the operating wavelength of the microcavity.

[1] The detailed description of the MC design and fabrication process are given in [5–9].

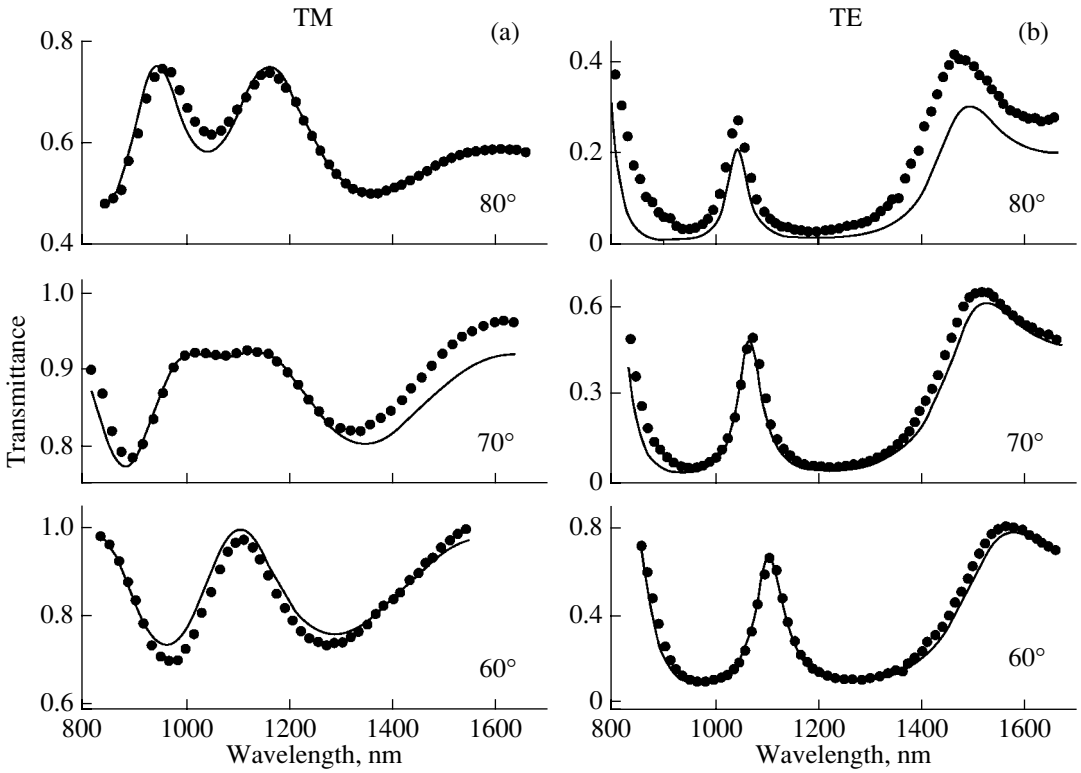

Fig. 2. Transmission spectra of the SnO_x/a-SiO_x:H-based microcavity at the angles of incidence φ = 60°, 70°, and 80° for (a) TM and (b) TE polarizations. Circles show the experimental results and solid curves show the results of calculations.

lies within the range from 1.3 to 1.5 μm, which corresponds to the range used by modern fiber-optics communication devices.

The materials of the layers were selected so that the microcavity structure grown had a fairly high optical contrast $2(n_1 - n_2)/(n_1 + n_2)$, which allows one to observe the MC eigenmodes with a minimum number of periods within DBR. The latter circumstance plays an important role in simplifying the technological process of growing a multilayer structure.

Spectroscopic studies were carried out using a computer-controlled grating monochromator equipped with an InGaAs-based photodiode as a radiation detector. We performed the measurements in the synchronous-detection mode. The transmission signal was collected from the surface area of 1 mm^2. The angular aperture did not exceed 0.7° during the measurements, which enabled us to avoid undesirable broadening of resonance lines as a result of collimation of beams passed through the MC at different angles.

We measured the MC transmission spectra both in TM and TE polarizations at different angles of incidence in the range from 0° to 85°. The spectra were recorded in the interval including the value corresponding to the photonic band gap [1]. As long as the angle of incidence is no greater than 70°, the spectrum shows a clearly pronounced resonance peak, which is attributed to the excitation of an MC eigenmode. At larger angles, a doublet structure of the resonance peak appears in TM polarization; whereas, in TE polarization, such a structure is absent at any angle of light incidence.

The MC transmission spectra in the region of the photonic band gap is shown by dotted curves in Fig. 2 for (a) TM and (b) TE polarizations and three angles of incidence (φ = 60°, 70°, and 80°). It is seen that, in TM polarization, the doublet structure is absent at φ = 60°, arises at 70°, and becomes pronounced at 80°. The splitting of the doublet increases with increasing φ. In TE polarization, only one resonance peak is detected at the same angles of incidence. The TE peak turns out to be narrower than the TM peak. The photonic band gap most clearly manifests itself in TE polarization as an appreciable increase in the transmission coefficient at the long- and the short-wavelength edges of the spectral range considered.

Dots in Fig. 3 show the spectral position of the experimental resonance peaks versus the angle of light incidence. As the angle increases, the resonance wavelength corresponding to the maximum transmission decreases. For angles ranging from 0° to 70°, the resonance frequencies for TM and TE polarizations coincide. At the angles exceeding 70°, a distinct splitting of the resonance peak is observed in TM polarization. It should be noted that the appearance of the splitting is threshold-like.

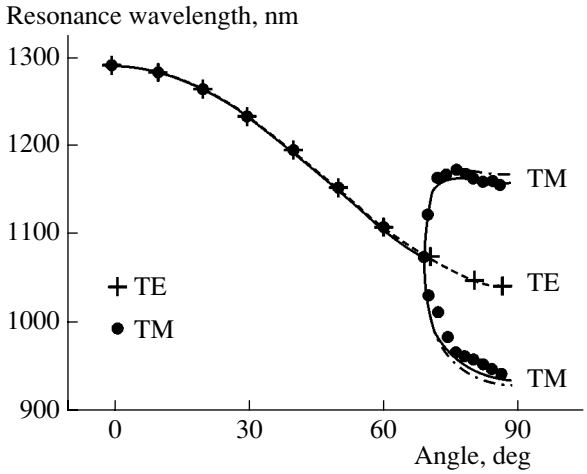

Fig. 3. Angular dependence of the resonance wavelengths of the SnO_x/a-SiO_x:H-based microcavity for TM and TE polarizations. Circles represent the experimental results. Solid and dashed curves show the wavelengths of the resonance transmission peaks obtained from the spectra calculated by the transfer-matrix method for TM and TE polarizations, respectively. The dot-and-dash line is the result of calculating TM polarization according to analytical expression (3).

In order to explain the experimental results, in what follows, we suggest a model for the formation of transmission spectra of an MC structure at large angles of light incidence.

THEORETICAL MODEL

The transmission spectra of the structure studied were calculated by the transfer-matrix method [10]. The calculated spectra (solid curves in Fig. 2) were fitted to the experimental data by varying the refractive index of SnO_x and the MC layers' thickness. As can be seen, good agreement between the theoretical and the experimental results was achieved. The calculated curves reproduce all the special features of the experimental spectra including the photonic band gap and the resonance peak with its doublet structure.

The resonance wavelengths providing for the maximum transmission through the studied MC structure ($n_1 > n_2$) versus the angle of light incidence were derived from the calculated spectra for TM polarization (solid line in Fig. 3) and TE polarization (dashed line). The calculated values correlate well with the experiment. The resonance wavelength decreases with increasing angle of incidence. For angles in the range from 0° to 70°, the resonance wavelengths for both polarizations are very close (small polarization splitting [11]). This fact is attributed to the relatively low value of the optical contrast, as well as to the fact that the optical thicknesses of the DBR layers and the active layer are equal to $\lambda/4$ and $\lambda/2$, respectively, with high accuracy.

In order to establish the reasons for TM-peak splitting, we make a number of simplifying assumptions. Let us assume the optical thickness of the active layer and that of the DBR layers to be equal to $\lambda/2$ and $\lambda/4$, respectively. The relationship between the refractive indices of the MC layers is such that, at any angle of incidence, the Brewster effect does not occur at the interfaces between the adjacent DBR layers ($n_V > 1/\sqrt{n_1^2 + n_2^2}$, where n_V is the refractive index of the external medium).

Analysis shows that, under certain conditions, a constructive interference of waves (summation of waves with the same phase) in the region of the photonic band gap occurs at the internal boundaries of the external quarter-wave layer of the upper DBR (this layer is adjacent to the external medium). For TE polarization, such interference occurs at any angle of light incidence if $n_1 < n_2$ (see the arrangement of layers in Fig. 1). In TM polarization, the interference becomes constructive if $n_1 > n_2$ and the angle of incidence φ exceeds the Brewster angle $\varphi_{Br} = \arctan(n_1/n_V)$ or if $n_1 < n_2$ and $\varphi < \varphi_{Br}$. For angles of incidence close to 90°, the reflectivity at the upper boundary of the external layer tends to unity, which results in the formation of an additional MC denoted as $MC_{\lambda/4}$, in contrast to $MC_{\lambda/2}$ in the half-wave active layer. Thus, at large angles of incidence, we obtain a system of two MCs coupled by a common two-sided mirror, which is formed by the part of the upper DBR between the active and the upper (external) layers.

It is known that, in a system of two MCs coupled by a common mirror, the frequencies of eigenmodes may split [11]. Similar splitting should also be expected in the system under study.

In the region of the photonic band gap, the energy reflection coefficient of a DBR $R_{DBR} = |r_{DBR}|^2$ is nearly frequency-independent. The phase of the amplitude reflection coefficient r_{DBR} varies nearly linearly [8, 11]:

$$r_{DBR}^{\sigma} = \pm\sqrt{R_{DBR}^{\sigma}}\exp\{i\alpha^{\sigma}(\varphi)[\omega - \bar{\omega}^{\sigma}(\varphi)]\},$$

where σ = TM, TE denotes polarization, φ is the angle of incidence in the external medium, $\alpha^{\sigma}(\varphi)$ is the proportionality factor between the phase and frequency, and $\bar{\omega}^{\sigma}(\varphi)$ is the "central" frequency of the photonic band gap. The coefficient $\alpha^{\sigma}(0)$ is inversely proportional to the difference between the refractive indices:

$$\alpha^{\sigma}(0) \equiv \alpha(0) = \bar{\lambda}n_1n_2/[2c(n_1 - n_2)n],$$

where $\bar{\lambda} = 2\pi c/\bar{\omega}(0)$, c is the speed of light, n is the refractive index of the medium from which the wave falls on a DBR, and $\bar{\omega}(0) \equiv \bar{\omega}^{TM}(0) = \bar{\omega}^{TE}(0)$ [12]. The phase of the amplitude reflection coefficient at the frequency $\bar{\omega}^{\sigma}(\varphi)$ is equal to zero (sign "+") if $n \geq n_1, n_2$ and to π (sign "–") if $n \leq n_1, n_2$.

The amplitude transmission coefficient t_{MC} of a microcavity as a whole is described by the following expression (from here on, we omit the index σ, which denotes polarization):

$$t_{MC} = \frac{t_{top}t_{com}\Phi^{3/2}t_{BB}t_{SV}}{1-\tilde{r}_{top}r_{com}\Phi-\tilde{r}_{com}r_B\Phi^2+\tilde{r}_{top}r_B\Phi^3\tilde{r}_{com}/r^*_{com}}, \quad (1)$$

where t_{BB} and r_B are the amplitude coefficients of transmission and reflection of light of the DBR B in the case of incidence of light from the side of the active layer; t_{SV} is the amplitude transmission coefficient at the substrate–external-medium interface; $\Phi = \exp(i\beta\omega)$ determines the phase increment of the wave as it passes through an active layer with the thickness L_c, $\beta = L_c\sqrt{n_1^2 - n_x^2}/c$, $n_x = n_V\sin\varphi$; t_{com} and r_{com} are the amplitude coefficients of transmission and reflection of a common mirror placed in a medium with the refractive index n_1; t_{top} and $\tilde{r}_{top}$ are the amplitude coefficients of transmission and reflection at the interface between the external layer of the upper DBR (A) and the external medium. Symbol "~" indicates that the wave propagation is opposite the Z axis.

Analysis of the poles of expression (1) in the approximation $\arg r_B \approx \arg r_{com}$ (which is confirmed by exact numerical calculations) indicates the existence of a critical angle of incidence φ_{Sp}; exceeding this angle results in the splitting of the eigenmode frequencies. An approximate analytical expression for φ_{Sp} is given in the Appendix.

With the use of (1), the MC transmission spectrum in the region of the photonic band gap can be thought of as the product of three resonance factors:

$$T_{MC} = \frac{A}{|x-x_1|^2|x-x_2|^2|x-x_3|^2}, \quad (2)$$

where $x = \exp\{i[(\alpha+\beta)\omega - \alpha\bar{\omega}]\}$ and A and $x_{1,2,3}$ are the constants governed by the MC parameters (see Appendix).

The analytical expression for the splitting of the resonance transmission peak $\Delta\omega_r$ obtained on the basis of formula (2) is presented in the Appendix. The frequencies of the two resonance peaks $\omega_{r_{1,2}}$ are determined as

$$\omega_{r_{1,2}} = \omega_0 \pm \Delta\omega_r/2, \quad (3)$$

where $\omega_0 = (\alpha\bar{\omega} + \pi)/(\alpha + \beta)$ is the resonance frequency for uncoupled $MC_{\lambda/2}$ and $MC_{\lambda/4}$, i.e., when $|r_{com}| = 1$.

The resonance-peak splitting arises either in TM or TE polarization, depending on whether the refractive index of the material of the external DBR layer is greater or smaller than that of the other material composing the DBR structure. Irrespective of the polarization type, the splitting is described by the same formulas (1)–(3) presented in this section and by formula (A.1) in the Appendix.

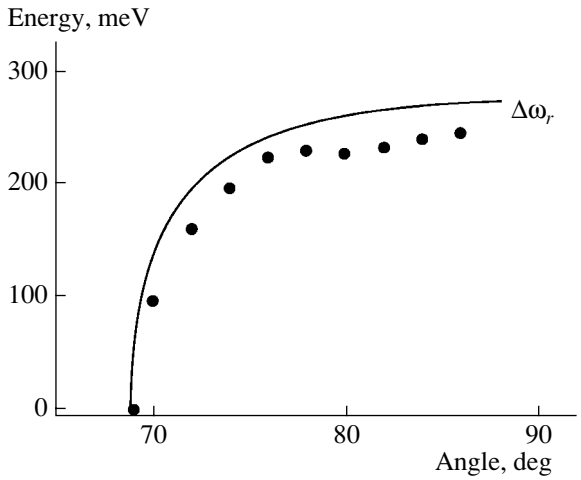

Fig. 4. Angular dependence of the TM-peak splitting for the SnO_x/a-SiO_x:H-based microcavity. Circles show the experimental data, and the solid line is the result of calculation by formula (A1).

The case considered is essentially different from that analyzed in [11] for the system consisting of two identical MCs coupled by a common internal DBR and sandwiched between two identical external DBRs. In the case under consideration, the system of two MCs is substantially asymmetric since the role of one of the external DBRs is played by the interface between the external layer of the microcavity structure and the external medium. The phase of the amplitude reflection coefficient of this interface is frequency-independent, and the reflection coefficient differs from that of the lower DBR. Furthermore, the thicknesses of the active layers in these two MCs differ by a factor of 2. This asymmetry controls the new characteristic features of the splitting, which will be discussed in the following section.

DISCUSSION

Figures 3 and 4 show the results of calculation in terms of the analytical model suggested in Section 3 in comparison with the experimental data. The spectral position of the TM-doublet components was determined from expression (3) with the use of the values $|r_{com}|$, $|r_B|$, $\bar{\omega}$, and α calculated by the transfer-matrix method. The theoretical curve in Fig. 3 (dot-and-dash line) closely correlates with the experimental points and with the results of calculation by the transfer-matrix method. When the angle of incidence is close to 70°, the splitting of the resonance peak manifests itself both in theory and experiment. Thus, the analytical model suggested allows one to interpret the observed splitting of the resonance peak as the splitting of the MC eigenmode frequencies, which arises at large

angles of incidence due to the interaction between two MCs: one in the active layer and the other in the external layer of the upper DBR.

The splitting of the resonance TM peak versus the angle of light incidence is shown in Fig. 4 (circles are the experimental data; the solid curve represents the results of calculation by formula (A.1)). The splitting process is of a threshold type. At the angles exceeding 80°, the splitting only slightly increases with increasing angle of incidence.

The splitting $\Delta\omega_r$ is governed by two parameters: the transmission coefficient t_{com} and the reflection coefficient $\tilde{r}_{top}$ under the condition that $|r_B| \approx 1$ (see Section 3). The common mirror mixes two degenerate modes of the system consisting of $MC_{\lambda/2}$ and $MC_{\lambda/4}$, thus lifting the frequency degeneracy of the modes. The transmission coefficient t_{com} controls the degree of interaction between the two modes and the value of splitting [11]. In the region $\varphi > \varphi_{Sp}$, this coefficient only slightly varies with the angle of incidence and the splitting increases mainly due to the increase in the coefficient of reflection of the interface between the upper DBR and the external medium $\tilde{r}_{top}$.

An important parameter is the minimum angle of light incidence at which the splitting of the resonance TM peak is initiated. This threshold angle can be reduced by increasing $|\tilde{r}_{top}|$ and decreasing $|r_{com}|$, which is achieved by reducing the refractive index n_1 of the DBR external layer.

The calculation of spectra by the transfer-matrix method shows that the reflection coefficient of the lower DBR $|r_B|^2$ has only a slight influence both on the threshold angle φ_{Sp} at which the splitting appears and on the value of splitting $\Delta\omega_r$ (if $|r_B|^2$ is larger than the reflection coefficient of the upper DBR). With an increase in the reflectivity of the common mirror, $\Delta\omega_r$ decreases and φ_{Sp} increases. The corresponding variation in the width of resonance peaks is small. The absorption of light in MC layers results in additional broadening of the resonance peaks.

The above results were taken into consideration when choosing the MC parameters (refractive indices, the number of DBR-containing layers, the active-layer thickness) so as to make the threshold angle low enough to be reliably detected in experiments.

CONCLUSION

A Fabry–Perot microcavity was fabricated on the basis of SnO_x/*a*-SiO_x:H by plasma-enhanced chemical-vapor deposition. The frequency of the resonance peak of transmission of this structure was studied experimentally as a function of the angle of light incidence in the range from 0° to 85° in TM and TE polarizations. Splitting of the resonance TM peak at large angles of incidence was revealed.

It is shown that resonance-peak splitting originates from the splitting of the eigenmode frequencies in a system of two microcavities coupled by a common mirror. The first microcavity represents an active layer. At large angles of incidence, the external layer of the distributed Bragg reflector adjacent to the external medium plays the role of the other MC. If the external layer consists of a material with the highest refractive index (from the refractive indices of the two materials comprising the distributed Bragg reflector), an external microcavity is formed only for TM polarization if the angle of incidence exceeds the Brewster angle at the interface between the external medium and the upper layer. This condition was met in the experiment. If the external layer is made of a material with a lower refractive index, an external microcavity is formed for TE polarization.

Approximate analytical expressions for the resonance-peak splitting and the threshold angle at which the splitting arises are obtained. The results of calculations by these expressions are in good agreement with the experimental data.

APPENDIX

Splitting of the Resonance Peaks in Transmission Spectra

At large angles of incidence, the DBR reflection coefficients $|r_{com}|$ and $|r_B|$ show only a weak angle dependence and may be calculated analytically using the formulas reported in [11] or by the transfer-matrix method. With reflection coefficients taken for the interval of angles where splitting is expected, one can find an approximate value of the angle φ_{Sp} at which splitting arises. In TM polarization (the refractive index of the external layer is n_1),

$$\varphi_{Sp} = \arcsin\sqrt{\frac{dn_V^2 - n_1^2}{n_V^2(d-1)}},$$

where

$$d = \left(\frac{n_1}{n_V}\right)^4\left(\frac{1+|\tilde{r}_{top}|}{1-|\tilde{r}_{top}|}\right)^2.$$

In TE polarization (the refractive index of the external layer is n_2, $n_2 < n_1$),

$$\varphi_{Sp} = \arcsin\sqrt{\frac{dn_2^2 - n_V^2}{n_V^2(d-1)}},$$

where

$$d = \left(\frac{1-|\tilde{r}_{top}|}{1+|\tilde{r}_{top}|}\right)^2.$$

For both polarizations,

$$|\tilde{r}_{\text{top}}| = \frac{1}{2\sqrt{2}}\sqrt{27\frac{|r_B|}{|r_{\text{com}}|^3} - 18\frac{|r_B|}{|r_{\text{com}}|} - |r_{\text{com}}||r_B| + |r_B|(|r_{\text{com}}|^2 - 9)^{3/2}\frac{\sqrt{|r_{\text{com}}|^2 - 1}}{|r_{\text{com}}|^3}}$$

The splitting of the resonance peaks in transmission spectra is expressed as

$$\Delta\omega_r = \frac{2}{\alpha + \beta}\arccos(g), \qquad \text{(A.1)}$$

where

$$g = (s\{-3s + a[-2 + s(a + 2s)]\} + v^2$$
$$+ a(a + 2s)v^2 - \sqrt{f})/(6(a + 2s)(s^2 + v^2)),$$
$$f = (s\{-3s + a[-2 + s(a + 2s)]\}$$
$$+ v^2 + a(a + 2s)v^2)^2 + 3(a + 2s)(s^2 + v^2)$$
$$\times((1 + s^2)[2a^2s + 6s^3 + a(7s^2 - 1)]$$
$$+ 2[a + (3 + a^2)s + 3as^2 + 2s^3]v^2 - (a + 2s)v^4),$$
$$s = u - a/3, \quad u = \frac{1}{2}\left(\frac{p/3}{\Lambda} - \Lambda\right),$$
$$v = \frac{\sqrt{3}}{2}\left(\frac{p/3}{\Lambda} + \Lambda\right), \quad \Lambda = \left(-\frac{q}{2} + \sqrt{\left(\frac{q}{2}\right)^2 + \left(\frac{p}{3}\right)^3}\right)^{1/3},$$
$$p = -\frac{a^2}{3} + b, \quad q = \frac{2}{27}a^3 - \frac{ab}{3} + c,$$

$a = -\mu|\tilde{r}_{\text{com}}|/\tilde{r}_{\text{top}}$, $b = -|r_{\text{com}}|/|r_B|$, $c = \mu/\tilde{r}_{\text{top}}|r_B|$, and μ is the sign of r_{com} at the photonic midgap. Under the condition $\arg r_{\text{com}} = \arg r_B$, the poles of expression (1) take the values $x_1 = u - a/3 - iv$, $x_2 = u - a/3 + iv$, and $x_3 = -2u - a/3$.

ACKNOWLEDGMENTS

This study was supported by the Ministry of Industry, Science, and Technology of the Russian Federation (under the program "Physics of Solid-State Nanostructures") and by the Russian Foundation for Basic Research, project no. 02-02-17601.

REFERENCES

1. *Microcavities and Photonic Band Gaps: Physics and Applications*, Ed. by J. Rarity and C. Weisbuch (Kluwer Academic, Dordrecht, 1996), NATO Adv. Study Inst. Ser., Ser. E, Vol. 324.
2. C. Weisbuch, M. Nishioka, A. Ishikawa, and Y. Arakawa, Phys. Rev. Lett. **69**, 3314 (1992).
3. R. P. Stanley, R. Houdré, U. Oesterle, *et al.*, Appl. Phys. Lett. **65**, 2093 (1994).
4. D. Baxter, M. S. Skolnick, A. Armitage, *et al.*, Phys. Rev. B **56**, 10032 (1997).
5. A. B. Pevtsov, A. V. Zherzdev, N. A. Feoktistov, *et al.*, Int. J. Electron. **78**, 289 (1995).
6. N. A. Feoktistov, N. L. Ivanova, L. E. Morozova, *et al.*, Mater. Res. Soc. Symp. Proc. **420**, 189 (1996).
7. A. A. Dukin, N. A. Feoktistov, V. G. Golubev, *et al.*, Appl. Phys. Lett. **77**, 3009 (2000).
8. V. G. Golubev, A. A. Dukin, A. V. Medvedev, *et al.*, Fiz. Tekh. Poluprovodn. (St. Petersburg) **35**, 1266 (2001) [Semiconductors **35**, 1213 (2001)].
9. A. A. Dukin, N. A. Feoktistov, V. G. Golubev, *et al.*, J. Non-Cryst. Solids **299–302**, 694 (2002).
10. A. Yariv and P. Yeh, *Optical Waves in Crystals* (Wiley, New York, 1984; Mir, Moscow, 1987).
11. G. Panzarini, L. C. Andreani, A. Armitage, *et al.*, Fiz. Tverd. Tela (St. Petersburg) **41**, 1337 (1999) [Phys. Solid State **41**, 1223 (1999)].
12. R. Ram, D. Babic, R. York, and J. Bowers, IEEE J. Quantum Electron. **31**, 399 (1995).

Translated by A. Sidorova

Semiconductors, Vol. 37, No. 7, 2003, pp. 838–842. Translated from Fizika i Tekhnika Poluprovodnikov, Vol. 37, No. 7, 2003, pp. 866–870.

ATOMIC STRUCTURE AND NONELECTRONIC PROPERTIES OF SEMICONDUCTORS

The Use of Magnesium to Dope Gallium Nitride Obtained by Molecular-Beam Epitaxy from Activated Nitrogen

A. A. Vorob'ev*, V. V. Korablev*, and S. Yu. Karpov**

**St. Petersburg State Technical University, St. Petersburg, 195251 Russia*

e-mail: type@bk.ru

***Soft-Impact, P.O. Box 33, St. Petersburg, 194156 Russia*

Submitted December 10, 2002; accepted for publication December 10, 2002

Abstract—A kinetic model for doping gallium nitride with magnesium in the course of molecular-beam epitaxy from plasma-activated nitrogen is suggested; the model parameters are determined. The theory relies on competitive quasi-equilibrium incorporation of Mg and Ga into the Group III sublattice and accounts for the main observed special features of doping, specifically, the dependence of Mg incorporation on temperature and on the V/III ratio in the incident fluxes. *© 2003 MAIK "Nauka/Interperiodica".*

1. INTRODUCTION

Nitrides of Group III elements are materials that find increasingly wide application in modern solid-state electronics. The unique properties of these direct-gap semiconductors include a band gap that varies from 1.9 to 6.2 eV as the composition changes, the presence of spontaneous polarization and a pronounced piezoeffect, high thermal conductivity, and the possibility of obtaining doped materials of both the *n*- and p-types; the above properties make it possible to use these materials for the fabrication of optical emitters (light-emitting diodes and lasers operating in the blue–green and, recently, ultraviolet spectral regions) and high-power transistors, as well as other electronic devices operating at high frequencies and temperatures and in aggressive media [1].

The first nitride epitaxial layers had a high residual *n*-type conductivity related to intrinsic point defects in the material; this conductivity could not be converted to the *p*-type conductivity by introducing relevant dopants. The *p*-type material was obtained for the first time in 1989 by a team headed by Akasaki [2], who used magnesium as an acceptor impurity in GaN epitaxy from metal–organic compounds (MOCs) (the so-called MOC-hydride epitaxy). Akasaki ascertained that irradiation of the grown GaN with low-energy electrons leads to activation of Mg acceptors (a similar effect of activation for Zn acceptors as a result of irradiation with a high-current electron beam was reported in earlier publications [3, 4]). In 1992, Nakamura *et al.* [5] suggested using thermal annealing at 500–700°C in nitrogen atmosphere in order to activate magnesium; this annealing was found compatible with the technology of growing nitride structures from the gaseous phase. As was found in subsequent studies, the cause of low Mg activity in GaN grown from the gaseous phase was related to hydrogen, which was introduced into the crystal during growth and passivated acceptors by forming complexes with neighboring nitrogen atoms [6]. In fact, both types of annealing (electron-beam and thermal) lead to decomposition of hydrogen-containing complexes, to extraction of hydrogen from the crystal, and, as a result, to activation of Mg acceptors (see, for example, [1]).

In contrast to gaseous-phase epitaxy, additional annealing for magnesium activation is not needed in molecular-beam epitaxy (MBE) because, in the latter case, there is no hydrogen medium in the course of growth. It has been experimentally ascertained that the Mg concentration increases linearly as the incident Mg flux increases [7, 8] and decreases with increasing growth temperature, which is typically equal to 600–800°C. The efficiency of introducing Mg into GaN depends heavily on the V/III ratio in the incident fluxes [8], so that the growth conditions which are related to enrichment with Ga and ensure good morphology of the GaN surface will be nonoptimal from the standpoint of doping. Finally, it was mentioned in a number of publications [7, 9] that the magnesium concentration levels off at a value of $\sim(1–3) \times 10^{19}$ cm^{-3} when the Mg flux incident on the growth surface increases. However, this phenomenon was not observed in other studies where MBE was employed using either plasma-activated nitrogen [10] or ammonia [11] as sources. The concentration of Mg introduced into the solid phase was as high as $\sim(2–5) \times 10^{20}$ cm^{-3} without any signs of leveling off [10, 11]. Thus, the experimental pattern of doping GaN with Mg in the course of MBE is found to be rather intricate and requires a detailed analysis of its basic mechanism.

To the best of our knowledge, a model that describes doping of GaN and can interpret the aforementioned experimental findings has not been suggested so far. In order to explain the levelling-off of the Mg concentra-

tion in GaN as the incident Mg flux increased, it was assumed [8] that Mg adsorption occurred in two stages, i.e., via the physical- and chemical-adsorption states, with the number of chemisorption sites at the GaN surface being smaller than the total number of sorption sites by three–four orders of magnitude. We believe that the existence of a physical-adsorption state for monatomic gases (e.g., for Mg) is unlikely since physical adsorption is typically associated with the van der Waals interaction of a gas with the surface. In addition, model [8] does not provide insight into the physical origin of limitation of the number of chemisorption sites, which constitutes an important element of the theory.

A kinetic model of doping, in which various modes of GaN MBE growth were considered separately, was suggested by Sipe and Venkat [12]. This publication was mainly aimed at explaining the inverse effect of Mg on the growth kinetics (this effect is not typical of the majority of experiments, see [13]). An important element of the theory [12] consists in the assumption that there is a high Mg concentration in the adsorption layer, which is inconsistent with observations [14] indicating that the lifetime of Mg at the GaN surface is short.

In this study, we suggest an alternative model of doping GaN with Mg MBE conditions; various modes of crystal growth are considered from a generalized standpoint in this model. We use this model to interpret the majority of available experimental data and quantitatively compare theory with experiment.

A description of the model and estimates of the parameters used in this model are given in Section 2. In Section 3, we report the results of comparing theory with experiment and consider the main trends in doping GaN with Mg using MBE with an activated nitrogen source. Conclusions from our study and unresolved issues are discussed in Section 4.

2. MODEL

In order to analyze the process of doping GaN with Mg, we used a kinetic approach similar to that described by Karpov *et al.* [15, 16]. This approach is based on the assumption that there is a quasi-equilibrium between the atoms adsorbed at the surface and those adsorbed in the crystal bulk. In fact, this assumption implies that the processes of adatom migration at the surface and the adatom incorporation into solid phase occur much more rapidly than those of adsorption and desorption of corresponding gaseous components. We also assume that Mg enters into the Ga sublattice and forms a solid substitutional solution within the Mg solubility limits in the solid phase. In this case, basic equations describing both GaN growth and the incorporation of Mg into the crystal can be written as

$$F_{\mathrm{Ga}} - k_{\mathrm{Ga}}\Theta_{\mathrm{Ga}} = V_g(1 - x_{\mathrm{Mg}}), \tag{1a}$$

$$F_{\mathrm{N}} - 2k_{\mathrm{N}}\Theta_{\mathrm{N}}^2 = V_g, \tag{1b}$$

$$F_{\mathrm{Mg}} - k_{\mathrm{Mg}}\Theta_{\mathrm{Mg}} = V_g x_{\mathrm{Mg}}, \tag{1c}$$

$$\frac{\Theta_{\mathrm{Ga}}\Theta_{\mathrm{N}}}{1-\Theta_{\mathrm{N}}} = \eta_{\mathrm{GaN}}\gamma_{\mathrm{GaN}}(1 - x_{\mathrm{Mg}}), \tag{1d}$$

$$\frac{\Theta_{\mathrm{Mg}}\Theta_{\mathrm{N}}}{1-\Theta_{\mathrm{N}}} = \eta_{\mathrm{MgN}}\gamma_{\mathrm{MgN}}x_{\mathrm{Mg}}, \tag{1e}$$

where F_{Ga}, F_{N}, and F_{Mg} are the fluxes of Ga, activated N, and Mg, respectively (measured in monolayers per second); k_{Ga}, k_{N}, and k_{Mg} are the desorption constants for Ga, molecular N, and Mg, respectively; Θ_{Ga}, Θ_{N}, and Θ_{Mg} are surface coverage with gallium, nitrogen, and magnesium, respectively (the values of Θ vary from zero to unity); V_g is the growth rate expressed in monolayers per second; x_{Mg} is the atomic fraction of magnesium in the gallium sublattice; and γ_{GaN} and γ_{MgN} are the activity coefficients for GaN and a hypothetical MgN compound which is incorporated into the substitutional solid solution. In the context of the model of regular solutions, the activity coefficients can be written as

$$\gamma_{\mathrm{GaN}} = \exp\left[\frac{W}{RT}x_{\mathrm{Mg}}^2\right],$$

$$\gamma_{\mathrm{MgN}} = \exp\left[\frac{W}{RT}(1 - x_{\mathrm{Mg}}^2)^2\right], \tag{2}$$

where W is the parameter of interaction between GaN and MgN in solid phase and R is the universal gas constant.

Equations (1a)–(1c) account for conservation of the number of atoms at the growth surface, whereas Eqs. (1d) and (1e) describe the quasi-equilibrium between atoms and the crystal [15, 16]. The constants η_{GaN} and η_{MgN} can be expressed in terms of equilibrium constants for reactions of formation of GaN and MgN from the corresponding gaseous-phase components [16] as

$$\eta_{\mathrm{GaN}} = (\alpha_{\mathrm{N_2}}^0 K_{\mathrm{GaN}}/k_{\mathrm{Ga}}^2 k_{\mathrm{N}})^{1/2}, \tag{3a}$$

$$\eta_{\mathrm{MgN}} = (\alpha_{\mathrm{N_2}}^0 K_{\mathrm{MgN}}/k_{\mathrm{Mg}}^2 k_{\mathrm{N}})^{1/2}. \tag{3b}$$

Here, $\alpha_{\mathrm{N_2}}^0$ is the temperature-dependent coefficient of attachement of molecular nitrogen to the GaN surface [17].

The concentration of magnesium in n_{Mg} crystal is calculated using the Mg atomic fraction x_{Mg} in the solid phase; i.e.,

$$n_{\mathrm{Mg}} = N_A(\rho_{\mathrm{GaN}}/M_{\mathrm{GaN}})x_{\mathrm{Mg}}, \tag{4}$$

where N_{A} is Avogadro's number; M_{GaN} is the molar mass of gallium nitride; and ρ_{GaN}, the density of gallium nitride.

Constants of desorption from the gallium nitride surface for the gaseous-phase components

ν	k_ν^0 (s^{-1})	E_ν/k (K)
N	1.50×10^{22}	53000
Ga	2.43×10^{13}	31448
Mg	7.71×10^{12}	14994

Temperature dependences of the constants describing the desorption of atoms and molecules from the crystal surface usually correrspond to the Arrhenius equation, i.e., $k_\nu = k_\nu^0 \exp(-E_\nu/kT)$, where ν = Ga, Mg, or N. The value of k_N was determined experimentally in [18]. It has been shown [16] that the values of k_{Ga} measured in a wide temperature range [19] are in good agreement with the rate of gallium desorption from the surface of the gallium liquid phase. Assuming that the behavior of magnesium, which also leaves the surface as a monatomic gas, is similar to that of gallium, we can estimate the desorption constant k_{Mg} as the rate of magnesium desorption from the surface of corresponding liquid. The resulting coefficients k_ν^0 and E_ν/k for the desorption constants appearing in Eqs. (1) are listed in the table.

Typically, the magnesium concentration in the crystal is found to be much lower than the gallium concentration; therefore, we may assume that $x_{Mg} \ll 1$. As a result, $\gamma_{GaN} \cong 1$ and Eqs. (1a), (1b), and (1d) form a decoupled system, which define the crystal-growth rate and the degrees of coverage of the surface with Ga and N, Θ_{Ga} and Θ_N.

At $x_{Mg} \ll 1$, the quantity $\gamma_{MgN} \cong \exp(W/RT)$ depends only on temperature. We then use Eqs. (1d) and (1e) to obtain

$$\frac{\Theta_{Mg}}{\Theta_{Ga}} = \frac{\eta_{MgN}(T)}{\eta_{GaN}(T)}\gamma_{MgN}\frac{x_{Mg}}{1-x_{Mg}} = \omega(T)\frac{x_{Mg}}{1-x_{Mg}}$$

and

$$x_{Mg} = \frac{\Theta_{Mg}}{\Theta_{Mg} + \omega\Theta_{Ga}}. \quad (5)$$

Substituting (5) into (1c) and taking into account that $x_{Mg} \ll 1$, we obtain

$$x_{Mg} = \frac{F_{Mg}}{V_g + k_{Mg}\omega\Theta_{Ga}}, \quad \Theta_{Mg} \cong \frac{F_{Mg}\omega\Theta_{Ga}}{V_g + K_{Mg}\omega\Theta_{Ga}}. \quad (6)$$

Expressions (6) make it possible to analyze various modes of Mg incorporation into GaN. If $V_g \gg k_{Mg}\omega\Theta_{Ga}$, magnesium is directly trapped by growing crystal, so that the magnesium atomic fraction $x_{Mg} = \Gamma_{Mg}/V_g$ is independenct of the growth conditions (of whether gallium or nitrogen are dominant in the incident fluxes) and of temperature. In the reverse situation ($V_g \ll k_{Mg}\omega\Theta_{Ga}$), the atomic fraction of introduced impurity $x_{Mg} = F_{Mg}/k_{Mg}\omega\Theta_{Ga}$ depends heavily on the V/III ratio in the incident fluxes in terms of the surface coverage Θ_{Ga} and on the growth temperature. The experimental data (see Section 1) show that incorporation of magnesium into GaN follows exactly this pattern. The magnesium concentration depends linearly on the incident flux F_{Mg} in both above-considered cases.

The temperature dependence of the Mg concentration is governed by the quantity ω(*T*), which can be treated, according to expression (5), as the magnesium segregation coefficient. This quantity differs from the generally accepted definition of the segregation coefficient as the ratio Θ_{Mg}/x_{Mg} in the factor Θ_{Ga}. However, we believe that such an introduction of the segregation coefficient ω(*T*) is correct since this definition accounts for the thermodynamic features of competitive incorporation of Mg and Ga into the Group III sublattice of the crystal.

Unfortunately, we cannot directly estimate the quantity ω(*T*), owing to the lack of experimental data on the equilibrium solubility of Mg in GaN. Therefore, in this study we used the Arrhenius approximation $\omega(T) = \omega_0\exp(-E_\omega/kT)$ and determined the values of ω_0 and E_ω/k by fitting them to the experimental dependence of the Mg concentration on temperature (the latter dependence was reported in [9]). As a result, we found that $\omega_0 = 3.523 \times 10^5$ and $E_\omega/k = 21070$ K. As the temperature is increased from 600 to 800°C, the segregation coefficient increases from 10^{-5} to 10^{-3}. Since the dependence ω(*T*) is governed only by the fundamental properties of the material and gaseous-phase components, which react at the crystal surface, this quantity should depend only slightly on the technology used to grow GaN.

3. RESULTS

The suggested model, where parameters were defined in Section 2, was used to analyze the main mechanisms behind the doping of GaN with magnesium in the course of MBE from plasma-activated nitrogen.

Figure 1 illustrates the linear relation between the Mg concentration in GaN and the incident flux of magnesium F_{Mg}; this relation is observed experimentally for an Mg concentration of $\sim 2 \times 10^{19}$ cm^{-3}. According to the data reported in [7–9], the Mg concentration in the solid phase levels off as the incident Mg flux increases further. Such behavior cannot be described in the context of the suggested model. In our opinion, this apparent change of the doping mechanism is most probably related to the formation of a large number of defects at a certain critical Mg concentration in the solid phase. Indeed, it has been noted [20, 21] that the polarity of a growing crystal changes at high Mg concentrations; this change should inevitably manifest itself in the formation of antiphase domains. Since the

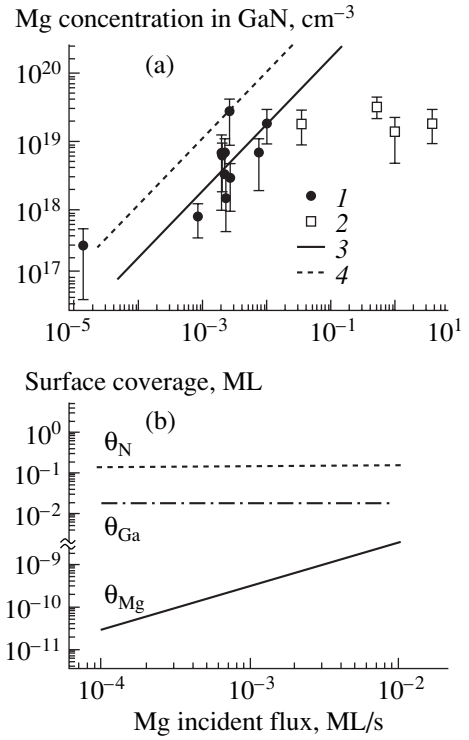

Fig. 1. Dependences of (a) the magnesium concentration and (b) the degrees of surface coverage on the incident flux of Mg. F_{Ga} = 0.30 ML/s and F_N = 0.35 ML/s. In (a): (*1*) represent the data obtained in [7, 8], (*2*) represent the data reported in [9], curve (*3*) represents theoretical results for T = 750°C, and curve (*4*) represents theoretical results for T = 700°C. In (b), the results correspond to T = 750°C.

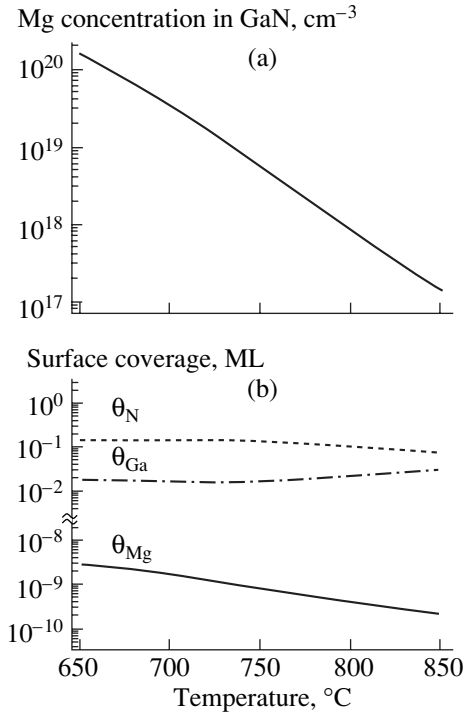

Fig. 2. Dependences of (a) the magnesium concentration and (b) the degrees of surface coverage on the growth temperature. The incident fluxes were equal to F_{Ga} = 0.30 ML/s, F_N = 0.35 ML/s, and F_{Mg} = 0.003 ML/s.

polarity itself affects Mg incorporation [22, 23] and the boundaries of antiphase domains can act as sinks for impurity atoms, it is hardly appropriate to state, under these conditions, that there is a single dominant mechanism for the incorporation of acceptors. The fact that a leveling-off of the Mg concentration was not observed in other studies concerned with growing GaN from both ammonia [11] and plasma-activated nitrogen [10] can also be treated as support of the assumption that the levelling-off of the magnesium concentration is related to the degree of imperfection of the material.

The behavior of the Mg coverage of the surface in relation to the Mg incident flux is illustrated in Fig. 1b. It can be seen that the surface coverage with magnesium is found to be smaller than thate with gallium and nitrogen by many orders of magnitude; this inference is consistent with that reported by Ramachandran *et al*. [14]. Such behavior is expected for the entire temperature range (550–850°C) of interest for GaN epitaxy.

We calculated the temperature dependence of the magnesium concentration in the solid phase for typical parameters of the growth process; this dependence is shown in Fig. 2a. The appreciable decrease in the efficiency of Mg incorporation with increasing temperature is related both to (i) enhancement of Mg desorption from the GaN surface and to (ii) an increase in the seg-

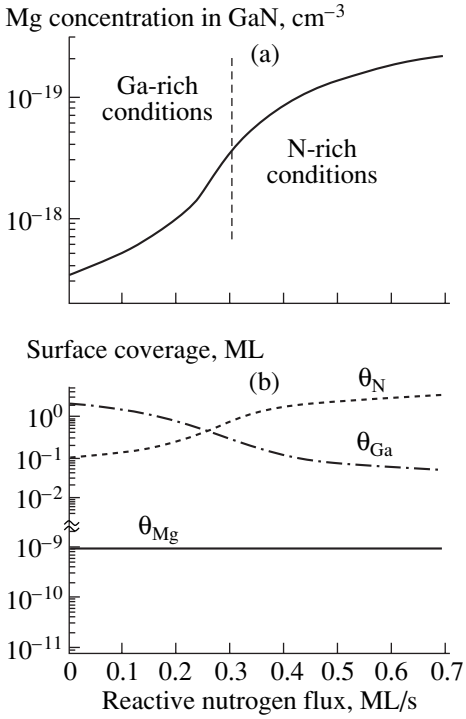

Fig. 3. Dependences of (a) the magnesium concentration and (b) the degrees of surface coverage on the flux of activated nitrogen at a constant gallium flux. T = 750°C, F_{Ga} = 0.30 ML/s, and F_{Mg} = 0.003 ML/s.

regation coefficient $\omega(T)$. As a result of factor (i), the surface coverage with magnesium decreases gradually with temperature, as is shown in Fig. 2b.

In order to gain insight into the effect of the V/III ratio of the incident fluxes on the Mg incorporation, we varied the activated nitrogen flux while keeping the incident gallium flux constant (Fig. 3). As can be seen, the most drastic change in the incorporation efficiency is observed at the transition from Ga-enriched ($F_N <$ 0.3 ML/s) to N-enriched ($F_N >$ 0.3 ML/s) surface-growth conditions. Notably, the N-enriched conditions at the surface ensure far more (by an order of magnitude) efficient incorporation of Mg into the crystal, which is in good agreement with experimental data [8, 22]. This effect is caused by the appreciable variation in the Ga surface coverage in the course of transition from the Ga- to N-enriched surface-growth conditions (Fig. 3b), which, according to (6), affects the efficiency of Mg incorporation into GaN.

4. CONCLUSION

In this paper, we suggested a kinetic model of doping gallium nitride with magnesium, with GaN being grown by molecular-beam epitaxy using plasma-activated nitrogen. The model is based on the assumption that there is quasi-equilibrium between atoms in the adsorption layer and those in the crystal bulk. The theoretical predictions of the model are in good agreement with experimental data reported in a number of publications. We determined the basic parameters of the model and their temperature dependences, which made it possible to predict quantitatively the acceptor concentration in the solid phase on the basis of the GaN growth conditions (temperature and incident fluxes of gallium, active nitrogen, and magnesium). Theory shows that magnesium incorporation proceeds in the quasi-equilibrium mode; i.e., the magnesium concentration in the solid phase depends weakly on the growth rate of the crystal but depends heavily on both the rate of Mg desorption from the surface and the coverage of the surface with Ga. The latter factor allows for competitive incorporation of the gallium and magnesium atoms into the sublattice of Group III elements and, in fact, brings about a strong dependence of the efficiency of Mg incorporation into GaN on the V/III ratio in the incident fluxes.

In this study, the segregation coefficient for magnesium $\omega(T)$ was determined empirically, i.e., by fitting the results of calculations to the chosen experimental data. Therefore, it is of particular interest to estimate theoretically the above coefficient on the basis of the difference between covalent radii of Mg and Ga, a comparison of the Ga–N and Mg–N bond energies, and so on. Such an estimate, in combination with more detailed experimental studie, would make it possible to refine this (most critical) parameter of the model and, correspondingly, to make more clear the mechanism of doping, which is used as the basis for the model.

In our opinion, the suggested model of doping is quite general and relies to a small extent on specific features of the epitaxial process under consideration (MBE). This circumstance makes it possible to generalize the model to other methods for growth, i.e., vapor-phase epitaxy and molecular-beam epitaxy from ammonia. A comparison of the theoretical results obtained for these epitaxial methods with experimental data would provide additional corroboration of the theory developed in this study.

REFERENCES

1. O. Ambacher, J. Phys. D **31**, 2653 (1998).
2. H. Amano, M. Kito, K. Hiramatsu, and I. Akasaki, J. Appl. Phys. **28**, 2112 (1989).
3. G. V. Saparin, S. K. Obyden, M. V. Chukhichev, and S. I. Popov, Microelectron. Eng. **1**, 179 (1983).
4. S. K. Obyden, G. A. Perlovskiĭ, G. V. Saparin, and A. G. Nikolaev, Izv. Akad. Nauk SSSR, Ser. Fiz. **51**, 452 (1987).
5. S. Nakamura, T. Mukai, M. Senoh, and N. Iwasa, J. Appl. Phys. **31**, 139 (1992).
6. N. M. Johnson, W. Götz, J. Neugebauer, and C. G. Van de Walle, Mater. Res. Soc. Symp. Proc. **395**, 723 (1996).
7. D. J. Dewsnip, J. W. Orton, D. E. Lacklison, *et al.*, Semicond. Sci. Technol. **13**, 927 (1998).
8. J. W. Orton, C. T. Foxon, T. S. Cheng, *et al.*, J. Cryst. Growth **197**, 7 (1999).
9. S. Guha, N. A. Bojarzuk, and F. Cardone, Appl. Phys. Lett. **71**, 1685 (1997).
10. I. P. Smorchkova, E. Haus, B. Heying, *et al.*, Appl. Phys. Lett. **76**, 718 (2000).
11. M. Kamp, M. Mayer, A. Pelzmann, and K. J. Ebeling, MRS Internet J. Nitride Semicond. Res. **2**, 26 (1997).
12. N. Sipe and R. Venkat, MRS Internet J. Nitride Semicond. Res. **7**, 1 (2002).
13. B. Dadin, G. Mula, and P. Peyla, Phys. Rev. B **61**, 10330 (2000).
14. V. Ramachandran, R. M. Feenstra, J. E. Northrup, and D. W. Greve, MRS Internet J. Nitride Semicond. Res. **5S1**, W3.65 (2000).
15. S. Yu. Karpov and M. A. Maiorov, Surf. Sci. **393**, 108 (1997).
16. S. Yu. Karpov, R. A. Talalev, Yu. N. Makarov, *et al.*, Surf. Sci. **450**, 191 (2000).
17. S. Yu. Karpov, Yu. N. Makarov, and M. S. Ramm, MRS Internet J. Nitride Semicond. Res. **2**, 45 (1997).
18. O. Brandt, H. Yang, and K. H. Ploog, Phys. Rev. B **54**, 4432 (1996).
19. S. Guha, N. A. Bojarczuk, and D. W. Kisker, Appl. Phys. Lett. **69**, 2879 (1996).
20. V. Ramachandran, R. M. Feenstra, W. L. Sarney, *et al.*, Appl. Phys. Lett. **75**, 808 (1999).
21. P. Vennegues, M. Benaissa, B. Beaumont, *et al.*, Appl. Phys. Lett. **77**, 880 (2000).
22. L. K. Li, M. J. Jukovic, W. I. Wang, *et al.*, Appl. Phys. Lett. **76**, 1740 (2000).
23. T. H. Myers, A. J. Ptak, L. Wang, and N. C. Giles, in *Proceedings of International Workshop on Nitride Semiconductors*, IPAP Conf. Ser. 1, 451 (2000).

Translated by A. Spitsyn

Semiconductors, Vol. 37, No. 7, 2003, pp. 843–845. Translated from Fizika i Tekhnika Poluprovodnikov, Vol. 37, No. 7, 2003, pp. 871–873.

ATOMIC STRUCTURE AND NONELECTRONIC PROPERTIES OF SEMICONDUCTORS

Simulation of Growth Kinetics of Octahedral and Platelike Oxygen Precipitates in Silicon

V. V. Svetukhin*, A. G. Grishin, and O. V. Prikhod'ko

Ulyanovsk State University, ul. Tolstogo 42, Ulyanovsk, 432700 Russia

**e-mail: slava@sv.uven.ru*

Submitted October 28, 2002; accepted for publication December 3, 2002

Abstract—A model describing the growth kinetics of the characteristic size of octahedral and platelike oxygen precipitates in silicon is suggested. It is shown that the experimental data of various authors on the growth kinetics of precipitates are adequately described by the assumption that their growth is limited by diffusion, while the geometry of precipitates is characterized by constant eccentricity. *© 2003 MAIK "Nauka/Interperiodica".*

It is well known that, depending on temperature, oxygen precipitates in silicon can assume two different shapes: a platelike shape at low temperatures and octahedral shape at high temperatures [1, 2]. Data on the geometry of oxygen precipitates are usually obtained using in an electron microscope. The experimental data of various authors are analyzed in [1], and it is shown that the time dependence of the size of growing precipitates is characterized by the power law ($t^{0.5}$) and that this dependence is obeyed for both octahedral and platelike precipitates.

In this study, we suggest a model describing the kinetics of growth of oxygen precipitates with various shapes.

A theoretical model of the precipitation of point defects in crystals was suggested in [3]. It was shown that the kinetics of precipitation of point defects in semiconductors can be described by the differential equation

$$\frac{dN(t)}{dt} = -k_0 N_c^{1-\alpha}[N(t) - N_e][N(0) + mN_c - N(t)]^{\alpha}, \quad (1)$$

where $N(t)$ is the concentration of interstitial oxygen unbound to precipitates, N_c is the concentration of centers of nucleation of oxygen precipitates, N_e is the equilibrium concentration of interstitial oxygen in silicon, and m is the number of oxygen atoms in the nucleation center (it is assumed that $m = 5$). The parameter α accounts for the geometry of precipitates (for the precipitates with a constant eccentricity $\alpha = 1/3$ [3]). The kinetic coefficient k_0 is related to the diffusion coefficient D of interstitial oxygen by the formula $k_0 = 4\pi Da$, where $a = 2.5$ Å and can be calculated from the density of the SiO_2 phase.

Asymptotics of Eq. (1) for long and short times are consistent with the Ham theory and have the following form:

$$\frac{N(t) - N_e}{N(0) - N_e} = \exp\left\{-N_c\{(1-\alpha)[N(0) - N_e]^{\alpha}k_0 t\}^{\frac{1}{1-\alpha}}\right\}, \quad (2)$$

$$\frac{N(t) - N_e}{} = A\exp\{-N_c^{1-\alpha}[N(0) + mN_c - N_e]^{\alpha}k_0 t\}. \quad (3)$$

The average number of oxygen atoms in precipitates $n(t)$ can be found from the law of conservation of the number of oxygen atoms in silicon:

$$n(t) = \frac{N(0) - N(t)}{N_c}. \quad (4)$$

The average size of precipitates $R(t)$ and the number of particles in precipitates $n(t)$ at the initial stage of precipitation are described by the following asymptotic expressions [3]:

$$R(t) \propto t^{\frac{\alpha}{1-\alpha}}, \quad n(t) \propto t^{\frac{1}{1-\alpha}}. \quad (5)$$

The temperature dependence of the concentration of nucleation centers is determined from the data obtained by electron microscopy [2]:

$$N_c = 0.15\exp(2.65/kT). \quad (6)$$

The temperature dependence of the equilibrium concentration of interstitial oxygen in silicon is given by [2]:

$$N_e = 9 \times 10^{22}\exp(-1.52/kT). \quad (7)$$

1063-7826/03/3707-0843$24.00

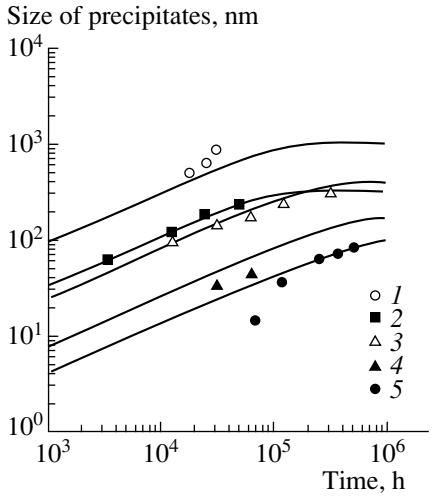

Fig. 1. Dependence of average size of (*1*, *3*–*5*) platelike and (*2*) octahedral precipitates on the time of annealing at various temperatures T = (*1*) 1050, (*2*) 1100, (*3*) 900, (*4*) 800, and (*5*) 750°C. Simulation by formulas (11) and (14) is shown by lines; experimental data [1] are shown by circles, squares, and triangles.

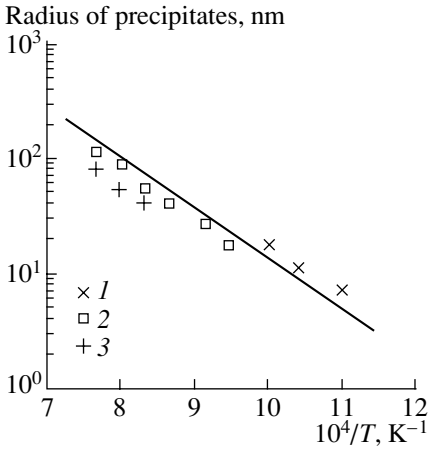

Fig. 2. Equilibrium radius of oxygen precipitates as a function of reciprocal temperature. Simulation by formula (15) is shown by the line. Experimental data [2] are obtained by (*1*) neutron scattering, (*2*) chemical etching, and (*3*) light scattering.

The kinetic coefficient in Eq. (1) was found from proposed experimental data on the kinetics of oxygen precipitation at various temperatures [3]:

$$k_0 = 3.08 \times 10^{-8} \exp(-2.44/kT). \quad (8)$$

Consider a platelike precipitate having a square base with a side L and thickness d. We assume that the ratio $\gamma = d/L$ remains constant during the growth of a precipitate. The volume of a precipitate is

$$V = L^2 d = \gamma L^3, \quad (9)$$

while the oxygen precipitate consisting of n_p molecules of SiO_2 occupies, in a silicon lattice, the volume

$$V = n_p v_p = n v_p/2 = n v, \quad (10)$$

where $v_p = 4.5 \times 10^{-23}$ cm^3 is the volume occupied by a single SiO_2 molecule in silicon crystal lattice, and $v = v_p/2$ is the volume per single oxygen atom in a precipitate.

Combining formulas (9) and (10), we can obtain the time dependence of parameters L and d in the process of growth of platelike precipitate with constant eccentricity:

$$L(t) = \left(\frac{vn(t)}{\gamma}\right)^{1/3}, \quad (11)$$

$$d(t) = [v\gamma^2 n(t)]^{1/3}. \quad (12)$$

The volume of a precipitate shaped as an octahedron with an edge length l can be written as

$$V = \frac{\sqrt{2}}{3} l^3. \quad (13)$$

By equating expressions (10) and (13) we can obtain the time dependence of the edge length l of growing precipitate:

$$l(t) = \left(v\frac{3n(t)}{\sqrt{2}}\right)^{1/3}. \quad (14)$$

Using the idealized concept of spherical precipitates and expressions similar to (11) and (14), we can obtain the following relation for the average radius of precipitates:

$$R(t) = \left(v\frac{3n(t)}{4\pi}\right)^{1/3}. \quad (15)$$

Solving Eq. (1) and determining the time dependence of the mean number of particles in a precipitate with the aid of the expression (4), we can determine the average size of platelike (11)–(12) or octahedral (14) precipitates at any instant of time t.

Figure 1 shows the results of numerical simulation of the kinetics of the average size of platelike and octahedral precipitates as compared to the experimental data [1]. Taking into account the rather large error in the experimental estimation of precipitate sizes, the agreement between theory and experiment may be considered quite satisfactory. In accordance with expression (11), the characteristic size of precipitates with constant eccentricity varies with time at the initial stage of precipitation according to a power law ($t^{0.5}$), which is consistent with experimental data [1].

We can also determine the temperature dependence of the average size of precipitates subjected to long annealing periods (equilibrium size). Since the geometry of precipitates varies with temperature, the calculations are performed using formula (15) assuming a spherical shape of precipitates. Figure 2 shows the results of numerical simulation of the average equilibrium size of precipitates compared to the experimental data [2].

In summary, our calculations showed that the growth kinetics of oxygen precipitates of various shapes is adequately described by the model suggested in [3] assuming that the growth of precipitates is limited by the diffusion of interstitial oxygen and that the precipitates themselves are characterized by constant eccentricity.

REFERENCES

1. J. J. Vanhellemont, J. Appl. Phys. **78**, 4297 (1995).
2. A. Borghesi, B. Pivac, A. Sassella, and A. Stella, J. Appl. Phys. **77**, 4169 (1995).
3. S. V. Bulyarskiĭ, V. V. Svetukhin, and O. V. Prikhod'ko, Fiz. Tekh. Poluprovodn. (St. Petersburg) **33**, 1281 (1999) [Semiconductors **33**, 1157 (1999)].
4. F. S. Ham, Phys. Chem. Solids **6**, 335 (1958).

Translated by A. Zalesskiĭ

Semiconductors, Vol. 37, No. 7, 2003, pp. 846–854. Translated from Fizika i Tekhnika Poluprovodnikov, Vol. 37, No. 7, 2003, pp. 874–882.

ELECTRONIC AND OPTICAL PROPERTIES OF SEMICONDUCTORS

Special Features of Electron Spin Resonance in 4*H*-SiC in the Vicinity of the Insulator–Metal Phase Transition: I. Effects of Spin Interaction

A. I. Veĭnger*, A. G. Zabrodskiĭ, T. V. Tisnek, and E. N. Mokhov

Ioffe Physicotechnical Institute, Russian Academy of Sciences, Politekhnicheskaya ul. 26, St. Petersburg, 194021 Russia

**e-mail: anatoly.veinger@mail.ioffe.ru*

Submitted January 14, 2003; accepted for publication January 21, 2003

Abstract—Special features of electron spin resonance in the vicinity of the insulator–metal phase transition in *n*-type 4*H*-SiC:N were investigated. It was shown that, in the insulating state, an antiferromagnetic phase of the spin-glass type is formed in this region. As a result, with increasing doping level, the content of the paramagnetic phase decreases, and, at an impurity concentration close to critical (corresponding to the transition), the resonance line of nitrogen atoms disappears. Instead of it, a line of deep-level impurity centers is observed at the same position in the metallic state. In addition, two new lines are observed in the metallic state in strong fields; these lines are attributed to free charge carriers. © *2003 MAIK "Nauka/Interperiodica"*.

1. INTRODUCTION

To date, the magnetic properties of doped semiconductors in the vicinity of the insulator–metal (IM) phase transition have been much less studied than their electrical properties. According to existing concepts (see, for example, [1]), with increasing the level of doping of an *n*-type semiconductor with shallow-level impurities, the approach to the IM-transition point should substantially manifest itself in the appearance of antiferromagnetic interaction, which transforms into Pauli paramagnetism in the metallic state.

The experimental studies of electron spin resonance (ESR) in various *n*-type semiconductors (Si:P, Si:As [2–6], Ge:As [7], 6*H*-SiC:N [8–10]) showed that, at a rather high doping level, the spins of individual atoms indeed become collectivized. This phenomenon manifests itself in the fact that a set of ESR spectral lines, which corresponds to the spin of an isolated nucleus of a shallow-level impurity center, transforms into a characteristic exchange-narrowed single line. A further increase in the concentration of donors makes the spin density tend toward a constant value in Si:P [11] and even results in decreasing spin density in 6*H*-SiC:N [9, 10]. Investigations of ESR in Si in the metallic state near the IM phase transition [5, 11, 12] showed that a noticeable decrease in an ESR signal occurs in this region, which should be expected if Curie paramagnetism transforms into Pauli paramagnetism.

In comparison with Si, ESR has been studied much less in other semiconductors. With respect to Ge, the reason is that the lines in the ESR spectrum of Ge are fairly broad. In addition, in some cases, the spectral line disappears in the vicinity of the IM phase transition [13, 14]. ESR was observed in Ge near the transition point at a frequency of 63.2 MHz [15]. The ESR signal decreased upon cooling Ge samples to ultralow temperatures and increased upon their uniaxial compression. A number of special features was observed in the ESR spectrum of compensated Ge in the vicinity of the IM phase transition in [16]. Among these were the transformation of the line shape from Lorentzian into Dysonian; narrowing of the line with increasing temperature; the temperature dependence on the degree of line distortion; and the appearance of an additional line of unusual shape, which rapidly shifts to stronger fields with decreasing temperature. Thus, it turned out that the behavior of ESR near the IM-transition point in Si, which has been well studied, is not the only possible variant and, in order to understand the whole variety of processes that may occur in a semiconductor in the vicinity of the IM phase transition, one should expand the range of materials under study.

For such investigations, silicon carbide, in which ESR can be easily observed, seems to be attractive. However, the most abundant polytype 6*H*-SiC is not very appropriate for studies near the IM-transition point because, in the case of doping with nitrogen, which is a donor impurity with the shallowest level, the IM phase transition occurs at the concentration $n_c \approx 10^{20}$ cm^{-3}. It is difficult to obtain such a doping level from the technological point of view. As a result, investigations of ESR in the vicinity of the IM phase transition in this material are scarce [9, 10]. It has been shown that, with an increase in the impurity concentration to the critical value, the spin density decreases, whereas the ESR spectral line broadens.

The polytype 4*H*-SiC, which is characterized by the lowest activation energy of nitrogen (35 meV) among other polytypes, is much more convenient for such

investigations. The IM phase transition in 4*H*-SiC should occur at the donor concentration, which can easily be obtained. The electrical characteristics of this polytype have not been adequately investigated, especially for the case of heavy doping. However, its basic parameters are known (see Table 1).

This study is devoted to the experimental investigation of special features of ESR in the vicinity of the IM phase transition in 4*H*-SiC. Due to the large volume of experimental data, the effects of spin interaction are considered separately from the analysis of the width and shape of resonance lines.

2. EXPERIMENTAL

For measuring the ESR spectra of 4*H*-SiC samples, we used a Varian ESR *E*-112 spectrometer (operating at a frequency of 10 GHz) in combination with an ESR-9 (Oxford Instruments) cryostat, which allowed us to record spectra in a wide temperature range from 3.2 to 300 K. Generally, at temperatures above 100 K, the spectra broadened and disappeared even in the case of the most lightly doped samples.

The experimental samples were grown by the sublimation sandwich method [17] and had a nitrogen impurity concentration in the range of 2.3×10^{17}–2.6×10^{19} cm^{-3}. The impurity concentration was determined Hall effect measurements at room temperature. It was assumed that all impurities are ionized and the concentration of intrinsic carriers is negligible at this temperature. This holds true for 4*H*-SiC, since the donor level of nitrogen impurity is rather shallow and the band gap is large for this material. The parameters of the samples obtained from measuring the Hall effect are listed in Table 2.

The sandwich method allows one to obtain single crystals with a fairly large area, which are commonly not quite uniform and highly strained. Generally, the compensation by intrinsic carriers in SiC single crystals amounted to about 20%. Since the calculation of the impurity concentration from measuring the Hall effect in the depletion region makes it possible to determine only the difference between the concentrations of donors and acceptors, it is this difference which is meant when speaking of the impurity concentration in what follows. Compensation and inhomogeneities in samples lead to uncontrolled spread in experimental data; however, as will be seen below, the trends in the dependences measured can be traced quite distinctly.

Recording ESR signals involved specific features caused by an increase in the conductivity of samples in the range of liquid-helium temperatures. Specifically, we observed changes in the resonator *Q* factor, which at first decreased with increasing conductivity due to increasing nonresonant microwave absorption. Then, the *Q* factor started to increase when the absorption diminished due to decreasing skin depth. In order to take this feature into account, we used a resonator with

Table 1. Electrical parameters of 4*H*-SiC

Most probable localization of the absolute minimum of the *C* band	Near *M*–*L*
Most probable number of valleys	6
Band gap ΔE_g, eV	3.29 at $T = 0$ K 3.10 at $T = 300$ K
Ionization energy of shallow-level donors (nitrogen), eV	$E_{D1} = 0.035$ $E_{D2} = 0.09$
Anisotropy of conductivity ($\rho_\parallel/\rho_\perp$)	0.9
Effective electron mass in a valley $m_{e,\,val}$	0.17–0.21
Effective mass corresponding to the density of states in the *C* band	0.55–0.70
Electron mobility at 300 K, $\mu_n(\perp c)$, cm^2 V^{-1} s^{-1}	800
Hole mobility at 300 K, μ_p, cm^2 V^{-1} s^{-1}	80
Relative permittivity	9.7

two antinodes from a magnetic microwave field and, when measuring the spin density, along with the ESR signal from the sample being studied, the signal from a Varian reference sample was simultaneously recorded as well. The reference sample had a spin density of 2.58×10^{15} cm^{-1} and $g = 2.0028$ (the sample had the form of a long cylindrical cell of 4 mm in diameter; the above value of concentration is for 1 cm of the sample length). The spin density was calculated by comparing signals from the sample under study and the reference sample.

In the calculations of spin density, we disregarded the fact that, due to increasing sample conductivity, the skin depth layer became less than the sample thickness; therefore, the effective volume of the sample decreased as well. The maximum dimensions of the samples studied were $3 \times 1 \times 0.3$ mm^3. At present, it is impossible to calculate exactly the skin depth; however, we can estimate the error appearing when the effective volume of a sample is replaced with its total volume in calculations. It is known that the IM phase transition occurs in Ge:Ga, Si:P, and 6*H*-SiC when the resistivities in these semiconductors become as low as 0.1 Ω cm [18], 0.05 Ω cm [19], and 0.008 Ω cm [20], respectively. The value of resistivity corresponding to the IM transition in 4*H*-SiC should be between the values typical of Si and 6*H*-SiC. In our opinion, we may assume with a fair degree of confidence that this transition occurs in 4*H*-SiC when its resistivity attains the value of about 10^{-2} Ω cm. In this case, the skin depth should be about 0.05 mm. Consequently, the effective volume is about 1/3 of the total volume, and the measurement error in determining the spin density is no larger than a factor of 3. We disregard this error because it is insignificant in comparison with the decrease in the spin density by two

Table 2. Parameters of *n*-4*H*-SiC:N samples under study

Sample no.	Conductivity σ, $(\Omega\ \text{cm})^{-1}$, at 300 K	Mobility μ, $\text{cm}^2\ \text{V}^{-1}\ \text{s}^{-1}$, at 300 K	Hall concentration n_H, cm^{-3}	Spin density n_s, cm^{-3}
1	1.73	48	2.26×10^{17}	5×10^{17}
2	4.63	81	$(3.3–3.85) \times 10^{17}$	1.25×10^{18}
3	24.1	38.8	3.89×10^{18}	2.4×10^{18}
4	49.3	53.5	5.76×10^{18}	2.2×10^{18}
5	47	40	$(6.8–7.6) \times 10^{18}$	3.3×10^{18}
6	57	47	$(7.3–7.7) \times 10^{18}$	4×10^{18}
7	48.3	39.4	7.66×10^{18}	2.5×10^{18}
8	56.7	43	8.32×10^{18}	2.1×10^{18}
9	51.8	38	$(7.9–9.1) \times 10^{18}$	2.3×10^{18}
10	221	150	$(8.3–9.7) \times 10^{18}$	1.3×10^{18}
11	63.1	42.5	9.3×10^{18}	1.5×10^{18}
12	65	40	1×10^{19}	8.5×10^{17}
13	62	38	1×10^{19}	3.1×10^{17}
14	63.5	35.5	1.1×10^{19}	7×10^{17}
15	67	35	$(1.1–1.3) \times 10^{19}$	1.2×10^{17}
16	78.6	36	1.38×10^{19}	9.6×10^{16}
17	87.2	33	$(1.5–1.8) \times 10^{19}$	2.4×10^{17}
18	110.5	28.6	2.42×10^{19}	1.8×10^{16}
19	107.4	26	2.53×10^{19}	1.35×10^{17}
20	129	32	2.53×10^{19}	7.37×10^{16}
21	118.9	29	2.56×10^{19}	2.6×10^{16}

orders of magnitude observed in the vicinity of the transition (see Table 2).

Changes in the resistivity of samples at the temperature at which an experiment is performed, depending on the concentration of nitrogen impurity, can be traced by changes in the resonator *Q* factor, and, thus, the critical concentration at which the IM phase transition occurs can be estimated. As is known, the amplitude of the reference ESR signal *A* is proportional to the resonator *Q* factor, which, in turn, is inversely proportional to the conductance Σ of a sample when its resistance is high. Thus, the relation for *A* can be written as

$$A \propto Q \propto 1/\Sigma \propto 1/\sigma V, \quad AV \propto 1/\sigma = \rho, \qquad (1)$$

where *V* is the volume of a sample and σ and ρ are the sample conductivity and resistivity, respectively.

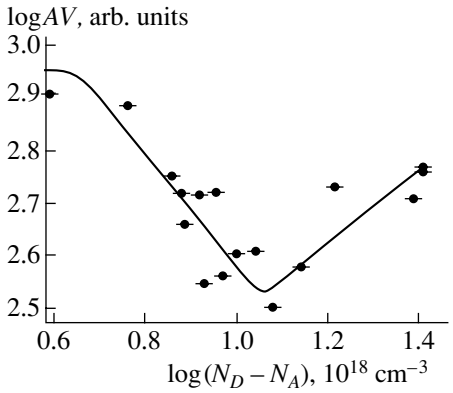

Fig. 1. The product of the amplitude of the ESR reference line and the volume of a 4*H*-SiC sample studied as a function of the impurity concentration.

Figure 1 shows the dependence of the product $A \times V$ on the electron density. It can be seen that the resonator *Q* factor has a minimum at an electron density of about 1.1×10^{19} cm^{-3}. This means that the conductivity of samples with such an electron density becomes fairly high at liquid-helium temperatures and that the IM phase transition should occur somewhere in this region. The increase in the *Q* factor with a further increase in the density of charge carriers is due to the decrease in the thickness of the skin layer.

3. RESULTS

Figure 2 shows how the ESR spectrum recorded at $T = 3.2$ K changes with the concentration of uncompensated nitrogen impurity increasing. One can see that, with increasing donor concentration, a number of radical changes occurs in 4*H*-SiC, as well as in other semiconductors. At a low impurity concentration, in accor-

dance with the value of the nuclear spin of the nitrogen atom ($S = 1$), the spectrum consists of three lines of hyperfine structure (spectrum *1*). In addition, two weaker lines from donor pairs of nitrogen atoms, in which one electron interacts with two nuclei in the triplet state, are observed between these three lines. The nuclear spin of such pairs ($S = 2$) should yield five lines of hyperfine structure; however, the positions of three of these lines coincide with the positions of the main lines. The other two are located between the three above-noted lines and are well resolved in the ESR spectrum. The presence of such lines directly points to some interaction between donors in 4*H*-SiC even when their concentration $N = 2.3 \times 10^{17}$ cm^{-3}.

When the donor concentration increases to $3–4 \times 10^{18}$ cm^{-3}, the hyperfine structure vanishes completely, and the spectrum is transformed into a homogeneously broadened single line (spectrum *2*). This effect, as applied to 6*H*-SiC, is considered in detail in [8]. With the impurity concentration increasing further, this line, remaining single, begins to distort and acquires a Dysonian shape (spectrum *3*). This means that, at such concentrations, the sample conductivity begins to affect the line shape at the liquid-helium temperature. In this region, the spin density begins to decrease with the Hall concentration increasing (the procedure for determining the spin density is given below). Let us denote the line in spectrum *3* by the index *I*. In the next stage (spectra *4*, *5*), a narrower undistorted line appears against the background of the main line and gradually begins to dominate in the spectrum. We denote it by the index *II*. The width of this line does not change with increasing impurity concentration, whereas the main line decreases in amplitude and broadens.

Finally, at a concentration of about 1.4×10^{19} cm^{-3}, the next radical change in the spectrum is observed (spectrum *6*). The main line broadens so much and becomes so distorted that it begins to resemble a dispersion line. An additional broad, positive low-field wing arises in it. Apparently, this wing is also observed at lower concentrations, but turns out to be much weaker than the negative strong-field wing. The presence of these features is the consequence of the Dyson theory, but, in the theory of the line shape for metals, the amplitudes of additional wings turn out to be much smaller than those of the main lines; hence, the additional wings are disregarded. In our case, these additional peaks are comparable with the main line.

In addition, two additional lines begin to manifest themselves in strong fields in the same concentration range: a narrower line *III* and a broader line *IV*, which are observed as single lines only when $H \parallel c$. At other sample orientations, the lines split into several components. A further increase in the impurity concentration leads to disappearance of the broad line, which was dominant at low concentrations. At such concentrations, the ESR spectrum of 4*H*-SiC consists of the narrow line *II* at approximately the same position where the central line of hyperfine structure was observed at low nitrogen concentrations and of two lines in the strong-field region: line *III*, which is narrower and stronger, and line *IV*, which is broader and weaker (spectrum *7*).

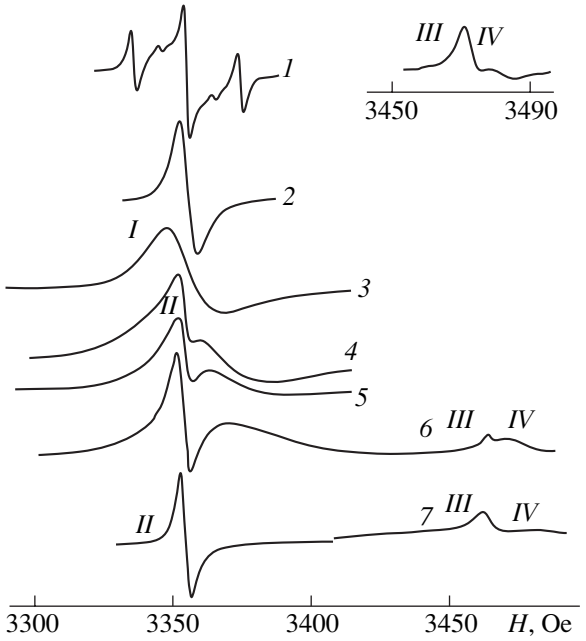

Fig. 2. Transformation of the ESR spectrum of 4*H*-SiC at a temperature of 3.2 K in the vicinity of the IM phase transition; the impurity concentration $N_D–N_A$ is (*1*) 2.3×10^{17}, (*2*) 3.9×10^{18}, (*3*) 9.3×10^{18}, (*4*) 1×10^{19}, (*5*) 1.1×10^{19}, (*6*) 1.4×10^{19}, and (*7*) 2.5×10^{19} cm^{-3}.

Thus, in the vicinity of the IM phase transition, the ESR spectrum of 4*H*-SiC radically changes.

4. ANALYSIS AND DISCUSSION

4.1. Concentration- and Temperature-Related Changes in Spin Density

Mott suggested [1] that, by increasing the concentration of impurities in a semiconductor, either ferromagnetic or antiferromagnetic ordering of spins due to the interaction between charge carriers should occur even in the insulating state. Notably, the antiferromagnetic state arises in an electron subsystem with a symmetric *s*-type wave function. In the ESR, a decrease in the spin density with an increase in the Hall concentration corresponds to a transition which was observed previously in 6*H*-SiC [9, 10]. However, this phenomenon was only observed in a small number of samples, and it was not traced directly to the critical concentration, because it was impossible to heavily dope 6*H*-SiC (above 10^{20} cm^{-3}). In 4*H*-SiC, because the nitrogen impurity has shallower levels it is quite possible to attain the critical concentration (see Table 1), even

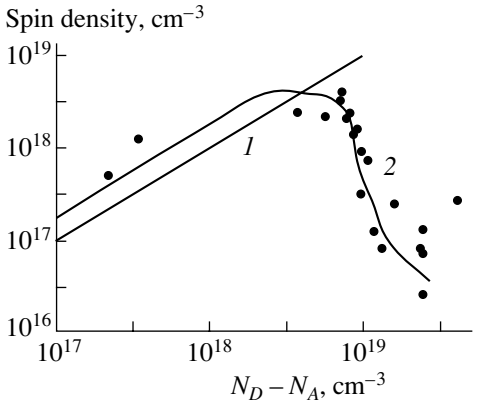

Fig. 3. (*1*) Dependence $n_s = n_H$ and (*2*) dependence of the spin density on the impurity concentration in 4*H*-SiC.

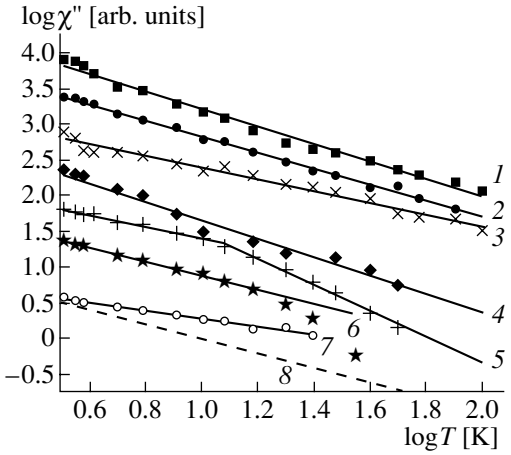

Fig. 4. Temperature dependence of the paramagnetic susceptibility χ" at impurity concentrations (*1*) 3.9×10^{18}; (*2*) 7.7×10^{18}; (*3*) 1.1×10^{19}; (*4*) 1.38×10^{19}; and (*5–7*) 2.53×10^{19} (for lines II–IV, respectively) cm^{-3}; dashed line (*8*) represents the Curie law (χ" $\propto T^{-1}$).

though the value of the critical concentration is still unknown.

Figure 3 shows the dependence of the spin density n_s on the Hall concentration $n_H = N_D - N_A$ at a temperature of 3.2 K. The spin density was determined by double integration of the narrower weak-field part of the ESR line and then comparing the result with the similarly integrated spectrum of a calibrated Varian sample. In order to find the error arising due to disregarding carriers responsible for the broader strong-field wing of the Dysonian absorption line, we also performed double integration of this part of the line for several samples. It turned out that the double integrals of both parts of the Dysonian absorption line only slightly differ from each other, but, since the strong-field wing is broader, it is less convenient for integrating. Accordingly, we estimated the spin density using the weak-field part of the line. When additional (narrow) lines were present in the ESR spectrum, their double integrals were summed. However, the corresponding correction was small, since additional lines were significantly narrower. For the case of the most heavily doped samples (17–21), when the broad line completely disappeared, the plot in Fig. 3 shows the spin density obtained by double integration of the narrow symmetric line II.

Two parts can be clearly distinguished in this dependence: at low nitrogen concentrations, the spin density increases with increasing Hall concentration, and, at high impurity concentrations, the situation is reversed. In order to make the data more illustrative, the straight line $n_s = n_H$ is shown in the region of increasing spin density in Fig. 3. It can be seen that the spin density somewhat exceeds the Hall concentration when the latter is lower than 10^{18} cm^{-3}. It is most likely due either to the fact that the additional ESR lines coinciding with the central nitrogen line are ignored or to some underestimation of the values of n_H measured at room temperature. At $N_D - N_A \cong 3 \times 10^{18}$ cm^{-3}, the spin density levels off, and, beginning with $n_H \cong 6 \times 10^{18}$ cm^{-3}, abruptly starts to decrease and becomes lower than the Hall concentration.

The cause of the observed decrease in the spin density is, most probably, antiferromagnetic interaction between spins, which is enhanced when the IM phase transition is approached. Due to this circumstance, when the impurity concentration is about 2.5×10^{19} cm^{-3}, the measured value of the spin density is only 2.5×10^{16} cm^{-3}, i.e., about 0.001 of the concentration of introduced nitrogen impurity.

The temperature dependences of double integrals of lines for a number of samples with different concentrations of impurity are shown in Fig. 4. These dependences govern the behavior of the paramagnetic susceptibility χ" in these samples. As can be seen from Fig. 4, for all concentrations at which the main ESR line appears (dependences *1–4*), χ" is approximately proportional to $1/T$. After the main broad line *I* disappears, the remaining narrow line II behaves somewhat differently. The width of this line is independent of temperature; hence, the double integral is proportional to the line amplitude. Curve *5* represents the temperature dependence of the amplitude of this line. The dependence χ"(T) for this line is also almost linear at low temperatures, but transforms into a quadratic dependence at high temperatures.

The behavior of the new lines III and IV, which arise in strong fields at a rather high doping level, is also unusual. The width of both lines is independent of temperature. Therefore, the dependence χ"(T) can be expressed in terms of the temperature dependences of the corresponding amplitudes of the weak-field wing *A*. They are also shown in Fig. 4 (curves *6* and *7*, respec-

tively). It can be clearly seen that the amplitude of the weaker line decreases approximately proportionally to the root of temperature, and the amplitude of the stronger line is characterized by a more complex dependence: at low temperatures, it obeys the Curie law, and, at higher temperatures, it decreases more steeply. In addition, the g factor of both lines is anisotropic. We should note that the shape of the strong line III is also unusual because its derivative has only positive values. Notably, its central part, which generally decreases superlinearly with increasing field, decreases sublinearly in the case under consideration.

4.2. Antiferromagnetic Interaction between Spins

The characteristic dependence of the spin density on the impurity concentration, shown in Fig. 3, indicates unambiguously that, in the insulating state in the vicinity of the IM phase transition, coupling of spins with the formation of an antiferromagnetic system of the spin-glass type occurs at low temperatures. This coupling is characterized by the magnitude of the exchange interaction, which depends exponentially on the distance between spins in a pair. Evidently, with increasing concentration of a randomly distributed impurity, the spin coupling begins at pairs in which the spins are located closest together.

If we assume that pairs are formed by centers the distance between which is smaller than some value R_0 and are occupied with electrons, we can estimate the density of such pairs by recognizing that the probability W of the nearest neighbor being located at a distance from $r + \delta r$ is determined by the expression [8]

$$W = \exp(-4/3\pi r^3 N_0)4\pi r^2 N_0 dr, \qquad (2)$$

where $N_0 = N_D - N_A$ is the concentration of occupied impurity centers.

Then, the relative concentration of impurity centers forming coupled pairs, the distance between the spins of which is smaller than USSR, is determined by the integral

$$N/N_0 = \int_0^{R_0} \exp(-(4/3)\pi r^3 N_0)4\pi r^2 N_0 dr = 1 - \exp[-(4/3)\pi R_0^3 N_0]. \qquad (3)$$

The relative density of free spins involved in resonance absorption turns out to be exponentially decreasing with increasing impurity concentration:

$$n_s/N_0 = \exp[-(4/3)\pi R_0^3 N_0]. \qquad (4)$$

It can be seen from (4) that the dependence $\log(n_s/N_0) = f(N_0)$ should be linear. Figure 5 shows the corresponding portion of the concentration dependence of n_s (Fig. 3). We can see that, beginning with a nitrogen concentration of 7.2×10^{18} cm^{-3}, the points fall into a straight line with fairly good accuracy. This confirms the statistical nature of the coupling mechanism considered above. In addition, the characteristic distance, which governs the interaction between spins, can be found from the plot. This yields the following estimate: $R_0 = 5.1 \times 10^{-7}$ cm. It turns out (see below) that this distance has the same order of magnitude as the average distance between impurity atoms at which the IM phase transition occurs.

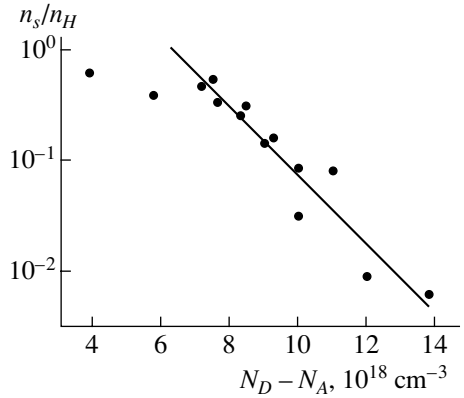

Fig. 5. Dependence of the relative spin density n_s/n_H on the concentration of uncompensated nitrogen impurity N_D–N_A.

Since the ESR signal is formed by unpaired spins located in the regions where the number of spins is relatively small in the vicinity of the IM transition, it is quite reasonable to assume that the temperature dependence of the paramagnetic susceptibility χ" is similar to the Curie law in these regions; i.e., the subsystem of free spins is nondegenerate. This is confirmed by the fact that χ" decreases approximately in inverse proportion to T (Fig. 4) in all samples from which a signal formed by unpaired spins of nitrogen atoms was measured.

However, with increasing temperature, the antiferromagnetic coupling of spins must cease to exist and they must convert to the paramagnetic state. This circumstance should weaken the temperature dependence of χ". Figure 4 shows that, with increasing impurity concentration, this dependence indeed tends to weaken (dependences *1–3*). Nevertheless, even in the most heavily doped samples (curve *4*), this dependence again becomes stronger. This circumstance points to the appearance of an additional mechanism of decay of the paramagnetic state at the impurity concentrations close to those at which line I vanishes.

For the lines that remain in the spectrum after the main nitrogen line disappears, other temperature dependences are observed. We will discuss these below when considering the origin of these lines.

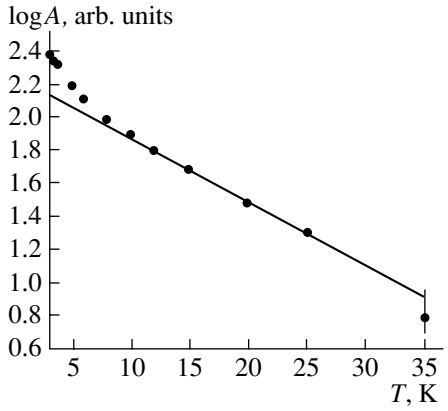

Fig. 6. Dependence of the amplitude of line III on temperature on the scale log (*A*) = *f*(*T*); (sample 20).

4.3. On the Origin of Additional ESR Lines in 4H-SiC

We will now discuss in more detail the possible origin of the additional ESR lines, denoted previously by the indices II–IV.

Line II appears even in the ESR spectra of relatively lightly doped samples and is present in the spectra up to the highest nitrogen concentrations. The main feature of this line is that it retains its high-symmetry shape even at the concentrations at which line *I* becomes strongly distorted and disappears. The *g* factor of line *II* is very close to that of the calibrated reference sample ($g = 2.0028$) and is independent of the crystallographic direction.

Since the theory of distortion of the Dysonian line shape is based on the concept of freely moving spins [21–23], we may suggest that the high symmetry of line II points to the fact that the spins responsible for this line are localized at certain impurity centers. This localization also remains in the metallic phase; thus, we may conclude that the localization centers are deep-level defects. The fact that the amplitude of this line is independent of the doping level is also in favor of this conclusion.

It follows from our measurements that the concentration of such defects is about 10^{16} cm^{-3} and that, at a nitrogen concentration in the range of 10^{17}–10^{18} cm^{-3}, line II is obscured by a strong, narrow nitrogen line. In some cases, upon increasing temperature, when the nitrogen line begins to broaden, this line can be distinguished against the background caused by nitrogen in the form of a certain change in the slope of the derivative of line I. In addition, as can be seen from Fig. 2, the central line in the ESR spectrum at a nitrogen concentration of 2.3×10^{17} cm^{-3} is not quite symmetric (it is disturbed), which is also indicative of the presence of an additional line in the ESR spectrum at relatively low concentrations of a shallow-level impurity. The origin of defects with deep states related to line II remains unknown.

Lines III and IV become distinct only at concentrations exceeding 10^{19} cm^{-3}, when the material transforms into the metallic state. Therefore, they are most probably related to the metallic phase. A line similar to line III was previously observed by us in the spectrum of compensated Ge [16], where it had a number of special features. First, this line was observed only when the sample became insulating in its entirety and the metal conductivity remained only in isolated clusters; in other words, this line appeared in the insulating phase in the vicinity of the IM phase transition. Second, this line appeared at temperatures below 4.1 K. Third, it manifested itself in the splitting of the main resonance line and rapidly shifted to stronger fields with decreasing temperature.

The important general feature of the split-off line in the spectrum of Ge and of line III is that both have an unusual shape. Specifically, the negative part of the derivative is completely absent, and the falloff of the positive part is retarded as it approaches zero; i.e., the line itself is shaped as a step or is highly asymmetric in shape with an abrupt increase and very gradual falloff. (In the latter case, the negative part of the line cannot be observed due to insufficient sensitivity of measurements.)

We should also note that line III is located in the strong-field region; i.e., its *g* factor is significantly smaller than 2. This line is observed as being a single one only when the field is directed along the *c* axis. At other directions of the magnetic field, this line splits into three, one of which does not change its position under rotation around the axis perpendicular to the *c* axis, and the other two shift to weaker fields. The measurements showed that $g_\perp = 1.9383$, $g_{\parallel 1} = 1.9556$, and $g_{\parallel 2} = 1.9584$. The relationship observed, $g_\parallel > g_\perp$, indicates that it is electrons that are most probably responsible for this line [24]. For electrons, the *g* factor is directly related to the effective mass. The relationship $g_\parallel > g_\perp$ is consistent with the anisotropy of conductivity in 4*H*-SiC, for which $\rho_\parallel/\rho_\perp = 0.9$. We could not rotate samples in the *C* plane; therefore, the extent of anisotropy of the line in this plane is not accurately known. However, it is clear that the components g_x and g_y should not differ significantly from the values of $g_\parallel$ obtained.

The temperature dependence of the amplitude of line III is also unusual. At low temperatures, it obeys the Curie law (Fig. 4, curve *6*); i.e., the density of spins responsible for this line remains constant in the low-temperature region. At higher temperatures ($T > 10$–12 K), the falloff becomes appreciably more steep. Since the line width remains constant in this case, this phenomenon should be attributed to the decrease in the density of spins responsible for this line. The analysis of this dependence in other coordinates showed that its high-temperature part becomes close to linear in the coordinates $\log(A) = f(A)$ (Fig. 6).

Such an unusual temperature dependence of line III resembles the Shubnikov–de Haas effect, in which the amplitude of oscillations also decreases with increasing temperature and obeys the same law due to the fact that the Landau levels become diffuse with increasing temperature [25]. We may suggest that, in our case, the density of spins responsible for line III also decreases due to the temperature-induced spreading.

We suggested previously [16] that a line with such a shape is due to free electrons moving with different velocities in an external electromagnetic field. Interacting with fluctuations of the potential at the bottom of the conduction band, a free electron is affected by alternating electric fields, whose frequency depends on the velocity of the electron itself and, consequently, on its energy. The higher the energy of an electron, the higher the frequency of the field it is affected by and the higher the magnetic-field strength required to satisfy the resonance conditions

$$h(\nu + \nu_0) = g\mu_B(H + \Delta H), \quad (5)$$

where ν is the frequency of an external microwave field; ν_0 is the frequency arising due to the motion of an electron across spatial potential fluctuations; and ΔH is the strength of an additional magnetic field required to satisfy the resonance conditions for a free electron.

In addition, in the case of antiferromagnetic interaction between electrons, when impurity centers form the spin-glass state, regions of local magnetic fields arise in a semiconductor between magnetically coupled but spatially separated spins. A moving spin, passing through such regions, also perceives their magnetic fields as alternating. These fields, along with the fluctuations of electric fields considered above, must shift the resonance line to stronger fields according to relation (5). Thus, in the vicinity of the IM phase transition, there may exist two systems of spatially nonuniform internal fields in a semiconductor, which shift the resonance line to stronger external magnetic fields.

We may assume that, when a system of spins transforms into the metallic state, only a very small fraction of these spins are involved in the resonance absorption of energy, since the major fraction of spins are antiferromagnetically coupled. Due to this circumstance, the amplitude of line III is much smaller than that of line I.

In contrast to line III, line IV splits into three lines and shifts to stronger fields when the direction of an external magnetic field does not coincide with the *c* axis. For this line, $g_\perp = 1.9268$, $g_{\parallel 1} = 1.9004$, and $g_{\parallel 2} = 1.8846$. Concerning shallow-level impurities in semiconductors, such a relationship between $g_\parallel$ and $g_\perp$ ($g_\parallel < g_\perp$) is typical of holes [25]. The ESR for holes was observed in Si upon uniaxial compression, which removes the degeneracy at the top of the valence band. In the 4*H*-SiC samples under study, internal stresses are sufficiently strong to remove the degeneracy at the top of the valence band. However, it is unclear how holes can appear in heavily doped and moderately compensated *n*-type material. Thus, the origin of line IV remains unclear.

5. CONCLUSIONS

(1) The main resonance line I is due to microwave absorption by individual spins and is observed only in the insulating state. With increasing doping level, absorption increases linearly with increasing donor concentration; however, at a nitrogen concentration of ~ 2–3×10^{18} cm^{-3}, this dependence levels off and, at $N \geq 6 \times 10^{18}$ cm^{-3}, abruptly falls off, turning to zero in the vicinity of the IM phase transition.

(2) The abrupt falloff of the resonance line I can be attributed to spin coupling and the formation of a state of the type of antiferromagnetic spin glass. The IM phase transition occurs specifically from this state.

(3) In the metallic state, new resonance lines arise in 4*H*-SiC samples in strong magnetic fields (with a reduced *g* factor); these lines have noticeable anisotropy (lines III and IV). Line III is attributed to the appearance of free spins (in the upper Hubbard band).

ACKNOWLEDGMENTS

We thank M.V. Alekseenko for characterization of samples. We are also grateful to the participants of the Laboratory Seminar of Nonequilibrium Processes in Semiconductors, Ioffe Physicotechnical Institute, for their helpful participation in discussions.

This study was supported by the Russian Foundation for Basic Research, project nos. 00-15-96750 and 01-02-17813.

REFERENCES

1. N. F. Mott, *Metal–Insulator Transitions* (Taylor and Francis, London, 1974; Nauka, Moscow, 1979).
2. G. Feher, Phys. Rev. **114**, 1219 (1959).
3. B. G. Zhurkin and N. A. Penin, Fiz. Tverd. Tela (Leningrad) **6**, 1143 (1964) [Sov. Phys. Solid State **6**, 882 (1964)].
4. S. Maekawa and N. Kinoshita, J. Phys. Soc. Jpn. **20**, 1447 (1965).
5. H. Ue and S. Maekawa, Phys. Rev. B **3**, 4232 (1971).
6. K. Morigaki and S. Maekawa, J. Phys. Soc. Jpn. **32**, 462 (1972).
7. D. K. Wilson, Phys. Rev. A **134**, 265 (1964).
8. A. I. Veĭnger, Fiz. Tekh. Poluprovodn. (Leningrad) **1**, 20 (1967) [Sov. Phys. Semicond. **1**, 14 (1967)].
9. M. V. Alekseenko, A. I. Veĭnger, A. G. Zabrodskiĭ, *et al.*, Pis'ma Zh. Éksp. Teor. Fiz. **39**, 255 (1984) [JETP Lett. **39**, 304 (1984)].
10. A. G. Zabrodskii, M. V. Alekseenko, V. A. Il'in, *et al.*, in *Proceedings of 16th International Conference on Physics of Semiconductors* (Stockholm, 1986), p. 283.
11. M. A. Paalanen, S. Sachdev, and R. N. Bhatt, in *Proceedings of 16th International Conference on Physics of Semiconductors* (Stockholm, 1986), p. 1249.

12. J. D. Quirt and J. R. Marko, Phys. Rev. B **7**, 3842 (1973).
13. K. Morigaki and T. Mitsushita, J. Phys. Soc. Jpn. **20**, 62 (1965).
14. K. Morigaki and M. Onda, J. Phys. Soc. Jpn. **33**, 103 (1972).
15. D. P. Tungstall, P. J. Mason, A. N. Ionov, *et al.*, J. Phys.: Condens. Matter **9**, 403 (1997).
16. A. I. Veĭnger, A. G. Zabrodskiĭ, and T. V. Tisnek, Fiz. Tekh. Poluprovodn. (St. Petersburg) **34**, 46 (2000) [Semiconductors **34**, 45 (2000)].
17. Yu. A. Vodakov, E. N. Mokhov, G. Ramm, and A. D. Roenkov, Krist. Tech. **14**, 729 (1979).
18. A. G. Zabrodskiĭ and K. N. Zinov'eva, Zh. Éksp. Teor. Fiz. **86**, 727 (1984) [Sov. Phys. JETP **59**, 425 (1984)].
19. R. F. Miligan, T. F. Rosenbaum, R. N. Bhatt, and G. A. Thomas, in *Electron–Electron Interaction in Disordered Systems*, Ed. by A. L. Efros and M. Pollak (North-Holland, Amsterdam, 1985), p. 231.
20. M. P. Timofeev, Candidate's Dissertation (Physicotechnical Inst., USSR Academy of Sciences, Leningrad, 1990).
21. F. J. Dyson, Phys. Rev. **98**, 349 (1955).
22. G. Feher and A. F. Kip, Phys. Rev. **98**, 337 (1955).
23. C. P. Poole, Jr., *Electron Spin Resonance* (Wiley, New York, 1967; Mir, Moscow, 1970).
24. G. W. Ludwig and H. H. Woodbury, in *Solid States Physics*, Ed. by F. Seitz and F. Turnbull (Academic, New York, 1962; Mir, Moscow, 1964), Vol. 13.
25. K. Seeger, *Semiconductor Physics* (Springer, Berlin, 1973; Mir, Moscow, 1977).

Translated by Yu. Sin'kov

Semiconductors, Vol. 37, No. 7, 2003, pp. 855–860. Translated from Fizika i Tekhnika Poluprovodnikov, Vol. 37, No. 7, 2003, pp. 883–889.

ELECTRONIC AND OPTICAL PROPERTIES OF SEMICONDUCTORS

Theoretical and Experimental Study of the Effect of InAs Growth Rate on the Properties of QD Arrays in InAs/GaAs System

V. G. Dubrovskiĭ, V. A. Egorov*, G. E. Cirlin*, N. K. Polyakov*, Yu. B. Samsonenko*, N. V. Kryzhanovskaya**, A. F. Tsatsul'nikov**, and V. M. Ustinov****

**Institute for Analytical Instrumentation, Russian Academy of Sciences, St. Petersburg, 190083 Russia*

***Ioffe Physicotechnical Institute, Russian Academy of Sciences, St. Petersburg, 194021 Russia*

e-mail: v_dubr@mail.ru

Submitted December 15, 2002; accepted for publication December 19, 2002

Abstract—The dependence of properties of quantum dot (QD) arrays in an InAs/GaAs system on the InAs growth rate has been investigated theoretically and experimentally. The derived kinetic model of the formation of coherent nanoislands allows the calculation of the average size, surface density of islands, and wetting layer thickness as functions of the growth time and conditions. Optical properties of InAs/GaAs QDs have been studied for the case of two monolayers (ML) of the material deposited at different growth rates. Predictions of the theoretical model are compared with the experimental data. It is shown that with two ML of the deposited material the characteristic lateral size of QDs decreases and the thickness of the residual wetting layer increases with rising growth rate. © *2003 MAIK "Nauka/Interperiodica".*

1. INTRODUCTION

The spontaneous formation of coherent nanosize islands in heteroepitaxial systems is currently used for the production of quantum dot (QD) arrays exhibiting 3D quantization [1]. Growing attention to QD semiconductor heterostructures is due to their unique optical properties defined by the atomic-like energy spectrum of electron states. The optical properties of semiconductor light-emitting devices with an active region based on QD heterostructures are defined, among other things, by the average lateral size, shape, size uniformity, space ordering, and surface density of islands [2]. The necessity to control the geometrical parameters of the QD arrays by modifying the growth technology parameters has stimulated theoretical [3–5] and experimental [6, 7] studies dealing with the kinetics of coherent island formation.

In this study, a theoretical model of the kinetics of QD formation in mismatched heteroepitaxial systems [4, 5] is developed. The model offers analytic dependences of the average size and surface density of islands at the kinetic stage as functions of the surface temperature and growth rate. Growth experiments in the InAs/GaAs system were performed, and the photoluminescence (PL) spectra of QDs grown at different rates of InAs growth at a fixed temperature of the surface were studied. The predictions of the theoretical model were compared with the obtained experimental data.

2. THEORY

The free energy of formation of a strained coherent island of i atoms by the Stranski–Krastanow mechanism is [4, 5]

$$\Delta F(i) = \Delta F_{elas} + \Delta F_{surf} + \Delta F_{attr}. \quad (1)$$

Here, ΔF_{elas} is the difference of the elastic energies of i atoms in an island and in the wetting layer, ΔF_{surf} is the difference of the surface energies of an island and the area of wetting layer covered with it, ΔF_{attr} is the difference of the energies of the attraction of the deposited atoms to the surface in an island and on the wetting layer surface. Further, an island is assumed to be a pyramid with a square base with a side L and base angle θ. In this case, the lateral size L and the number of atoms in an island i are related by

$$i = \left(\frac{L}{\alpha l_0}\right)^3, \quad (2)$$

where $\alpha = (6h_0 \cot\theta / l_0)^{1/3}$, h_0 is the monolayer height, and l_0 is the average interatomic distance at the surface. According to [4, 5], the free energy of the island formation $F \equiv \Delta F/k_BT$ (T is the substrate temperature; k_B is the Boltzmann constant) expressed in thermal energy units is given by

$$\frac{\Delta F}{k_BT} \equiv F = \frac{\sigma(\theta)/\cos\theta - \sigma(0)}{k_BT} L^2 - \frac{1}{k_BT}\left[(1-z)\lambda\varepsilon_0^2 - \frac{\Psi_0}{h_0}\exp\left(-\frac{h}{k_0h_0}\right)\right] l_0^2 h_0 i. \quad (3)$$

Here, $\sigma(0)$ and $\sigma(\theta)$ are the specific surface energies of the base and lateral facets of a pyramid with account for the renormalization caused by the lattice mismatch [1], z is the θ-dependent relaxation coefficient of the elastic energy in an island [8], λ is the elastic modulus of the deposit, ε_0 is the lattice mismatch, Ψ_0 is the density of

wetting energy on the substrate surface, and k_0 is the relaxation coefficient of the attractive force between atoms and the substrate [9]. The expression in square brackets in (3) is the difference of the chemical potentials of atoms in a wetting layer and in an island. The equilibrium wetting layer thickness is defined by the ratio of wetting to elastic forces, in accordance with the Müller–Kern criterion [9]:

$$h_{eq} = h_0 k_0 \ln\left(\frac{\Psi_0}{h_0(1-z)\lambda\varepsilon_0^2}\right). \quad (4)$$

The transition from 2D to 3D growth may occur only when $h > h_{eq}$, i.e., when the decrease of elastic energy in the system exceeds the energy expended to form an additional surface of an island and to overcome an attraction force. Introducing the degree of metastability $\zeta = h/h_{eq} - 1$, using (2), and linearizing (3) in ζ, we obtain a representation that is common in the theory of first-order phase transitions

$$F(i) = Ai^{2/3} - B\zeta i. \quad (5)$$

The constants A and B are defined as

$$A \equiv \frac{\sigma(\theta)/\cos\theta - \sigma(0)}{k_B T}\alpha^2 l_0^2,$$
$$B \equiv \frac{h_{eq}}{h_0 k_0}\frac{(1-z)\lambda\varepsilon_0^2 l_0^2 h_0}{k_B T}. \quad (6)$$

The obtained expression for the free energy of the island formation yields the following for the principal parameters of the classical theory of condensation [10]:

$$i_c(\zeta) = \left(\frac{2A}{3B\zeta}\right)^3, \quad F(\zeta) = \frac{4}{27}\frac{A^3}{B^2\zeta^2},$$
$$-F''(i_c) = \frac{9}{8}\frac{B^4\zeta^4}{A^3}. \quad (7)$$

Here, i_c is the number of atoms in a critical nucleus, $F(\zeta) = F(i_c(\zeta))$ is the activation barrier of nucleation, and $-F''(i_c)$ is the inverse half-width of the nucleus formation energy in the near-critical range.

The island nucleation rate is determined by the Zel'dovich relation [4, 10]

$$I = \frac{W^+(i_c)}{l_0^2}\sqrt{-\frac{F''(i_c)}{2\pi}}\exp(-F), \quad (8)$$

where $W^+(i_c)$ is the number of atoms incorporated into a critical nucleus in unit time. Taking into account (5), we obtain the rate of the island growth $\nu_i = di/dt$ in the overcritical range

$$\nu_i = W^+(i)B\zeta. \quad (9)$$

Apparently, two mechanisms of island growth are theoretically possible: the consumption of a material from the metastable "sea of adatoms" on the wetting layer surface [11] or directly from the wetting layer [4, 5]. In the former case, the wetting layer thickness remains invariable or increases, in the latter it decreases in the course of island growth. The experimental data obtained by ellipsometry in the Ge/Si(110) system [4] show that the wetting layer thickness decreases with time after reaching a critical value. Therefore, theoretical models [4, 5] assumed material consumption from the wetting layer to be the principal growth mechanism. In this case, the rate constant $W^+(i)$ can be approximated by the expression

$$W^+(i) = \frac{4D}{\nu l_0^2}\alpha i^{1/3}, \quad (10)$$

where D is the volume diffusion constant in the wetting layer and ν is the cutoff parameter for the elastic-stress field.

Using the Kuni method [12], the evolution equation for the island size distribution in the overcritical range can be expressed in terms of a natural variable for which the rate of island growth is size-independent. As follows from (9) and (10), the natural variable of the problem

$$\rho = i^{2/3} = \left(\frac{L}{\alpha l_0}\right)^2 \quad (11)$$

equals the island base area in $(\alpha l_0)^2$ units. The equation for the distribution function $g(\rho, t)$ is [4, 5, 11, 12]

$$\frac{\partial g}{\partial t} = -\frac{\zeta}{\tau}\frac{\partial g}{\partial \rho},$$
$$g(\rho, t=0) = 0, \quad g(\rho=0, t) = g_s(\zeta(t)). \quad (12)$$

Taking (10) into account, the characteristic time τ is defined by the expression

$$\tau = \frac{3l_0^2\nu}{8\alpha BD}. \quad (13)$$

The steady-state distribution

$$g_s(\zeta) = \frac{\tau}{\zeta}I(\zeta) = \frac{a}{l_0^2}\exp(-F(\zeta)) \quad (14)$$

is proportional to the nucleation rate and depends very strongly on the degree of metastability. Expression (14) is obtained by substitution of (10) into (8) with account of (13); the constant $a \equiv 3/4(\pi A)^{1/2}$. The instant of time $t = 0$ corresponds to $\zeta = 0$ and $h = h_{eq}$; i.e., the time is counted from the instant when the equilibrium thickness of the wetting layer is reached. The boundary condition for Eq. (12) is set at the point $\rho = 0$, because the near-critical islands are small and their contribution to the material balance equation is insignificant [11,12].

Equation (12) for the size distribution of islands contains an unknown function $\zeta(t)$, which can be found

using an equation for the material balance on the surface,

$$h_{eq} + h_0\int_0^t dt' V(t') = h + h_0 l_0^2 \int_0^\infty d\rho \rho^{3/2} g(\rho, t), \quad (15)$$

where $i = \rho^{3/2}$ is taken into account. The left-hand side of this equation defines the total amount of material deposited onto the unit surface area by the instant of time t; the integral term on the right-hand side gives the total volume of islands per unit surface area by the instant of time t. Below, the growth rate V expressed in monolayers per second (ML s^{-1}) is assumed to be constant at $t \le t_0$ and zero at $t > t_0$, where t_0 is the instant of growth interruption. Considering the definition of $\zeta(t)$, equation (15) can be transformed into

$$\Phi(t) = \zeta(t) + G(t), \quad (16)$$

where $G(t)$ is the total volume of islands divided by h_{eq}. The function $\Phi(t)$ defines the law according to which the amount of deposited material varies with time:

$$\Phi(t) = \begin{cases} t/t_\infty, & 0 \le t \le t_0 \\ t_0/t_\infty, & t > t_0, \end{cases} \quad (17)$$

where $t_\infty = h_{eq}/h_0 V$ is the time necessary for the formation of the wetting layer of equilibrium thickness.

Equations (12) and (16) constitute a closed system of equations for determining the island size distribution function $g(\rho, t)$ and the degree of metastability $\zeta(t)$. As shown in [12], an extremely steep dependence of the island nucleation rate on ζ and the independence of the island growth rate of their size allow an analytical solution of this problem. The physical prerequisite for the solution is the hierarchy of times of different stages in island formation. The duration of the nucleation stage, Δt, is much less than the time t_R of relaxation of the island-size distribution, which, in its turn, is much less than the time t_* of the formation of a wetting layer of critical thickness. Therefore, the nucleation of islands and the formation of an essential part of the size distribution proceed at a virtually constant wetting layer thickness corresponding to the maximum degree of metastability $\zeta_* \approx \Phi_*$. During the time interval Δt, the surface density of islands reaches its constant value N, which remains unchanged during subsequent island growth. Further, we will present the resulting relations [5] for the principal characteristics of the island formation process as functions of the energy parameters A and B and the control parameter $Q = t_\infty/\tau$.

The critical wetting-layer thickness $h_* = (\Phi_* + 1)h_{eq}$, where

$$\Phi_* = 0.24\frac{A^{3/2}}{B\ln^{1/2} Q}. \quad (18)$$

The time t_* of formation of the layer with critical thickness is $\Phi_* t_\infty$.

The surface density of islands on completion of the nucleation stage is given by

$$N = \frac{30}{l_0^2}\frac{h_{eq}}{h_0}\frac{B^2}{A^3}\frac{\ln^{3/2} Q}{Q^{3/2}}. \quad (19)$$

The time dependence of the average island size is given by

$$\frac{t - t_*}{t_R} = \ln\left[\frac{(1 + l + l^2)^{1/2}}{1 - l}\right] - \sqrt{3}\arctan\left(\frac{2l + 1}{\sqrt{3}}\right) + \frac{\pi}{2\sqrt{3}}. \quad (20)$$

Here, $l(t) \equiv L_*(t)/L_R$, $L_*(t)$ is the average size corresponding to islands that were nucleated at the instant of time when the critical wetting layer thickness was reached. The time of relaxation of the size distribution $t_R = 0.47 t_*/\ln^{1/3} Q$.

The characteristic lateral size of islands upon completion of the relaxation stage is defined by the expression

$$L_R = 0.2\alpha l_0 \frac{A^{3/2}}{B}\frac{Q^{1/2}}{\ln^{2/3} Q}. \quad (21)$$

The time dependence of the wetting layer thickness is $h(t) = (\zeta(t) + 1)h_{eq}$, where $\zeta(t) \approx \Phi(t)$ at $t < t_*$ and

$$\zeta(t) = \Phi_*(1 - l^3(t)), \quad t \ge t_*. \quad (22)$$

Taking into account the definition of the control parameter Q, Eq. (13) for τ, the definition of t_∞, expressions (6) for energy parameters A and B, and approximating the temperature dependence of the diffusion constant by the Arrhenius equation, we obtain from (19) and (21) the dependences for the average size and surface density of islands as functions of the surface temperature and growth rate:

$$\frac{L_R(\varphi, V)}{L_R^0} = \left[\frac{\ln(\lambda\varphi_0/V_0) - 2k\varphi_0}{\ln(\lambda\varphi/V) - 2k\varphi}\right]^{2/3} \times \frac{\varphi}{\varphi_0}\left(\frac{V_0}{V}\right)^{1/2} \exp(k(\varphi_0 - \varphi)), \quad (23)$$

$$\frac{N(\varphi, V)}{N_0} = \left[\frac{\ln(\lambda\varphi_0/V_0) - 2k\varphi_0}{\ln(\lambda\varphi/V) - 2k\varphi}\right]^{1/2}\left(\frac{\varphi}{\varphi_0}\right)^{1/2}\left(\frac{L_R^0}{L_R}\right)^3. \quad (24)$$

In these expressions, $\varphi = 1000\ \mathrm{K}/T$ is the dimensionless inverse temperature, $k \equiv T_D/2000$ K, $T_D \equiv E_D/k_B$ is the characteristic diffusion temperature, E_D is the activation barrier for diffusion in the wetting layer, $\varphi_0 = 1000\ \mathrm{K}/T_0$, and λ is the constant determined by reference values of L_R^0 and N_0 at the temperature T_0 and growth rate V_0. For the majority of heteroepitaxial systems, the control parameter Q is very large, usually in the range from 10^3 to 10^5, thus ensuring the applicabil-

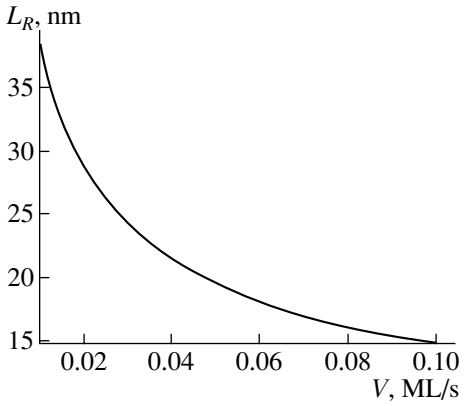

Fig. 1. The average island size upon termination of the stage of relaxation of the size distribution vs. the growth rate at T = const and $\lambda = 2 \times 10^6$.

ity of the classical theory of condensation to the description of the QD formation process and giving rise to the hierarchy of times for different stages in this process [5]. As follows from (23) and (24), the theoretical model predicts decreasing lateral size and increasing surface density of islands with rising growth rate by approximate power laws $1/V^{1/2}$ and $V^{3/2}$, respectively.

Figure 1 shows the average lateral size of the size distribution upon completion of the stage of relaxation which is calculated from (21) and (23). Figure 2 shows time dependences of the wetting layer thickness at different growth rates, which are calculated using relations (20) and (22) with the parameters of the heteroepitaxial InAs/GaAs system. The equilibrium layer thickness is 1.07 ML. The figure shows the results calculated for V = 0.03, 0.05, and 0.1 ML s^{-1}. The corresponding calculated critical thicknesses are 1.74, 1.76, and 1.79 ML; i.e., their dependence on the growth rate is weak. In the figures presented, the time is counted from the instants (30.8, 18.5, and 9.2 s, respectively) when the equilibrium layer thickness is reached.

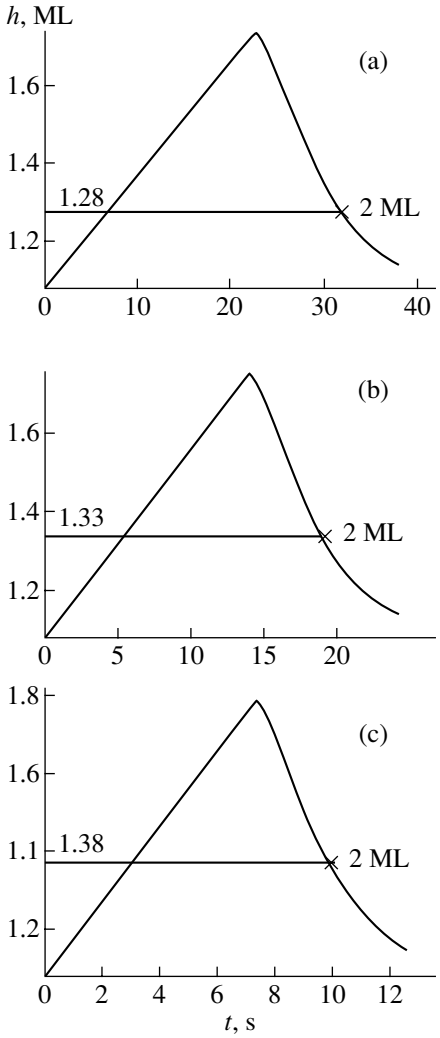

Fig. 2. Time dependences of the wetting layer thickness calculated for the parameters of an InAs/GaAs heteroepitaxial system for T = 485°C and different rates of InAs growth, V: (a) 0.03, (b) 0.05, and (c) 0.1 ML s^{-1}. The wetting layer thicknesses corresponding to two ML of the deposited material are shown.

3. EXPERIMENT

Growth experiments were performed in an EP1203 MBE machine with semi-insulating singular (100)GaAs substrates. After the oxide layer removal at 630°C and the GaAs buffer growth, an active region consisting of an InAs QD layer with an effective thickness of 2 ML was grown. The active region was confined within $Al_{0.3}Ga_{0.7}As$/GaAs short-period superlattices (25 Å/25 Å, 10 pairs) to prevent the transport of nonequilibrium carriers to the surface and substrate regions in the course of optical studies. On top, the structure was covered with a 50-Å-thick capping layer. The active region was grown at a substrate temperature of 485°C. To prevent the evaporation of In from the QD layer, a 50-Å-thick GaAs layer was grown immediately after the deposition of the active region at the same substrate temperature. Further, the substrate temperature was raised and the remaining part of the structure was grown at 600°C. To study the fundamental aspects of the growth of the InAs/GaAs QD system, a set of samples was grown with the In deposition rate varied from 0.01 to 0.1 ML s^{-1}. In all experiments, the residual pressure of As_4 vapor in the growth chamber was 1.8×10^{-6} Pa.

The deposition of InAs QDs was monitored by recording and analyzing RHEED patterns. An analysis of how the RHEED patterns vary has shown that a characteristic (of the Stranski–Krastanow mechanism) sharp transition from a streaky diffraction pattern, which corresponds to planar growth, to a pointlike pattern, which corresponds to 3D growth, was observed after the deposition of a 1.7–1.8 ML thick InAs layer in the entire range of growth rates under study.

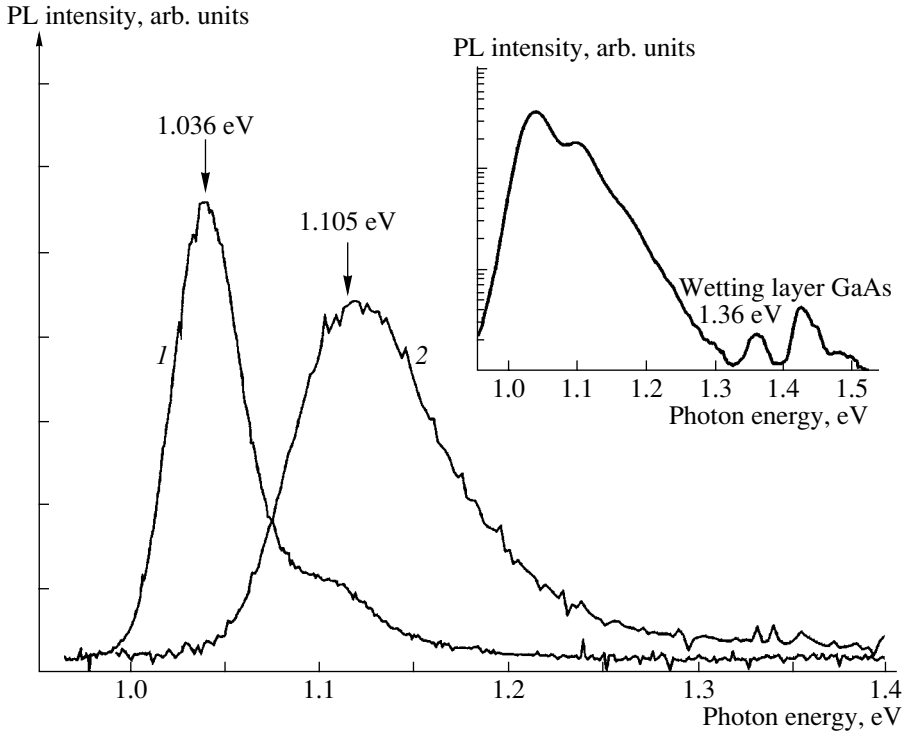

Fig. 3. PL spectra of samples with 2.0-ML InAs QDs deposited at growth rates of (*1*) 0.1 and (*2*) 0.01 ML s^{-1}, recorded at room temperature (300 K). Inset: a spectrum measured with enhanced excitation density in the spectral range corresponding to the emission from the wetting layer (wetting layer, GaAs) for a growth rate of 0.01 ML s^{-1}.

The PL was excited using an argon-ion laser (λ = 514.5 nm, the excitation density ~100 W cm^{-2}). The emission was detected with a cooled Ge photodiode.

The obtained spectra show that a PL peak related to recombination via QDs shifts steadily to longer wavelengths, from 1126 to 1196 nm, as the deposition rate decreases from 0.1 to 0.01 ML s^{-1} (Fig. 3). Figure 4 shows the dependence of the PL peak position on the growth rate. The red shift of the PL peak is associated with the increase of the lateral size of QDs, which occurs upon deposition for a longer time at a lower growth rate. A similar red shift of the PL peak is clearly pronounced when submonolayer migration-enhanced epitaxy [13] is used. In this case, the growing structure is kept for a certain time in an arsenic flow and the metal flow is interrupted, which enhances the surface migration of adatoms, thus making larger the lateral size of nanoislands. Hence, the red shift of the emission wavelength agrees qualitatively with the trends following from the results of theoretical calculations, which are shown in Fig. 1.

At a lower rate of InAs deposition, the PL spectra exhibit a second peak at a higher energy, which is increasingly pronounced at lower growth rates. This peak lies ~70 meV away from the main peak, and it can be associated either to the existence of excited levels in InAs QDs or to the appearance of two groups of nanoislands which differ in lateral size. To elucidate this effect, we are going to apply transmission electron microscopy to study the structural properties. The PL integral intensity decreases at lower rates of InAs deposition, which is presumably related to the decreasing of the surface density of nanoislands, and agrees with the theoretical predictions given in Section 2.

To determine the wetting layer thickness experimentally, we have studied PL spectra with the pumping density enhanced to 2 kW cm^{-2}. In this case, the spectra exhibit a line related to optical recombination in the wetting layer (see the inset in Fig. 3). The "effective"

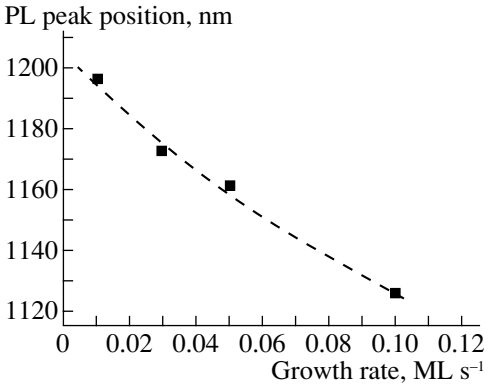

Fig. 4. The position of the PL peak related to InAs QDs vs. the InAs deposition rate.

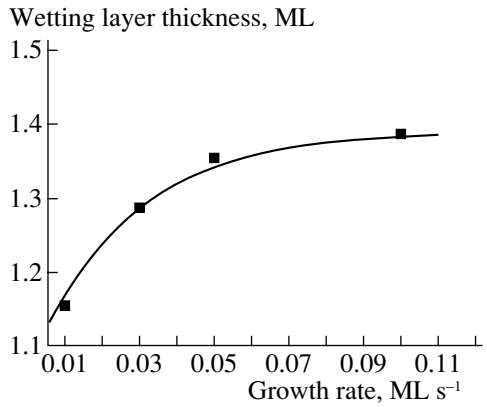

Fig. 5. Wetting layer thickness vs. the InAs deposition rate. Solid line: calculated dependence.

wetting layer thickness can be calculated from the position of this peak in the approximation of a thin InAs/GaAs QW.[1] In this approximation, we neglect the local fluctuations of the wetting layer thickness in the areas where finite-height QDs are situated; all of these contributions of QDs to the QW thickness are regarded as "averaged" over the sample. Since the QD density is not high ($\sim 10^{10}$ cm^{-2}), the error introduced by heterogeneities, i.e., QDs, to the wetting layer thickness is also not too significant. Figure 5 shows the experimentally determined wetting layer thickness in the InAs/GaAs system as a function of the InAs deposition rate and the results of calculations (solid line). As seen, the wetting layer thickness increases steadily from ~1.15 to ~1.36 ML as the growth rate increases from 0.01 to 0.1 ML s^{-1}, which is in good agreement with the theoretical calculations carried out in Section 2.

4. CONCLUSION

The dependence of the properties of QD arrays in an InAs/GaAs system on the InAs growth rate has been investigated theoretically and experimentally. The derived kinetic model of the formation of coherent nanoislands allows the calculation of the average size, surface density of islands, and the wetting layer thickness as functions of time and conditions of growth. The optical properties of InAs/GaAs QDs fabricated at different growth rates have been studied, and the predictions of the theoretical model are compared with the experimental data.

[1] Locally, the wetting layer consists of surface regions one-two atoms high. However, at room temperature, the PL spectral peaks related to corresponding QWs are superimposed. Therefore, here we use the term "energy position of the wetting layer peak" implying the superposition of peaks contributed by one- and two-atom surface areas with corresponding surface densities. It is necessary to note that the probability of thermal transport of carriers between the wetting-layer areas of different thicknesses is high at room temperature.

ACKNOWLEDGMENTS

This study was supported in part by programs of the Ministry of Industry and Science of the Russian Federation. G.E.C. acknowledges the support of the Alexander von Humboldt Stiftung.

REFERENCES

1. D. Bimberg, M. Grundmann, and N. N. Ledentsov, *Quantum Dot Heterostructures* (Wiley, Chichester, 1999).
2. N. N. Ledentsov, V. M. Ustinov, V. A. Shchukin, *et al.*, Fiz. Tekh. Poluprovodn. (St. Petersburg) **32**, 385 (1998) [Semiconductors **32**, 343 (1998)].
3. M. Meixner, E. Schöll, V. A. Shchukin, and D. Bimberg, Phys. Rev. Lett. **87**, 236101 (2001).
4. A. V. Osipov, F. Schmitt, S. A. Kukushkin, and P. Hess, Appl. Surf. Sci. **188**, 156 (2002).
5. A. A. Tonkikh, V. G. Dubrovskii, G. E. Cirlin, *et al.*, Phys. Status Solidi B **236**, R1 (2003).
6. N. N. Ledentsov, V. A. Shchukin, D. Bimberg, *et al.*, Semicond. Sci. Technol. **16**, 502 (2001).
7. A. A. Tonkikh, V. A. Egorov, N. K. Polyakov, *et al.*, Pis'ma Zh. Tekh. Fiz. **28** (5), 44 (2002) [Tech. Phys. Lett. **28**, 191 (2002)].
8. C. Ratsh and A. Zangwill, Surf. Sci. **293**, 123 (1993).
9. P. Müller and R. Kern, Appl. Surf. Sci. **102**, 6 (1996).
10. D. Kashchiev, *Nucleation: Basic Theory with Applications* (Butterworth Heinemann, Oxford, 2000).
11. A. V. Osipov, S. A. Kukushkin, F. Schmitt, and P. Hess, Phys. Rev. B **64**, 205421 (2001).
12. F. M. Kuni, Preprint No. 84-178.E (Kiev Inst. Teor. Fiz., 1984).
13. G. É. Tsyrlin, A. O. Golubok, S. Ya. Tipisev, *et al.*, Fiz. Tekh. Poluprovodn. (St. Petersburg) **29**, 1697 (1995) [Semiconductors **29**, 884 (1995)].

Translated by D. Mashovets

Semiconductors, Vol. 37, No. 7, 2003, pp. 861–865. Translated from Fizika i Tekhnika Poluprovodnikov, Vol. 37, No. 7, 2003, pp. 890–895.

LOW-DIMENSIONAL SYSTEMS

Control over the Parameters of InAs–GaAs Quantum Dot Arrays in the Stranski–Krastanow Growth Mode

N. A. Cherkashin*, M. V. Maksimov*, A. G. Makarov*, V. A. Shchukin*, V. M. Ustinov*, N. V. Lukovskaya*, Yu. G. Musikhin*, G. E. Cirlin*, N. A. Bert*, Zh. I. Alferov*, N. N. Ledentsov, and D. Bimberg****

**Ioffe Physicotechnical Institute, Russian Academy of Sciences, St. Petersburg, 194021 Russia*

e-mail: maximov@beam.ioffe.ru

***Technicshe Universität Berlin, Berlin, D-10623 Germany*

Submitted October 22, 2002; accepted for publication October 28, 2002

Abstract—The effect of the growth temperature on the density, lateral size, and height of InAs–GaAs quantum dots (QD) has been studied by transmission electron microscopy. With the growth temperature increasing from 450 to 520°C, the density and height of QDs decrease, whereas their lateral size increases; i.e., the QDs are flattened. The blue shift of the photoluminescence line indicates decreasing QD volume. The observed behavior is in agreement with the thermodynamic model of QD formation. The effect of lowering the substrate temperature immediately after the formation of QDs on the QD parameters has been studied. On lowering the temperature, the lateral size of QDs decreases and their density increases; i.e., the parameters of QD arrays tend to acquire the equilibrium parameters corresponding at the temperature to which the cooling is done. The QD height rapidly increases with cooling and may exceed the equilibrium value for a finite time of cooling, which enables fabrication of QD arrays with a prescribed ratio between height and lateral size by choosing the time of cooling. *© 2003 MAIK "Nauka/Interperiodica".*

1. INTRODUCTION

The prevalence of structures with unidimensional localization of carriers, i.e., quantum wells (QW), in modern semiconductor electronics is largely connected with the simplicity of their 2D bandgap engineering, which allows varying the width and composition of QWs and the bandgap of a matrix. Quantum-cascade lasers—very complex devices demanding a strictly defined band structure—have been proposed and designed. As further progress in semiconductor electronics will be associated with the wide application of structures with 3D localization of carriers, i.e., quantum dots (QD), the development of the bandgap engineering for these structures is an important fundamental and applied problem.

A recent breakthrough in the technology, physics, and device applications of QDs is associated with the use of self-organization processes in the course of epitaxial growth. It was shown experimentally and in theory that an array of elastically strained islands ordered in shape and size can be formed on the surface during the heteroepitaxial growth of strained layers [1]. Currently, the InAs-GaAs system, in which QDs are formed via Stranski–Krastanow growth mechanism, is the best studied and the most important for device applications. In spite of the fact that the self-ordering represents a decisive factor which enables the use of QDs as an active region in semiconductor devices, this effect imposes serious limitations on the possibility to control the shape and size of islands and, correspondingly, their band diagram. To overcome these limitations, a variety of techniques have been proposed, such as the formation of vertically-coupled QDs [2], the deposition of an initial layer of stressors [3], and the activated decomposition of a solid solution [4]. These technological approaches allowed for substantial progress in controlling the parameters of QD arrays. It is necessary to note that in all of the above-listed methods a layer of initial dots is formed at the first stage and subsequent growth is determined by the elastic field induced by this layer. Thus, control over the shape, size, and density of QDs in the Stranski–Krastanow growth mode can offer additional versatility in the application of more sophisticated technologies. In the present study, we have investigated the impact of temperature conditions on the height, lateral size, and density of InAs–GaAs QD arrays, and demonstrated that changing the temperature after the deposition of QDs allows the tuning of their parameters to be controlled.

2. EXPERIMENT

The structures were MBE-grown on semi-insulating (100)GaAs substrates. After removing the oxide from the substrate, a GaAs buffer layer was grown at the substrate temperature T_s = 600°C. To prevent the diffusion of nonequilibrium carriers into the substrate, a six-period GaAs/$Al_{0.25}Ga_{0.75}As$ (20 Å/20 Å) superlattice was grown on the buffer-layer surface. Further, a

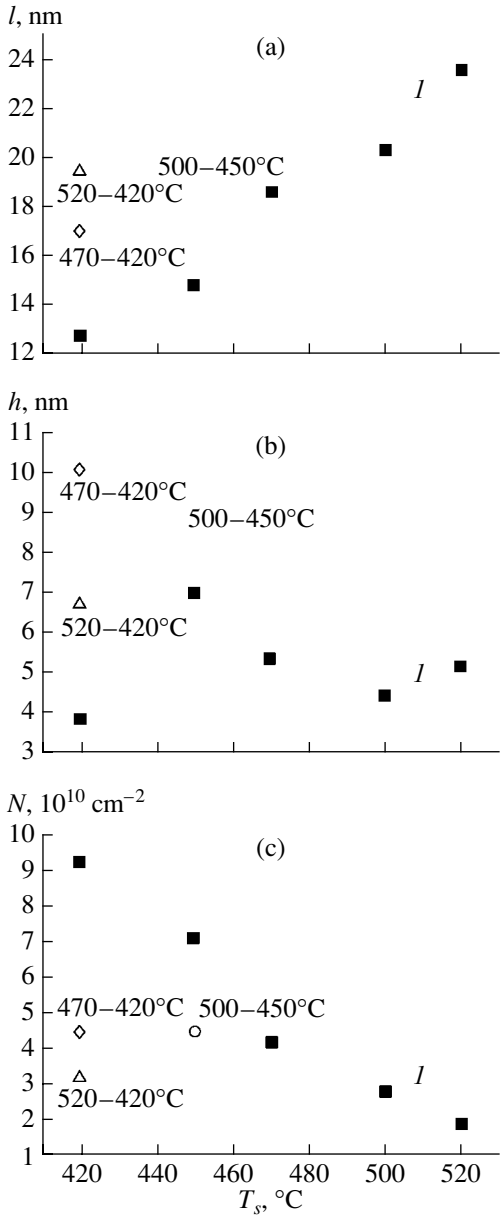

Fig. 1. Average (a) lateral size *l*, (b) height *h*, and (c) density *N* of QDs vs. the substrate temperature T_s. (*1*) Structures grown at fixed T_s; for structures grown with T_s lowered immediately after QD deposition, the growth temperatures and the final temperature of cooling are indicated.

0.1 μm-thick GaAs layer was grown, and then the substrate was cooled to the temperature of the QD deposition. Next, three InAs monolayers (ML) were deposited at temperatures of 520, 500, 470, 450, or 420°C. The formation of islands began at approximately 1.7 ML InAs. The formed QD layer was overgrown with a 100-Å-thick GaAs layer at the temperature of InAs deposition after a 10-s-interruption of growth. The 10-s interruption was necessary to improve the size uniformity of the island arrays [5]. Further, the substrate temperature was raised to T_s = 600°C, and a 400-Å-thick

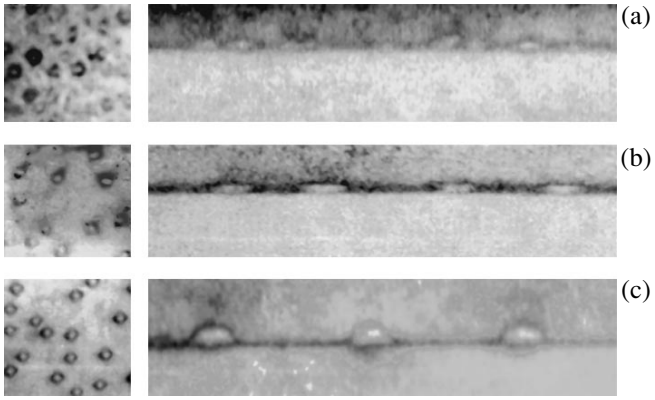

Fig. 2. TEM images of structures grown at (a) 450°C and (b) 500°C, and (c) cooled from 500 to 450°C for 120 s. Left: plan view images obtained under multiple-beam conditions along (001) zone axis; right: cross-sectional (010) images obtained under double-beam conditions with (200) reflection excited.

GaAs layer, a superlattice similar to the lower one, and a capping GaAs layer were grown in series. Another batch of samples was grown with the substrate temperature lowered after the deposition of QDs. In the modes used, the substrate was cooled for 120 s: from 520 to 420, 500 to 450, or 470 to 420°C. The QDs were overgrown with a GaAs layer at the final temperature.

The PL was excited by an argon-ion laser (λ = 514.5 nm, the excitation density 500 W cm^{-2}) and recorded using an MDR-23 monochromator and a North Coast E0/817R Ge *p–i–n* photodiode. A Philips EM 420 microscope with 100 kV acceleration voltage was used for transmission electron microscopy (TEM). The samples in planar (001) and transverse (110) and (010) configuration were prepared by standard thinning technology, i.e., grinding, polishing, and final sputtering of the material with Ar^+ ions at grazing angles to the sample surface.

3. THE EFFECT OF GROWTH TEMPERATURE ON THE PARAMETERS OF QD ARRAYS

Figures 1a, 1b, and 1c show, respectively, average values of the QD lateral size *l*, height *h*, and density *N* as functions of the substrate temperature. These dependences were obtained from an analysis of TEM images; typical images are shown in Fig. 2. As seen in Fig. 1, raising the substrate temperature from 420 to 520°C results in an increase in lateral size of QDs and a decrease in their density. The dependence of the QD height on T_s is more complicated: it is 4 nm for T_s = 420°C, decreases from 7 to 4.5 nm in the range 450–500°C, and at 500°C it is 6 nm. It is noteworthy that the values of the lateral size and height of an island determined from TEM images are very sensitive to the conditions of image recording, as well as the film thickness. Thus, the data shown in Fig. 1 indicate only a general tendency under similar conditions of image

recording. It should also be noted that the density and average lateral size were estimated based on the analysis of planar images containing several hundred QDs, whereas the height was determined from several cross-sectional images with the number of QDs an order of magnitude smaller. Therefore, the density and lateral size were determined with higher precision than the height.

To analyze the temperature dependence of the average QD volume, we can use the position of the PL spectral peak, i.e., the localization energy of the electron-hole pairs, E_{exc}. The localization energy depends on the QD volume and shape. The effect of the QD shape on the optical transition energy was calculated in [6]. It was shown that, for a fixed-volume InAs QD in a GaAs matrix, the change in its shape from a pyramid to a flat island results in a red shift of about 30 meV. Figure 3 shows the PL spectra of QDs grown at different temperatures. The temperature increase in the range from 450 to 520°C results in a blue shift of the PL spectrum, which indicates decreasing QD volume. Taking into account the increasing QD lateral size with rising substrate temperature (Fig. 1), we can conclude that the blue shift related to the decreasing QD volume and the red shift associated with decreasing QD height cancel one another.

It is evident that the experimentally observed decrease in the volume of islands contradicts the kinetic models of self-limited growth in the Stranski–Krastanow mode [7–9], which predict increasing island volume with rising temperature, due to a high coefficient of surface diffusion of adatoms and a weaker effect of the diffusion barriers at higher temperatures.

According to thermodynamic theories [10–13], arrays of 3D islands ordered in shape, size, and relative positions are a new class of equilibrium surface structures. According to the thermodynamic model, the effects of entropy make a smaller volume of islands more favorable at elevated temperatures [14]. For flat 2D islands of fixed height and different lateral sizes, the theory yields an approximate dependence of the island volume V on temperature T_s in the following form:

$$V(T_s) \approx V(0)\left[1 - \frac{T_s}{2T_{s\,\mathrm{ch}}}\right], \qquad (1)$$

where the characteristic temperature $T_{s\,\mathrm{ch}}$ depends on the island volume and has a value >800 K (530°C) for islands containing more than 1000 atoms. The observed decrease in the average volume of islands with rising temperature emphasizes the role of effects related to entropy, therefore being, in agreement with the thermodynamic model of island formation. Notwithstanding the fact that a real system of 3D islands with different shapes requires more sophisticated theoretical treatment than the one in [14], the general tendencies are the same because the effects of entropy in an equilibrium array of islands are responsible for a smaller volume at higher temperatures.

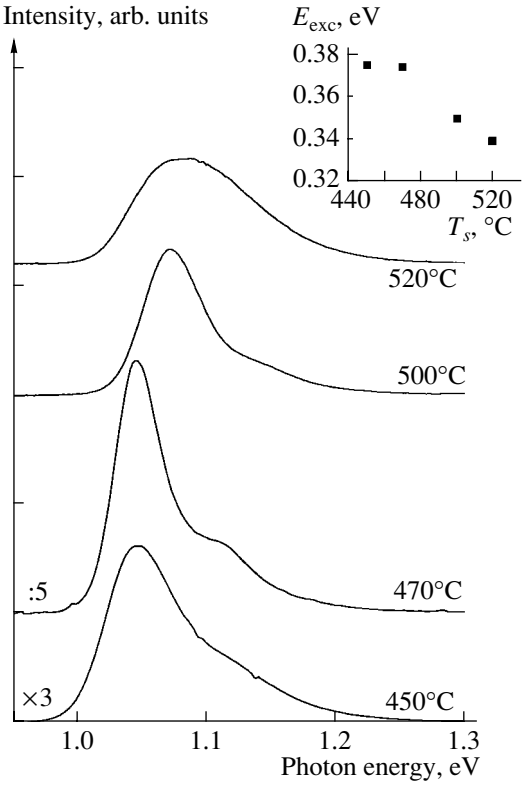

Fig. 3. PL spectra of QDs grown at different temperatures. Inset: the exciton localization energy in a QD, E_{exc}, with respect to the GaAs matrix. The spectra were recorded at T = 300 K.

It is necessary to note that the attainment of an equilibrium QD volume at low temperatures is possible only with prolonged interruptions in growth, because the exchange reactions at the surface are hindered. The small volume of the QDs grown at 420°C is due to the fact that, in our case, the same short-term interruption was made during the growth of all of the structures after InAs deposition. The increasing QD height at 520°C, which was observed in TEM images, can be attributed to broadening of the composition profile at high growth temperatures [18], which is confirmed by the blue shift of the PL line.

4. THE EFFECT OF DECREASING THE TEMPERATURE AFTER InAs DEPOSITION ON THE PARAMETERS OF QD ARRAYS

We have studied the behavior of an array of islands in the case of prolonged interruption of growth, and also in the case of lowering the temperature immediately after the deposition of InAs (prior to overgrowing with GaAs). The interruption of growth for 10 s improves the size uniformity of QDs [5]. Raising the period interruption to ~120 s at a fixed temperature does not modify the size and density of QDs, but results in the formation of large, randomly arranged clusters. With the interruption time made even longer, the den-

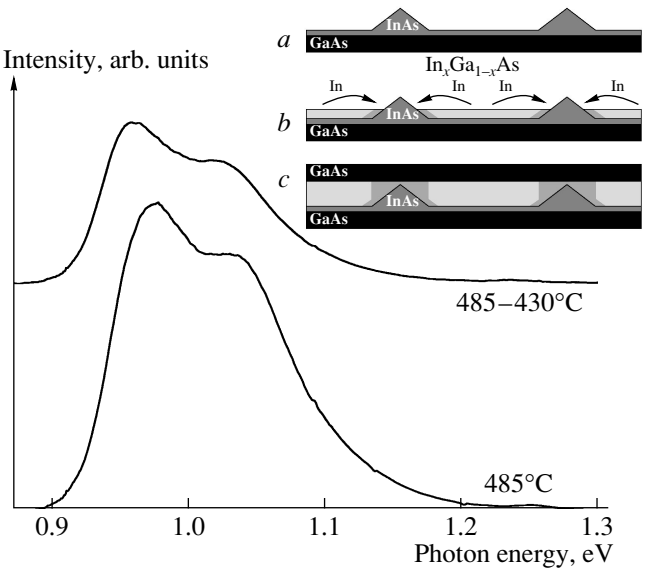

Fig. 4. PL spectra of QDs grown by activated decomposition of InGaAs solid solution at a fixed substrate temperature T_S = 485°C with the substrate cooled from 485 to 430°C after QD formation. Inset: the scheme of activated decomposition. The spectra were recorded at T = 300 K.

sity of large islands increases and that of coherent islands decreases [14, 5]. This effect can be accounted for as follows: according to the thermodynamic model, there exists a probabilistic size distribution of QDs. Though the probability of formation of large dots is low, a certain number of these exists on the surface. If the volume of an island exceeds some critical value, dislocations can develop within it. Such islands can be formed also due to nonideality of the substrate, i.e., the presence of defects and dislocations. The islands with dislocations attract In from small coherent islands located nearby. It is interesting to note that, even upon prolonged interruptions of growth, the size and shape of coherent QDs undergo only small changes, and no islands of intermediate size are observed. Thus, despite the fact that the applicability of the thermodynamic approach is, strictly speaking, limited by the presence of islands with dislocations, it appears to be valid for the subsystem of coherent QDs in this case as well.

Now we will discuss the effect of lowering the temperature after QD formation on the density, lateral size, and height of QDs. As seen from Figs. 1 and 2, cooling induces a decrease in the lateral size of QDs and a significant rise in their density. These trends are in qualitative agreement with the thermodynamic model, because, on lowering the temperature from T_{s_1} to T_{s_2}, the parameters of an array of islands tend towards the values corresponding to T_{s_2}. Owing to the finite time of cooling, the lateral size and density of dots do not have enough time to reach their equilibrium values corresponding to the final temperature. It is noteworthy that the average heights of QDs in structures grown with cooling significantly exceeds the heights of dots grown either at the initial or at the final temperature. This effect, which is presumably associated with the specific kinetics of attaining the equilibrium size by QDs, invites further study. The increase in the QD volume during cooling is confirmed by a strong red shift of the PL in the structures grown with the substrate temperature lowered in the course of deposition (Fig. 4).

Cooling the QD array immediately after InAs deposition offers new ways to control the density, lateral size, and height of QDs. For example, the density and lateral size of QDs grown at 500°C and cooled to 450°C nearly coincide with those for dots grown at 470°C, but the former are nearly two times higher. We believe that, with proper choice of the cooling rate and time, the parameters of QD arrays can be varied within certain limits.

We have also studied the effect of cooling on the properties of QDs produced by more sophisticated technology, specifically, the stimulated decomposition of InGaAs solid solution [4]. In this growth process, the initial InAs–GaAs points obtained by depositing a D_{IS} InAs ML are overgrown with $In_xGa_{1-x}As$ with an average thickness H (usually, D_{IS} = 1.7–3.5 ML InAs, x = 0–0.3, H = 0–6 nm). In the course of overgrowth with InGaAs, it is more energetically favorable for In atoms to diffuse toward QDs, in which the lattice constant is closer to that of InAs, and for Ga atoms to diffuse to inter-QD regions, in which the lattice constant is closer to that in GaAs. This process entails an effective increase in size of the initial QDs, with a corresponding red shift of the PL line. The inset to Fig. 4 schematically shows the activated decomposition of a solid solution. The fact that QDs are buried under the InGaAs layer provides an additional contribution to the red shift of the PL line because of a decrease in the band gap of the matrix and a redistribution of strain fields within QDs. The existence of several parameters of growth (D_{IS}, x, H) opens the way to efficiently control the parameters of QD arrays, in particular, to obtain an emission wavelength of 1.3 μm, while maintaining the high structural and optical quality of the samples.

Figure 4 shows the PL spectrum of a structure with QDs grown by activated decomposition of a solid solution at 485°C. In this case, the initial InAs islands obtained by depositing 2.4 MLs were overgrown with $In_xGa_{1-x}As$ (x = 0.15) with an average thickness of 6 nm. Cooling the structure to 430°C (after the formation of dots) resulted in a red shift of the PL line by ~30 meV. Thus, the general trends which are valid for the Stranski–Krastanow growth mode are also observed for QDs produced by more complicated technology—the activated decomposition of a solid solution.

5. CONCLUSION

The effect of substrate temperature on the parameters of QD arrays (density, lateral size, height) and on

the position of the PL spectral peak has been studied. As the temperature rises from 420 to 520°C, the lateral size of QDs increases from 13 to 23.5 nm and their density decreases from 9.2×10^{10} to 1.9×10^{10} cm^{-2}. The blue shift of the PL line, which is observed as the temperature rises from 450 to 520°C, is indicative of a decrease in the QD volume with rising temperature. The increasing lateral size with decreasing volume means that the dot height decreases, i.e., dots become flatter. The conclusion on decreasing QD height is confirmed by the TEM data (a slight increase in the height at 520°C observed in TEM images can be attributed to the broadening of the composition profile at higher growth temperatures). Decreasing QD volume with rising substrate temperature is in agreement with the predictions of the thermodynamic model for the Stranski–Krastanow growth mode, which predicts the existence of an equilibrium shape, volume, and density of QDs for a given substrate temperature. The small height of QDs at 420°C is accounted for by the low rate of exchange reactions at the surface, which results in a long time being required for QDs to reach the equilibrium size.

When the temperature is lowered immediately after the formation of QDs, their density, lateral size, and height tend to the equilibrium values, which correspond to the temperature at which cooling is done. In our experiments the time of cooling was limited (120 s), so the density and lateral size of QDs reached values intermediate between the equilibrium parameters for the initial and final temperatures. At the same time, the height of QDs increased very rapidly and exceeded the equilibrium value corresponding to the final temperature. Thus, the appropriate choice of the rate and time of cooling allows fabrication of QD arrays with the prescribed ratio between the height and lateral size of QDs. The choice of the growth temperature and the use of cooling immediately after the formation of QDs provides the opportunity to control the QD parameters in the Stranski–Krastanow growth mode, and also in the case of more complex technologies such as the formation of vertically coupled QDs [2], growth in the strain field of the initial layer of stressors [3], and activated decomposition of a solid solution [4].

ACKNOWLEDGMENTS

This study was supported by INTAS, the Russian Foundation for Basic Research, and the Ministry of Industry and Science of the Russian Federation program “Physics of Solid-State Nanostructures.”

M.V.M. and V.A.Shch. are grateful to the Alexander von Humboldt Foundation for research funding.

REFERENCES

1. D. Bimberg, M. Grundmann, and N. N. Ledentsov, *Quantum Dots Heterostructures* (Wiley, Baffins Line, Chichester, 1999).
2. N. N. Ledentsov, V. A. Shchukin, M. Grundmann, *et al.*, Phys. Rev. B **54**, 8743 (1996).
3. I. Mukhametzhanov, R. Heitz, J. Zeng, *et al.*, Appl. Phys. Lett. **73**, 1841 (1998).
4. M. V. Maximov, A. F. Tsatsul’nikov, B. V. Volovik, *et al.*, Phys. Rev. B **62**, 16671 (2000).
5. N. N. Ledentsov, M. Grundmann, N. Kirstaedter, *et al.*, Solid-State Electron. **40**, 785 (1996).
6. V. A. Shchukin, N. N. Ledentsov, V. M. Ustinov, *et al.*, Mater. Res. Soc. Symp. Proc. **618**, 79 (2000).
7. A. Madhukar, in *Low Dimensional Structures Prepared by Epitaxial Growth or Regrowth on Patterned Substrates*, Ed. by K. Eberl, P. Petroff, and P. Demeester (Kluwer, Dordrecht, 1995), p. 19.
8. A. L. Barabási, Appl. Phys. Lett. **70**, 2565 (1997).
9. D. E. Jesson, K. M. Chen, S. J. Pennycook, *et al.*, Phys. Rev. Lett. **77**, 1330 (1996).
10. V. A. Shchukin, N. N. Ledentsov, P. S. Kop’ev, and D. Bimberg, Phys. Rev. Lett. **75**, 2968 (1995).
11. I. Daruka and A. L. Barabási, Phys. Rev. Lett. **79**, 3708 (1997).
12. G. Medeiros-Ribeiro, A. M. Bratkovski, T. I. Kamins, *et al.*, Science **279**, 353 (1998).
13. V. A. Shchukin, N. N. Ledentsov, and D. Bimberg, *Epitaxy of Nanostructures* (Springer, Berlin, 2002), p. 320.
14. V. A. Shchukin, N. N. Ledentsov, and D. Bimberg, Mater. Res. Soc. Symp. Proc. **583**, 23 (2000).

Translated by D. Mashovets